Utah State University

DigitalCommons@USU

5-2002

Evapotranspiration Using a Satellite-Based Surface Energy Balance with Standardized Ground Control

Ricardo Trezza
Utah State University

Recommended Citation

EVAPOTRANSPIRATION USING A SATELLITE-BASED

SURFACE ENERGY BALANCE WITH

STANDARDIZED GROUND CONTROL

by

Ricardo Trezza

A dissertation submitted in partial fulfillment
of the requirements for the degree

of

DOCTOR OF PHILOSOPHY

in

Biological and Agricultural Engineering

Approved:

Dr. Wynn R. Walker
Major Professor

Dr. James L. Wright
Committee Member

Dr. Richard G. Allen
Research Director

Dr. Lawrence E. Hipps
Committee Member

Dr. Christopher M. U. Neale
Committee Member

Dr. Thomas Kent
Dean of Graduate Studies

UTAH STATE UNIVERSITY
Logan, Utah

2002

ABSTRACT

Evapotranspiration Using a Satellite-Based

Surface Energy Balance with

Standardized Ground Control

by

Ricardo Trezza, Doctor of Philosophy

Utah State University, 2002

Major Professor: Dr. Wynn R. Walker
Research Director: Dr. Richard G. Allen
Department: Biological and Irrigation Engineering

This study evaluated the potential of using the Surface Energy Balance Algorithm for Land (SEBAL) as a means for estimating evapotranspiration (ET) for local and regional scales in Southern Idaho. The original SEBAL model was refined during this study to provide better estimation of ET in agricultural areas and to make more reliable estimates of ET from other surfaces as well, including mountainous terrain. The modified version of SEBAL used in this study, termed as $SEBAL_{ID}$ (ID stands for Idaho) includes standardization of the two SEBAL "anchor" pixels, the use of a water balance model to track top soil moisture, adaptation of components of SEBAL for better prediction of the surface energy balance in mountains and sloping terrain, and use of the ratio between actual ET and alfalfa reference evapotranspiration (ET_r) as a means for obtaining the temporal integration of instantaneous ET to daily and seasonal values.

Validation of the SEBAL$_{ID}$ model at a local scale was performed by comparing lysimeter ET measurements from the USDA-ARS facility at Kimberly, Idaho, with ET predictions by SEBAL using Landsat 5 TM imagery. Comparison of measured and predicted ET values was challenging due to the resolution of the Landsat thermal band (120m x 120 m) and the relatively small size of the lysimeter fields. In the cases where thermal information was adequate, SEBAL$_{ID}$ predictions were close to the measured values of ET in the lysimeters.

Application of SEBAL$_{ID}$ at a regional scale was performed using Landsat 7 ETM+ and Landsat 5 TM imagery for the Eastern Snake Plain Aquifer (ESPA) region in Idaho during 2000. The results indicated that SEBAL$_{ID}$ performed well for predicting daily and seasonal ET for agricultural areas. Some unreasonable results were obtained for desert and basalt areas, due to uncertainties of the prediction of surface parameters. In mountains, even though validation of results was not possible, the values of ET obtained reflected the progress produced by the refinements made to the original SEBAL algorithm.

(339 pages)

to my daughter Rebecca

ACKNOWLEDGMENTS

First of all, I am deeply grateful to God for all the help he gave me while carrying out this study about just a very small part of his amazing creation. Also thanks to God who gave me the happiness of becoming the father of my lovely daughter Rebecca during the time I was doing this research.

My sincere thanks to my major advisor, Dr. Richard Allen, for his wonderful guidance and encouragement through all the different stages of this research; it was a really great experience working under his direction. My sincere thanks to Masahiro Tasumi and Chris Bright for their constant input and friendship which made my learning experience more enjoyable, and to Dr. James Wright for making available his unique dataset and for many timing suggestions that really helped me to finish this work.

I also wish to express my gratitude to Dr. Wynn Bastiaanssen for sharing his wonderful ideas, and for all the valuable contributions he made during the course of this research, to Dr. Larry Hipps, Dr. Carlos Grassi, and Dr. Christopher Neale for all the knowledge they transmitted to me that was very helpful for this work, and to Dr. Wynn Walker who supported me as my major professor.

Special thanks to Dr. Lyman Willardson from whom I received constant encouragement and guidance since the first day I arrived at USU to pursue my degree, and to Clarence W. Robison (University of Idaho) for all his support and help.

I would like to express my gratitude to the institutions that have financially supported my study and research: NASA, Fulbright program, University of Idaho, Utah State University, CONICIT, and the University of Los Andes (Venezuela).

Finally, I want to thank my wife, Neyle, my parents, brother and sister, and Dr. Dario Canelon, Mrs. Igle Umbria, and Mrs. Linda John (USU) for all the support I always receive from them. My appreciation also goes to all my friends, classmates, faculty, and staff of the BIE department at Utah State University, USDA-Kimberly, and University of Idaho.

Ricardo Trezza

CONTENTS

LIST OF TABLES

LIST OF FIGURES

LIST OF SYMBOLS AND NOTATIONS

Symbol	Definition	Units
A	available energy for the above-canopy fluxes	W/m^2
A_s	available energy at the soil surface	W/m^2
B	radiation emitted from the body	W/m^2
c	speed of light	
C_c	coefficient for canopy evaporation	m/s
C_d	denominator constant for ASCE Penman-Monteith.	-
C_E	bulk transfer coefficients for water vapor	-
C_H	bulk transfer coefficients for sensible heat	-
C_n	numerator constant for ASCE Penman-Monteith eq.	-
Cp	specific heat of air	J/kg/K
$C_{radiation}$	radiation correction coefficient for 24-hour ET estimation	-
C_s	coefficients for soil evaporation	-
C_{wind}	windspeed correction coefficient for mountainous region	-
C_{zom}	surface roughness correction coefficient for sloping surfaces	-
d	zero displacement plane	m
D_e	cumulative depletion of soil water	mm
DN	digital number	-
DOY	day of year (Julian day)	-
d_r	inverse squared relative distance of the Earth-Sun	-
dT	near surface air temperature difference	K, °C
e_a	actual vapor pressure	kPa
e_s	saturation vapor pressure	kPa
E	evaporation	mm/hr, mm/day
EF	evaporative fraction	-
$ESUN_\lambda$	mean solar exoatmospheric irradiance for band λ	$W/m^2/sr/\mu m$
ET	evapotranspiration	mm/hr, mm/day
ET_o	grass reference evapotranspiration	mm/hr, mm/day
ET_p	potential evapotranspiration	mm/hr, mm/day
ET_r	alfalfa reference evapotranspiration	mm/hr, mm/day
ET_{ref}	standardized reference crop evapotranspiration	mm/hr, mm/day
ETrF	ET_r fraction	-
ETM+	enhanced thematic mapper	

f_g	fractional coverage of plant canopy	-
g	gravitational acceleration	m/s^2
G	ground heat flux	W/m^2
G_{sc}	solar constant	W/m^2
h	plank's constant	
h	crop height	m
h_i	instantaneous convective exchange coefficient	-
H	sensible heat flux	W/m^2
k	Von Karman's constant	J s
K_B	sky clearness index	-
K_c	crop coefficient	-
K_{cb}	basal crop coefficient	-
K_{cr}	reflectance-based crop coefficient	-
K_D	diffuse radiation index	-
K_e	coefficient for soil evaporation	-
K_h	turbulent exchange coefficients for sensible heat	-
K_s	water stress coefficient	-
K_t	air turbidity coefficient	-
K_{TS}	thermal conductivity of the soil	$m^{-1}s^{-1}\,°C^{-1}$
K_w	turbulent exchange coefficients for water vapor	-
L	adjustment constant for SAVI	-
L	Monin-Obukhov length	m
LAI	leaf area index	-
LE	latent heat flux	W/m^2
L_m	longitude of the measurement site	degree
L_z	longitude of the center of the local time zone	degree
L_λ	at-satellite spectral radiance of the band λ	$W/m^2/sr/\mu m$
NDVI	normalized difference vegetation index	-
NIR	reflectance of near infrared band	-
P	air pressure	kPa
P	energy consumed by photosynthesis	W/m^2
q	specific humidity	kg/kg
q'	instantaneous deviation of specific humidity from the temporal mean value	kg/kg
q_{sat}	saturation specific humidity	kg/kg
r_a	aerodynamic resistance	s/m
r_{ah}	aerodynamic resistance for heat transport	s/m

r_{ex}	extra resistance	s/m
r_s	surface resistance	s/m
R_a	extraterrestrial solar radiation	W/m^2
R_{ae}	thermal path radiance	$W/m^2/sr/\mu m$
R_c	corrected radiance	$W/m^2/sr/\mu m$
REW	readily evaporable water	mm
r_f	resistance of the leaf boundary layer	s/m
R_L	outgoing longwave radiation	W/m^2
R_n	net radiation	W/m^2
R_s	incoming solar radiation	W/m^2
R_{so}	clear sky solar radiation	W/m^2
	incoming shortwave reflected from the surface	W/m^2
R_{sky}	downwelling sky irradiance	$W/m^2/sr/\mu m$
s	surface slope	rad
S	amount of energy that goes into vegetation storage	W/m^2
SAVI	soil adjusted vegetation index	-
$SAVI_{ID}$	soil adjusted vegetation index - Idaho implementation	-
S_c	seasonal correction for solar time	-
S_{KB}	regression parameter	-
SM	soil moisture in percent by mass	%
SR	simple ratio	-
t	standard local time	hour
T	temperature	K, ºC
T'	instantaneous deviation of air temperature from the temporal mean value	K, ºC
T_a	air temperature	K, ºC
T_{aero}	aerodynamic surface temperature	K, ºC
T_c	radiometric temperature of a given crop	K, ºC
T^*_c	temperature of a crop that is transpiring under optimal soil moisture conditions	K,
T_{dew}	dew point temperature	K, ºC
TEW	total evaporable water	mm
T_f	temperature of the air within the foliage	K, ºC
TM	thematic mapper	-
T_{rad}	radiometric surface temperature	K, ºC
T_{ref}	near surface air temperature at a reference point	K, ºC
T_s	surface temperature	K, ºC
$T_{s\,DEM}$	DEM adjusted surface temperature	K, ºC
T_{soil}	temperature of soil surface	K, ºC
u	windspeed	m/s
u_*	friction velocity	m/s

VI	vegetation indices	
w	vertical wind speed	m/s
w_λ	weighting coefficient for band λ	-
W	precipitable water in the atmosphere	mm
x	parameter for calculation of Monin-Obukhov length	-
z	height	m
Z_e	depth of the surface soil subject to evaporation	m
z_{oh}	surface roughness for heat transport	m
z_{om}	surface roughness for momentum transport	m
Δ	slope of the saturation vapor pressure-temperature relationship	-
Γ'	proportional factor for G/R_n ratio	-
Γ''	extinction factor for G/R_n ratio	-
Ψ_h	stability correction factor for heat transfer	-
Ψ_m	stability correction factor for momentum transfer	-
α	surface albedo	-
$\alpha_{path\ radiance}$	albedo path radiance	-
αPT	Priestley-Taylor constant (1.26)	-
α_{toa}	albedo at the top of the atmosphere	-
β	bowen ratio	-
β_n	net radiation extinction coefficient	-
ε_{air}	atmospheric emissivity	-
ε_{NB}	narrow-band surface emissivity	-
ε_o	broad-band surface emissivity	-
ε_λ	emissivity of the body for a specific wavelength	-
ϕ	solar declination	rad
γ	psychrometric constant	kPa/^{o}C
γ	surface aspect	rad
φ	latitude	rad
λ	latent heat of vaporization	J/kg
λ	wavelength	μm

ν	kinematic viscosity of the air	-
θ	solar incident angle	rad
θ	potential air temperature	K
θ	volumetric soil water content	m^3/m^3
θ_{FC}	soil water content at field capacity	m^3/m^3
θ_{WP}	soil water content at wilting point	m^3/m^3
ρ	air density	kg/ m^3
ρ_λ	reflectance of band	-
σ	Stefan-Boltzmann constant	$W/m^2/K^4$
τ_{sw}	one-way shortwave transmittance of air	-
ω	hour angle of the sun	rad

CHAPTER I

INTRODUCTION

The management of water resources is one of the greatest challenges for humankind in this century. The knowledge of the physical laws and features that govern each component of the hydrologic cycle has an increasing importance. Within the hydrologic cycle, the evaporation process inherent to the different surfaces present on the Earth needs to be properly understood, so that we achieve a sustainable development of our water resources.

Particularly, the determination of consumptive use of water by crops at the regional scale is elementary in understanding whether resources management is adequate. Irrigated agriculture is the largest consumer of water in river basins in arid and semiarid regions, and water savings upstream can lead to additional water developments downstream in the basin (Bastiaanssen, 2000).

Experimentally, the measurement of evaporation can be made accurately with equipment that evaluates Bowen Ratio Energy Balance approach (Tanner, 1988), with eddy covariance techniques (Kizer and Elliot, 1991), and with weighing lysimeters (Wright, 1991). A limitation of these techniques is that they essentially produce point or small-area values of evaporation, and therefore, are applicable only to a relatively homogeneous area surrounding the equipment that is exposed to the same environmental factors (Moran and Jackson, 1991). Therefore, these methods fail to provide a proper indication of the evaporative conditions at the regional scale where water has to be shared by different sectors and users.

An evaluation of the spatial distribution of evaporation over a large area would be prohibitive using conventional point measurement techniques. To overcome the limitation of these methods, hydrological models and remote sensing techniques have been developed to estimate the evaporation and the related hydrological processes at the regional scale. However, hydrological models have the disadvantage that considerable expertise in model use and extensive field data are required to make proper model simulations at the regional scale feasible (Bastiaanssen et al., 2000).

Over the past decades there has been an effort to evaluate evapotranspiration (ET) over larger areas from primarily remotely sensed data. The major advantage of applying remote sensing is that the water consumed by the soil-water-vegetation can be derived directly without the need for quantifying other complex hydrological processes. A review of remote sensing algorithms to estimate evapotranspiration is presented in Kustas and Norman (1996) and Bastiaanssen (1998). Basically, there are three main approaches: a) semi-empirical and statistical methods, b) analytical, and c) numerical approaches. In the first approach, the total daily evapotranspiration is estimated from remotely sensed one-time-of-day radiometric surface temperature measurements, air temperature, and usually some correlation with a remote sensed vegetation index (Jackson et al., 1977). Analytical approaches estimate ET by combining remotely sensed spectral data with ground-based meteorological data to evaluate net radiation (R_n), sensible heat (H), and soil heat flux (G), and obtain latent heat flux (LE) as the residual from the energy balance (Kustas et al., 1990). The third class uses models that simulate the water and energy balance by solving numerical equations for heat and mass transfer, combining remotely sensed data and ground-based information (Choudhury and DiGirolamo, 1998).

Among the most promising approaches currently available to estimate ET, the Surface Energy Balance Algorithm for Land (SEBAL) has been designed to calculate the energy balance components at both local and regional scale with minimum ground data (Bastiaanssen, 1995). SEBAL has been tested under several irrigation conditions in Egypt, India, Sri Lanka, Pakistan and Argentina to diagnose the uniformity in crop consumptive use and crop water stress and irrigation performance. Because it requires a minimum amount of ground-level inputs, SEBAL has a great potential for use in developing countries where policies for water management are generally inadequate.

In this study, the SEBAL procedure was used to estimate evapotranspiration from the Snake River plain in Idaho, USA using Landsat 5-TM and 7-ETM+ imagery. Validation of the methodology at the local scale was performed by taking advantage of the lysimeter ET measurements available at Kimberly, Idaho, under the supervision of Dr. J. L. Wright. Seasonal ET maps developed for the region will be used by the Idaho Department of Water Resources as an input of the Eastern Snake River Plain ground water model, which is used to simulate groundwater levels, movement, and interactions of the aquifer system with stream-flows of the Snake River. A better ET estimate (spatially, temporally and in total magnitude) will improve the accuracy of the estimation of the net recharge input term for the groundwater model.

Statement of the Problem

Remote sensing is currently applied to estimate evapotranspiration and a variety of methods for estimating ET have been proposed. However, the majority of methods require calibrations that involve intensive ground measurements and local calibration.

The ground-based calibrations are used to predict ET for areas located near where the measurements were taken. This fact makes many current methods site-specific and far from being operationally applied.

To overcome this dependency of in situ measurements, the Surface Energy Balance Algorithm for Land (SEBAL) was proposed by Bastiaanssen et al. (1998). The advantage of the SEBAL procedure is that it allows the estimation of evapotranspiration for large areas using a small amount of ground based input. A self-calibration procedure is applied in SEBAL that "trains" the surface energy balance by defining it at two "anchor" pixels.

SEBAL is based on the energy balance, which gives it a robust theoretical framework. The original SEBAL (Bastiaanssen et al., 1998) makes use of some semi-empirical equations in order to keep the model as operational as possible. Examples of these equations are functions that estimate soil heat flux from albedo and surface temperature, and surface roughness from vegetation indices. Although tested and validated in a variety of environments, these empirical equations may need further calibration when applied to a new environment. Fortunately, the flexibility and open framework of SEBAL allows the modification of its components if better functions are available.

The advantage of remote sensing for operational large scale estimates of ET over traditional methods for ET estimation (such as lysimeters, eddy covariance, and Bowen ratio) is the ability to describe the spatial distribution of ET over relatively large areas. However, the values of ET derived from remote sensing applications, such as the ones that utilize satellite imagery, represent instantaneous values corresponding to the time

that the image was taken. Those instantaneous ET values are not very useful inputs for many hydrological and ecological applications where daily, weekly, and monthly values are commonly needed. For that reason, methodologies that provide the extrapolation of instantaneous ET values to longer periods are a subject that is being widely researched by the scientific community.

Some of the methods used to extrapolate instantaneous to daily values attempt to obtain daily ET directly from instantaneous measurements (Kustas and Norman, 1996). These methods rely strongly on local ground-based calibration. Other approaches are based on the evaporative fraction (EF), assuming that the ratio between ET and the available energy at the surface (i.e., the EF) is constant during the day (Brutsaert and Sugita, 1992; Shuttleworth et al., 1989; Bastiaanssen et al., 2000). However this assumption might not be applicable in areas where there is strong afternoon advection of desert heat into irrigated areas.

In the present study, besides the EF approach, the use of the alfalfa-based ET fraction (ETrF), defined as $ETrF = ET/ET_r$, where ET_r is the alfalfa reference evapotranspiration (Wright, 1982; Allen et al., 1998), is investigated as a means of extending instantaneous ET to daily ET values. The term ETrF was introduced by Allen et al. (2001), and Allen et al. (2002) to extend the traditional crop coefficient K_c (traditionally used for agricultural crops) to any kind of surface. The hypothesis here is that a fairly constant value of ETrF is expected to occur during the daytime, and is due to the similar radiative and aerodynamic response that both actual ET and reference ET might have with variation in weather parameters. Therefore, the value of instantaneous

ETrF, and the assumption that instantaneous and daily ETrF values are similar, might be useful to predict daily ET values.

The disadvantage of ETrF is the requirement of hourly weather measurements, including air temperature, humidity, wind speed, and solar radiation at one location in the satellite image. Therefore, use of ETrF removes SEBAL from operational use in many developing countries.

In addition to extrapolation within a day, the extrapolation of daily ET values to longer periods (i.e weekly, in between two satellite images or seasonal) represents a more complex problem, in which remote sensing ET has encountered one of its bigger limitations. Numerical and hydrological models have been incorporated to assist remote sensing in the description of the day to day variation of ET due to temporal changes in hydrological parameters within the study area (Mauser and Schadlich, 1998; Olioso et al., 1999; Ottle and Vidal, 1994; Drooger and Bastiaanssen, 2002).

To deal with the issue of estimating ET values over large periods of time, in particular the periods in between satellite images, an approach based on the crop coefficient (i.e. ETrF) was explored. By using local weather station data, the day by day variation in reference evapotranspiration can be estimated using a standardized operational expression of the Penman-Monteith equation for the alfalfa reference (ASCE-EWRI, 2002). Therefore, the same ETrF used for monitoring the temporal evolution of ET over a period of time is used to interpolate ET between images. The approach of considering ETrF as constant during a particular period of time is examined.

In this study, the application of the water balance model proposed by FAO-56 (Allen et al., 1998) is preliminarily tested for its use in accounting for changes in ET

resulting from precipitation between images. The approach of FAO-56 has the advantage that it is highly operational, but still considers all of the most relevant soil and hydrologic parameters needed to describe the evolution of the surface soil moisture. The use of the FAO-56 water balance will permit the adjustment of ETrF in response to the natural drying process of the surface stemming from the occurrence of wetting events such as precipitation.

In conclusion, the proposed study explores current and acceptable scientific procedures for estimating evapotranspiration from remote sensing in a operational way. According to Allen et al. (2002), ET maps generated using SEBAL or similar remote sensing based processing system will be routinely used in the near future as input to daily and monthly operational and planning models for dam operations, ground water management, irrigation water supply planning, water rights regulation, and hydrologic studies. Therefore, it is critical that dependable and robust methods for generating ET maps be evolved.

Objectives

The overall intent of this research is to improve means for generating ET maps for the Eastern Plain Aquifer region in Southern Idaho. An operational remote sensing model is required to be routinely applied by the Idaho Department of Water Resources (IDWR) as a tool for providing both historical and near-real time ET for modeling of groundwater, solving water rights disputes, and performing better management of the water resources of the area.

This study verifies and refines the remote sensing SEBAL procedure for estimating evapotranspiration and recommends enhancements of the approach by comparing estimated ET values from remote sensing to measurements of ET using precision lysimeters collected by Dr J.L Wright at Kimberly, Idaho, during the 1988-1991 period. The objectives of this study are the following:

1. Validate accuracy of the SEBAL remote sensing model in estimating ET by comparing against lysimeter ET measurements, and improve prediction of various components of the energy balance.

2. Evaluate different methods to extrapolate instantaneous ET to daily ET values:

   - Constant evaporative fraction EF method.

   - Constant reference ET fraction (ETrF) approach.

3. Evaluate different methods to extrapolate daily ET values to seasonal ET

CHAPTER II

LITERATURE REVIEW

Evaporation is the process where liquid water is converted into water vapor. The combination of the evaporation process that occurs from the soil surface and the transpiration from plants is called evapotranspiration (ET). The occurrence of the ET process has two major requirements: a) a source of energy that provides the latent heat of vaporization needed to produce the phase change from liquid to water vapor, and b) a vapor transport mechanism that moves the water vapor away from the surface, maintaining a vapor pressure gradient between the evaporating surface and the surrounding air.

Evapotranspiration has been a subject of study for many centuries. However, there are still uncertainties involved in the mentioned processes and a big effort is being made by the scientific community to improve the methodologies available for estimating evapotranspiration in different temporal and spatial scales. Next, a review of some approaches used for estimating ET is presented.

Lysimeter Water Balance Approach

According to Wright (1982) and Allen et al. (1996), highly sensitive weighing or floating lysimeters are one of the best methods for precisely measuring water loss from soil and crop canopy surfaces, and they have had very important input in the development and testing of the more theoretical micrometeorological methods for estimating ET.

Wright (1982) described two weighing lysimeters installed at Kimberly, Idaho, and their use to measure ET and to develop evapotranspiration crop coefficients.

Although being very accurate, lysimeters require constant maintenance and care to assure that plant density, height, and leaf area of vegetation inside and immediately outside the lysimeter are close to that of the surrounding fields.

Bowen Ratio Energy Balance
Formulation

According to Tanner (1988), the surface energy budget can be described in terms of the four major components by:

$$R_n - G - H - LE = 0 \tag{2.1}$$

where R_n is the net radiation, G is the heat stored in the soil, LE is the latent heat flux, and H is the sensible heat flux. Using the flux-gradient approach, latent and sensible heat fluxes can be expressed as:

$$LE = \lambda \rho K_w \frac{\partial \bar{q}}{\partial z} \tag{2.2}$$

$$H = \rho Cp K_h \frac{\partial \bar{\theta}}{\partial z} \tag{2.3}$$

where λ is the latent heat of vaporization; ρ is the density of moist air, K_w and K_h are the turbulent exchange coefficients for water vapor and sensible heat, respectively; $\partial q / \partial z$ and $\partial \theta / \partial z$ are the gradients of specific humidity and potential air temperature, respectively; and Cp is the specific heat of air at constant pressure.

If the difference in height between the two measurements of temperature is small, the potential temperature gradients can be approximated by the actual air temperature gradients. By definition, the Bowen ratio represents the relationship between the magnitudes of sensible and latent heat, therefore :

$$\beta = \frac{H}{LE} = \gamma \frac{K_h}{K_w} \frac{\partial \overline{T} / \partial z}{\partial \overline{e} / \partial z} \tag{2.4}$$

where γ is the psychrometric constant and $\partial e / \partial z$ is the gradient of vapor pressure. Assuming that K_h is equal to K_w and that $\partial T / \partial z \, / \, \partial e / \partial z \approx \Delta T / \Delta z \, / \, \Delta e / \Delta z$ Eq. (2.4) can be displayed as:

$$\beta = \gamma \frac{\partial \overline{T}}{\partial \overline{e}} \tag{2.5}$$

where ΔT and Δe are the vertical gradients of temperature and vapor pressure, respectively. Substituting H/β for LE and $LE*\beta$ for H in Eq. (2.1) yields:

$$H = \beta \frac{(R_n - G)}{1 + \beta} \tag{2.6}$$

and

$$LE = \frac{R_n - G}{1 + \beta} \tag{2.7}$$

The main requirement for the application of the Bowen ratio method is that temperature and humidity gradients be measured within the portion of the fully adjusted

boundary layer that is in equilibrium with the surface. Validation of Bowen ratio

measurements are described in Ohmura (1982) and Payero (1997).

Eddy Covariance Formulation

The fluxes of latent and sensible heat can be measured directly by correlating

fluctuations of vertical wind speed with fluctuations of the transported scalar. The

general theory of fluid transport includes a mean and a fluctuating component (Tanner,

1988; Kizer and Elliott, 1991). Therefore, assuming that perpendicular to the earth's

surface the mean vertical wind speed is zero due to conservation of mass, one can express

the turbulent fluxes by:

$$H = \rho Cp \overline{w'T'} \tag{2.8}$$

and

$$LE = \rho \overline{w'q'} \tag{2.9}$$

where the primes represent instantaneous deviations from the temporal mean value, w is

vertical wind speed, and q is specific humidity.

According to Hipps (1999) some conditions are required to get correct fluxes

through Eqs. (2.8) and (2.9). First an appropriate averaging period is required. This

period has to be long enough to include a number of samples large enough for statistical

reliability , but at the same time it has to be short enough to ensure that no long-term

trends in the mean are present. Hipps noted that for heights below 10 m, an averaging

period of about 30 min. is sufficient. In addition, the sampling rate has to be rapid

enough ($\approx 5 - 10$ Hz) to take into account all the fluctuations produced by the small, high frequency eddies present near the ground. The fluxes measured using the eddy correlation technique must be corrected for oxygen absorption (Tanner, 1988) and for density effects due to heat and water vapor transfer (Webb et al., 1980)

Resistance-Based ET Models

Jensen and Allen (2000) described the evolution of resistance-based evapotranspiration functions from the original equation developed by Howard Penman in 1948, and modified by John Monteith in 1965 to account for the surface resistance imposed by different surfaces and vegetations types. The Penman-Monteith equation combines the energy balance and aerodynamic transport theory being written as follows:

$$LE = \frac{\Delta(R_n - G) + \rho Cp \frac{(e_s - e_a)}{r_a}}{\Delta + \gamma\left(1 + \frac{r_s}{r_a}\right)} \tag{2.10}$$

where R_n is the net radiation, G is the soil heat flux, (e_s - e_a) is the vapor pressure deficit of the air, ρ is the mean air density at constant pressure, Cp is the specific heat of the air, Δ is the slope of the saturation vapor pressure temperature relationship, γ is the psychrometric constant, and r_s and r_a are the (bulk) surface and aerodynamic resistances, respectively.

The Penman Monteith equation assumes that the canopy and soil constitutes a "big leaf" from which all the transfer of energy and water vapor occurs. In the case of sparse vegetation, the sources and sinks of energy and mass are different for soil and

canopy. This fact has promoted the develop of multiple-layer models such as the

Choudhury and Monteith (1988) four-layer model and the Shuttleworth and Wallace

(1985) model. The Shuttleworth and Wallace (SW) model is basically a extension of the

Penman-Monteith model to two layers that considers the energy partitioning on the

canopy as well as the soil. In the SW model, the net evapotranspiration is given by:

$$LE = C_c PM_c + C_s PM_s \qquad (2.11)$$

where PM_c and PM_s are terms similar to the Penman-Monteith equation, corresponding

to evaporation from a closed canopy and from bare soil, respectively. C_c and C_s are

coefficients that weights the contribution of soil and canopy evaporation. The terms

PM_c and PM_s are expressed as follows:

$$PM_c = \frac{\Delta A + \left[\rho CpD - \Delta r_a^c A_s \right] / (r_a^a + r_a^c)}{\left[\Delta + \gamma \left(1 + (r_s^c / (r_a^a + r_a^c)) \right) \right]} \qquad (2.12)$$

$$PM_s = \frac{\Delta A + \left[\rho CpD - \Delta r_a^s (A - A_s) \right] / (r_a^a + r_a^s)}{\left[\Delta + \gamma \left(1 + (r_s^s / (r_a^a + r_a^s)) \right) \right]} \qquad (2.13)$$

where A is the available energy for the above-canopy fluxes, A_s is the available energy at

the soil surface, D is the water vapor deficit, r_a^a is the aerodynamic resistance between

the canopy source height and the reference height (s m-1), r_a^c is the bulk boundary layer

resistance of the vegetation elements within the canopy (s m-1) , r_s^c is the bulk stomatal

resistance of the canopy (s m-1), and $r_s{}^s$ is the surface resistance of the substrate (s m-1).

The SW aerodynamic term was later modified by Shuttleworth and Gurney (1990). Dolman (1993) extended the SW model to a multiple source model that considers the interaction between canopy, subcanopy, and soil surface.

Reference Evapotranspiration

Modified versions of the Penman equation were presented by Doorenbos and Pruitt (1977) and Wright (1982) to estimate evapotranspiration for reference crops (grass and alfalfa). More recently, Allen et al. (1998) presented the FAO-56 Penman-Monteith equation which is a reduced version of the full-form PM equation:

$$ET_o = \frac{0.408\Delta(Rn-G) + \gamma\frac{900}{T+273}u_2(e_s-e_a)}{\Delta + \gamma(1+0.34u_2)} \tag{2.14}$$

where ET_o is the grass reference evapotranspiration [mm day^{-1}], R_n is the net radiation at the crop surface [MJ m^{-2} day^{-1}], G is the soil heat flux density [MJ m^{-2} day^{-1}], T is the mean daily air temperature at 2 m height [°C], u_2 wind speed at 2 m height [m s^{-1}], e_s is saturation vapor pressure [kPa], e_a actual vapor pressure [kPa], Δ slope vapor pressure curve [kPa °C^{-1}], and γ is the psychrometric constant [kPa °C^{-1}].

In Eq. (2.14), ET_o represents the evapotranspiration occurring from a hypothetical well-watered grass surface with a crop height of 0.12 m, a fixed surface resistance of 70 s/m, and an albedo of 0.23 (Allen et al., 1998).

Walter et al. (2000) and ASCE-EWRI (2002), presented an equation for calculating reference evapotranspiration considering two different reference surfaces: a short crop with an approximate height of 0.12 m (similar to grass) and a tall crop with an approximate height of 0.50 m. (similar to alfalfa). The equation, referred as "the ASCE-EWRI Standardized Penman Monteith equation" is the following:

$$ET_{ref} = \frac{0.408 \Delta (R_n - G) + \gamma \frac{C_n}{T+273} u_2 (e_s - e_a)}{\Delta + \gamma (1 + C_d u_2)} \tag{2.15}$$

where ET_{ref} is standardized reference crop evapotranspiration for short (ET_o) or tall (ET_r) surfaces (mm d^{-1} for daily time steps or mm h^{-1} for hourly time steps), C_n a numerator constant that changes with reference type and calculation time step, and C_d is a denominator constant that changes with reference type and calculation time step.

Crop Evapotranspiration

The traditional routine for estimating the actual ET from a given crop involves the multiplication of the reference evapotranspiration (grass or alfalfa) by a crop coefficient K_c, which takes into account the ratio between the ET of a particular crop and that of a reference crop.

Wright (1982) and Allen et al. (1998) both presented two procedures (single and dual crop coefficients) for estimating the evapotranspiration of crops. In the crop coefficient approach the crop evapotranspiration (ET_c), is estimated by multiplying the reference crop evapotranspiration, (ET_o) by a crop coefficient K_c :

$$ET_c = K_c * ET_o \qquad (2.16)$$

It is presumed that the ET_o calculation incorporates the majority of effects of the various weather conditions. The coefficient K_c represents an integration of four characteristics closely related to the crop. These characteristics are:

a) crop height, which influences the aerodynamic resistance r_a, and the turbulent transfer of vapor from the crop into the atmosphere.

b) albedo, which influences the net radiation of the surface R_n.

c) canopy resistance, influenced by stomatal controls.

d) evaporation from soil, which influences the surface resistance r_s.

The value of K_c can be calculated as a single crop coefficient or as a dual crop coefficient. The single crop coefficient procedure incorporates average effects of soil moisture evaporation and includes the selection and adjustment of values of K_c for different growth stages of the crop and the construction of the K_c curve. The crop evapotranspiration is then calculated using Eq. (2.16).

The dual crop coefficient procedure involves the separation of K_c into two separate coefficients, one for primarily crop transpiration, called the basal crop coefficient (K_{cb}) and one for soil evaporation (K_e). The basal crop coefficient K_{cb} is defined as the ratio of ET_c / ET_o when the soil surface is dry, and transpiration is occurring at a potential rate. Mathematically, the dual crop coefficient procedure is expressed as:

$$ET_c = (K_{cb} + K_e) * ET_o \qquad (2.17)$$

Values of K_{cb} corresponding to different crops and different development stages are presented in Wright (1982) for alfalfa reference ET_r and in Allen et al. (1998) for grass reference ET_o. With regard to the coefficient of soil evaporation (K_e), the FAO-56 calculation procedure involves a water balance in the first 10 to 15 cm of the soil profile.

To account for the reduction of ET under soil water stress conditions, Wright (1982), Allen et al. (1998), and others proposed the use of a water stress coefficient K_s, so that one can calculate the resulting crop evapotranspiration as follows:

$$ET_{c\ adj} = (K_s K_{cb} + K_e) * ET_o \qquad (2.18)$$

where $ET_{c\ adj}$ represents the value of ET from the water-stressed vegetation, K_s is the stress coefficient, defined as $K_s = 1$ when there is not soil water stress, and $K_s < 1$ when the soil moisture is below a threshold value, which can generate stress in the crop.

The estimation of the values of reference evapotranspiration and actual ET values depends directly on the integrity of the weather data, and procedures for assessing this integrity are reported by Allen (1996) and Allen et al. (1998). The procedures include using clear-sky envelopes for evaluating calibration and functioning of solar radiation sensors and using net radiation estimation equations to compare with net radiation measurements; daily maximum relative humidity and relationships between air vapor content and air temperature for evaluating humidity data, and procedures for adjusting air temperature and air vapor content data in the cases where weather measurements have been affected by the dryness of the weather sensing environment

**Remote Sensing Approaches for
Estimating Evapotranspiration**

The use of remote sensing (RS) to estimate surface evapotranspiration has been

widely investigated in the last decades. The main objective of using remote sensing for

the prediction of ET is to overcome the spatial limitation of micrometeorological

methods. Spatial distribution of ET is needed as input of water balance related studies at

local and regional scales. Discussion of ET estimation using remote sensing can be

found in Bastiaanssen (1998), and Kustas and Norman (1996). Most authors recognized

that remote sensing ET is in its infancy.

Kustas and Norman (1996) divided the approaches used to estimate

evapotranspiration from remote sensing into three main categories: a) empirical/statistical

and semi-empirical approaches, b) analytical approaches, and c) numerical / hydrologic

models.

Empirical/Statistical and Semi-Empirical
Approaches

Basically, empirical approaches have been developed to predict ET from various

regression-type of relationships and to extrapolate "instantaneous" remote sensing

observations of derived fluxes to daily totals that are required for many hydrological and

agricultural applications. Perhaps the first approach for estimating ET from remote

sensed data was presented by Jackson et al. (1977), cited by Kustas and Norman (1996),

and it was based on the following equation:

$$R_{nd} - LE_d = B(T_{rad,i} - T_{a,i}) \qquad (2.19)$$

where the subscripts i and d represent instantaneous and daily values, respectively, B is a regression coefficient, T_a is air temperature at screen height (2 meters) and T_{rad} is an observation of radiometric surface temperature near midday. This relationship was modified by Seguin and Itier (1983), cited by Kustas and Norman (1996):

$$R_{nd} - LE_d = B'(T_{rad,i} - T_{a,i})^n \tag{2.20}$$

where B' is dependent on surface roughness and n depends on atmospheric stability (n =1 for stable, and 1.5 for unstable).

Reginato et al. (1985) conducted an experiment in Arizona, in which multispectral measurements were made over six cultivars of wheat. Evapotranspiration was estimated by combining remotely sensed reflected solar radiation and surface temperature with ground station meteorological data. Estimated ET was compared with measurements of ET using lysimeters. ET was estimated using the following equation:

$$LE = R_n - (0.1 - 0.042h)R_n - 1200(T_{rad} - T_a)/r_a \tag{2.21}$$

where h is the crop height, the term (0.1- 0.042h) is the G/R_n ratio, r_a is the aerodynamic resistance, and T_{rad} is the radiometric surface temperature.

The results suggested that this method could be used to get ET maps of relatively large areas using airbone imagery. However, the extent of the area where the ET

estimates may be accurate is limited by the distance that air temperature and wind speed data can be extrapolated.

Carlson and Buffum (1989) proposed a modification of the method of Seguin and Itier (1983), which does not require measurement of an air temperature:

$$R_{nd} - LE_d = B^{"}(\Delta T / \Delta t)^n \tag{2.22}$$

where $(\Delta T / \Delta t)$ is an average rate of surface temperature rise during the morning (e.g., between 8 and 10 local time) [°C/hour], B'' and n are constansts.

Vidal and Perrier (1989) modified the equation developed by Jackson et al. (1977), assuming that the ratio of H/R_n remains relatively constant during the day so that:

$$\left(\frac{H}{R_n}\right)_i = \left(\frac{H}{R_n}\right)_d \tag{2.23}$$

where H is the sensible heat flux, R_n is the net radiation, and the subscripts i and d represent instantaneous and daily values, respectively.

To extrapolate the instantaneous fluxes to daily values the following equations were proposed by Vidal and Perrier (1989):

$$LE_d - R_{nd} = -(R_{nd} / R_{ni})\rho Cph_i (T_{rad} - T_a)_i \tag{2.24}$$

where h_i is the instantaneous convective exchange coefficient, defined as:

where k is the von Karman constant, z_{om} is the roughness length for momentum transfer, and u(z) is wind velocity at height z.

Thunnissen and Nieuwenhuis (1990) developed the following empirical equation to extrapolate instantaneous LE values to 24 hours fluxes:

$$LE_d = LE_{p,d} - B'(T_c - T_c^*) \qquad\qquad (2.26)$$

where $LE_{p,d}$ is the potential 24 hours ET, calculated from a standard equation (such as Penman-Monteith), T_c is the radiometric temperature of a given crop, T_c^* is the temperature of a crop that is transpiring under optimal soil moisture conditions; B' is an empirical coefficient. According to the authors, for the application of this relationship only a few parameters have to be known: wind velocity, crop type and height, potential 24-hour ET values of the present crops, and the temperature of the crops that are potentially transpiring.

A procedure based on Eq. (2.26) was applied by Caselles et al. (1998) to estimate actual evapotranspiration in Spain using Landsat TM and NOAA-AVHRR imagery. The temperature difference between each pixel and the pixel that has the maximum evapotranspiration $(T_c - T_c^*)$ was calculated for each crop from NOAA data. The maximum ET $(LE_{p,d})$ was obtained using local weather station data. The author found an acceptable error of +/- 0.8 mm/day for barley, and +/- 1.0 mm/day for maize when comparing estimated ET and values of ET calculated using the Penman equation.

Qi et al. (1998) used an approach based on Eq. 2.19 to produce an ET map in the San Pedro Riparian area. They computed ET as:

$$ET = A - B * dT \qquad (2.27)$$

where $A = R_n - G$ (available energy), $dT = T_{rad}-T_a$ is the air-surface temperature difference, and B is a coefficient that is determined empirically using ground data. The authors pointed out that Eq. (2.27) was not able to explain the variation in ET values in the study area, so other factors such as water vapor and wind speed are needed. In addition Eq. (2.27) implies the knowledge of spatially distributed air temperature, so that it is limited to the amount of air temperature data available in the area.

The approaches described above attempt to extrapolate "instantaneous" remote sensing observations of the derived fluxes to daily totals which are required for many hydrological and agricultural applications. However, Seguin et al. (1994) pointed out that the use of these equations can lead to error of around +/- 1 mm/day, which may not be a good performance for daily values. On the other hands, these empirical equation can be useful when applied to longer periods (10-days or monthly). The analysis of experimental data obtained in France and North Africa produced estimates of ET with an error of +/- 5 mm for 10 days values and about +/- 10 mm for monthly periods, using the following expression:

$$\sum ET_d = \sum R_n + a - b \sum (T_{rad} - T_a) \qquad (2.28)$$

where ET_d is the 24-hour evapotranspiration, and a and b are correlation coefficients.

Physically Based Analytical Approaches

The most common approaches of the physically-based methods for estimating evapotranspiration through remote sensing are based on the surface energy balance and the Penman-Monteith resistance model.

Surface energy balance methods consist of estimating R_n, G, and H from remotely sensed data and getting ET as residual of the energy balance:

$$LE = R_n - G - H \qquad (2.29)$$

However, the application of Eq. (2.29) involves the accurate estimation of R_n, G, and H, because all residual errors are incorporated in the estimate of LE. In particular, the estimation of the sensible heat (H) from remotely sensed data has been a topic of wide discussion. H is commonly calculated by using the following equation:

$$H = \rho C p \frac{T_{aero} - T_a}{r_{ah}} \qquad (2.30)$$

where T_{aero} is the aerodynamic surface temperature (Norman and Becker, 1995), T_a is the reference height air temperature, and r_{ah} is the aerodynamic resistance to sensible heat transport between the surface and the reference height which is computed as follows:

$$r_{ah} = \frac{\left[\ln \frac{z_u - d}{z_{om}} - \psi_m \right]\left[\ln \frac{z_T - d}{z_{oh}} - \psi_H \right]}{k^2 u} \qquad (2.31)$$

where r_{ah} is the aerodynamic resistance to sensible heat transport, d is the zero-displacement height, u is the wind velocity measured at height z_u, k is the von Karman's

constant, z_t is the height of the T_a measurement, ψ_m and ψ_H are the Monin-Obukhov

stability functions for momentum and heat, z_{om} is the roughness length for momentum

transport, and z_{oh} is the roughness length for heat transport.

Because the aerodynamic temperature (T_{aero}) is difficult to measure, remote

sensing approaches have been trying to replace T_{aero} by the radiometric surface

temperature (T_{rad}), which can be derived from remotely sensed data. For uniform

canopy cover, the difference between T_{aero} and T_{rad} is typically less than 2°C

(Choudhury et al., 1986), but for partial vegetation cover the differences can reach 10° C

(Kustas and Norman, 1996). This has forced many investigators to account for that

difference via a variety of methods.

One of the most common approaches consists of adjusting z_{oh} ,or the ratio

$\ln(z_{om}/z_{oh})$, to account for the difference between aerodynamic and radiometric

temperature and to obtain good agreement with measured values of sensible heat flux.

Mathematically, the z_{om}/z_{oh} ratio is expressed as (Kustas and Norman, 1996) :

$$kB^{-1} = \ln\left(\frac{z_{om}}{z_{oh}}\right) \tag{2.32}$$

where k is the von Karman constant, and B^{-1} is a parameter. The term kB^{-1} is used to

express the extra resistance heat flow experiences above a crop as compared to

momentum flux (Mekonnen and Bastiaanssen, 2000). However, analysis of thermal

infrared data over sparse vegetation revealed that the added resistance to the heat transfer

from the surface, represented by the quantity kB^{-1}, have to range in value from about 3.5

to around 12.5 in order to obtain estimates of H and LE comparable to

micrometeorological measurements in semiarid areas (Stewart et al., 1994). Verhoef et al. (1997) found values of $kB^{-1} = 8$ for a vineyard and equal to 12 for a savannah. These values are significantly greater than $kB^{-1} = 2.3$, which is usually assumed to hold for vegetation, considering $z_{oh} = 0.1\ z_{om}$ (Brutsaert, 1982).

Brutsaert (1982) proposed the following semi-empirical equation to estimate the value of kB^{-1}:

$$kB^{-1} = \ln\left(\frac{z_{om}}{z_{oh}}\right) = kC\sqrt{\frac{u_* z_{om}}{\nu}} \qquad (2.33)$$

where k is the von Karman constant, u_* is the friction velocity, ν is the kinematic viscosity of the air, $C = 0.1$ (Chen constant), and the expression $u_*\,z_{om}/\nu$ represents the Reynold's number.

Chen et al. (1997) presented the following expression to scale z_{oh} relative to roughness length for momentum transfer z_{om}:

$$kB^{-1} = 2.46\left(\frac{u_* z_{om}}{\nu}\right)^{0.25} - 2.0 \qquad (2.34)$$

Zhan et al. (1996) used data obtained from the FIFE '87(Kansas), Monsoon '90 (Arizona) and the Washita '92 (Little Washita River Basin, Oklahoma) experiments to test single and two-sources models for obtaining sensible heat fluxes from radiometric temperature. A description of the models the author considered is included next.

Single-source approaches. The model of Kustas et al. (1989) assumes that the aerodynamic surface temperature (T_{aero}) is equal to the radiometric temperature (T_{rad}).

However, to account for the difference between T_{aero} and T_{rad}, they adjusted the value of z_{oh} as $z_{oh}=z_{om}exp(-kB^{-1})$. Then, the sensible heat flux is calculated as follows:

$$H = \rho Cp \frac{T_{rad} - T_a}{r_a + r_{ex}} \qquad (2.35)$$

where r_a is the aerodynamic resistance between the reference height and the $z_{om}+d$ plane and, r_{ex} is an "excess resistance" accounting for the difference between z_{om} and z_{oh}, so that:

$$r_{ah} = r_a + r_{ex} = \frac{1}{ku_*} \ln \left(\frac{z-d}{z_{om}} - \psi_h \right) + \frac{1}{ku_*}(kB^{-1}) \qquad (2.36)$$

Kustas et al. (1989) defined kB^{-1} as:

$$kB^{-1} = s_{KB}u(T_{rad} - T_a) \qquad (2.37)$$

where S_{KB} is a regression parameter varying between 0.05 and 0.25, and u is the wind speed.

On the other hand, Trofleau et al. (1997) assumed that $T_{aero} = T_{rad} - \delta T$, and $r_{ah}= r_a$, so that the calculation of sensible heat flux becomes as:

$$H = \rho Cp \frac{(T_{rad} - T_a) - \delta T}{r_a} \qquad (2.38)$$

where δT is estimated as $\delta T = \alpha(T_{rad} - T_a) + \beta$, with α and β being empirical coefficients determined from experimental data.

Dual source models. Dual sources model have been created to deal with the difference between the surface temperatures of soil and vegetation surfaces, especially for the case of sparse vegetation. The dual source models of Lhomme et al. (1994) and Norman et al. (1995) estimated sensible heat flux as:

$$H = \rho Cp \frac{(T_{ac} - T_a)}{r_a} = \rho Cp \frac{(T_f - T_{ac})}{r_f} + \rho Cp \frac{(T_{soil} - T_{ac})}{r_{sa}} \qquad (2.39)$$

where r_f is the resistance of the leaf boundary layer, r_{sa} is the resistance of the air layer above the soil surface, and T_{ac}, T_f, and T_{soil} are the temperature of the air within the canopy, the foliage, and the bare soil surface. These temperatures are estimated using the following equations:

According to Lhomme et al. (1995):

$$T_{soil} - T_f = a(T_{rad} - T_a)^m \qquad (2.40)$$

$$T_{rad} = f_c T_f + (1 - f_c) T_{soil} \qquad (2.41)$$

and according Norman et al. (1995):

$$T_{rad}^4 = f_c T_f^4 + (1 - f_c) T_{soil}^4 \qquad (2.42)$$

$$\rho Cp \frac{(T_f - T_{ac})}{r_f} = R_n (-\exp(\beta_n LAI)) \times (1 - \alpha_{PT} f_g \frac{\Delta}{\Delta + \gamma}) \qquad (2.43)$$

where LAI is the leaf area index, f_g is the fractional coverage of plant canopy, a and m are fitted parameters (a=0.1, m=2), α_{PT} is the Priestley-Taylor constant (1.26), β_n is a net radiation extinction coefficient.

Zhan et al. (1996) concluded that, after comparing modeled versus measured sensible heat flux for the different sites and surfaces, the two-source model of Norman et al. (1995) gave the best results. Furthermore, from a sensitivity analysis it appears to have the greatest potential for operational applications since it is not very sensitive to the uncertainty in the estimates of most parameters. On the other hand, single-source models rely heavily on the specification of the surface roughness (z_{om}) and empirical relationships in accounting for differences between aerodynamic and radiometric temperature. The disadvantage for operational remote sensing is the need for air temperature, and T_f and T_{soil} separately.

Li and Lyons (1999) tested three models to estimate evapotranspiration in Western Australia through remote sensing. They used the kB^{-1} extra resistance model of Kustas et al. (1989), based on Eq. 2.35, the two source model of Lhomme et al. (1994), and the soil adjusted vegetation index model of Moran et al. (1996). The models of Kustas et al. (1989) and Moran et al. (1996) performed better than the two source model over both native and agricultural vegetation. The authors pointed out that the use of these models strongly depends on the knowledge of air temperature, which can limit their use for regional-scale applications.

Kustas and Norman (1997) tested a two-source model for computing the surface energy balance that uses radiometric surface temperature measured at two different view angles. The authors compared the results achieved by using the two-source model against Bowen ratio and Eddy correlation measurements obtained from the FIFE experiment. This model was later modified by the authors (Kustas and Norman, 1999). This two-source model uses radiometric temperature observations for estimating the components

of the surface energy balance from soil and vegetation. The total or combined estimated

fluxes from the soil and vegetation agreed to within 20 % of observed values from a row

crop (cotton). To estimate the latent fluxes from soil and vegetation, the following

expressions were used:

$$LE_c = \alpha_{PT} f_g \frac{\Delta}{\Delta + \gamma} R_{nc} \tag{2.44}$$

$$LE_s = R_{ns} - G - H_s \tag{2.45}$$

where LE_s, LE_c, R_{ns}, R_{nc} are the latent heat flux and net radiation from the soil (subscript

s) and canopy (subscript c), G is the soil heat flux, calculated as a fraction of R_{ns}, H_s is

the sensible heat flux from the canopy, α_{PT} is the Priestley-Taylor parameter, Δ is the

slope of the saturation vapor pressure-temperature curve at canopy temperature, γ is the

psychrometric constant, and f_g is the fraction of LAI that is actively transpiring. The use

of this model implies the measurement of radiometric temperatures from soil and canopy.

Another approach to deal with the problem of inferring T_{aero} from T_{rad} is to

directly estimate dT, the temperature difference between T_1 and T_2, taken at two levels

z_1 and z_2 over the surface, without explicitly measuring the absolute temperature at a

given height. This approach is used by the one-layer resistance Surface Energy Balance

Algorithm for Land (SEBAL) developed by Bastiaanssen (1995). SEBAL calculates the

sensible heat flux at extreme dry and cold pixels, where one can assume that $ET \approx 0$ (dry

pixel), and $ET \approx R_n - G$ (cold pixel). Then, the estimation of near-surface air temperature

difference (dT) values at the two extreme points can be achieved from the inversion of the sensible heat transfer equation:

$$T_1 - T_2 = dT = \frac{Hr_{ah}}{\rho Cp} \qquad (2.46)$$

where r_{ah} is the aerodynamic resistance for heat transfer from level 1 (z_1) to level 2 (z_2), corrected for atmospheric stability.

The assumption implicit in SEBAL is that hot areas (with large thermal emittance) create higher vertical differences in air temperature dT than cold surfaces and that this relationship is linear with surface temperature. According to this assumption, a linear relationship between surface temperature and dT can be established:

$$dT = c_1 T_{rad} - c_2 \qquad (2.47)$$

where T_{rad} is the radiometric surface temperature, c_1 and c_2 are regression coefficients valid for one particular moment and region. The linearity of Eq. 2.47 has been shown to be valid in several field experiments carried out in Egypt and Niger (Bastiaanssen et al., 1998), China and Kenya (Farah, 2000), and in the US (Frank and Beven, 1997).

In SEBAL the whole discussion of the accuracy attainable in deriving a correct value of surface temperature from remote sensing measurements, as well as the difference between T_{rad} and T_{aero}, becomes less important if dT is derived by inversion of the H-flux equation rather than from independent T_{rad} and T_a measurements and kB^{-1} adjustment (Bastiaanssen et al., 1998). The dT computed from the inversion of Eq. (2.30) incorporates all biases in T_{rad} and r_{ah}.

Kustas et al. (1990) applied a remote sensing approach to estimate evapotranspiration in an agricultural region in Arizona. Instantaneous and daily values of ET were estimated from different flux sites with an energy balance model that is based on a reference ET. They assumed that deviation from the reference energy balance components can be used to estimate LE over another surface, so that:

$$LE = LE_r + (R_n - R_{nr}) - (G - G_r) - (H - H_r) \qquad (2.48)$$

where LE, G, and H are the energy balance components for the study area, and LE_r, G_r, and H_r are the fluxes for the reference area taken as an alfalfa field. A comparison with flux measurements carried out through Bowen ratio and Eddy correlation techniques suggested that the model fails to predict ET over partial canopy conditions, mostly due to the difficulty of predicting sensible heat flux using a single-layer scheme, pointing out that it would be more appropriate to employ a two-layer model.

Remote sensing observations along with micrometeorological and atmospheric boundary layer data were used to compute the surface energy balance over semiarid rangelands by Kustas et al. (1994). Radiation, wind speed, air temperature, and local roughness parameters were available in eight different sites within the study area, which allowed to obtain excellent results. However, the authors mentioned that such a dense network of ground measurement is not commonly available so that there is a need for improving the methods for estimating some key parameters.

Chehbouni et al. (2000) tested three methods to aggregate turbulent fluxes over heterogeneous surfaces using remotely sensed surface temperature in the San Pedro Basin, Mexico within the Semi-Arid Land-Surface Atmosphere (SALSA) research.

Sensible heat fluxes over different surfaces were measured using eddy covariance

systems, and standard instruments recorded micrometeorological variables. They

obtained the best results by using a physically based method where the sensible heat flux

was calculated by using the following expression:

$$H = \rho\, Cp\, \xi\, \frac{T_{rad} - T_a}{r_a} \tag{2.49}$$

where ξ is a empirical function of LAI that relates aerodynamic to radiometric surface

temperature. However, the authors pointed out that this procedure requires the

knowledge of surface parameters such as radiometric temperature, aerodynamic

resistance and ξ or its equivalent for every surface involved which cannot be obtained

from remote sensing at the appropriate time-scale-space.

Granger (2000) applied a remote sensing approach to estimate regional

evapotranspiration in the Gediz basin in Turkey. The approach is based on a so-called

feedback methodology (Granger, 1997, cited by Granger, 2000), where the vapor

pressure deficit near the surface is obtained from the surface temperature. Surface albedo

from satellite visible channels is used to estimate net radiation. Then, the satellite-derived

net radiation and vapor pressure deficit values are introduced in an extension of the

Penman equation. The author used NOAA-AVHRR and Landsat-TM satellite images, as

well as meteorological data collected in the site as inputs for the ET predictions.

Friedl (1995) presented a sparse canopy model that uses radiometric surface

temperature measurements to estimate land surface fluxes. The theoretical framework for

this model is the multi-layer model originally presented by Shuttleworth and Wallace

(1985), and subsequently refined by Choudhury and Monteith (1988) and Shuttleworth and Gurney (1990). In this model, land surface thermal infrared radiance is treated as being composed of soil and canopy components with different temperatures and emissivities. Model simulations demonstrated that modeled fluxes agreed well with observed fluxes, when correct values of emissivities were used for both the soil and canopy. Because the large number of surface variables required to run the model, and model sensitivity of these input variables, the author concluded that the model would be difficult to apply outside experiments such as FIFE where detailed micrometeorological measurements are available.

Numerical Models

The evaporation of water from soil and plant surfaces represents the connecting link between the energy balance and the water balance at the earth's surface. This fact has encouraged the development of a variety of models that use remote sensing to evaluate the surface energy balance and hydrologic models that handle the variation of surface moisture.

Sucksdorff and Ottle (1990) used a method that combines weather data and satellite imagery to estimate evapotranspiration over the Eurajoki River basin in Finland. NDVI and surface temperature derived from NOAA/AVHRR data was used to obtain leaf area index and minimum resistance to evaporation. The authors applied the principle that, when the soil water is restricted, the plant reduces its transpiration and the system temperature rises; so the radiometric surface temperature measurements may be used to monitor the soil water budget and evapotranspiration during the growing periods for

crops. The different land use classes over the river basin were interpreted from Landsat images.

Ottle and Vidal (1994) showed how satellite remote sensing could be used to improve the simulation of the hydrology of a large watershed. Visible (VIS) and near infrared (NIR) data were used to predetermine land surface parameters, and thermal (IR) were used to estimate the flux of evaporation through the surface energy balance. The authors used a numerical water-balance hydrological model that allows the simulation of soil moisture in the surface layer of the watershed and the waterflows on a daily time basis. At the same time, when a clear sky image was available (using NOAA-AVHRR imagery), an interface model was used to simulate the energy balance in the watershed, and calculate vegetation and surface parameters. Then, the estimated ET was integrated in the water-balance model of the watershed. The authors applied the model on the Adour, River Basin in France, in the framework of the HAPEX-MOBILHY experiment.

Choudhury and DiGirolamo (1998) developed a biophysically process-based methodology to estimate evaporation, transpiration and biomass production. This methodology combines the water, energy, and carbon processes and uses satellite and ancillary data as main inputs. Satellite information is used to obtain vegetation cover, surface albedo, incoming solar radiation, photosynthetically active radiation (PAR), cloud cover, air temperature, and air pressure. Ancillary data is used to define other characteristics such as land cover, and carbon assimilation. The estimation of transpiration is based on the Penman-Monteith equation and the rate of leaf carbon assimilation. The model was used to predict evaporation at a global scale (Choudhury et al., 1998) and a regional level in the Gediz Basin, Turkey (Choudhury, 2000).

Olioso et al. (1999) discussed how to assimilate remote sensing data into soil-vegetation-atmosphere transfer (SVAT) models to estimate evapotranspiration and photosynthesis. SVAT models simulate energy and mass transfers using descriptions of turbulent, radiative, and water exchanges, as well as a description of stomatal control. Remote sensing data can give information in regard to surface temperature and albedo, solar radiation, canopy structure, and surface soil moisture. They encountered some problems when combining remote sensing and SVAT models: difficulty to retrieve soil moisture from thermal infrared measurements, and sensitivity of the models to turbulent exchange coefficients, which implies that an accurate assessment of vegetation height is required to obtain good estimation of fluxes.

Mauser and Schadlich (1998) applied the PROMET (Process Oriented Model for Evapotranspiration) model for estimating ET on different scales in Upper Bavaria. Basically, PROMET contains a kernel model (a SVAT based on Penman-Monteith and a plant physiological model), and a spatial modeler, which takes care of the information provide by remote sensing. The spatial modeler uses LANDSAT data to estimate ET at a microscale, and NOAA-AVHRR to evaluate ET at a mesoscale.

A field experiment was conducted by Soegaard (1999) in a agricultural area of Sweden within the framework of the Northern Hemisphere Climate Processes Land-Surface Experiment (NOPEX). Fluxes of water vapor and heat were monitored above winter wheat, spring barley and bare soil using Bowen ratio and Eddy correlation equipment. Additional measurements of LAI, short wave radiation, radiometric temperature, and wind speed were performed routinely. Then, by combining photosynthesis models and the Penman-Monteith equation with remote sensing data the

surface fluxes were calculated at a landscape level. To extrapolate the field

measurements up to landscape levels the author used a SPOT image, and calculated LAI

from NDVI. To get the sensible heat fluxes, the author used the spatial variance of

surface temperature as an indicator for the sensible heat flux at the landscape level,

considering the range of surface temperatures from the warmest surface (bare soil) and

the air temperature.

Silberstein et al. (1999) developed a procedure that combines the water balance

with an energy balance model to describe the hydrology of a watershed. The coupling of

the energy balance to the water balance is established by conversion of thermal and

radiative energy to latent heat flux. Effective surface temperatures (T_{eff}) were calculated

using measurements of canopy and soil temperatures. Landsat TM images were used to

describe the spatial variation of the surface's fluxes.

Van Der Keur et al. (2001) used a SVAT model and remote sensing data to infer

information on the photosynthetic capacity and the minimum or unstressed canopy

resistance (r_c^{min}) from spectral vegetation indices.

Droogers and Bastiaanssen (2002) combined SEBAL and the soil-water-

atmosphere-plant (SWAP) model to evaluate the performance of an irrigation project in

Western Turkey. SWAP is a one-dimensional physically based model for water, heat and

solute transport in the saturated and unsaturated zones, and includes modules for

simulating irrigation practices and crop growth. According to the authors the

combination of hydrological models and remote sensing can compensate for the low

spatial coverage of the numerical models and the low temporal resolution of high spatial

resolution remotely sensed images. Landsat imagery were used to classify crops, calculate LAI, and compute ET.

Franks and Beven (1999) pointed out that physically based models are generally overparameterized with respect to the data available for calibration, with the result of multiple acceptable simulations. As soil vegetation-atmosphere transfer models get more complex and include more processes and parameters, the potential for over-parameterization increases.

**Alternative Approaches in Using Remote
Sensing for Estimating ET**

Using the Relationship between Vegetation
Indexes and Radiometric Surface
Temperature

Two important features have been used in remote sensing to characterize vegetation status. One is the low reflectance that vegetated surfaces shows in the red band of the visible spectrum (due to chlorophyll absorption of visible radiation), and the other is the high reflectance in the near infrared (NIR) region of the spectrum (because of reflectance properties of the mesophyll structure in the leaf). These two reflectivity properties of vegetation have constructed the basis for several vegetation indices.

The simplest vegetation index is the SR (simple ratio), which is the ratio of NIR and red bands (Jensen, 2000):

$$SR = \frac{NIR}{R} \tag{2.50}$$

where NIR is reflectance of the near infrared band, and R is reflectance of the red band.

A normalized difference vegetation index (NDVI) was suggested by Tucker in 1979 cited by Jensen (2000), which has been one of the most commonly used vegetation indices :

$$NDVI = \frac{(NIR - R)}{(NIR + R)} \qquad (2.51)$$

The soil adjusted vegetation index (SAVI), proposed by Huete (1988), attempts to eliminate the effect of wetness and color of background soil on the vegetation index:

$$SAVI = \frac{(1+L)(NIR - R)}{(NIR + R + L)} \qquad (2.52)$$

where L is the SAVI constant, often taken as 0.5

In different studies, vegetation indices have been related to radiometric surface temperature to predict transpiration and soil evaporation. In general, a negative correlation between NDVI and radiometric surface temperature is found (Nemani and Running, 1989). However, besides vegetation cover, surface temperature is strongly related to surface soil moisture, so that the consideration of this parameter is required for estimations of ET.

Moran et al. (1994) derived a vegetation index temperature trapezoid, which combines satellite vegetation indices with radiometric surface temperature, and extended crop water stress index theory. The method is based on the hypothesis that a trapezoided shape results from a plot of the difference between radiometric surface temperature and air temperature $(T_{rad}-T_a)$ against vegetation cover. In addition, the method considers that,

for a given R_n, vapor pressure deficit of the air, and aerodynamic resistance are linearly related with ET. This concept is illustrated in Fig. 2.1.
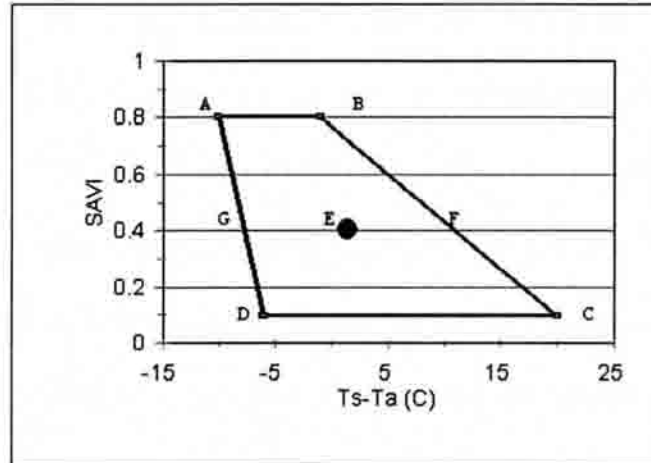
FIGURE 2.1. The Trapezoidal Shape that Results from the Relationship Between $(T_{rad}-T_a)$ and SAVI (Ranging from 0.1 for Bare Soil and 0.8 for Full Cover Vegetation). Point A: Well Watered Vegetation B: Water-Stressed Vegetation C: Dry Bare Soil, and D: Saturated Bare Soil.

In Fig. 2.1, if one measures T_s-T_a at point E, then the relationship between actual and potential ET, called as Water Deficit Index (WDI) is WDI=1- ET/ET$_{pot}$ = 1-distance EF / distance FG, where ET$_{pot}$ is the potential evapotranspiration. The authors defined the vertices of the trapezoid by using measurements of radiometric and air temperatures for diverse conditions, so that:

$$WDI = 1 - \frac{ET}{ET_p} = \left[\frac{(T_{rad} - T_a)_m - (T_{rad} - T_a)_r}{(T_{rad} - T_a)_m - (T_{rad} - T_a)_x} \right] \qquad (2.53)$$

where ET is the actual evapotranspiration, ET_p is the potential evapotranspiration, and the subscripts m, x, and r refer to minimum, maximum, and measured values for a specific SAVI.

Moran et al. (1996) combined the Penman-Monteith (PM) equation and measurements of surface temperature and reflectance to estimate evaporation rates of semiarid grassland. They used the concept explained in Fig. 2.1 and combined the PM equation and the energy balance equation to compute the vertices of the trapezoid (points A, B, C, and D in Fig. 2.1), assuming that for bare dry soil the surface resistance $r_s = \infty$, for a wet bare soil $r_s = 0$, for a well watered vegetation the surface resistance was minimum ($\approx 25 - 100$ sm^{-1}), and for stressed vegetation r_s was large ($r_s \approx 1000 - 1500$ sm^{-1}). Then, linear interpolations between T_s values computed for full-cover and bare soil conditions were used to provide information at intermediate states based on measurement of actual surface reflectance and temperature.

Gilles et al. (1995) showed that the surface energy fluxes are strongly affected by surface wetness and vegetation cover. The authors used the "triangle method," so-called because the shape formed by the envelope of pixels on a scatterplot of radiometric surface temperature versus NDVI resembles a triangle, where the vertices define the following conditions: full cover vegetation, dry bare soil, and wet bare soil. A soil-atmosphere-vegetation (SVAT) model is used to produce isolines of T_s/ NDVI corresponding to different levels of surface soil moisture.

A relationship between NDVI and percent of vegetation cover is established with the following expression:

$$Fr = \left(\frac{NDVI - NDVI_o}{NDVI_{max} - NDVI_o} \right)^2 \qquad (2.54)$$

where Fr is the fractional vegetation cover, which varies from 0 to 1, $NDVI_o$ is the value

of NDVI corresponding to bare soil, and $NDVI_{max}$ is the value of NDVI corresponding

to full cover vegetation.

Using Relative Differences of Radiometric Surface Temperature

Norman et al. (2000) developed a dual-temperature-difference method (DTD) to

estimate sensible heat flux from surface brightness temperature, vegetative cover and

type, and measurements of near-surface wind speed and air temperature from a synoptic

weather station network. The method requires the knowledge of both radiometric

surface and air temperatures at two times of the day. The first time of the day usually

is chosen when all the fluxes are small and temperatures are similar (one hour after

sunrise) and the second time can be any hour of the day. The purpose is to cancel out any

offset between measurements of radiometric surface and air temperatures, so that the

dependency of using accurate temperatures is removed. The authors pointed out that the

DTD method reduces the effect of errors associated with radiometric calibration,

emissivity variations, and use of non local air temperature and wind speed data.

However, the need for data from two different times of the day make this method

only applicable to satellite imagery like that obtained from GOES, where data are

available at least twice a day.

Remote-Sensing Based Crop Coefficients

Neale et al., (1989) developed reflectance-based crop coefficients for corn using alfalfa ET as the reference evapotranspiration. Evapotranspiration from corn was measured in lysimeters located at the Northern Colorado Research Center. Reflected radiation was measured using a radiometer with channels corresponding to the Landsat Thematic Mapper bands 3 and 4. Reference (alfalfa) evapotranspiration was obtained using three lysimeters planted with well-watered alfalfa. The reflectance-based crop coefficients were obtained by linear scaling; relating minimum values of basal crop coefficient K_{cb} ($K_{cb}=ET_{corn}/ET_{alfalfa}$) with minimum values of NDVI and maximum values of K_{cb} with maximum values of NDVI. The resulting reflectance-based crop coefficient equation was the following:

$$K_{cr} = 1.02\left(\frac{TM4 - TM3}{TM4 + TM3}\right) + 0.053 \tag{2.55}$$

where K_{cr} is the reflectance-based crop coefficient for corn, TM4 is the thematic mapper band 4 reflectance; TM3 is the thematic mapper band 3 reflectance.

Eq. 2.55 worked well for any combination of crop development and weather conditions. The authors concluded that reflectance-based crop coefficients represent real time coefficients that are sensitive to periods of slow and/or rapid growth induced by climate conditions, which is an advantage over traditional crop coefficient approaches.

Baush (1995) used the Soil Adjusted Vegetation Index (SAVI) for developing reflectance-based crop coefficients for corn. The following expression was developed:

$$K_{cr} = 1.416 \times SAVI + 0.017 \tag{2.56}$$

The author found that irrigation scheduling for corn could be improved using canopy reflectance data to determine crop coefficients. Situations of overirrigation as well as underirrigation are minimized due to better estimates of crop water.

Choudhury et al. (1994) evaluated the possibility of expressing K_c by means of a spectral vegetation index. They used a radiative transfer model to calculate vegetation indices during a crop life cycle and a four-layer simulation model (Choudhury et al., 1988) for heat and water vapor exchange processes at the land surface to calculate ET of wheat. The Priestley and Taylor equation was used to compute ET_o. Then, K_c was defined as the ratio of ET and ET_o. The authors concluded that considering that net radiation and near-surface air temperature (derived from satellite data) can be used to provide an estimate of ET_o, it appears possible to estimate values of K_c corresponding to unstressed crops.

Mekonnen and Bastiaanssen (2000) used Landsat TM satellite data to derive crop coefficients in the Lake Naivasha Basin, Kenya. The Priestley and Taylor (PT) equation was used to estimate reference evapotranspiration, because its radiation and temperature parameters can be assessed from remotely sensed data. The authors argued that this equation might behave better than a Penman-Monteith (PM) based equation because the PM equation requires weather parameters, such as vapor pressure and wind speed, that are impossible to describe at a regional scale. The authors found first a good correlation between PM-ET and PT-ET using weather data, which indicated that the PT equation could be used under the humid conditions present in the study area. They concluded that the K_c approach, based in the PT equation for calculating reference evapotranspiration,

can be used in remote sensing to determine regional scale crop water requirements as long as the vapor pressure deficit remains within acceptable limits.

Discussion of Other Issues Concerning the Estimation of ET Through Remote Sensing

Soil Heat Flux (G)

Calculation of the soil heat flux from remote sensing has been based on net radiation and vegetation indices. Results from empirical studies have shown that the daytime ratio of G/R_n is related to, among other factors, the amount of vegetation cover (De Bruin and Holtslag, 1982 cited by Moran and Jackson, 1991) or the leaf area index (Choudhury and Monteith, 1988). Thus, an approximation of G could be achieved by assuming that it is a fraction of R_n, dependent on spectral estimates of surface vegetation cover. For example, Jackson et al. (1987) cited by Moran and Jackson (1991), developed the following expression:

$$G/R_n = 0.583 \exp(-2.13 \text{NDVI}) \tag{2.57}$$

where NDVI is the normalized difference vegetation index.

Daughtry et al. (1990) found that multispectral data collected from aircraft and satellites may provide a means for calculating the relative magnitude of G/R_n from estimates of R_n for different surfaces and vegetation indices such as NDVI. They correlated measurements of R_n, and G with NDVI computed from three different surfaces: cotton, bare soil and alfalfa. They proposed the following expression, with a standard error of 0.02:

$$G/R_n = 0.32 - 0.21NDVI \qquad (2.58)$$

Clothier et al. (1986) developed a relation between G/R_n and the ratio of NIR/red reflectances for alfalfa:

$$G/R_n = 0.295 - 0.0133(NIR/red) \qquad (2.59)$$

where Eqs. 2.58 and 2.59 are only reliable for midday periods.

Kustas et al. (1994) used the following expression over semiarid rangelands:

$$G/R_n = 0.36 - 0.02NIR/RED \qquad (2.60)$$

Eq. 2.60 was originally developed by Daughtry et al. (1990), which predicted G/R_n with a standard error of 0.04.

Payero et al. (2001) presented results of a field experiment conducted at Kimberly, Idaho. The authors correlated measurements of net radiation, soil heat flux and radiometric temperature over surfaces of grass and alfalfa, obtaining the following relationships:

For grass:

$$G = -13.46 + 0.507[4\exp(0.123T_{rad}) - 55] + 0.0863R_n \qquad (2.61)$$

for alfalfa (h >0.3 m)

$$G = -52.73 + 0.368R_n + 49.1h - 0.368R_n * h \qquad (2.62)$$

and for alfalfa (h<0.3 m)

$$G = 71.96 + 0.51R_n - 0.61R_n * h - 6.55T_{rad} \qquad (2.63)$$

where h is the crop height (m), T_{rad} is the radiometric surface temperature (^oC), R_n and G are in W/m^2. The authors reported the following values of the regression coefficient (r^2) and standard error (SEE): Eq. 2.61: ($r^2 = 0.94$, SEE = 11 Wm^{-2}), Eq. 2.62: ($r^2 = 0.87$, SEE = 17 Wm^{-2}), and Eq. 2.63: ($r^2 = 0.85$, SEE = 32 Wm^{-2}). According to the authors, these equations can be used to obtain G estimates at anytime during the day or night and for any plant height.

Tasumi et al. (2000) used the following equations for estimating G in Bear Lake, which is a clear, cold lake, based on previous works of Amayreh (1995), and Yamamoto and Kondo (1968). The following equations were used for the July - December period:

-for instantaneous G, at the time that the satellite image was taken ($\approx$ 10:40 am):

$$G_{water} = R_n - 90 \qquad (2.64)$$

and for 24hr G:

$$G_{water} = R_n - 100 \qquad (2.65)$$

For the January - June period, the following equations were used:
-for instantaneous G at the time that the satellite image was taken ($\approx$ 10:40 am):

$$G_{water} = 0.9R_n - 40 \qquad (2.66)$$

and for 24hr G:

$$G_{water} = 0.9R_n - 50 \qquad (2.67)$$

where G_{water} and R_n are expressed in W/m^2

For wetland surfaces, Burba et al. (1999) found the following G/R_n relationship

for a wetland area in northcentral Nebraska, using half-hourly values of G and R_n:

$$G = 0.41R_n - 51 \qquad\qquad (2.68)$$

Souch et al. (1996) in the Indiana Dunes National Lakeshore wetlands, using

hourly data found:

$$G = 0.53R_n - 37.5 \qquad\qquad (2.69)$$

In Eqs. (2.68) and (2.69), G and R_n are also expressed in W/m^2.

Extrapolating Instantaneous to Daily ET
Values

Methods that use remotely sensed inputs yield data for each resolution element of

the sensor (pixel), thus spatially distributed values of evaporation, but at only an instant

in time. Unfortunately, the instantaneous evapotranspiration flux (LE) is not very useful

for many hydrological and ecological applications where totals of daily LE are needed.

A relatively simply approach to extrapolate from instantaneous flux to daytime

average flux is to assume that the partitioning of the available energy into H and LE is

constant or "self-preserving" (Brutsaert and Sugita, 1992) which implies that over most

of the daytime, the evaporative fraction (EF) between the evaporation and the available

energy remains nearly constant. The evaporative fraction is defined as:

$$EF = \frac{LE}{R_n - G} \qquad\qquad (2.70)$$

where EF is the evaporative fraction.

Therefore, with estimates of daily R_n and G, one can simply compute daytime LE, assuming that the relationship between instantaneous and daily values is constant through the day, using the expression:

$$LE_d = EF_{inst}(R_n - G)_d \qquad (2.71)$$

where the subscript d is related to daily values, and EF_{inst} is the instantaneous evaporative fraction calculated from measurements or estimates of R_n, G, and LE near midday.

Shuttleworth et al. (1989) did find that the evaporative fraction remained stable during daylight hours using data from 20 different sites within the First International Satellite Land Surface Climatology Project (ISLSCP) Field Experiment (FIFE) project in Kansas. In addition, the authors showed that the midday evaporative fraction was statistically representative of the all-day evaporative fraction. These two characteristics of EF, a) stability during daylight hours and b) the fact that the midday value was statistically representative of the daily data, show the possibility of using EF for partitioning the surface energy balance in remote sensing applications. The spatial scale in these cases was limited and the prairie surface was relatively homogeneous.

Nichols and Cuenca (1993) evaluated the evaporative fraction using data obtained from the HAPEX-MOBILHY experiment in France. Analysis of the EF was performed for the period beginning 1 hour after sunrise until 1 hour before sunset. Within their results, they found that EF decreased sharply with increasing available energy $(R_n\text{-}G)$ up to a level of 200 Wm^{-2}, after which the EF remained almost constant. Although finding

a strong correlation between the midday and all-day mean evaporative fraction, they found that those values were not statistically equal. Because of that, using midday measurements and midday EF to predict all-day LE resulted in a consistent over-prediction compared to mean measured values.

Qualls et al. (1999) evaluated the evaporative fraction from data obtained from FIFE. The author concluded that to characterize the spatial variability of the energy partitioning, in addition to EF, it would be useful to include soil moisture and a thermal response variable like the diurnal surface temperature range.

Zhang and Lemeur in 1995, cited by Kustas and Norman (1996), found that, although EF is fairly constant for short vegetation, it may not be for forest.

Another approach to extrapolate instantaneous to daily values is to use the Priestley-Taylor coefficient α to extrapolate half hour values of LE to daily values by using the following expression (Crago, 1996) :

$$LE_d = \alpha_m * [\Delta /(\Delta + \gamma)]_d (R_n - G)_d \qquad (2.72)$$

where α_m is calculated from instantaneous or near midday averages of the fluxes as follows:

$$\alpha_m = \frac{LE_m}{[\Delta /(\Delta + \gamma)]_m (R_n - G)_m} \qquad (2.73)$$

where the subscript m indicates a half hour average value taken near the middle of the day, and the subscript d indicates a daytime operator.

Crago (1996), using data obtained from Bowen ratio stations at FIFE in northeastern Kansas, found that the value of both EF and α near midday were significantly different from the daytime average value due to the concave-up shape of the diurnal progression of these variables. The estimation of daily EF and α improved when they were adjusted by a soil moisture content function expressed as:

$$(EF, \alpha)_m = a\left\{1 - \exp\left[-b(SM - c)/SM_{max}\right]\right\} \tag{2.74}$$

where a, b, and c are empirical parameters, SM is the soil moisture in percent by mass, and SM_{max} was taken to be the maximum area-average soil moisture observed in either 0-5 cm or 5-10 cm subsurface layers.

Soil Moisture

To simulate the temporal variation of the soil water processes, numerical models have been commonly used. Generally, these models are based on the Richard's equation to describe the dynamics of soil water flow and uptake by roots (D'Urso et al., 1999). The numerical solution of the Richard's equation requires the knowledge of soil hydraulic properties, groundwater table, and vegetation status at different time steps, which represents a major difficulty in large-scale applications. According to D'Urso et al. (1999), this task can be simplified by combining remote sensing techniques, geographical information systems and hydrological simulation models.

With regard to soil moisture obtained from remote sensing data, Schultz (1988) pointed out that, although visible and infrared data have been used, the most promising approaches are based on passive and active microwave data. According to Jackson et al.

(1996), an advantage of microwave sensors (as opposed to visible and infrared) is that observations can be made under conditions of cloud cover. In addition, these measurements are not dependent on solar illumination and can be made at any time of the day.

However, microwave RS sensors give only information on the top few centimeters layer of the soil, while for hydrologic processes one is interested in the soil moisture down to about 2 m below the surface. Therefore there are two problems: estimation of soil moisture properties at or near the surface, and inference from the information obtained to soil moisture profiles down to about 2 m. Besides, Jackson et al. (1996) indicated that at the present time it is recognized that at some level of biomass the vegetation will mask the signal from the soil. This can be avoided by using longer wavelengths..

Shih and Jordan (1992) discussed the use of Landsat TM images to assess regional surface soil moisture conditions. They presented a methodology in which mid-infrared data of TM band 7 were used to evaluate four qualitative surface-soil moisture conditions: water, very wet, wet, moist, and dry. Reflectance of mid-infrared radiation is, in general, inversely related to the soil moisture content.

Pelgrum and Bastiaanssen (1996) and Bastiaanssen et al. (1997) used a procedure that combines SEBAL estimates of evaporative fraction with soil moisture measurements to describe the spatial variation of near-surface soil moisture. They found that with increasing surface water content, the evaporative fraction increases logarithmically. This concept was used by Mekonnen and Bastiaanssen (2000) to

evaluate soil moisture content from NOAA imagery. Relative soil water content (fraction of pores filled with water) was determined from the evaporative fraction (EF) as:

$$\frac{\theta^{NOAA}}{\theta_{sat}} = (1/0.51)\exp\left\{\left(EF^{NOAA} - 1.28\right)/0.42\right\} \tag{2.75}$$

where θ is the volumetric soil water content in the effective root zone, θ_{sat} is the saturated soil water content and EF is the evaporative fraction. Bastiaanssen (2000) postulated that Eq. (2.75) can predict surface moisture.

Allen et al. (1998) proposed a methodology that can be used to evaluate the evolution of the soil moisture within the root zone. This methodology involves the knowledge of certain hydraulic characteristics of the soil and reference ET. Actual evaporation is computed by considering the soil moisture content at each given time step. The author applied this methodology to evaluate the actual evapotranspiration in the Gediz Basin, in Turkey (Allen, 2000).

Applications of the SEBAL Approach

Because the Surface Energy Balance Algorithm for Land (SEBAL) was the basis of the remote sensing approach to estimate evapotranspiration from satellite data for this study, a review of some of the applications of SEBAL is included next.

Bastiaanssen (1995) and Bastiaanssen et al. (1998) presented the model SEBAL which permits the estimation of surface fluxes using remote sensing information and limited weather data. The SEBAL procedure has been applied in various ecosystems in Egypt, Spain, Portugal, France, Italy, Argentina, China, India, Pakistan, Niger, Zambia, Ethiopia, USA, and the Netherlands (Bastiaanssen et al., 1998). Results obtained using

SEBAL have been validated with data available from the large-scale field experiments EFEDA (Spain), HAPEX-Sahel (Niger) and HEIFE (China).

SEBAL is a satellite image-processing model for computing evapotranspiration maps for large areas. In SEBAL the evapotranspiration is obtained as a residual of the basic energy balance equation (Eq. 2.29). The net radiation (R_n) is computed for each pixel using albedo and transmittances obtained from short wave bands and using long wave emission estimated from the thermal band. Soil heat flux (G) is predicted from net radiation together with other parameters such as vegetation indices, radiometric surface temperature, and albedo. Sensible heat (H) is calculated from wind observations, estimated surface roughness and surface-to-air temperature differences, using an iterative process based on the Monin-Obukhov similarity theory.

Bastiaanssen et al. (1997) applied the SEBAL procedure to estimate surface fluxes in Castilla la Mancha, Central Spain. The authors tested SEBAL using a variety of remote sensing data at resolutions ranging from 18.5 m (NSOO1) to the 4 km resolution of METEOSAT observations, using also Landsat-TM and NOAA-AVHRR imagery. The results indicated that the SEBAL procedure for estimating evaporation and evaporation resistances provided promising possibilities to describe the spatial variability of the evaporation process, if locally validated.

Bastiaanssen (2000) used the SEBAL model to estimate evapotranspiration for a homogeneous cotton area and a heterogeneous river valley floor (grapes, citrus, peaches, olives, and cotton) in Western Turkey using Landsat-5 imagery. The ground data consisted of incoming short wave radiation and wind speed. Daily values of ET were

derived from instantaneous ET values using the concept of self-preservation of the evaporative fraction.

Hamimed (2000) used Landsat TM data and SEBAL to produce a map of actual evapotranspiration and water stress degree in the Misserghine plains in West Algeria. The author found the use of this algorithm to be promising for estimating evapotranspiration and moisture indicators without the input of the numerous parameters that some physically-based models needed.

NOAA satellite data were used to determine monthly values of actual evapotranspiration, soil moisture and biomass growth in the Nilo Coehlo Irrigation area, Pernambuco, Brazil using the SEBAL approach (Mekonnen and Bastiaanssen, 2000, Bastiaanssen et al., 2001). According to the authors, this was the first time that low-cost satellite data, complemented with water flows and rainfall information, were used to evaluate indicators of yearly irrigation performance of a modern and commercialized irrigation scheme, which showed the potential of the SEBAL procedure on the evaluation of existing irrigation systems. Daily potential evapotranspiration was computed using the Priestley and Taylor equation, where the net radiation was derived from the satellite image considering the leaf area index, thermal infrared emissivity, and surface albedo:

$$\text{ET}_{\text{pot}}^{\text{NOAA}} = 1.26 \text{Rn} \frac{\Delta}{\Delta + \gamma} \tag{2.76}$$

where $\text{ET}_{\text{pot}}^{\text{NOAA}}$ is the potential evapotranspiration retrieved from NOAA imagery.

Morse et al. (2000) used the SEBAL procedure to produce ET maps for large

areas in the Bear River Basin of Idaho, Utah, and Wyoming. Estimated ET fluxes from

SEBAL were compared to ET measurements obtained from three drainage-type

lysimeters. The good agreement between estimates of ET and actual ET data supported

the potential of SEBAL to predict surface fluxes at a regional scale. The final results are

shown in Fig. 2.2.
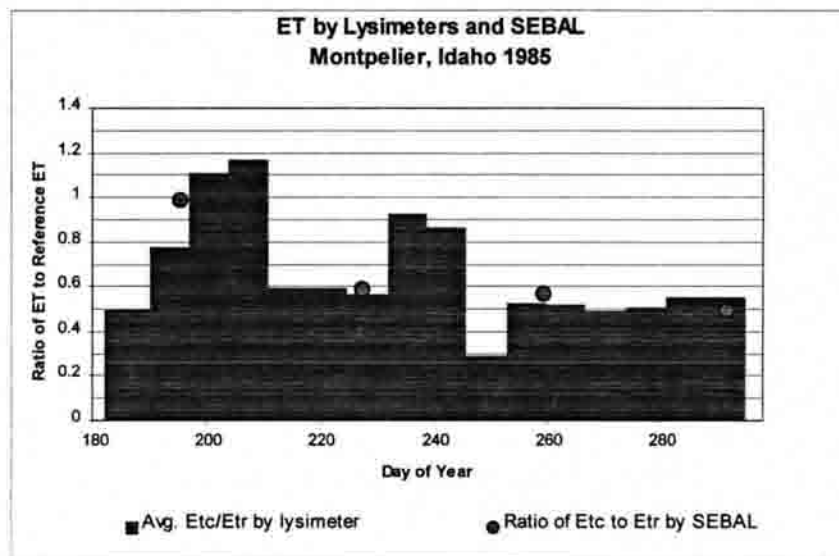
FIGURE. 2.2   Comparison of K_c (i.e. ETrF) Values Derived from 7-day Lysimeter
Measurements near Montpelier, Idaho During 1985 and Values from
SEBAL for Four Landsat Dates (Etc = crop ET; Morse et al., 2000).

Farah (2000) applied SEBAL to describe the spatial and temporal variation of

evaporation in the Naivasha Basin, Kenya on both clear and cloudy days. Two methods

to predict daily evaporation on days without satellite images due to cloud cover are

presented. The first method consisted of the application of the Penman-Monteith

equation and the Jarvis-Stewart method with standard weather data and the assumption of

gradual soil moisture changes between consecutive days. The procedure required a land-cover classification to assign land cover dependent coefficients in the Jarvis-Stewart model. The second method assumed a constant evaporative fraction between cloud free days, an approach that did not give satisfactory results in predicting evaporation on individual days. The author used NOAA-AVHRR satellite images to produce daily evaporation maps. Local ET values were validated with field data and overall good agreement was obtained.

CHAPTER III

THEORETICAL CONSIDERATIONS

The Surface Energy Balance

The law of conservation of energy, when it is related to a given vegetated or bare

soil surface, is expressed as follows:

$$R_n = LE + H + G + S + P \tag{3.1}$$

where R_n is the net radiation, LE is the latent heat flux, H is the sensible heat flux, G

is the soil heat flux, S is the amount of energy that goes into vegetation storage and P is

the amount of energy that is consumed by photosynthesis.

According to Eq. 3.1, net radiation constitutes the total amount of energy

available at the surface to be spent in several biophysical processes. Among those

processes, the energy consumed by photosynthesis is small and is usually neglected. In

addition, the amount of energy used in plant storage is small for land surfaces with short

vegetation; therefore, the energy balance is commonly expressed as:

$$R_n = LE + H + G \tag{3.2}$$

Figure 3.1 shows the surface energy balance for a vegetated surface, which is

characteristic during daytime. In this study, the flux of net radiation (R_n) is considered

positive when it is directed toward the surface, latent heat (LE) and sensible heat (H)

fluxes are considered positive when coming from the surface toward the atmosphere, and
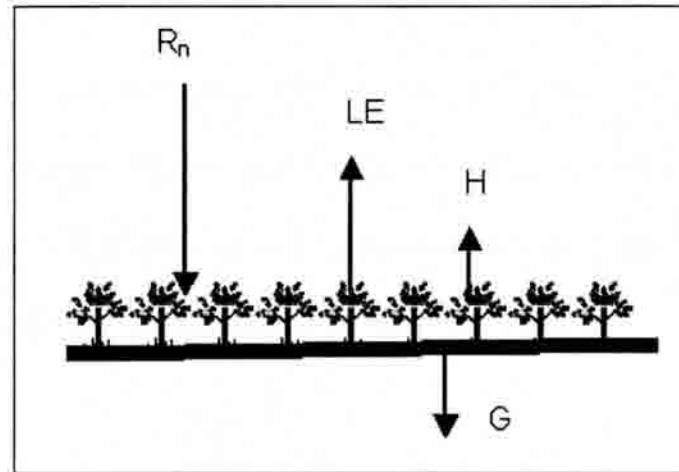
FIGURE 3.1.   Surface Energy Balance for a Vegetated Surface

soil heat flux (G) is taken as positive when going away from the surface to deeper depths

in the soil.

A useful way to calculate net radiation is to consider the radiation balance

between net shortwave (R_{ns}) and net longwave radiation (R_{nL}) at the surface, which

can be written as:

$$R_n = R_{ns} + R_{nL} \qquad (3.3)$$

Net shortwave and net longwave radiation can be separated into incoming and

outgoing terms, so that Eq. 3.3 can be expressed as:

$$R_{ns} = R_s\downarrow + R_s\uparrow \qquad (3.4)$$

and

$$R_{nL} = R_L\downarrow + R_L\uparrow + (1 - \varepsilon_0)^* R_L\downarrow \qquad (3.5)$$

where $R_s\downarrow$ and $R_s\uparrow$ are the incoming and outgoing (reflected) shortwave radiation, $R_L\uparrow$ is the longwave (thermal) radiation emitted by the surface, $R_L\downarrow$ is the longwave radiation emitted by the atmosphere that reaches the surface, ε_o is the thermal emissivity of the surface, and $(1-\varepsilon_o)^* R_L\downarrow$ represents the amount of $R_L\downarrow$ that is reflected back by the surface. Thus, the term $(1-\varepsilon_o)$ represents the albedo of the surface for longwave radiation.

Finally, the reflected shortwave radiation can be expressed as $R_s\uparrow = (1-\alpha)^* R_s\downarrow$, where α is the albedo of the surface for shortwave radiation, so that Eq 3.3 can be written as:

$$R_n = (1-\alpha)^* R_s\downarrow + R_L\downarrow + R_L\uparrow + (1-\varepsilon_o)^* R_L\downarrow \qquad (3.6)$$

Figure 3.2 displays the surface radiative balance components included in Eq. 3.6.
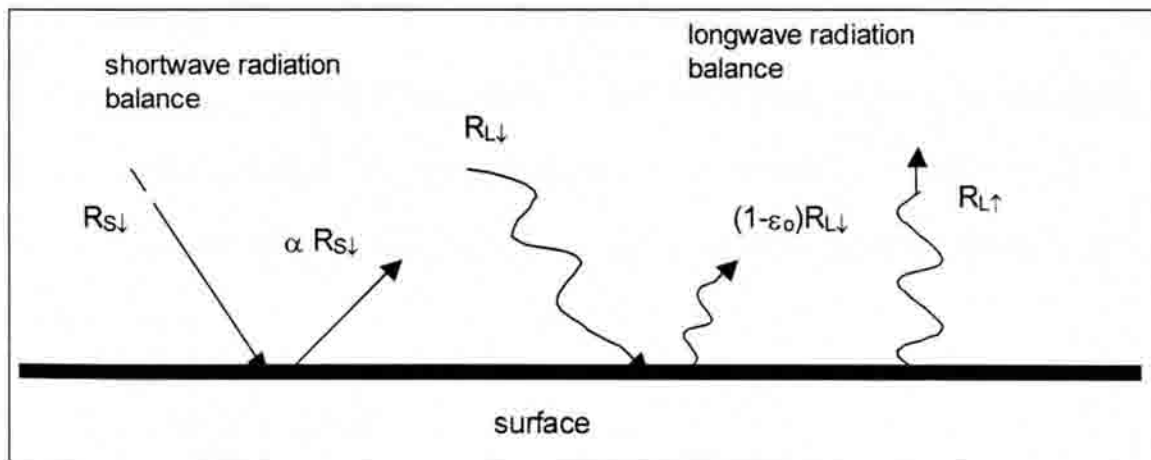
FIGURE 3.2.   Surface Radiation Balance

The incoming shortwave radiation $R_s\downarrow$ is composed of both the direct solar radiation and the diffuse radiation, having a strong diurnal variation. Reflected shortwave radiation $\alpha^* R_s\downarrow$ depends on the albedo of the surface, that is its ability to reflect shortwave radiation. In Table 3.1 common values of albedo are included for many different surfaces.

TABLE 3.1.   Albedo Values for Different Surfaces (Brutsaert,1982)

Surface	Albedo
Green grass and other short vegetation	0.15 – 0.25
Coniferous forest	0.10 - 0.15
Dry soils; deserts	0.20 - 0.35
Gray soils; bare fields	0.15 - 0.25
White sand; lime	0.30 - 0.40
Moist dark soils	0.05 - 0.15
Deep water	0.04 - 0.08
Fresh dry snow	0.80 - 0.90

As describe by Ayra (1988) the incoming longwave radiation from the atmosphere ($R_L\downarrow$) depends on the distributions of temperature, water vapor, and carbon dioxide in the atmosphere. The outgoing longwave or terrestrial radiation ($R_L\uparrow$) is strongly dependent on surface temperature, being proportional to the fourth power of it, in absolute units.

Theoretical Basis of SEBAL

The Surface Energy Balance Algorithm for Land (SEBAL) is a satellite image-processing model that has been commonly used to produce evapotranspiration maps for

large areas. The principles and steps needed to apply SEBAL to estimate

evapotranspiration are described in Bastiaanssen (1995) and Bastiaanssen et al. (1998).

SEBAL uses digital image data collected by a remote-sensing satellite measuring

visible, near-infrared and thermal infrared radiation. Evapotranspiration is computed as a

residual of the energy balance (Eq 3.2) on a pixel-by-pixel basis:

$$LE_{pixel} = R_{n\,pixel} - H_{pixel} - G_{pixel} \tag{3.7}$$

where LE_{pixel} is the latent heat flux for the pixel, and $R_{n\,pixel}$, H_{pixel}, and G_{pixel}, are the

net radiation, sensible heat flux and soil heat flux for each pixel, respectively. A general

description of the SEBAL model is presented in Fig. 3.3.

Calculation of the Energy Balance
Components in SEBAL

This section discuss the mechanics of SEBAL. Some components have been

modified during this study as explained in Chapters IV and V. Where components of the

original SEBAL model developed by Bastiaanssen et al. (1998) are described, SEBAL is

denoted as $SEBAL_B$.

In $SEBAL_B$, net radiation calculation is based on Eq. 3.6, being performed in

every pixel. The following steps are used to predict R_n in $SEBAL_B$.

Incoming Solar Radiation

The incoming short wave radiation $(R_S\downarrow)$ is predicted from the radiation

received at the top of the atmosphere as:
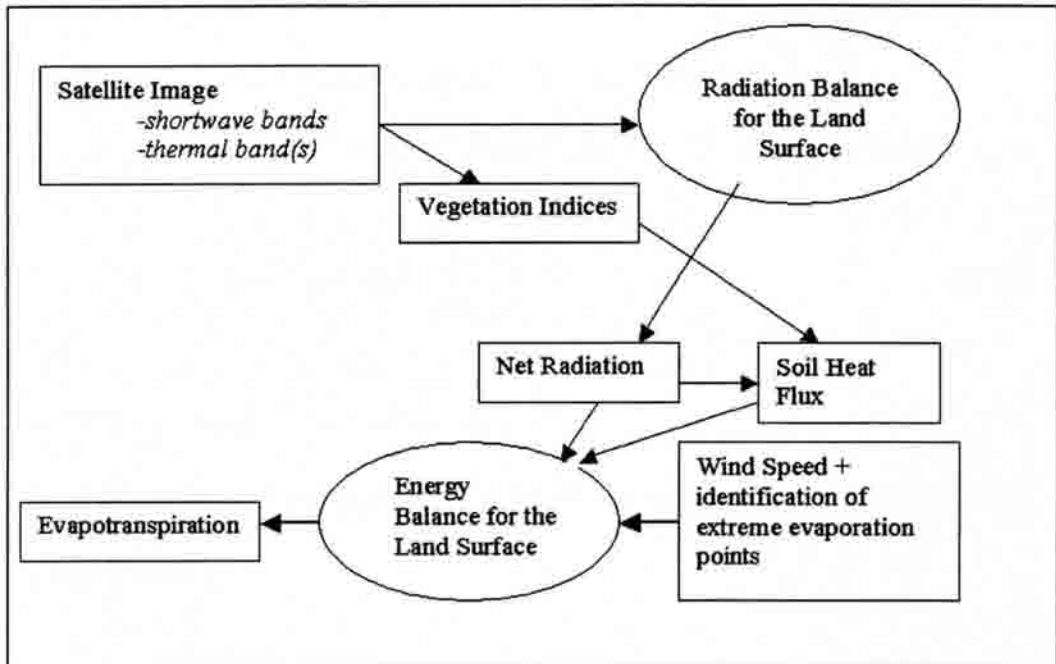
FIGURE. 3.3   Schematic of the General Computational Process for Determining
                Evapotranspiration Using SEBAL.

$$R_s\downarrow = R_a * \tau_{sw} \tag{3.8}$$

where τ_{sw} is the one-way shortwave transmittance for the atmosphere. The term τ_{sw}
accounts for the reduction of the radiation received at the top of the atmosphere due to
absorption and scattering effects by the atmosphere. Therefore, the ratio between the
radiation received at the surface ($R_s\downarrow$) and the radiation received at the top of the
atmosphere (R_a) defines the transmittance of the atmosphere for shortwave radiation
(τ_{sw}).

The amount of radiation receive at the top of the atmosphere, R_a, is calculated as:

$$R_a = G_{sc} * \cos\theta * d_r \tag{3.9}$$

where Gsc is the solar constant = 1367 W/m², cosθ is the cosine of the solar zenith

angle, and dr is the inverse relative squared distance Earth to Sun.

The value of dr is calculated following Duffie and Beckman (1980) as:

$$d_r = 1 + 0.033 \cos\left(DOY \frac{2\pi}{365}\right)$$ (3.10)

where DOY is the sequential day of the year.

For a flat surface, the cosine of the solar incident angle is calculated from the

solar elevation angle as:

$$\cos\theta = \cos\left(\frac{\pi}{2} - \phi\right)$$ (3.11)

where ϕ is sun elevation angle in radians. Figure 3.4 shows the definition of the angles

θ and ϕ:

FIGURE 3.4.   Definition of the Angles θ and φ.

$$R_L\uparrow = \varepsilon_o\, \sigma\, T_S^4 \tag{3.14}$$

where ε_o is the broadband surface emissivity, and T_S is the surface temperature.

<u>Surface Albedo</u>

Albedo is the ratio of reflected to incident solar radiation at the surface:

$$\alpha = \frac{R_{s\uparrow}}{R_{s\downarrow}} \tag{3.15}$$

where α is the albedo, $R_{s\downarrow}$ is the incoming short wave radiation, and $R_s\uparrow$ is the outgoing short wave radiation.

In the SEBAL$_B$ procedure, the hemispherical surface albedo (α) is obtained from the broadband directional planetary reflectance (α_{toa}). According to Chen and Ohring (1984), cited by Bastiaanseen et al. (1998), the surface albedo can be approximated with the following equation:

$$\alpha = \frac{\alpha_{toa} - \alpha_{path\_radiance}}{\tau_{sw}^2} \tag{3.16}$$

where α is the surface albedo, αt_{oa} is the clear-sky shortwave hemispherical albedo at the top of the atmosphere, $\alpha_{path\ radiance}$ is the albedo path radiance, and τ_{sw} is the broadband shortwave atmospheric transmittance.

The Albedo path radiance is the part of the incoming radiation that is reflected by the atmosphere before it reaches the surface and can be eventually sensed by the satellite, increasing the amount of measured radiation. It has an approximate value between 0.025

to 0.04 (Bastiaanssen, 2000). Equation 3.16 presumes a consistent "mixture" of spectral

density in the use of a constant value for the broadband transmittance.

The albedo at the top of the atmosphere, α_{toa}, is computed by performing a

narrow-band to broad-band integration of all reflectance bands in the visible and

near-infrared region of the spectrum:

$$\alpha_{toa} = \int_{0.3}^{3.0} \rho_\lambda \, d\lambda = \sum_{i=1}^{n} w_\lambda \rho_{\lambda i} \qquad (3.17)$$

where n represents the total number of spectral bands i of the sensor corresponding to

the 0.3 to 3.0 μm region of the spectrum, w_λ is a weighting factor that accounts for

the uneven distribution of the extraterrestrial radiation for each narrow band region of the

spectrum, and $\rho_{\lambda i}$ is the narrow band spectral reflectance (ρ_λ) corresponding to band i.

Thermal Infrared Surface Emissivity, ε_o

The emissivity of an object is the ratio of the energy radiated by that object at a

given temperature to the energy radiated by a blackbody at the same temperature

(according to Plank's Law). Since the thermal radiation of the surface is observed in the

thermal band, one can compute the surface temperature from this band if the emissivity

of the land surface is estimated.

In SEBAL$_B$ (Bastiaanssen et al., 1998) surface emissivity for the 8-14 μm spectral

range is estimated using NDVI and an empirically-derived method:

$$\varepsilon_O = 1.009 + 0.047 \ln (NDVI) \qquad (3.18)$$

where NDVI is the normalized difference vegetation index (Jensen, 2000), which is calculated as follows:

$$NDVI = \frac{\rho_{nir} - \rho_{red}}{\rho_{nir} + \rho_{red}} \tag{3.19}$$

where, ρ_{nir} is near-infrared reflectance, and ρ_{red} is the reflectance in the red region of the visible spectrum.

Surface Temperature, T_s

The total radiation emitted by a body, at a given temperature, is explained by the Stefan-Boltzman law:

$$B = \varepsilon_0 \, \sigma \, T_s^4 \tag{3.20}$$

where, B is radiation emitted from the body, ε_0 is the emissivity of the surface, σ is the Stefan Boltzman constant ($5.67 * 10^{-8}$ ($W/m^2/K^4$), and T_s is the surface temperature of the body (K). In the thermal region, the total emitted radiation used in the Stefan Boltzman equation corresponds to wavelengths from $3.0 \mu m$ to infinity. However, since satellite thermal bands are related to narrower ranges, $SEBAL_B$ uses Plank's law which is given by the following equation:

$$B_\lambda = \varepsilon_\lambda \frac{2 \pi h c^2}{\lambda^5 \times \exp\left(\frac{hc}{k\lambda T}\right) - 1} \tag{3.21}$$

where B_λ is the intensity of the radiation emitted by the body at a given wavelength λ (W/m^2), ε_λ is the emissivity of the body for a specific wavelength λ, h is Plank's constant $6.626*10^{-34}$ Joule*sec, c is the speed of light $= 2.998*10^8$m/s , k is the Stephan-Boltzman constant, $1.381*10^{-23}$JK^{-1}, and T is the temperature of the body, in K.

Soil Heat Flux

As describe by Oke (1996) soil heat flux at any depth z can be expressed by:

$$G = K_{TS} \frac{\partial T_{soil}}{\partial z} \tag{3.22}$$

where T_{soil} is the temperature of the soil and K_{TS} is the thermal conductivity of the soil in Jm^{-1}s^{-1} $^\circ$C^{-1}, G in Wm-2, for T_{soil} in $^\circ$C and z in m.

In SEBAL$_B$, an empirical equation is applied to estimate the surface soil heat flux G. This equation was developed based on the concept proposed by Choudhury et al. (1987) where the ratio between soil heat flux and net radiation for bare soil conditions was expressed as:

$$G/R_n = \Gamma' \tag{3.23}$$

and for a vegetated soil:

$$G/R_n = \Gamma' * \Gamma'' \tag{3.24}$$

where Γ' is a proportionality factor that describes the conductive heat transfer in soil and Γ'' is an extinction factor that takes into account the attenuation of radiation through the canopy.

The empirical equation proposed by Bastiaanssen et al. (1998) to compute the soil heat flux for any condition of vegetation cover and type of soil is the following:

$$G/R_n = \frac{T_s}{\alpha}\left(0.0038\alpha + 0.0074\alpha^2\right)\left(1 - 0.98\text{NDVI}^4\right) \tag{3.25}$$

where α is the daytime-representative albedo. In Eq. 3.25 the first term $(T_s/\alpha)*(0.0038*\alpha+0.0074\alpha^2)$ represents the factor Γ' and the term $(1-0.98\text{NDVI}^4)$ represents the term Γ'' of Eq. (3.24). Eq. 3.25 was validated using data collected by Bastiaanssen (1995), as well as using data obtained from Choudhury et al. (1987), Daughtry et al. (1990), and Clothier et al. (1986).

Sensible Heat Flux

After calculating R_n and G, the calculation of the sensible heat flux H is required to obtain the terms that will allow the computation of ET as a residual from the energy balance. The aerodynamic transfer of heat to air, H, is predicted using the following equation (Brutsaert, 1982):

$$H = \rho C p \frac{T_{aero} - T_a}{r_{ah}} \tag{3.26}$$

where ρ is the air density, function of atmospheric pressure, Cp is the specific heat capacity of air 1004(J/kg/k), T_{aero} is the aerodynamic surface temperature, T_a is the

reference height air temperature, and r_{ah} is the aerodynamic resistance to sensible heat transport between the surface and the reference height, which is computed from Eq. 2.31.

In SEBAL, instead of T_{aero}, the reference temperature is taken to be T_1, an air temperature located at height z_1 close to the surface. This consideration was initially proposed by Qualls et al. (1993) and Bastiaanssen (1995) to eliminate some of the challenges of being $T_{aero} \neq T_{rad}$. Previous works by Bastiaanssen et al. (2000) considered z_1 to be located at 0.01 m over the surface. However, because of logarithmic K-theory, the temperature profile can not be extrapolated below z_{oh} (roughness length for heat transfer), in this study the height z_1 is defined to be located at a height $z_1 = 0.1$ meters over the zero-displacement plane (d).

The upper height is taken at a height $z_2 = 0.2$ meters and its corresponding temperature is called T_2. The difference between T_1 and T_2 is referred to as "near surface air temperature difference" (dT). The sensible heat flux is then defined as:

$$H = \rho \ Cp \frac{dT}{r_{ah}} \tag{3.28}$$

where r_{ah} is the aerodynamic resistance to heat transport between z_1 and z_2, and dT is the air temperature difference between the two heights z_1 and z_2 above the surface, $dT = T_1 - T_2$. The location of z_1 and z_2 is illustrated on Fig. 3.5.

In consistency with the profile formulation shown in Fig. 3.5, the value of r_{ah} is estimated with the following equation:
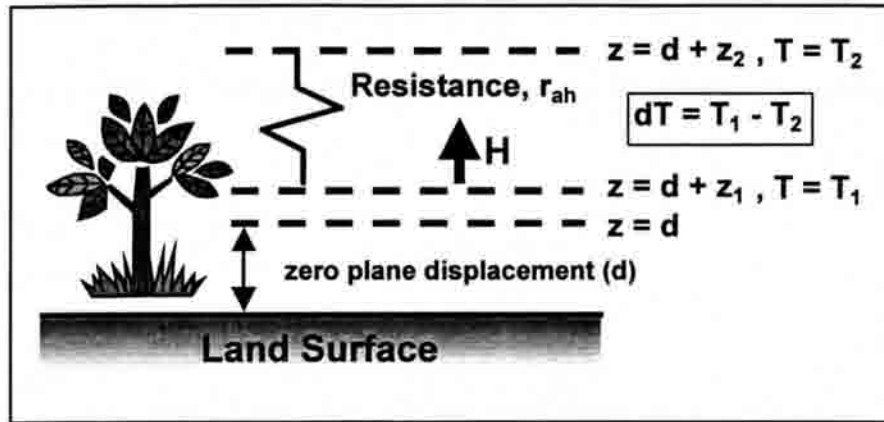
FIGURE 3.5.   Definition of Aerodynamic Resistance for Heat Transfer (Tasumi et al., 2000).

In consistency with the profile formulation shown in Fig. 3.5 , the value of r_{ah} is estimated with the following equation:

$$r_{ah} = \frac{\ln\left(\dfrac{z_2}{z_1}\right) - \Psi_{h(z_2)} + \Psi_{h(z_1)}}{u_* \times k} \tag{3.29}$$

where, z_1 and z_2 are heights defined in Fig. 3.5, u_* is the friction velocity, k is the von Karman constant ($= 0.41$), and ψ_h is the integrated stability correction factor for atmospheric heat transfer, where $\psi_{h(z1)}$ is ψ_h corresponding factor between the surface and z_1 and $\psi_{h(z2)}$ is ψ_h between the surface and z_2.

Procedure for calculating sensible heat flux. Bastiaanssen (1995) developed a procedure based on the Monin-Obukov similarity-stability theory to compute the sensible heat flux accounting for stability effects on r_{ah} and H. The procedure is the following:

1) The $SEBAL_B$ procedure needs as input, a measurement of wind speed corresponding to the moment in which the satellite image is taken. In addition, information about the

station location and for the specific time of the satellite overpass by using the logarithmic

wind law and considering neutral conditions surrounding the weather station site:

$$u_* = \frac{ku_x}{\ln\left(\dfrac{z_x}{z_{om}}\right)} \tag{3.30}$$

where u_x is the wind speed measured at height z_x at the weather station.

In Eq. 3.30 z_{om} is empirically estimated from the average of vegetation height

around the meteorological weather station by the following equation (Brutsaert, 1982):

$$z_{om} = 0.123 * h \tag{3.31}$$

where h is the vegetation height in meters

2) Assuming a constant value of the friction velocity with height, above the weather

station, $SEBAL_B$ calculates a value of wind speed at some "blending" height in the

atmosphere, where one can assume that the wind velocity just begins to be unaffected by

surface roughness elements. Considering a height of 200 m over the ground, wind speed

at 200 m (u_{200}) is calculated as:

$$u_{200} = u_* \frac{\ln\left(\dfrac{200}{z_{om}}\right)}{k} \tag{3.32}$$

3) Because the blended wind speed at 200 meters is assumed to be independent of

specific surface features, $SEBAL_B$ considers that u_{200} is equal for all pixels of the

satellite image, but can still be extrapolated to specific pixels and cover conditions using

Eq. 3.30 to calculate a unique friction velocity (u_*) corresponding to each pixel, using the particular value of z_{om} for each pixel.

4) Assuming neutral conditions initially ($\psi_{h(z2)} = \psi_{h(z1)} = 0$), a starting value of aerodynamic resistance is calculated for each pixel using Eq. 3.29.

5) Sensible heat for each pixel is calculated using the near-surface air temperature difference (dT) using Eq. 3.28. To determine the value of dT for each pixel, the SEBAL$_B$ procedure assumes the existence of a linear relationship between dT and surface temperature T_s:

$$dT = a\,T_S + b \tag{3.33}$$

where dT is the near-surface air temperature difference, T_S is the surface temperature, and "a" and "b" are empirical coefficients.

The assumption implicit in SEBAL is that hot areas (with larger thermal emittance) create higher vertical differences in air temperature dT than cold surfaces and that this relationship is linear. The linear relationship between T_s and dT has been explored in field experiments carried out in Egypt and Niger (Bastiaanssen et al., 1998), China (Wang et al. 1994, cited by Bastiaanssen et al., 1998), Kenya (Farah, 2000), and USA (Frank and Beven, 1997).

To define the coefficients "a" and "b" for Eq. 3.33, the SEBAL approach involves the selection of two extreme "anchor" pixels, where the value of H can be reasonably assumed:

5.1)   Cold (wet) pixel. In SEBAL$_B$, a cold pixel corresponds to a surface having the following characteristics:

$$ET_{cp} = R_{n\ cp} - G_{cp} \ ; \quad H_{cp} = 0 \ ; \quad dT_{cp} = T_2 - T_1 = 0$$

where the subscript "cp" represents fluxes and air temperatures corresponding to the cold pixel. Thus, the cold pixel is one pixel where all of the available energy $(R_n\text{-}G)$ is converted into evaporation or evapotranspiration. Bastiaanssen (2002, personal communication) has routinely used a water surface as the cold pixel in $SEBAL_B$ In this current study, the use of alfalfa reference ET has been investigated to represent conditions at the cold pixel, as explained in Chapter V.

5.2)   Hot Pixel (or dry pixel): In $SEBAL_B$ the hot pixel is related to a surface having the following characteristics:

$$ET_{hp} = 0 \ ; \quad H_{hp} = R_{n\ hp} - G_{hp} \ ; \quad dT_{hp} = T_2 - T_1 = H_{hp} \times r_{ah} / (\rho\ Cp)$$

where the subscript "hp" represents values corresponding to the hot pixel. In the hot pixel all of the available energy is assumed to be converted into sensible heat. To select the hot pixel, one has to explore the image for pixels having the highest or near highest surface temperature. For definition, the hot pixel has to be dry so that there is no moisture available for evaporation. However, often some range in surface temperature is observed for the population of pixels that are presumed to have nearly zero ET. This is caused by impacts of albedo, G, or aerodynamic roughness. Therefore, care must be exercised in selecting an appropriate hot pixel. Bastiaanssen (2000) used the Aegian Sea and a dry area with burned vegetation as cold and dry pixels for application in Turkey.

In the current study, a dry, bare agricultural soil was selected as the best candidate for the hot pixel due to better knowledge of z_{om} and G.

Once one has selected the hot and cold pixels, two dT vs T_S pairs are defined, and the coefficients "a" and "b" for Eq. 3.33 can be derived as shown in Fig. 3.6. The dT function allows for the prediction of dT for each pixel based on the corresponding pixel surface temperature. Using the predicted dT, a first approximation of the value of sensible heat flux (H) can be obtained for each pixel using Eq. 3.28.
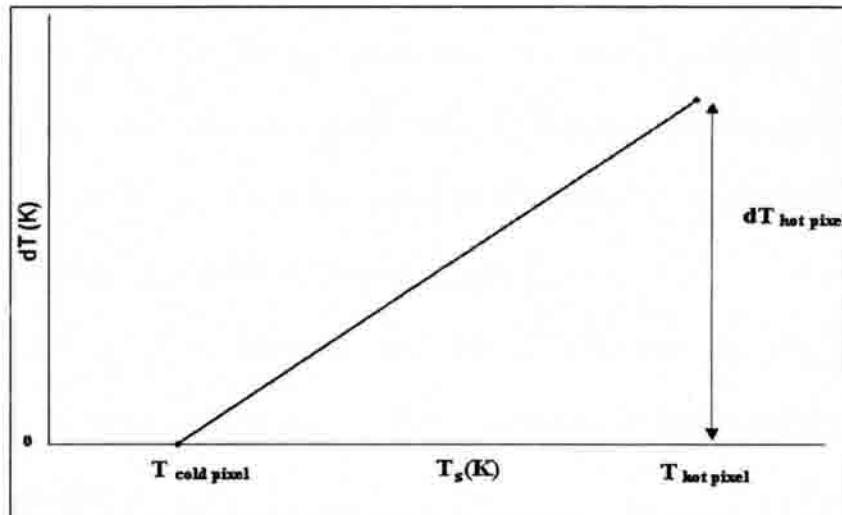
FIGURE 3.6.   SEBAL$_B$ Definition of the   dT vs T_s Relationship.

6) Adjustment of aerodynamic resistance for atmospheric stability

The first estimate of sensible heat flux is obtained by assuming neutral atmospheric conditions in the calculation of r_{ah}. To account for the buoyancy effects that surface heating generates in the lower atmosphere, SEBAL uses the Monin-Obukov similarity theory through the following iterative process:

6.1)   The Monin-Obukhov Length parameter (L)   is calculated as in Monteith and

Unsworth (1990) :

$$L = -\frac{\rho\ Cp * u.^{3} T_{s}}{k\,g\,H} \qquad\qquad (3.34)$$

where ρ is air density in kg/m^{3}, Cp is heat capacity of air (= 1004 J/kg/K), T_{s} is in K, g is

gravitational acceleration (= 9.81 m/s^{2}), k is the von Karman constant = 0.41, and H is the

sensible heat flux in W/m^{2}.

In $SEBAL_{B}$, T_{s} is used instead of T_{a} for the calculation of L from Eq. 3.34.

Uncertainties in the value of T_{a} for each pixel, makes the use of T_{a} from Eq. 3.34

difficult. In addition, sensitivity analysis performed by Tasumi et al.(Appendix K) during

this study, showed that a variation of less than 2 % in the final estimation of LE results

is obtained when using T_{s} instead of air temperature, T_{a}

The value of L defines the stability condition of the atmosphere. If L < 0

(H > 0) the atmosphere is unstable, L > 0 indicates stable conditions, and L = ∞,

(H=0), neutral conditions.

Theoretically, the absolute value of L represents the thickness of the layer where

wind shear effects dominates over buoyancy forces in the production of turbulence. For

that reason, when H = 0 (no buoyancy forces), L is infinite. On the other hand, when H

is positive L tends to be numerically smaller as H increases.

6.2)   Depending on the atmospheric stability condition, the values of the stability

parameters for momentum and heat transfer are calculated as follows (Allen et al.,

1996) :

If $L < 0$

$$\Psi_{m(200m)} = 2\ln\left(\frac{1 + x_{(200m)}}{2}\right) + \ln\left(\frac{1 + x_{(200m)}^2}{2}\right) -$$
$$- 2ARCTAN\left(x_{(200m)}\right) + 0.5\pi \tag{3.35}$$

where

$$\Psi_{h(z1)} = 2\ln\left(1 + \frac{x_{(z1)}^2}{2}\right) \tag{3.36}$$

$$\Psi_{h(z_2)} = 2\ln\left(1 + \frac{x_{(z_2)}^2}{2}\right) \tag{3.37}$$

where:

$$x_{(200)} = \left(1 - 16\frac{(200)}{L}\right)^{0.25} \tag{3.38}$$

$$x_{(z1)} = \left(1 - 16\frac{(z_1)}{L}\right)^{0.25} \tag{3.39}$$

$$x_{(z_2)} = \left(1 - 16\frac{(z_2)}{L}\right)^{0.25} \tag{3.40}$$

and If $L > 0$

$$\Psi_{h(z1)} = -5\left(\frac{z_1}{L}\right) \tag{3.41}$$

$$\Psi_{h(z_2)} = \Psi_{m(200)} = -5\left(\frac{z_2}{L}\right) \tag{3.42}$$

The use of $z = z_2$ (which is 2 m) in Eq.3.42 assumes that the height of any stable layer is 2 m. Above this height, the procedure assumes that the air profile is nearly neutral during calculation of friction velocity

6.3) A new value of the friction velocity u_* is calculated for each pixel as:

$$u_* = \frac{k \, u_{200}}{\ln\left(\dfrac{200}{z_{om}}\right) - \Psi_{m(200)}} \tag{3.43}$$

Eq. 3.43 presumes that, over each pixel, the wind profile is impacted by the instability of the surface on the pixel. This requires the assumption that surrounding pixels are similar in aerodynamic and energy balance characteristics. This is generally the case when agricultural fields are in the order of 400 m or greater and desert areas are relatively homogenous.

6.4) Then, a stability-corrected value of the aerodynamic resistance is computed with Eq. 3.29.

6.5) Because of the new value of r_{ah} corresponding to the hot pixel, the value of dT has to be recalculated for the hot pixel by inverting Eq. 3.28 as $dT_{hp} = H \times r_{ah} / (\rho \, Cp)$. This new value of dT_{hp} changes the linear equation that defines the dT versus T_s relationship (Eq. 3.33) and requires a new calculation of the value of sensible heat for each pixel. The iterative process for r_{ah}, dT, and H continues until values of r_{ah} become stable. Figure 3.7 shows the iterative process used in SEBAL to obtain the sensible heat flux for each pixel.
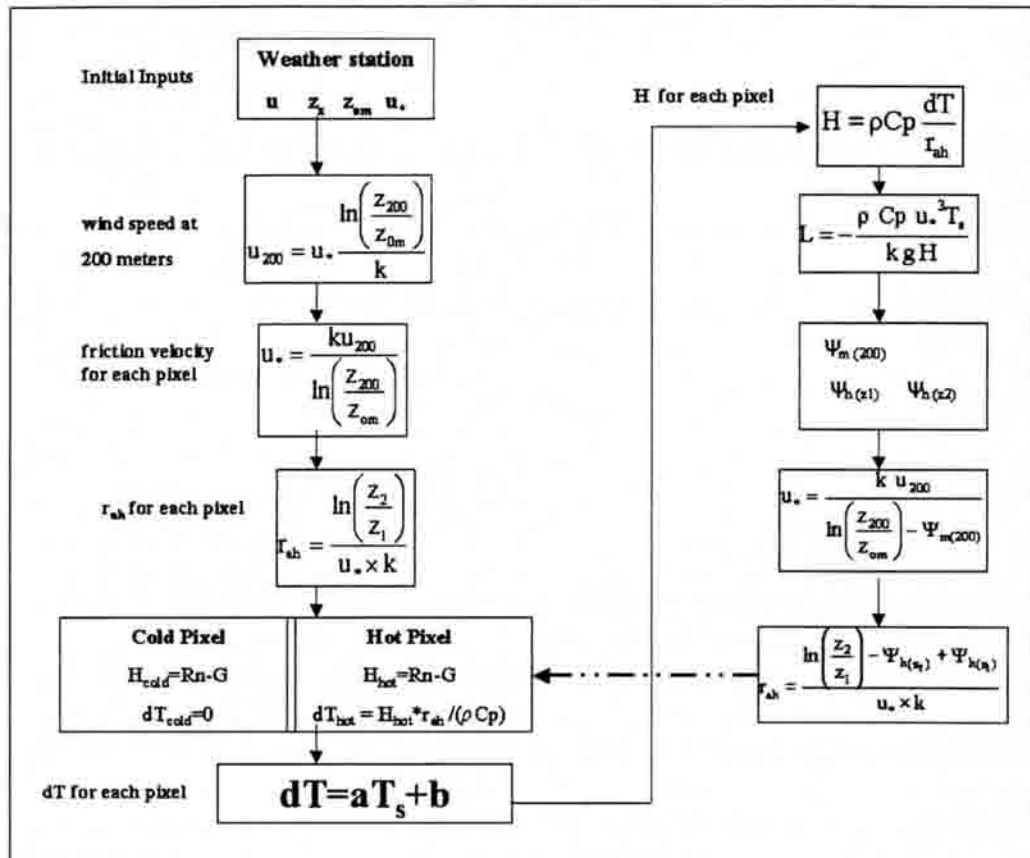
FIGURE 3.7. Monin-Obukov Based Iterative Process to Calculate Sensible Heat in SEBAL$_B$.

Surface Roughness for Momentum
Transport, z_{om}

Surface roughness for momentum transport z_{om} is defined as the height above the

"zero-plane displacement" where the zero-origin for the mean wind profile just begins

within the surface or vegetation cover.

In SEBAL$_B$ (Bastiaanssen, 1995), surface roughness is estimated from NDVI

$$z_{om} = \exp(a \times NDVI) + b \qquad (3.44)$$

or from SAVI, Bastiaanssen (1998):

$$z_{om} = \exp(a \times SAVI + b) \tag{3.45}$$

where, a and b are constants. These constants are derived by linearly correlating values of NDVI (or SAVI) to estimates of z_{om} for sample pixels representing specific vegetation types, and are therefore determined uniquely for each image based on knowledge of the or from SAVI, Bastiaanssen (1998):

$$z_{om} = \exp(a \times SAVI + b) \tag{3.45}$$

where, a and b are constants. These constants are derived by linearly correlating values of NDVI (or SAVI) to estimates of z_{om} for sample pixels representing specific vegetation types, and are therefore determined uniquely for each image based on knowledge of the operator. Allen (2002, personal communication) used NDVI/albedo as the independent variable in Eq. 3.45 to distinguish between forest and agriculture in Florida.

Calculation of 24-hour ET

Once the final (numerically stable) values for H are calculated, the latent heat flux LE for each pixel is calculated from Eq. 3.7 using values for H, G and R_n. This LE represents the instantaneous evapotranspiration at the time of the satellite overpass.

To estimate the 24-hour evapotranspiration for the day of the image, $SEBAL_B$ uses an approach based on the self-preservation theory of daytime fluxes (Shuttleworth et al., 1989; Brutsaert and Sugita, 1992), which states that the ratio between the latent heat flux and the available energy (R_n-G) remains fairly constant during the day. The ratio between LE and R_n-G termed evaporative fraction (EF) is expressed as follows:

$$EF = \frac{LE}{R_n - G} = \frac{LE_{24}}{R_{n24} - G_{24}} \qquad (3.46)$$

where EF is the evaporative fraction, LE, R_n, and G are the values of latent heat flux, net radiation, and soil heat flux corresponding to the time where the satellite image was taken, and LE_{24}, R_{n24}, G_{24} are the daily values (24 hours) for the same fluxes.

From Eq. 3.46, the 24 hour actual evaporation is calculated by the following equation:

$$ET_{24} = \frac{EF(R_{n24} - G_{24})}{\lambda} \qquad (3.47)$$

where λ is the latent heat of vaporization, calculated as:

$$\lambda = (2.501 - 0.00236(T_s - 273)) \times 10^6 \quad (J/kg) \qquad (3.48)$$

Considering that the total soil heat flux during a day is approximately equal to zero for vegetation and most bare soil conditions, Eq. 3.47 reduces to:

$$ET_{24} = \frac{EF * R_{n24}}{\lambda} \qquad (3.49)$$

The equation recommended by Bastiaanssen et al. (1998) for calculating R_{n24} under all-day clear sky conditions is:

$$R_{n24} = (1-\alpha)R_{a24}\tau_{sw} - 110\tau_{sw} \qquad (3.50)$$

where Ra_{24} is the daily extraterrestrial radiation. If the day of the satellite image is

known to have had some cloudiness during periods preceding or following the time of the

image, then one should use a locally (ground-based) measured value for 24-hour solar

radiation (R_s) in place of $R_{a24}\, \tau_{sw}$ in Eq. 3.50 and the value of τ_{sw} can be estimated as

$R_s/\, R_{a24}$.

   The details of calculation of R_{a24} are included in Allen et al. (2002).

CHAPTER IV

PROCEDURE

Overview

The overall intent of this research was to improve means for generating ET maps

for the Eastern Plain Aquifer region in Southern Idaho, an area that has more than

7,000 square km of irrigated farmland. An operational remote sensing model is desired

for routine application by the Idaho Department of Water Resources (IDWR) as a means

for predicting ET over large areas, modeling ground water, solving water rights disputes,

and performing a better management of the water resources of the region.

The Surface Energy Balance Algorithm for Land (SEBAL) was selected as the

basis to develop a model that can be adapted to the prevailing conditions of the study

area. To validate and refine SEBAL in this work, concurrent satellite imagery and

measured ET values were used. ET data were provided by measurements of ET

performed at the USDA-ARS facility located at Kimberly, Idaho, under the supervision

of Dr. James Wright (Wright, 1982). ET data are available for a wide range of weather

conditions, surface covers, and crop types. In addition, measurements of net radiation,

soil heat flux and plant canopy parameters were made at or near the lysimeter. This

dataset provides valuable information to evaluate and refine the accuracy of SEBAL for

instantaneous ET values as well as to verify procedures for extrapolating remote sensing

algorithms over various time scales and for various types and categories of land cover.

With regard to remote sensing data for the application of SEBAL, Landsat 5 TM and 7

ETM+ imagery were utilized.

Site Description

The study area is located in the Eastern Snake River Plain, Southern Idaho, USA. The site is comprised of a variety of surfaces such as agricultural lands, deserts, water bodies, and wetlands. Details of the study area are depicted in Fig. 4.1.

Evapotranspiration Data

Description of the Kimberly Lysimeters

The ET data used in this study were collected by Dr. J.L. Wright over two adjacent fields located about 1 km south of the USDA-ARS research facility at Kimberly, Idaho. Geographically, the experimental fields were located at a latitude of 42°33' N, a longitude of 114°21' W, with an elevation of 1195 m. The fields were within a large, nearly flat area surrounded by agricultural fields with prevailing winds blowing from the west. According to Vanderkimpen (1991) these western winds often carry hot and dry air from the desert to the study area, which is therefore subject to considerable regional advection.

Each experimental field was instrumented with weighing lysimeters from which ET values were obtained. The first weighing lysimeter (lysimeter 1) was installed in 1968 near the center of a 130 x 198 meters (2.6 ha) rectangular field. The second lysimeter (lysimeter 2) was installed in 1971, in a field west of lysimeter 1, with an area of 143 x 179 m. Both lysimeters were dismantled in late 1991. In Fig. 4.2 details of the location of the lysimeter are shown. Figure 4.3 shows a picture of lysimeter 2.
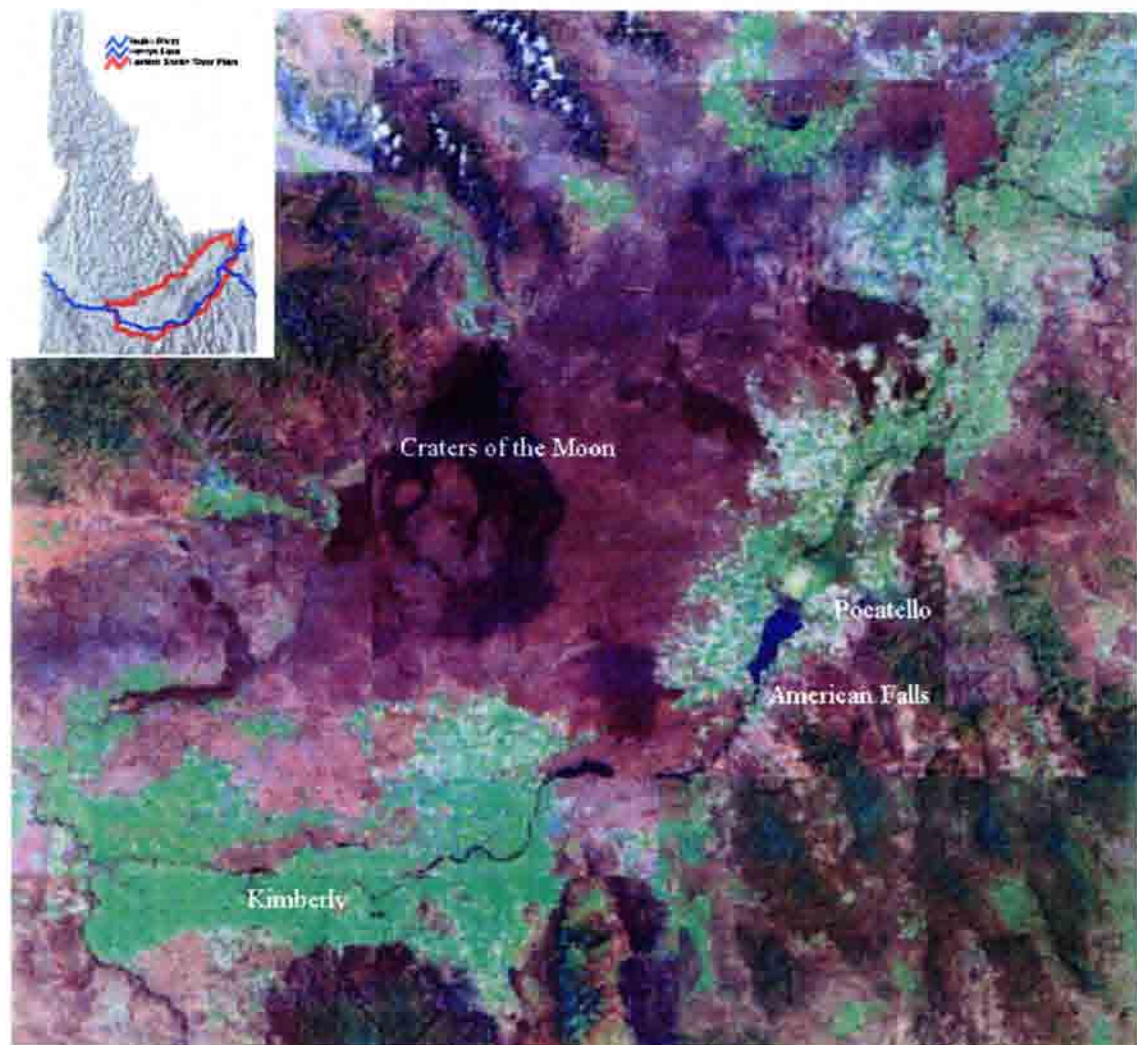
FIGURE 4.1.   True Color Landsat Mosaic Image of the Eastern Snake Plain Aquifer
(ESPA) Area.

The two weighing lysimeters had dimensions of 1.83 m x 1.83 m with a 1.22 m

depth, and full details of dimensions and operation can be found in Wright (1982) and

Wright (1991). Lysimeter had adequate fetch in all directions (Wright, personal

communication), which assure that ET measured at the lysimeter was representative of

the field conditions.
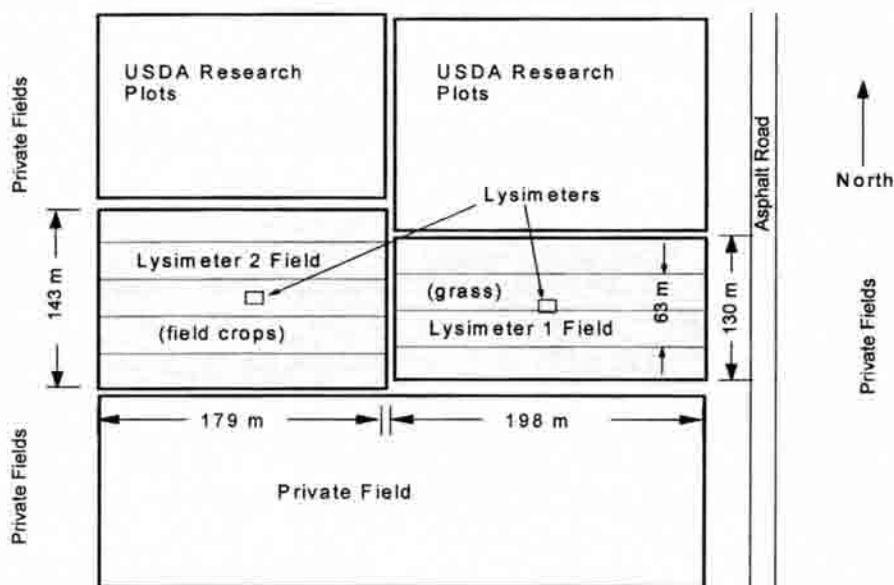
FIGURE 4.2.   Plan View of Kimberly Lysimeters and Surroundings.

FIGURE 4.3.   Picture of Sweet Corn in Lysimeter 2 at Kimberly, Idaho (picture provided by Dr. J.L. Wright, USDA, Kimberly, Idaho).

Weight changes in the lysimeters were determined with an electronic load cell. Lysimeter load cell volt readings were transformed to the corresponding water depth equivalents. Lysimeters were operated year round with measurements recorded continuously on ink charts and read hourly manually. ET data are available for a wide range of weather condition, surface covers, and crop types as shown in Table 4.1.

The climate of the study area is arid. Most of the annual precipitation occurs outside of the growing season. According to Wright (2002, personal communication) the soil present at the lysimeter sites is a Portneuf silt loam soil, about four meters deep and underlain by fractured, basalt, rock.

TABLE 4.1. Crops Grown on Kimberly Lysimeters, during 1969-1991. Dr. J.L. Wright (2002, personal communication).

Year	Lysimeter 1	Lysimeter 2
1969-1971	alfalfa	--------
1972	potatoes	alfalfa
1973-1974	snap beans	alfalfa
1975	sugar Beets	alfalfa
1976	sweet corn	field corn
1977	peas / bare soil	field corn
1978	winter wheat	spring barley
1979	spring wheat	spring wheat
1980-1982	alfalfa	oats / alfalfa
1983-1984	rye grass	alfalfa
1985	fescue grass	alfalfa / grass
1986	fescue grass	dry beans / winter wheat
1987	fescue grass	winter wheat (Stephens)
1988	fescue grass	potatoes (Kennebec)
1989	fescue grass	sugar beets
1990	fescue grass	peas / alfalfa
1991	fescue grass	alfalfa

The lysimeter data obtained at Kimberly, Idaho represent accurate and continuous measurements of ET fluxes over a long period of time, so that they represent a dataset that can be used to validate remote sensing algorithms at a local scale.

Weather Data

Micrometeorological data collected by Dr. J. Wright at the Lysimeter site were used as the main source of weather data for validation of SEBAL in this study. The high quality of the collected data and the location of the station near the lysimeter, is valuable in describing land-atmosphere related parameters. In addition, the use of other weather stations, such as the U.S. Weather Service Station (located within 1 km from the lysimeter site), adjacent to the USDA-ARS research center, as well as a co-located AGRIMET weather station were utilized. Weather data included measurements of air temperature, wind speed and direction, dewpoint temperature, and solar radiation at all the mentioned stations. In addition, at the lysimeter micrometeorological station, net radiation and soil heat flux were recorded.

Lysimeter And Weather Data Integrity
Assessment

All of the lysimeter and weather data used in this study were validated and corrected using a methodology based on Itenfisu (1998), Allen et al. (1998), and ASCE-EWRI. (2002). Details of the procedures are included in Appendix A.

Remote Sensing Data

Landsat 5 TM and Landsat 7 ETM+ imagery were used as the source of remote sensing data for this study. Landsat imagery was selected because it has the finest

resolution (28.5 to 30 m shortwave pixel size) of all satellite sensors equipped with a thermal band.

Outline of the Procedure

The procedure applied in this work is divided in two parts: a) Development and validation of the model, and b) Estimation of ET for year 2000 for the ESPA. Because of the many modification made to the original SEBAL$_B$, the model adapted in this study to the Idaho conditions is referred to as SEBAL$_{ID}$ (SEBAL Idaho). Therefore, SEBAL$_{ID}$ is an adaptation of SEBAL$_B$ for the conditions present in the study area.

<u>Development and Validation of the Remote
Sensing Model</u>

Here results obtained from SEBAL$_{ID}$, including modifications of some components, were compared to actual ET measurements from the Kimberly Lysimeters. The comparison between modeled and measured ET allowed the validation and refinement of various SEBAL$_B$ algorithms and the re-parameterization of some surface processes. A total of 12 Landsat 5 TM images (from 1988 to 1991) were selected from cloud free days and where lysimeter ET were available. Specifically, eight images were evaluated for the year 1989 for a crop of sugar beets, covering the period April to September. One scene was evaluated for potatoes in 1988, one for peas in 1990, and one for alfalfa in 1991. These images were additionally used to test the best approach for extrapolating instantaneous to daily ET and daily ET to seasonal values. Table 4.2 shows the dates of satellite imagery used in this part of the research as well as the crops present at the lysimeter sites.

TABLE 4.2.   Information of Remote Sensing Data and Crops Used in Validation of the
             Model

Date of the Landsat 5 Image	Crop in Lysimeter 1	Crop in Lysimeter 2
08/21/1988	Fescue Grass	Potatoes
04/18/1989	Fescue Grass	Sugar Beets
05/04/1989	Fescue Grass	Sugar Beets
06/05/1989	Fescue Grass	Sugar Beets
06/21/1989	Fescue Grass	Sugar Beets
07/07/1989	Fescue Grass	Sugar Beets
07/23/1989	Fescue Grass	Sugar Beets
09/25/1989	Fescue Grass	Sugar Beets
06/24/1990	Fescue Grass	Peas
07/29/1991	Fescue Grass	Alfalfa

Figure 4.4 shows an overview of the local region used for the validation of the

remote sensing approach.

FIGURE 4.4.   False Color Composite of Landsat 5 Image for 07/07/1989. The Area of
              Interest is a Subset of Path 40, Row 39. The Circle Shows the
              Approximate Location of the Kimberly Lysimeters and the Weather
              Station.

Estimation of ET for the Year 2000
for the Study Area

After calibrating and validating the proposed model in Kimberly, ET maps for the

year 2000 were produced using Landsat 5 TM and 7 ETM+ imagery (corresponding to

path 39, rows 29, 30, and 31) and weather data collected at several stations within the

study area. The application of the remote sensing model in 2000 allowed the evaluation

of the behavior of $SEBAL_{ID}$ in estimating ET for a diversity of surface types beyond

agricultural fields. Table 4.3 includes information for the imagery used for this part of

the work. Figure 4.4 shows the total area as well as the Agrimet (Agricultural Weather

Network) stations considered.

TABLE 4.3.   Landsat Imagery for Path 39 Used in the 2000 Application

Date of Image	Type
03/16/2000	Landsat 7 ETM+
04/01/2000	Landsat 7 ETM+
05/03/2000	Landsat 7 ETM+
06/04/2000	Landsat 7 ETM+
06/20/2000	Landsat 7 ETM+
07/06/2000	Landsat 7 ETM+
07/22/2000	Landsat 7 ETM+
08/07/2000	Landsat 7 ETM+
08/23/2000	Landsat 7 ETM+
09/08/2000	Landsat 7 ETM+
09/16/2000	Landsat 5 TM
10/18/2000	Landsat 5 TM

The western portion of the Snake River Plain, corresponding to path 40, was

processed by Tasumi (in preparation), for the year 2000. The information developed in

this study and the developed by Tasumi (in preparation) were used by the Idaho

Department of Water Resources in 2002 and 2003.
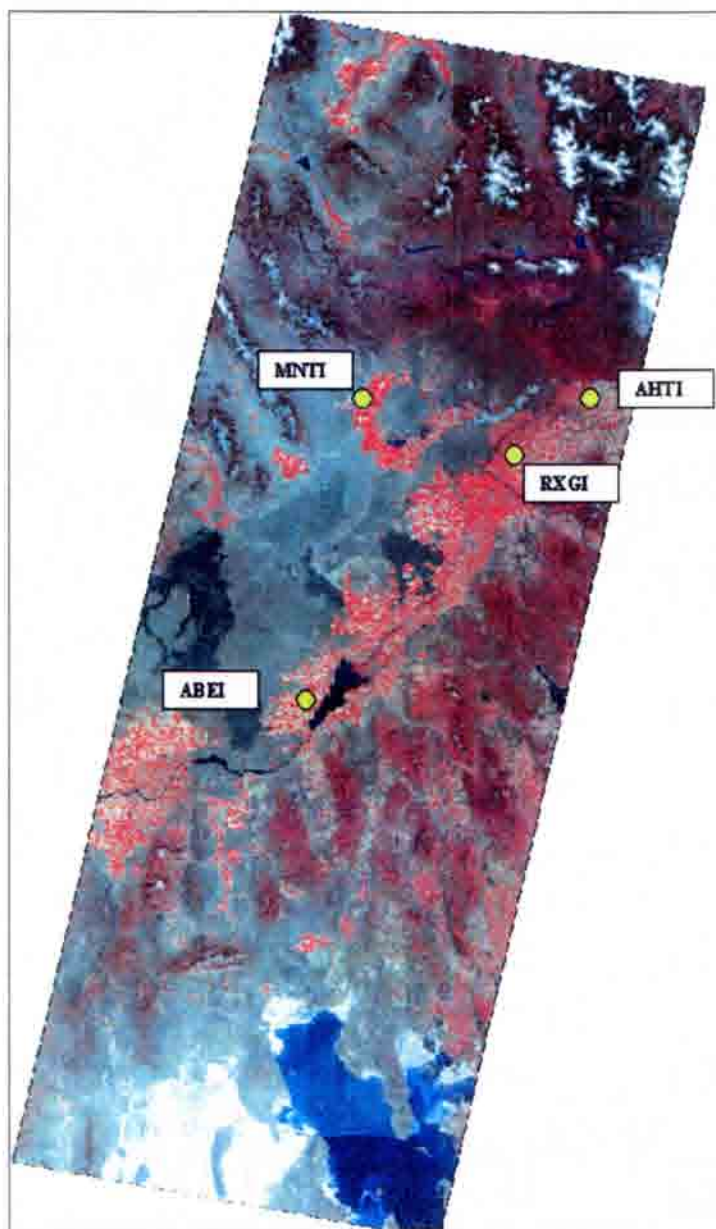
FIGURE 4.5   False Color Composite of Landsat 7 Image for 06/04/2000,
Corresponding to Path 39, Rows 29, 30, and 31, Showing the Four
Agrimet Weather Stations Used for Weather Data: ABEI (Aberdeen),
RXBI (Rexburg), MNTI (Monteview), and AHTI (Ahston).

Modifications of the SEBAL$_B$ Algorithm
for SEBAL$_{ID}$

Some extensions of the original SEBAL$_B$ model developed by Bastiaanssen et al. (1998) were proposed and tested in this study. As explained before the modified SEBAL$_B$ applied in this work is referred to as SEBAL$_{ID}$. These modifications are discussed in detail in Chapter V. In general, the most important modifications are:

1. The approach used by Bastiaanssen et al. (SEBAL$_B$) to anchor the endpoints of the dT versus T_s relationship (Eq. 3.3) was modified to improve the definition of the energy balance at both the "cold" and "hot" pixels. In this study, the cold pixel was taken from a agricultural field having surface characteristics similar to that of the reference crop (alfalfa). The hot pixel was selected as an agricultural bare soil surface where soil heat flux characteristics have been thoroughly investigated.

2. A water balance model was used to track soil moisture in the hot pixel, so that residual evaporation following antecedent rainfall could be accounted for in determining H for the hot pixel. The water balance model was based on the FAO-56 (Allen et al., 1998) approach.

3. New algorithms were considered to calculate the amount of short wave radiation received on sloping surfaces over 24-hour periods. The original SEBAL$_B$ model was developed for flat areas. An analytical procedure was developed to integrate clear sky radiation (R_{so}) for all combinations of slope, aspect, and latitude.

4. In the SEBAL$_B$ procedure, the evaporative fraction $EF = ET/(R_n-G)$ is used to extrapolate instantaneous to daily ET values. In this study, an approach based on the hypothesis that the ratio between actual and reference ET (ETrF) is more reasonably

assumed as constant during daytime, also was tested, considering that ETrF was a better

index of total evaporative energy for the study area.

**Methodology to Estimate Available
Energy from Landsat**

To estimate latent heat flux, SEBAL$_{ID}$ requires as main input, imagery

information collected by a remote sensing device measuring visible, near-infrared, and

thermal infrared radiation. SEBAL$_{ID}$ can be applied to a wide range of satellite-based

sensor platform such as ASTER, NOAA, MODIS, and LANDSAT. In this study, the

application of SEBAL$_{ID}$ was performed using Landsat 5 TM (Thematic Mapper) and

Landsat 7 ETM+ (Enhanced Thematic Mapper) imagery. Details of Landsat data are

included in Table 4.4.

TABLE 4.4. Landsat 5 TM and 7 ETM+ Sensor Characteristics

Band	Lansat 5 TM		Landsat 7 ETM +	
	Spectral Range (μm)	Spatial Resolution (m)	Spectral Range (μm)	Spatial Resolution (m)
1	0.45 - 0.52	30	0.45 - 0.52	30
2	0.52 - 0.60	30	0.52 - 0.60	30
3	0.63 - 0.69	30	0.63 - 0.69	30
4	0.76 - 0.90	30	0.76 - 0.90	30
5	1.55 - 1.75	30	1.55 - 1.75	30
6	10.4 - 12.5	120	10.4 - 12.5	60
7	2.08 – 2.35	30	2.08 – 2.35	30
Altitude	705 km			
Swath Width	185 km			
Return Period	every 16 days			

The landsat imagery used in this study was purchased by the Idaho Department of Water Resources (IDWR). Georectification of the imagery was performed by Earth Satellite Corporation (EarthSat).

The steps that were followed to compute available energy from Landsat using $SEBAL_{ID}$ are described next.

Spectral Reflectance (Unadjusted for Transmittance)

The reflectance for each band is computed following Markham and Barker (1987) and NASA (2002):

$$\rho_\lambda = \frac{\pi \cdot L_\lambda \cdot d^2}{ESUN_\lambda \cdot \cos\theta} \tag{4.1}$$

where ρ_λ is the at-satellite spectral planetary reflectance for band λ, L_λ is the at-satellite spectral radiance, which is the outgoing radiation energy of the band observed at the top of atmosphere by the satellite, d is the Earth-Sun distance in astronomical units, $\cos\theta$ is the cosine of the solar incident angle, and $ESUN_\lambda$ is mean solar exoatmospheric irradiances for each band. Values of $ESUN_\lambda$ are included in Table 4.5.

TABLE 4.5. $ESUN_\lambda$ for Landsat 5 TM (Markham and Barker, 1986), and for Landsat 7 ETM+ in $W/m^2/\mu m$ (NASA, 2002)

	Band 1	Band 2	Band 3	Band 4	Band 5	Band 7
Landsat 5	1957	1829	1557	1047	219.3	74.52
Landsat 7	1969	1840	1551	1044	225.7	82.07

The d^2 in Eq. 4.1 is equivalent to the "inverse squared relative distance between the Earth-Sun(d_r). Eq. (4.1) can be rewritten as:

$$\rho_\lambda = \frac{\pi \cdot L_\lambda}{ESUN_\lambda \cdot \cos\theta \cdot d_r} \tag{4.2}$$

The inverse relative distance Earth-Sun, was calculated from Eq. (3.10).

The values of at-satellite spectral radiance (L_λ) for Landsat 5 TM are calculated as follows:

$$L_\lambda = \left(\frac{LMAX - LMIN}{255}\right) * DN + LMIN \tag{4.3}$$

where, L_λ is sensor observed radiance for ""band λ" in W/m^2/ster/μm, LMAX and LMIN are constants given in Table 4.6, and DN is the digital number recorded in the satellite image.

TABLE 4.6.   LMIN and LMAX Values for Landsat 5 TM after 1/15/1984 (Markham and Barker, 1986)

Band	LMIN (Wm^{-2}ster^{-1}μm^{-1})	LMAX (Wm^{-2}ster^{-1}μm^{-1})
1	-1.50	152.10
2	-2.80	296.80
3	-1.20	204.30
4	-1.50	206.20
5	-0.37	27.19
6	1.24	15.60
7	-0.15	14.38

Unfortunately, the calibration constants contained in Table 4.6 have not been updated to account for the natural degradation of the Landsat 5 TM sensor. To overcome this problem, NASA (2002) presented a methodology to update the Landsat-5 TM calibration with respect to the Landsat-7 ETM+ sensor, which serves as a well calibrated reference sensor with a calibration uncertainty of +/- 3 %. Tasumi (in preparation) performed a cross calibration of Landsat 5 TM against Landsat 7 ETM+ visible and near-infrared bands for the year 2000 and the corresponding calibration coefficients are given in Table 4.7.

TABLE 4.7. LMIN and LMAX for Landsat 5 TM, Year 2000 (Tasumi, in preparation)

Band	LMIN ($Wm^{-2}ster^{-1}\mu m^{-1}$)	LMAX ($Wm^{-2}ster^{-1}\mu m^{-1}$)
1	-1.76	178.94
2	-3.58	379.05
3	-1.50	255.69
4	-1.76	242.30
5	-0.41	30.18
6	1.24	15.60
7	-0.14	13.16

Landsat 7 ETM+ images provide calibration constants in the header files of each satellite. The spectral radiance for each band is calculated by the following equation from NASA (2002):

$$L_\lambda = gain*DN + offset \tag{4.4}$$

where, L_λ is sensor observed radiance for band λ in W/m²/ster/μm, and "gain" and "offset" correspond to the "gain" and "bias" values provided in the header file of Landsat 7 images.

Surface Albedo

As discussed in Chapter III (Eq. 3.16), according to the SEBAL$_B$ procedure, the hemispherical surface reflectance (α_o) is obtained from the broadband directional planetary reflectance (α_{toa}).

$$\alpha = \frac{\alpha_{toa} - \alpha_{path\_radiance}}{\tau_{sw}^2}$$

where α is the surface albedo, α_{toa} is the albedo at the top of the atmosphere, $\alpha_{path\ radiance}$ is the albedo path radiance, and τ_{sw} is the shortwave atmospheric transmittance.

To calculate the albedo at the top of the atmosphere (unadjusted for transmittance), SEBAL$_{ID}$ uses the reflectance of each band calculated by Eq. (4.2). Basically, the calculation of α_{toa} involves the use of weighting coefficients for each band to convert the multiple narrowband reflectances (sensed by the satellite) to a single broadband reflectance:

$$\alpha_{TOA} = \Sigma[w_\lambda \times \rho_\lambda] \tag{4.5}$$

where w_λ is the weighting coefficient for a particular band, so that $\Sigma\, w_\lambda = 1$.

The weighting coefficientes are calculated as the radio of the solar constant for a particular band and the sum of the solar constant for all the bands:

$$w_\lambda = \frac{ESUN_\lambda}{\Sigma ESUN_\lambda}$$

(4.6)

Table 4.8 lists the weighting coefficients for each band.

TABLE 4.8.   Weighting Coefficients w_λ for Landsat 5 TM and 7 ETM+

	Band 1	Band 2	Band 3	Band 4	Band 5	Band 7
Landsat 5 TM	0.293	0.274	0.233	0.157	0.033	0.011
Landsat 7 ETM+	0.293	0.274	0.231	0.156	0.034	0.012

Shortwave Atmospheric Transmittance

The albedo at the top of the atmosphere is different from the one occurring at the surface for several reasons. First of all, because of absorption and reflection of short wave radiation by the atmosphere, only a portion of the solar radiation that occurs at the top of the atmosphere reaches the surface. Secondly, a part of the radiation reflected by the surface is also affected by absorption and reflection, so that the amount of radiation sensed by the satellite is different from that coming from the surface. In addition, some radiation received by the sensor is generated by atmospheric scattering and reflection that enters into the sensor path.

Corrections for atmospheric interference for specific spectral bands are generally based on detailed information of the state of the atmosphere (temperature, humidity and wind speed at different altitudes), as extracted from radiosoundings. However, the

radiosonde information must correspond to the area and time of interest to get realistic results (Wukelic et al., 1989).

Calibrated equations that predicts broadband solar radiation can be used to estimate the single way transmittance (τ_{sw}). Allen et al. (1998) presented an approach to estimate shortwave transmittance for clear sky conditions. This methodology was later updated in ASCE-EWRI (2002) and it was used in this study as a general means of conversion of α_{toa} to α. The impact of assuming a relatively constant broadband value for (τ_{sw}) was analyzed by Tasumi (in preparation) and important results are discussed in Chapter VI.

The methodology of ASCE-EWRI (2002) considers the effects of water vapor on absorption of short wave radiation, as well as the presence of pollutants in the atmosphere:

$$\tau_{sw} = \frac{R_{so}}{R_a} = K_B + K_D \tag{4.7}$$

where R_{so} is the clear-sky incoming solar radiation, K_B is the clearness index for direct beam radiation [-], and K_D is the index for diffuse beam radiation [-], which is calculated as:

$$K_B = 0.98 \exp\left[\frac{-0.00146\,P}{K_t \sin\phi} - 0.075\left(\frac{W}{\sin\phi}\right)^{0.4} \right] \tag{4.8}$$

where K_t is a turbidity coefficient, $0 < K_t \leq 1.0$ where $K_t = 1.0$ for clean air and $K_t = 0.5$ for extremely turbid, dusty or polluted air, P is the atmospheric pressure [kPa],

102

ϕ is the angle of the sun above the horizon [radians], and W is the precipitable water in the atmosphere [mm] that is computed as:

$$W = 0.14 e_a P + 2.1 \tag{4.9}$$

where W is the precipitable water in the atmosphere [mm], e_a is the actual vapor pressure [kPa], and P is the atmospheric pressure [kPa].

The diffuse radiation index K_D is computed from K_B as:

$$\begin{aligned} K_D &= 0.35 - 0.36 K_B \quad \text{for } K_B \geq 0.15 \\ K_D &= 0.18 + 0.82 K_B \quad \text{for } K_B < 0.15 \end{aligned} \tag{4.10}$$

The coefficient −0.36 in Eq. 4.10, and the coefficients 0.075 and 0.4 in Eq. 4.8 have been modified from that recommended in FAO-56 to better reproduce measurements of R_{so} from around the U.S. (Allen, 2002, personal communication).

As an alternative method, according to Allen et al. (1998) the one-way transmittance for clear sky conditions, and relatively dry atmospheric conditions can be predicted from site elevation as:

$$\tau_{sw} = 0.75 + 2 \times 10^{-5} \times z \tag{4.11}$$

where z is the elevation above sea level [m].

Net Radiation, R_n

Net radiation was calculated with Eq. (3.6):

$$R_n = (1-\alpha)*R_s\downarrow + R_L\downarrow + R_L\uparrow + (1-\varepsilon_o)* R_L\downarrow$$

The incoming short wave radiation, combining Eqs. (3.8) and (3.11), can be expressed as:

$$R_{s\downarrow} = G_{sc} \times \cos\theta \times d_r \times \tau_{sw} \qquad (4.12)$$

where G_{sc} is the solar constant = 1367 W/m^2, $\cos\theta$ is the cosine of the solar zenith angle, d_r is the inverse relative distance Earth-Sun, and τ_{sw} is the one-way transmittance for shotwave radiation.

The incoming longwave radiation, $R_L\downarrow$, was estimated using a modified version of Eq. (3.13):

$$R_{s\downarrow} = 0.85 * \sigma\left[-\ln(\tau_{sw})\right]^{0.09} T_{ref}^{4} \qquad (4.13)$$

where T_{ref} is the surface temperature at a reference point, generally selected to be a well-watered area (pixel), where surface and air temperatures are similar. Coefficients in Eq. (4.13) were developed by Allen et al. (2000) using "RAPID" study data collected near Kimberly, Idaho. The longwave radiation emitted by the surface ($R_L\uparrow$) is calculated using Eq. (3.14).

Surface Temperature, T_s

NASA (2002) presented the following equation to compute uncorrected (at satellite or apparent) surface temperature from band 6 radiance:

$$T = \frac{K_2}{\ln\left(\dfrac{K_1}{L_6} + 1\right)} \qquad (4.14)$$

where T is brightness temperature (K), L_6 is the spectral radiance for Landsat TM and ETM+ Band 6, and K_2 and K_1 are coefficients that were developed considering the amount of radiation (in the $10.4 - 12.5$ µm range) from a blackbody that the TM and ETM+ sensor would record, taking into account their spectral response, without the presence of the atmosphere. Values of and K_2 and K_1 are lists in Table 4.9.

TABLE 4.9. Constants K_1 and K_2, in $Wm^{-2}ster^{-1}µm^{-1}$, for Landsat 5 TM (Markham and Barker, 1986), and Landsat 7 ETM+ (NASA, 2002)

	K_1	K_2
Landsat 5 TM	607.76	1260.56
Landsat 7 ETM+	666.09	1282.71

To compute L_6 from the band 6 digital numbers, the following equation is used:

$$L_6 = gain*DN + offset \qquad (4.15)$$

where L_6 is in $W\ m^{-2}\ ster^{-1}\ µm^{-1}$, and DN is the pixel digital number for band 6. The values for gain and offset are presented in Table 4.10.

TABLE 4.10. Gain and Offset Values for Band 6, Corresponding to Landsat 5 TM (Markham and Barker, 1986), and Landsat 7 ETM+ (NASA, 2002)

	Gain	Offset
Landsat 5 TM	0.0056322	0.1238
Landsat 7 ETM+ (low gain)	0.0668235	0.0000
Landsat 7 ETM+ (high gain)	0.0370588	3.1999

To obtain the surface temperature, thermal surface radiances corrected for atmospheric losses and gains and surface emissivity are to be considered in Eq. (4.14), so that:

$$T_s = \frac{K_2}{\ln\left(\dfrac{K_1}{R_c / \varepsilon_{NB}} + 1\right)}$$

(4.16)

where R_c is the atmospheric-corrected blackbody radiance, and ε_{NB} is the narrow band emissivity for the $10.4 - 12.5$ µm band.

Calculation of corrected radiance. The radiance values received by a sensor (L_{sensor}) carried onboard an orbiting satellite in the thermal region of the electro-magnetic spectrum can be formulated as:

$$L_{sensor} = \tau\left[L_{sfc} + (1 - \varepsilon_o) * R_{sky}\right] + R_{ae}$$

(4.17)

where τ is the atmospheric transmissivity for longwave radiation, L_{sfc} is the thermal radiance originated at the surface, ε_o is the emissivity of the surface, R_{ae} is the atmospheric emission transmitted through the atmosphere above the point of emission which reaches the sensor (thermal path radiance), and R_{sky} is the downwelling sky radiance.

From Eq. (4.17) Wukelic et al. (1989) derived a expression to obtain the corrected radiance sensed by the Landsat band 6 sensor:

$$R_c = \frac{L_6 - R_{ae\,NB}}{\tau_{NB}} - (1 - \varepsilon_{NB})R_{skyNB}$$

(4.18)

where R_c is the corrected radiance [W m^{-2} ster^{-1} μm^{-1}], L_6 is the radiance for Landsat band 6 [W m^{-2} ster^{-1} μm^{-1}], $R_{ae\,NB}$ is the path radiance in the 10.4 – 12.5 μm band [W m^{-2} ster^{-1} μm^{-1}], τ_{NB} is the transmittance in 10.4 – 12.5 μm band, ε_{NB} is the narrow band emissivity in 10.4 – 12.5 μm band, $R_{sky\,NB}$ is the downwelling sky irradiance for a clear sky in the 10.4 – 12.5 μm band, estimated as a fraction of the value obtained by using the Idso-Jackson empirical formula for the 8 – 12 μm band (Wukelic et al., 1989):

$$R_{sky\,NB} = (1.807 \times 10^{-9})T_a{}^4 \left\{ 1 - 0.26\exp\left[-7.77 \times 10^{-4}(273.15 - T_a)^2 \right] \right\}$$ (4.19)

where T_a is the absolute ambient temperature at the ground, and $R_{sky\,NB}$ is in W m^{-2}.

Estimation of $R_{ae\,NB}$ and τ_{NB}. The estimation of $R_{ae\,NB}$ and τ_{NB} was made using the model MODTRAN 3 (Kniezys, 1996) to perform atmospheric correction for the dates of the satellite overpass. To make the atmospheric corrections, MODTRAN requires radiosonde information from the closest weather station and for the time closest to the satellite overpass. In this study, the radiosonde data from the Boise, Idaho station was used.

MODTRAN can provide values of average transmittance for the 10.4 – 12.5 μm narrow band, integrated radiance, as well as path radiance ($R_{ae\,NB}$). These spectral radiance values correspond to at sensor elevation.

To obtain the actual values of radiance recorded by the sensor, the values computed by MODTRAN must be cascaded with the sensor response function as described by Schott and Volchock (1985):

$$L_\beta = \left[\frac{\int_{\lambda_1}^{\lambda_2} L_\lambda * \beta_\lambda * d\lambda}{\int_{\lambda_1}^{\lambda_2} \beta_\lambda * d\lambda} \right] (\lambda_2 - \lambda_1) \tag{4.20}$$

where L_β is the integrated radiance observed by the sensor incorporating the spectral response characteristic of the sensor, L_λ is the spectral radiance reaching the sensor as computed by MODTRAN, β_λ is the relative spectral responsivity of the detector, and λ_1 and λ_2 are the passband limits of the sensor

Application of Eq. (4.20) is needed due to the fact that the sensor does not record equally in every wavelength. In SEBAL$_{ID}$, application of Eq. (4.20) was required to obtain the value of $R_{ae\ NB}$ to be used in Eq. (4.19) which can be expressed numerically as:

$$R_{aeNB} = \left[\frac{\sum_{\lambda_1}^{\lambda_2} R_{aeNB\lambda} * \beta_\lambda * d\lambda}{\sum_{\lambda_1}^{\lambda_2} \beta_\lambda * d\lambda} \right] (\lambda_2 - \lambda_1) \tag{4.21}$$

where $R_{ae\ NB}$ is the integrated path thermal radiance [W m^{-2} ster^{-1}μm^{-1}], $R_{ae\ NB\ \lambda}$ is the path thermal radiance for each wavelength from MODTRAN output [W m^{-2} ster^{-1}μm^{-1}], λ_1=10.4 μm and λ_2=12.5 μm.

Soil Heat Flux

In SEBAL$_B$ procedure (discussed in Chapter III), an empirical function (Eq. 3.25) is applied to estimate the surface soil heat flux G based on surface temperature (T_S), albedo (α), and NDVI.

In this study, Eq. 3.25 was tested for agricultural sites by comparing it with functions developed using soil heat flux measurements taken in the lysimeters operated by Dr. J. Wright (Appendix G). To get soil heat fluxes Wright (2002, personal communication) utilized the combination method described by Massman (1992) based on the use of soil heat flux plates and recording the change in temperature in the soil above the instruments. Because lysimeters were operated with a variety of surface covers, from bare soil to complete cover of different crops, validation of Eq. 3.25 was feasible for that ample range of conditions.

For other surfaces, where application of Eq. 3.25 can not be recommended, such as snow and water, expressions from literature were utilized. Morse et al. (2000) used the following expression to estimate G for snow surfaces in the Bear River Basin:

$$G_{snow} = 0.5R_n \tag{4.22}$$

Eq. (4.22) assumes that one-half of net radiation incident to snow, at satellite overpass time, penetrates the snow surface in the form of light and is absorbed into the snow mass as G.

The equation for G on a water surface was more difficult to define since there is a lack of information about it. Short-wave solar radiation penetrates into a water body as a function of the transparency of the water and is absorbed at a range of depths below the surface where it is converted into heat (G). The penetration of short wave radiation will vary with sun angle, depth of water, and turbidity of the water body. In this study, the following assumption was adopted, which is appropriate to water bodies with moderate turbidity and water depth.

$$G_{water} = 0.5R_n \qquad (4.23)$$

The ratio of $G_{water}/R_n = 0.5$ was assumed taking into account that water bodies

in the study area are shallower than those described by Eqs. (2.66) to (2.67), derived of

the works of Yamamoto and Kondo (1968) for lakes in Japan and Amayreh (1995) for

Bear Lake in Idaho and Utah. In addition, the ratio of $G/R_n = 0.5$ considers a higher

transfer of heat in water bodies in the study area, than that reported by Burba et al. (1999)

for a shallow wetland in Nebraska (Eq. 2.68).

Surface Parameters

Leaf Area Index

An important index that is useful for the estimation of surface parameters and

soil heat flux is the leaf area index (LAI). This parameter can be estimated from SAVI,

by inverting the following equation (Bastiaanssen, 1998):

$$SAVI = c_1 - c_2 \exp(-c_3 LAI) \qquad (4.24)$$

where SAVI is defined as (Eq. 2.52):

$$SAVI = \frac{(\rho_4 - \rho_3)}{(\rho_4 + \rho_3 + L)}(1 + L) \qquad (4.25)$$

where L is a dimensionless constant assumed to be 0.5 for a wide variety of LAI values

(Huete, 1988), ρ_4 is the Landsat band 4 reflectance (near infrared), and ρ_3 is the Landsat

band 3 reflectance (red). Measurements of LAI performed at the lysimeter site by

Dr. J.L. Wright made it possible to develop a SAVI versus LAI function for the crops

presented at the lysimeters (Tasumi, in preparation).

The equation that was developed was the following:

$$LAI = -\frac{\ln\left(\frac{0.69 - SAVI_{L=0.1}}{0.59}\right)}{0.91}$$

(4.26)

where $SAVI_{L=0.1}$ is the value of SAVI calculated with Eq. 4.25 and considering L=0.1.

The value of L=0.1 minimized the standard deviation between measured values of LAI

and predicted vales of LAI in Eq. (4.26), and produced the least amount of variation in

SAVI for bare soil conditions.

Surface Roughness (z_{om})

In SEBAL$_B$ (Bastiaanssen, 1995), surface roughness (z_{om}) is estimated from

NDVI using an empirical function (Eq. 3.44), or from SAVI (Eq. 3.45). However, these

equations are only applicable when there is a direct proportionality between NDVI and

the height of the vegetation. In cases of desert vegetation, like sage brush, low values of

NDVI can be associated with high values of z_{om}.

Therefore, considering that the area of study has a variety of surfaces: agricul-

ture, man-made structures, water, desert, vegetation etc, a decision was made to develop

z_{om} functions directly associated with each type of surface. This was accomplished

during this study by performing a land use classification of the study area using the

Landsat data. Thereafter, it was possible to relate z_{om} values with identifiable surface

conditions. Details of the land classification performed in this study are described in

Appendix F. In all land types, besides agriculture, a constant value of z_{om} was assumed. In agricultural classifications, z_{om} was predicted from LAI.

For the crops presented at the Lysimeters, Wright (1991) made continuous measurements of vegetation height, and leaf area index. Concurrent readings of vegetation height (h) and LAI, made it possible to develop an expression to predict h from LAI. Once a vegetation height versus LAI relationship was derived, it was combined with Eq. 3.31 to produce a expression for estimating surface roughness from leaf area index :

$$z_{om} = 0.018 * LAI \qquad (4.27)$$

where z_{om} is in meters and LAI is obtained from SAVI using Eq. 4.26. A description of the procedure used to develop Eq. 4.27 is included in Appendix F.

Table 4.11 contains a description of the values of z_{om} adopted for each surface type, in the study area.

Surface Emissivity

Two expressions for surface emissivity were developed for this study using field measurements and information from the MODIS emissivity library and from field observations as described in Appendix H. One equation describes the broadband surface emissivity (ε_0) to be used in the Stephan Boltzman equation for estimating the outgoing longwave radiation (Eq. 3.14):

$$\varepsilon_0 = 0.95 + 0.01 * LAI \qquad (4.28)$$

Eq. (4.28) is valid for values of $LAI \leq 3$. If $LAI > 3$ then $\varepsilon_0 = 0.98$. For water

and snow a constant value of emissivity $\varepsilon_0 = 0.985$ was adopted.

TABLE 4.11.   Surface Roughness for each Landuse Type, Applied for the Study Area

Landuse	z_{om} (m)
Agriculture	0.018 * LAI (min = 0.005)
Water	0.0005
City	0.2
Forest	0.5
Desert Grassland	0.02
Desert Sage Brush	0.1
Salty Soil	0.002
Basalt Rock	0.07
Mountain Bare Soil	0.05
Mountain Forest	0.5
Snow	0.005

Another equation describes the value of emissivity for the range between 10.4 –

12.5 μm which corresponds to the narrow range of the Landsat thermal band:

$$\varepsilon_{NB} = 0.97 + (0.01 / 3)*LAI \qquad (4.29)$$

where ε_{NB} is the emissivity of the surface in the 10.4-12.5 μm range of the thermal

spectrum. Eq. 4.29 is required to compute surface temperature from Eq. (4.16). Eq.

(4.29) is valid for values of $LAI \leq 3$. If $LAI > 3$ then $\varepsilon_{NB} = 0.98$.

CHAPTER V

SEBAL$_{ID}$ MODEL DEVELOPMENT

General

In this chapter a discussion of some significant modifications made to the original

SEBAL$_B$ model (Bastiaanssen et al., 1998) are described. The aim of these modifications

is to develop an operational model that is adapted to the specific conditions of the study

area, located in Southern Idaho.

Standardization of Anchor Pixels

As mentioned in Chapter III, SEBAL$_B$ considers two "anchor" pixels (the so-

called cold and hot pixels) to define a linear relationship between radiometric surface

temperature and near-surface air temperature difference (dT). Traditionally,

Bastiaanssen et al. (1998) considered that H and dT are equal to zero at the cold pixel

and that ET = 0 at the hot pixel. In this study modifications to both pixels were

considered, which are explained next.

<u>Cold Pixel</u>

In this study, the cold pixel is considered to be a well-watered full cover crop that

resembles an agricultural field covered by healthy alfalfa transpiring at a potential rate.

Therefore at the cold pixel the following relationships are assumed:

$$ET_{cp} = 1.05*ET_r \; ; \quad H_{cp} = R_{n\;cp} - G_{cp} - \lambda ET_{cp}$$

and

$$dT_{cp} = T_2 - T_1 = H_{cp} \times r_{ah\;cp} / (\rho\;Cp)$$

114

where ET_r is the alfalfa reference evapotranspiration, and the subscript "cp" refers to values for the cold pixel.

ET_r is predicted using the Standardized ASCE Penman-Monteith equation developed by ASCE-EWRI (2002) which considered the most updated approaches for calculating evapotranspiration of reference alfalfa. Reference alfalfa is defined as the ET rate from a uniform surface of dense, actively growing vegetation having a height of 50 cm, a fixed surface resistance, not short of soil water , and representing an expanse of a least 100 m of the same or similar vegetation. In the calculation of hourly ET_r , the ASCE-EWRI (2002) approach considers a fixed surface resistance of 30 s/m and 200 s/m for daytime and nighttime, respectively.

The assumption of taking $ET_{cold} = 1.05*ET_r$ presumes that in the nearly coldest pixel, evapotranspiration can be 5 % more than the calculated ET_r. The increase of ET_r in 5 % can be explained by several possible scenarios: a) it can represent a condition of alfalfa having a wet leaf surface (freshly irrigated) and/or wet underlying soil, b) the crop in the cold pixel might be a different crop from alfalfa (for example corn, with less aerodynamic resistance to evapotranspiration), c) crop characteristics (physiological, like degree of stomatal control or/and anatomical, like height, density) at the cold pixel can be different from the average characteristics taken into account in the development of the reference equation used to calculate ET_r. Figure 5.1 shows two cases where maximum ETrF was about 1.05, which means that ET was five percent more than the alfalfa reference evapotranspiration ET_r.
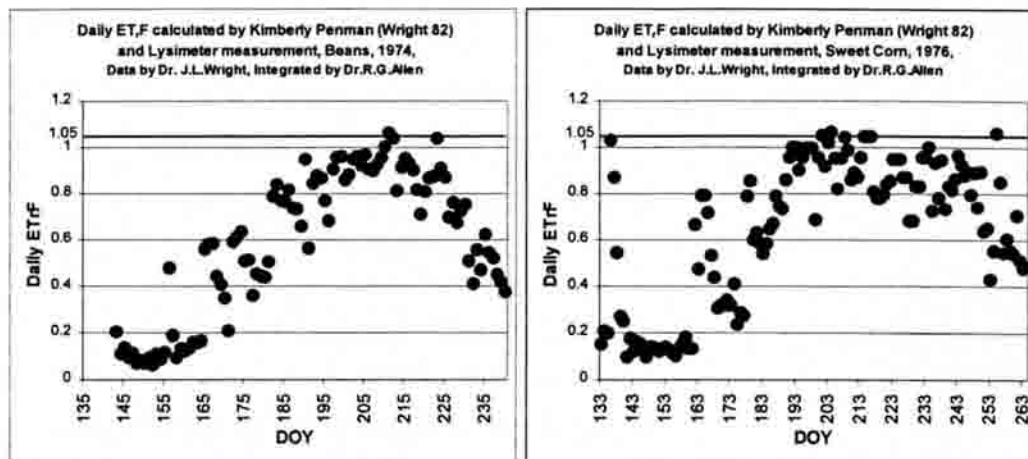
FIGURE 5.1. Measured daily ETrF in Corn (left) and in Bean (right), Showing a maximum value of 1.05.

The advantage of calculating ET_{cold} from ET_r is that it ties the prediction of ET at the cold pixel to a well-validated and robust equation, that considers local wind, solar radiation, and humidity conditions. ET_r integrates the effect of local weather parameters in the ET process so that the ET at the cold pixel will be representative of the weather conditions of the study area.

Details of the calculation of ET_r are included in Appendix B.

Hot Pixel

According to $SEBAL_B$ the hot pixel is one pixel where all the available energy is converted into sensible heat. Because at the hot pixel $H = R_n - G$, the prediction of sensible heat assumes a correct prediction of both R_n and G. Particularly, there are many uncertainties in the estimation of G for many surfaces that can be considered as candidates for hot pixels (for example, parking lots, desert areas with sparse vegetation, etc). In this study the hot pixel was always an agricultural bare soil where the prediction

of G was more dependable. Therefore at the hot pixel the following relationships were assumed:

$$H_{hp} = R_{n\ hp} - G_{hp} - \lambda ET_{hp} \ ;$$

and

$$dT_{hp} = T_2 - T_1 = H_{hp} * r_{ah\ hp} / (\rho\ Cp)$$

where the subscript "hp" refers to values for the hot pixel .

The definition of the surface temperature (T_s) vs near-surface air temperature difference (dT) relationship is illustrated in Fig. 5.2, considering the discussed assumptions for the cold and hot pixel,

To estimate ET for the hot pixel a water balance model for bare soil (Allen et al., 1998) was applied as described in the following section.
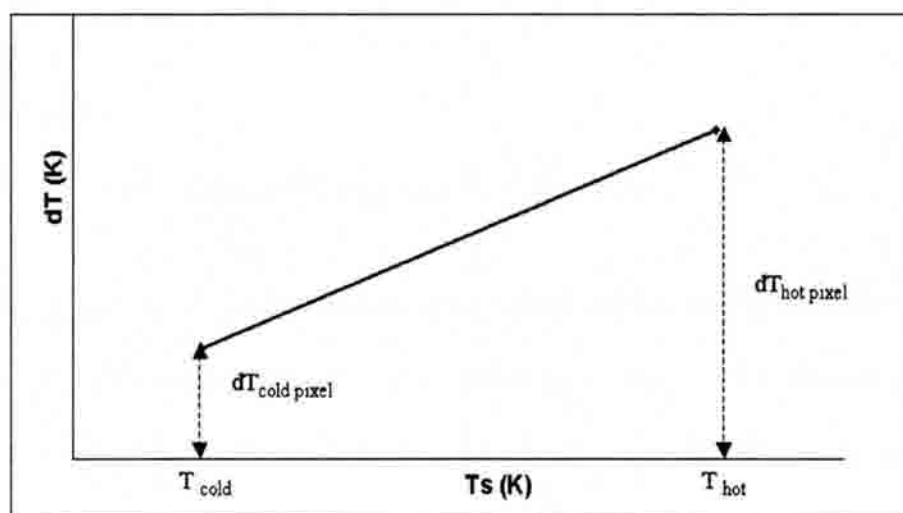
FIGURE 5.2. Definition of the dT vs T_s Linear Relationship To Be Used in This Study.

Water Balance Model for the Hot Pixel

A water balance model is proposed to be used in this SEBAL$_{ID}$ application to consider the presence of top soil moisture in the hot pixel due to surface wetting from precipitation. In a dry hot pixel, evaporation is considered to be equal to 0. However, when a precipitation event happens within 5 or 6 days before the time of satellite overpass, there may not be a pixel that is completely dry. In such cases the consideration of some evaporation at the hot pixel is required. Evaporation at the hot pixel was computed as :

$$ET_{hot\ pixel} = ETrF_{hot\ pixel} * ET_r \qquad (5.1)$$

The calculation of $ETrF_{hot\ pixel}$ is made using the methodology proposed in FAO-56 (Allen et al., 1998) based on a soil moisture balance in the top soil layer. Following the mentioned approach, the value of ETrF for the hot pixel was calculated as follows:

$$ETrF_{hot\ pixel} = K_{e\ hot\ pixel} = K_r * ETrF_{max} \qquad (5.2)$$

where $K_{e\ hot\ pixel}$ is the coefficient of evaporation corresponding to the hot pixel, $ETrF_{max}$ is the maximum value of ETrF following rainfall , and K_r is a dimensionless evaporation reduction coefficient which is dependent on the cumulative depth of water depleted (evaporated). The value of $ETrF_{max}$ was taken as $ETrF_{max} = 1.05$.

The procedure of FAO-56 (Allen et al., 1998) assumes that the soil can dry to an intermediate soil water content halfway between wilting point, θ_{WP}, and oven dry (no

water left). The amount of water that can be removed by evaporation during a complete

drying cycle is hence estimated as:

$$TEW = 1000(\theta_{FC} - 0.5\theta_{WP})Z_e \qquad (5.3)$$

where TEW (total evaporable water) is the maximum depth of water that can be

evaporated from the surface soil layer when the layer has been initially completely wetted

[mm], field capacity, θ_{FC}, and θ_{WP} are expressed in $[m^3\ m^{-3}]$ and Z_e is the depth of the

surface soil subject to drying by way of evaporation [0.10-0.15 m]. Typical values for

θ_{FC}, θ_{WP} and TEW are included in FAO-56 for various soil types as shown in Table 5.1.

TABLE 5.1.   Typical Soil Water Characteristics for Different Soil types
             (Allen et al., 1998)

Soil type (USA Soil Texture Classification)	Soil water characteristics			Evaporation parameters	
	θ_{FC}	θ_{WP}	$(\theta_{FC}-\theta_{WP})$	Amount of water that can be depleted by evaporation	
				stage 1 REW	stages 1 and 2 TEW $(Z_e = 0.10\ m)$
	m^3/m^3	m^3/m^3	m^3/m^3	mm	Mm
Sand	0.07 - 0.17	0.02 - 0.07	0.05 – 0.11	2 - 7	6 – 12
Loamy sand	0.11 - 0.19	0.03 - 0.10	0.06 - 0.12	4 - 8	9 - 14
Sandy loam	0.18 - 0.28	0.06 - 0.16	0.11 - 0.15	6 - 10	15 - 20
Loam	0.20 - 0.30	0.07 - 0.17	0.13 - 0.18	8 - 10	16 - 22
Silt loam	0.22 - 0.36	0.09 - 0.21	0.13 - 0.19	8 - 11	18 - 25
Silt	0.28 - 0.36	0.12 - 0.22	0.16 - 0.20	8 - 11	22 - 26
Silt clay loam	0.30 - 0.37	0.17 - 0.24	0.13 - 0.18	8 - 11	22 - 27
Silty clay	0.30 - 0.42	0.17 - 0.29	0.13 - 0.19	8 - 12	22 - 28
Clay	0.32 - 0.40	0.20 – 0.24	0.12 - 0.20	8 - 12	22 – 29

Evaporation from the exposed soil is presumed to take place in two stages: an energy limiting stage (stage 1), and a falling rate stage (stage 2). During stage 1, the soil surface remains wet and evaporation is assumed to occur at the maximum rate limited only by energy availability at the soil surface and therefore, $K_r = 1$ (see Eq. 5.2). Stage 1 runs until the cumulative depth of evaporation, or depletion of soil moisture, D_e, is such that the hydraulic properties of the upper soil become limiting and water cannot be transported to near the soil surface at a rate to supply the demand.

At the end of stage 1 drying, depletion from the evaporating layer, D_e, is equal to REW (readily evaporable water). Typical values of REW are included in Table 5.1. Therefore during stage 1:

$$K_r = 1 \quad ; \quad D_{e, i-1} \leq REW$$

where $D_{e,i-1}$ is the depletion from the previous day.

The FAO-56 procedure assumes that in stage 2 (which starts when $D_{e,i-1} > REW$), evaporation decreases in proportion to the amount of water remaining in the surface soil layer:

$$K_r = \frac{TEW - D_{e,i-1}}{TEW - REW} \quad ; \quad D_{e,i-1} > REW \tag{5.4}$$

where $D_{e,\ i-1}$ is cumulative depletion from the soil surface layer at the end of day i-1 (previous day) [mm], and TEW and REW are in mm (REW < TEW).

The cumulative depletion is computed by performing a daily water balance with the following equation:

$$D_{e,i} = D_{e,i-1} - (P - RO_i) + E_i \tag{5.5}$$

where $D_{e,i-1}$ is the cumulative depth of evaporation following complete wetting from the topsoil at the end of day i-1 [mm], $D_{e,i}$ is the cumulative depth of evaporation (depletion) following complete wetting at the end of day i [mm], P_i is the precipitation on day i [mm], RO_i is the precipitation runoff from the soil surface on day i [mm], E_i is the evaporation on day i ($E_i = K_e ET_r$, where K_e is the top soil evaporation coefficient) [mm].

In Eq. 5.5 the value of $D_{e,i}$ is constrained to the following range:

$$0 \le D_{e,i} \le TEW$$

If $D_{e,i}$ is greater than TEW then the amount of precipitation exceeds the soil storage in the evaporative layer, therefore the quantity $D_{e,i} = TEW$ is an upper limit for the water from the top soil.

Extrapolating Instantaneous to Daily ET Values

Values of ET obtained by residual from the energy balance correspond to the value of evapotranspiration at the moment of the satellite overpass. To convert those instantaneous ET values to 24-hour ET, SEBAL$_B$ (Bastiaanssen et al., 1998) uses the concept of the self-preservation of the daytime fluxes, which was explained in Chapter III.

In this study a new approach is tested based on the hypothesis that the relationship between actual and reference ET remains constant during the daytime.

In other words, this approach assumes that the reference ET fraction (ETrF) remains relatively constant, which is reasonable if one takes into account that both actual and reference ET might have similar response to the variation of the weather parameters. Of course, this response is not directly proportional because there are some physiological differences between certain crops and the reference crop (alfalfa). ETrF is essentially synonymous with the crop coefficient K_c (Allen et al., 2002). The ETrF is expressed as follows:

$$ETrF_{inst} = \frac{ET}{ET_r} \qquad (5.6)$$

where $ETrF_{inst}$, ET, and ET_r are the values of ET_r fraction, actual and reference evapotranspiration, for the time when the satellite image was taken. Considering that the value of ETrF remains constant during daytime, the following consideration was made:

$$ETrF_{inst} = ETrF_{24} = \frac{ET}{ET_r} = \frac{ET_{24}}{ET_{r24}} \qquad (5.7)$$

where $ETrF_{24}$ is the average daily value of ETrF, ET_{24}, and ET_{r24} are the corresponding daily values (24 hours) of evapotranspiration. Therefore, the value of ET_{24} for each pixel was calculated as:

$$ET_{24} = ETrF_{24} * ET_{r24} \qquad (5.8)$$

Both ET_r and ETr_{24} are calculated using information from local weather stations. The hypothesis behind the use of Eqs. (5.7) and (5.8) is that, in an advective environment

such as Southern Idaho, the ET_r is a better index of total evaporative energy than R_n-G (which is used in the EF approach given by Eq. 3.46).

The approach of using ETrF as a means of extrapolating instantaneous to daily ET values was tested by comparing estimated values of ET_{24} with the values of daily evapotranspiration measured in the two weighing lysimeters located at Kimberly, Idaho. This discussion is included in Chapter VI.

Estimation of Seasonal
Evapotranspiration

To create a cumulative evapotranspiration map that describes all of the growing season, the use of the following approaches were explored in this study:

The first approach was to extend 24-hour evapotranspiration, as predicted by $SEBAL_{ID}$ for the image date, in proportion to the reference evapotranspiration for intervening periods as derived from weather data. Tasumi et al. (2000) used this approach to estimate seasonal ET in the Bear River Basin. In this approach, the ETrF information obtained from a particular image represents a given period surrounding an image date. The length of the period depends on the frequency of image availability.

In this study, it was assumed that every image represents a period of about 16 days (frequency of Landsat imagery), with 8 days before and 8 days after the day of the processed image. Thus, the total ET for the period that a particular image represents was calculated as:

$$ET_{period_i} = ETrF_i \sum_{day=1}^{day=n} ET_{r\,day} \qquad (5.9)$$

where $ET_{period\,i}$ is total evaporation (mm/period) corresponding to the period i, $ETrF_i$ is the representative ETrF for such period, $ET_{r\,day}$ is the daily value of ET_r from day 1 to the end of the period (day n), calculated from weather station information for each day.

This approach considers the daily variation of ET_r, which is function of the daily variation of the weather parameters of the study site. However, the value of ETrF retrieved from the processed image is considered as constant during the whole period, thus neglecting the daily variation of ETrF due to changes in soil moisture and vegetation development. This assumption may introduce a significant source of error to the estimation of the total ET for a given period. However, as shown in Chapter VI, the introduced error tends to be random, so that there is some cancellation that produces a reasonable value of seasonal ET when a sufficient number of images are considered for the season.

After calculating total ET for each period, the seasonal ET was calculated by summing the ET for all periods:

$$ET_{season} = \sum_{period=1}^{period=n} ET_{period_i} \tag{5.10}$$

where ET_{season} is the total ET for the season (generally considered to be from March to October in Southern Idaho).

A second approach that was preliminarily explored in this study considers a daily adjustment of ETrF, based on effects of surface wetting due to precipitation. Variations of ETrF due to irrigation events were not considered due to the lack of information in the area. The adjustment of ETrF was made by using the coefficient of evaporation K_e

for the top 0.1 to 0.15 m. of the soil, using the methodology proposed in Allen et al. (1998) based on a soil moisture balance in the top soil layer. This methodology is explained in Appendix I.

Application of SEBAL to Sloping Terrains

$SEBAL_B$ was originally developed to be applied to flat areas (Bastiaanssen, 1995; Bastiaanssen et al., 2000). Later, Tasumi et al. (2000) included the first modifications of $SEBAL_B$ for application in mountains and sloping surfaces. Here, in addition to the considerations presented by Tasumi et al. (2000), corrected algorithms are described.

Apparent Surface Temperature for a
Reference Elevation for Calculation of
Sensible Heat Flux

As it was described before, the SEBAL approach involves the prediction of the surface-to-air temperature difference (dT) as a function of the radiometric surface temperature T_s according to Eq. (3.33). The relationship between dT and T_s presumes a relatively constant environment with regard to air pressure, density, and temperature. Therefore, the surface temperature that is used needs to be uniformly adjusted to a common reference elevation for accurate prediction of dT when land elevation varies. Otherwise, high elevations that appear to be "cool" (due to orographic cooling) may be misinterpreted as having low sensible heat flux (low dT) and therefore high evaporation. A previous application of SEBAL (Tasumi et al., 2000) considered a "lapsed" surface temperature for purposes of computing surface-to-air temperature differences by assuming that the rate of decrease in surface temperature by orographic effects is the same as that for a typical air profile.

Elevation data were taken from U.S. Geological survey Digital Elevation Model (DEM) data. The lapse-adjusted surface temperature is referred to as a DEM adjusted radiometric surface temperature, being calculated as:

$$T_{s\_dem} = T_s + 0.0065\Delta z \tag{5.11}$$

where, T_{s_dem} is the DEM adjusted radiometric surface temperature, and Δz is the difference of a pixel's elevation from the datum, in meters . The term Δz is positive if the elevation of a pixel is higher than the datum.

A discussion of the application of Eq. (5.11) is included in Appendix K.

Incoming Solar Radiation

In sloping terrain the amount of incoming short wave radiation is largely affected by the relative position of the surface with respect to the angle of incidence of the sunbeam. Therefore, in a sloped land surface, the solar incident angle changes by the surface slope and the aspect. The following equation, from Duffie and Beckman (1980) was applied to compute cosine of the solar incident angle (θ) in sloping terrains:

$$
\begin{aligned}
\cos\theta_{unadjusted} = &\sin(\delta)\sin(\varphi)\cos(s) - \sin(\delta)\cos(\varphi)\sin(s)\cos(\gamma) \\
&+ \cos(\delta)\cos(\varphi)\cos(s)\cos(\omega) \\
&+ \cos(\delta)\sin(\varphi)\sin(s)\cos(\gamma)\cos(\omega) \\
&+ \cos(\delta)\sin(\varphi)\sin(s)\sin(\omega)
\end{aligned}
\tag{5.12}
$$

where, $\cos\theta_{unadjusted}$ is the cosine of the solar incident angle for the land surface, δ is solar declination (positive in summer in northern hemisphere), φ is the latitude of the pixel (positive for northern hemisphere) in radians, s is the slope in radians, where "s = 0" for a horizontal surface and "s = $\pi/2$" for a vertical surface (s is always positive and

represents a upward/downward slope in any direction), γ is the surface aspect angle in radians, where "$\gamma = 0$" for surfaces facing south, γ is negative for east and positive for western aspect, "$\gamma = -\pi/2$" represents an east facing slope and "$\gamma = +\pi/2$" represents a west facing slope. "$\gamma = -\pi$" or "$\gamma = \pi$" represents a north facing slope, and ω is the hour angle. The value of ω is equal to 0 at solar noon, ω is negative in morning and positive in the afternoon.

Because SEBAL$_{ID}$ computes the energy balance from a horizontal plane, the value of the cosine of the incident angle is divided by the cosine of the slope:

$$\cos\theta = \cos\theta_{unajusted} / \cos(s) \qquad (5.13)$$

where $\cos(s)$ is the cosine of the land surface slope. The value of $\cos\theta$ computed by Eq. (5.13) is used later with Eq. 4.12 to obtain the horizontal-equivalent value of incoming solar radiation

Surface slope and aspect for each pixel were obtained from the digital elevation model of the area. The parameters δ and ω were calculated by the following equations (Allen et al., 1998):

$$\delta = 0.409 \sin\left(\frac{2\pi}{365}DOY - 1.39\right) \qquad (5.14)$$

and,

$$\omega = \frac{\pi}{12}\left[\left(t + \frac{L_z - L_m}{15} + S_c\right) - 12\right] \qquad (5.15)$$

where, t is the standard local time for the satellite overpass (daylight saving time should not be applied), L_z is the longitude of the center of the local time zone (degrees west of the Greenwich), L_m is the longitude of the study area (degrees west of the Greenwich), and S_c is the seasonal correction for solar time calculated as follows (Allen et al., 1998):

$$S_c = 0.1645 \sin\left(\frac{4\pi(DOY - 81)}{364}\right) - 0.1255 \cos\left(\frac{2\pi(DOY - 81)}{364}\right) \\ - 0.025 \sin\left(\frac{2\pi(DOY - 81)}{364}\right)$$

(5.16)

where DOY is the day of the year (1-366).

Correction of ETrF in Sloping Terrains

In sloping terrains, the amount of incoming radiation depends strongly on the way the surface is oriented to the sun at the moment of the satellite overpass. If for example, the satellite image was taken at 11:00, surfaces that have a south-east aspect will be receiving more radiation than south-west aspect slopes, and, in some cases, more radiation than flat surfaces.

However, the tendency of higher radiation received by south-east slopes will be not constant during the day. In the afternoon, for example at 16:00, south-east slopes will receive less radiation than south-west slopes. Therefore, in sloping surfaces, it is obvious that a correction to the value of ETrF for the 24-hour period ($ETrF_{24}$) has to be made to account for the variation of incoming solar radiation during the day due to slope and aspect conditions in each pixel. Without this adjustment, the assumption of constant

ETrF (Eq. 5.7) during the day is not valid. The correction on ETrF is accomplish by adjusting the reference ET_r for each sloping pixel.

Assuming that values of instantaneous and 24 hours ET_r are affected proportionally by the variation in incoming solar radiation, the following correction factor is applied:

$$C_{radiation} = \frac{R_{so(inst)Flat}}{R_{so(inst)Pixel}} * \frac{R_{so(24)Pixel}}{R_{so(24)Flat}} \qquad (5.17)$$

where, $C_{radiation}$ is the coefficient for ETrF correction, R_{so} is the clear sky solar radiation (W/m^2), the subscripts "(inst)" and "(24)" indicate the instantaneous value for the satellite image time and the 24-hour averaged value respectively, and the subscripts "Flat" and "Pixel" indicate the value for a horizontal flat surface and for each pixel, respectively.

In a sloping pixel, the value of ET_r is adjusted to reflect the difference in incoming radiation (compared to the flat surface) that the pixel is receiving. At 11:00, the ET_r (evapotranspiration for the hypothetical alfalfa surface) for a south-east pixel will be higher than the ET_r calculated from the weather station (flat area). This is obvious considering that the south-east surface is receiving more incoming radiation than the flat surface. The adjustment made is a simplification, because ET_r depends not only on the incoming solar radiation but also on the variation of other parameters such wind speed and vapor pressure deficit; however, the pixel to pixel variation of those parameters is unknown.

The first multiplier in Eq. (5.17) $R_{so(ins)Flat} / R_{so(ins)pixel}$ represents the ratio of instantaneous R_s for a horizontal plane to that for the pixel with a given slope and aspect combination. ET_r is calculated from a weather station located in an essentially flat area.

The second multiplier $R_{so(24)pixel} / R_{so(24)}$ takes into account the difference between the total radiation that the sloping surface would receive and the total radiation received by a flat area in a 24 hour period (considering a clear sky day).

Using the $C_{radiation}$ factor, 24-hour ET_rF and 24-hour ET is calculated for the specific combination of pixel slope and aspect:

$$ETrF_{24} = C_{radiation} * ETrF_{inst} \tag{5.18}$$

and

$$ET_{24} = ETrF_{24} * ET_{r24} \tag{5.19}$$

where ETrF is calculated with Eq. 5.6 and ET_{r24} is computed as described in Appendix B. The calculation of the R_{so} values to be used in Eq. 5.17 are described in Appendix E.

Adjustment of Wind Speed and Surface Roughness in Sloping Terrain

The air-flow over nonuniform terrain has a very complicated behavior, and each topographic feature can create an unique wind pattern. According to Oke (1996), over moderate topography, an increase in the ground elevation relative to a reference height will require the air flow to constrict vertically (venturi effect), which results in acceleration. On the other hand, a drop of surface elevation will result in a deceleration of the air flow. In a hill or mountain, the maximum wind speed will occur at the crest, and the minimum speed will occur at the base of the slope. If the upwind or downwind

slope is relatively abrupt (slope more than 17º), separation of the air flow can occur. In this case the pattern of air flow will be more complex. In addition, wind direction plays a very important role in determining wind velocity on specific portions of sloping terrains.

With regard to the aerodynamic surface roughness, z_{om}, besides the specific (local) roughness of the surface, the air flow is exposed to a terrain or "orographic" roughness at a larger scale. In addition, the value of z_{om} needs to adjusted to account for the fact that in non-flat pixels, there is a longer distance expressed to drag and turbulence mixing, so that the value of z_{om} actually relates to a larger area, and not just the equivalent horizontal surface that is display in the satellite image.

In this study, empirical equations were used to introduce correction factors to the wind speed and surface roughness. For z_{om}, the following equations were proposed by Tasumi (in preparation), assuming that z_{om} increases 50% for every 10º of surface slope increment. This adjustment is applied only where the surface slope is 5º or more.

$$z_{om\ adj} = C_{zom} * z_{om} \tag{5.20}$$

where, z_{om_adj} is the adjusted value of z_{om}, z_{om} is the surface roughness unadjusted for the geometrical effects (m) as described in Table 4.11, and C_{zom} is a z_{om} correction coefficient calculated by:

$$C_{zom} = 1 + \frac{s-5}{20} \tag{5.21}$$

where, s is the surface slope in degrees. Eq. (5.20) was applied only for slopes > 5º.

The adjusted value of windspeed at 200 meters is calculated as follows:

$$u_{200\_adj} = C_{wind} * u_{200} \qquad (5.22)$$

where, u_{200_adj} is the adjusted windspeed at 200m height (m/s) that account for elevation effects, u_{200} is the windspeed at 200m (m/s) unadjusted by elevation, and C_{wind} is an adjustment coefficient calculated by:

$$C_{wind} = 1 + 0.1 * \frac{z - z_{ws}}{1000} \qquad (5.23)$$

where, z (m) and z_{ws} (m) are elevation for each pixel and for the weather station where windspeed was measured. The idea of Eqs. (5.21) and (5.23) is that increasing terrain roughness and drag length are associated with increases in slope and that increased mean wind speed is associated with increased land elevation.

CHAPTER VI

RESULTS AND DISCUSSION

The results discussed in this chapter are presented in two parts. The first part is related to the validation and refinement of the remote sensing model, which was done by comparing measured ET with estimated ET using Landsat 5 imagery (path 40, row 30). The years used for model validation were 1988, 1989, 1990, and 1991 and the focus was the lysimeter fields in the area of Kimberly, Idaho. The second part includes an application of $SEBAL_{ID}$ for 2000 using Landsat 7 ETM+ and Landsat 5 TM imagery (path 39, rows 29, 30, and 31). This second part allowed for the evaluation of the behavior of $SEBAL_{ID}$ in agricultural, desert, mountains, water, and basalt areas in the Eastern part of the Snake River Plain in Southern Idaho, an area approximately 100 miles northeast of Kimberly.

Figure 6.1 shows an illustrative map of estimated daily ET predicted for the Landsat 5 scene corresponding to 06/21/89 for the area surrounding Kimberly. These maps were created for eleven dates during 1989-1991 when concurrent lysimeter measurements, micrometeorological data, and cloud free satellite images were available.

$SEBAL_{ID}$ Model Validation

As was explained in Chapter IV, concurrent lysimeter measurements and Landsat 5 imagery were used to validate the accuracy of SEBAL to predict latent heat fluxes. The original $SEBAL_B$ model was modified as described in Chapter V to improve the estimation of various components for agricultural fields.
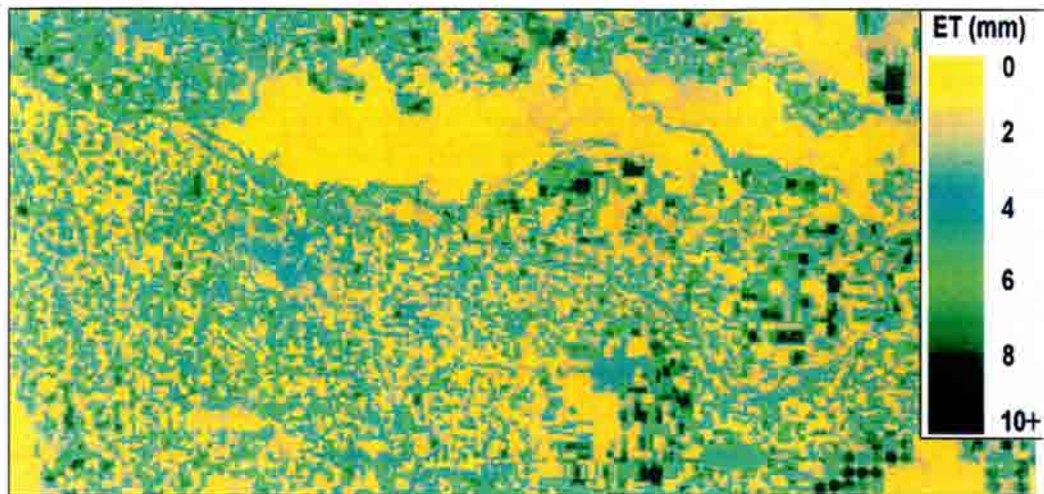
FIGURE 6.1   Estimated SEBAL$_{ID}$-ET (mm/day) for the Scene of 06/21/89.

This version of SEBAL, termed SEBAL$_{ID}$ was implemented in ERDAS-Imagine software and general description of the coding is included in Appendix C.

Model validation focused on the comparison of instantaneous (ET$_{inst}$) and daily values of ET (ET$_{24}$), measured with the Kimberly lysimeters, with estimates from SEBAL$_{ID}$. This comparison was limited by the fact that the spatial resolution of the Landsat 5 thermal band (band 6) is 120 x 120 m, the area of the lysimeter 2 field was 143 x 149m (see Fig. 4.2), and the area of the Lysimeter 1 field was 130 x 190 so that, in most cases, it was impossible to have a "pure thermal pixel" inside the lysimeter fields, that represents only those fields.

The challenge of obtaining a thermal pixel representative of the lysimeter fields was especially difficult for Lysimeter 1, since during the 1988-1991 period the northern 25 % and the southern 25 % of the field were planted to crops other than grass. This meant that the actual dimensions of Lysimeter 1 field were 190 m east-west, and just 63 m north south. During 1989 the northern 25 % of the field was planted to alfalfa and the

southern 25 % was planted to sugar beets. Therefore, it was impossible to obtain a thermal pixel that had a high percentage of grass.

The contamination of thermal pixels introduces significant errors in SEBAL$_{ID}$, because all energy balance components: net radiation, sensible heat and soil heat fluxes use surface temperature information, which is derived from the Landsat thermal band.

For that reason, lysimeter 1 was discarded from comparison purposes. Emphasis during the comparative study was therefore concentrated on lysimeter field 2.

With regard to the shortwave bands, the spatial resolution of Landsat 5 is 30 m x 30 m (bands 1, 2, 3, 4, 5,and 7). Therefore there were always four or more "pure" short-wave pixels inside the lysimeter field. This fact is important in SEBAL$_{ID}$, because short-wave band information is used to predict vegetation features such as surface albedo, NDVI, LAI and aerodynamic roughness.

Lysimeter Data

The integrity of the hourly lysimeter data was evaluated using the methodology described in Appendix A. Table 6.1 provides comments on the general soil and crop conditions present in Lysimeter 2 during the satellite days.

Most of the dates included in Table 6.1 correspond to 1989, where lysimeter field 2 was planted to sugar beets. The sugar beets were planted on April 27 and were harvested on October 18. Full cover conditions for the sugar beets were reached around July 20. Therefore, the first four images of 1989 represent mostly bare soil conditions. The July 7, July 23 and September 25 dates represent full-cover conditions.

TABLE 6.1. General Crop and Soil Conditions at the Lysimeter 2 on the Satellite Image Dates. Information Obtained from Field Logs provided by Dr. J.L Wright (2002)

Date	Lysimeter 2 (west)	
	Crop and stage	Soil Wetness Condition
08/21/1988	Potatoes planted 4/28. Variety Kennebec	some moisture. (3 days after 15 mm Irrigation)
04/18/1989	bare. Sugar beets planted later on April 27	Dry. 8 days since slight rain
05/04/1989	One week after planting of Sugar beets. no vegetation	wet. 1 day after irrigation
05/20/1989	S.Beets emerged May 8th on field, May 11th on lysimeter 2	dry. 5 days since 12 mm rain, > 8 days since Irrigation
06/05/1989	S. Beets – partial cover	most dry. 3 days since 3 mm P, > 15 days since irrig.
06/21/1989	S. Beets. Intermediate cover	Dry. 8 days since irrigation
07/07/1989	S. Beets – full cover	Dry. 9 days since Irrigation
07/23/1989	S. Beets – full cover	some moist. 3 days since 3 mm P, 5 days since Irr.
09/25/1989	S. Beets (harvested 10/11-18)	Dry. 6 days since Irrigation. Weather data was lost due to lightning damage on datalogger
06/24/1990	Peas, full-cover, harvested July 27	Field Irrigated this day, Lysimeter was irrigated the night before.
07/29/1991	Full cover alfalfa	

With regard to image dates for the other crops, potatoes (1988), peas (1990), and alfalfa (1991), all were in full cover condition for the considered dates.

Calculation of Alfalfa Reference ET

For the validation of the model, weather data registered at the micrometeo-rological weather station operated by Dr. J.L Wright were used. Information about solar radiation, air temperature, dewpoint temperature, and wind speed was validated as described in Appendix A, and then processed to calculate instantaneous values (satellite overpass time), and 24-hour values of alfalfa reference evapotranspiration (ET_r). Table

6.2 includes the values of instantaneous and daily ET_r considered in the validation of the model.

TABLE 6.2. Values of Instantaneous Wind Speed, Instantaneous ET_r, and 24-hour ET_r Corresponding to the Satellite Dates Used in This Study

Image Date	Inst. Winspeed at 2 m (m/s)	Inst. ET_r (mm/hr)	24 hour ET (mm/day)
04/18/89	3.36	0.72	6.8
05/04/89	5.81	0.68	7.8
05/20/89	2.59	0.71	7.3
06/05/89	2.53	0.71	6.7
06/21/89	1.67	0.60	6.3
07/07/89	0.90	0.74	8.4
07/23/89	0.77	0.67	7.4
09/25/89	4.10	0.87	8.0

Soil Heat Flux, G

Soil heat flux functions were derived from data collected by Dr. J.L. Wright during the period 1971-1974. Concurrent measurements of LAI, net radiation and soil heat flux were available from the lysimeter fields for different crops: alfalfa (1971), potatoes (1972), and beans (1973 and 1974). The G functions that were developed are the following, which represent mid-day values (11:00-13:00):

$$G = \left(0.05 + 0.18e^{-0.521LAI}\right)R_n \qquad \text{for } LAI \geq 0.5 \qquad (6.1)$$

$$G = 1.80(T_s - 273.16) + 0.084R_n \qquad \text{for } LAI < 0.5 \qquad (6.2)$$

where LAI is the leaf area index, T_s is the surface temperature, in K, and G and R_n are in Wm^{-2}.

Details of the development of Eqs. (6.1) and (6.2) are included in Appendix G.

Estimated G from Eqs (6.1) and (6.2) was compared with estimations made using the

general SEBAL$_B$ G equation developed by Bastiaanssen (Eq. 3.25), for a series of

agricultural pixels. The results were similar as shown in Fig. 6.2 for the scene

corresponding to 07/22/2000. Maximum differences in G averaged 20 W/m^2.
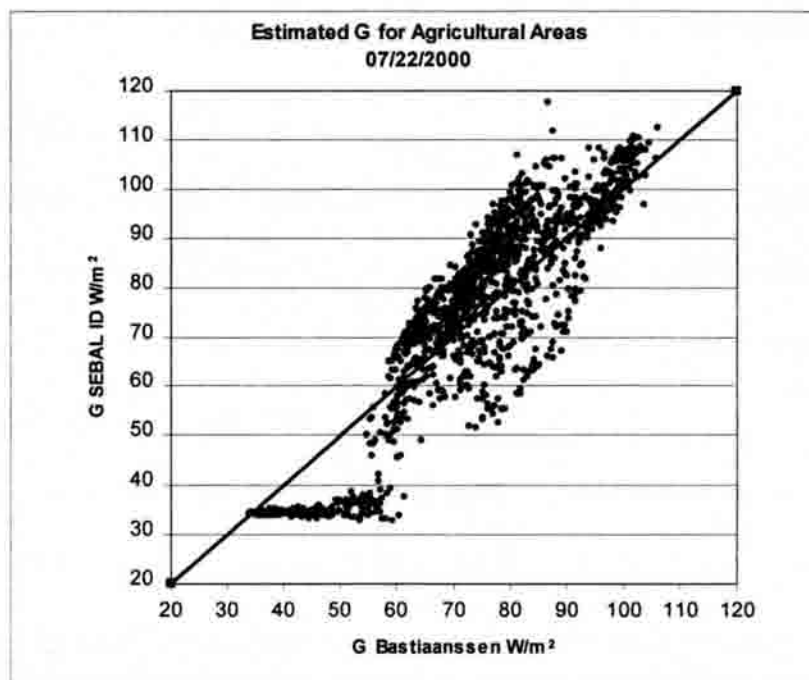
FIGURE 6.2.   Difference between Estimations of G with Eq. (3.25) and Estimations of
              G using Local Calibrated Equations (Eqs. 6.1 and 6.2) for Agricultural
              Areas and from the 06/04/2000 Landsat 7 Scene.

From Fig. (6.2), some larger differences in estimated G are observed when

SEBAL$_{ID}$ G estimations were around 35 W/m^2 . In SEBAL$_{ID}$ values of LAI (calculated

from SAVI) were constrained to a maximum value of LAI=6, therefore, SEBAL$_{ID}$

predicts the same value of G/R$_n$ when LAI = 6, independently of surface temperature and

surface albedo (Eq. 6.1). On the other hand, Eq. (3.25) incorporates T_s and albedo, therefore it is able to predict more variation in the values of G/R_n for LAI=6.

Because results from both equations were similar for agricultural fields in the study area, and because Eq. 3.25 has been widely tested in different environments, Eq 3.25 was used to estimate soil heat flux in this study, rather than the locally derived functions. This analysis constitutes an important validation of Bastiaanssen Eq. 3.25, since the Eqs. 6.1 - 6.2 were developed independently from an independent dataset.

Water Balance Model

The water balance model described in Chapter IV was applied to track the soil moisture in agricultural bare soil pixels, which were the preferred candidates for "hot" pixels. As was described in Chapter III and IV, the selection of a hot pixel is required to defined the T_s versus dT relationship (Eq. 3.33).

In the bare soil water balance model the main input is the precipitation occurring in the area. The type of soil was taken as silt loam, which is the predominant soil in the Kimberly area and in the lysimeter field. Figure 6.3 shows the daily variation of ETrF in bare soils in 1989 for the Kimberly area, after applying the water balance model described in Chapter IV. The occurrence of precipitation produces evaporation from bare soils, reflected by an abrupt increase of the value of ETrF following rain. Then, the value of ETrF decreased as a function of the depletion of soil water in the top soil. The results obtained with the water balance model provide for the estimation of ETrF (and amount of evaporation) for hot pixel candidates, commonly taken as bare agricultural soils.
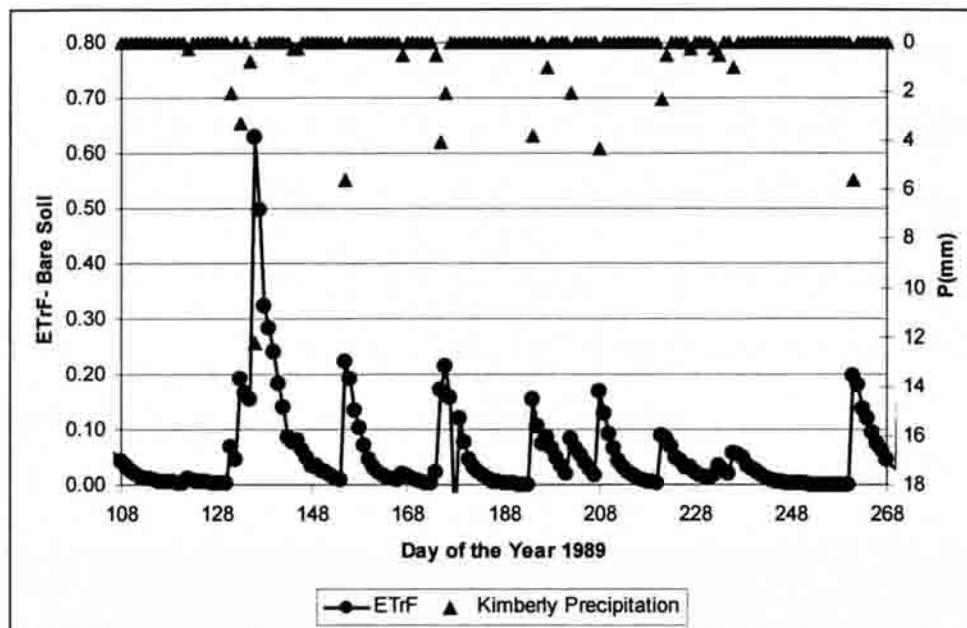
FIGURE 6.3.   Daily Evolution of ETrF Predicted for Bare Soil Conditions at Kimberly Area, During 1989

Table 6.3 lists the dates for 1989 were a value of ETrF greater than zero was

applied for the hot pixel.

TABLE 6.3.   Image Dates Where a Value of ETrF Greater Than Zero Was Applied to the Hot Pixel

Image date	Day of the year	Hot pixel ETrF
05/20/1989	140	0.24
06/05/1989	156	0.19

Relationship Between Surface Temperature
(T_s) and Near-Surface Air Temperature
Difference (dT)

The application of SEBAL$_B$ and SEBAL$_{ID}$ involves the definition of a T_s versus

dT relationship for every image (Eq. 3.33). The T_s vs dT function is representative for

the time that satellite image was taken. In every processed image, a cold and hot pixel

was defined, and the corresponding T_s and dT were used to define the linear relationship.

The cold pixel was always taken from a full-cover agricultural field in the

Kimberly area having lower temperature compared to similar pixels, which was taken as

an indication of the presence of a non-stressed crop having wet surface conditions. Hot

pixels were taken from bare agricultural soils having higher temperatures than other

similar fields, which was taken as an indication of substantial lack of soil moisture.

Figure 6.4 shows an example of cold and hot pixel selection.

FIGURE 6.4.   Approximate Location of the Cold (1) and Hot (2) Pixels for a Landsat 7
               ETM+ Scene (shown in true color) for 07/12/2002. The Cold Pixel Is in
               a Full-Cover Alfalfa Field, and the Hot Pixel Is in a Bare and Dry,
               Agricultural Field

Figure 6.5 shows a plot of LAI versus surface temperature corresponding to

several agricultural pixels. The location of cold and cold pixels is also displayed.

As can be seen in Fig. 6.5, the cold pixel was located in the zone of maximum

LAI (full cover conditions) and lowest surface temperature (indication of a non-stressed

crop). On the other hand the hot pixel was located in the zone of minimum LAI (bare soil

conditions) and highest surface temperature (indication of dry conditions). In both cases,
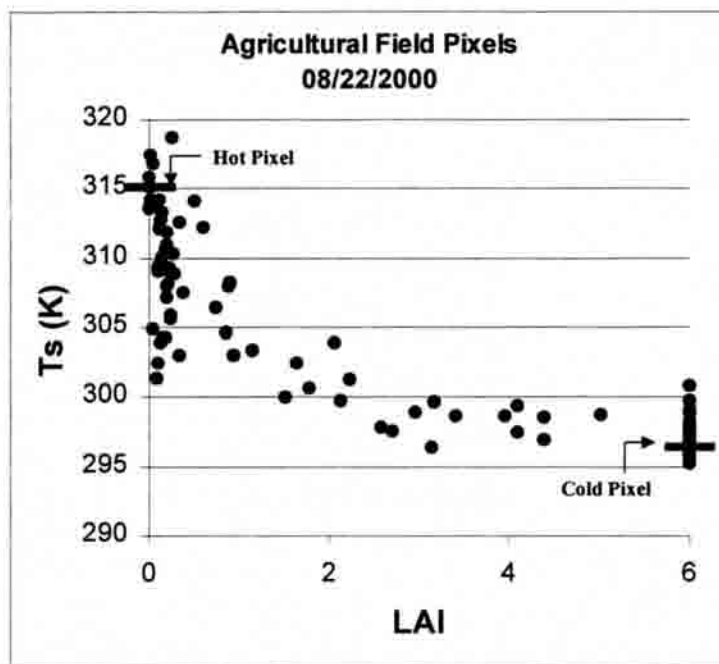
FIGURE 6.5.   Plot of LAI vs Surface Temperature for Several Agricultural Pixels on
the scene corresponding to 08/22/2000. The Location of Hot and Cold
Pixels Is Also Indicated.

extreme low and high temperatures were avoided because they might not be represen-

tative of the general conditions of the soils in the study area.

Table 6.4 shows radiometric surface temperature for cold and hot pixels

corresponding to every image as well as the corresponding dT values calculated for both

pixels.

As can be seen in Table 6.4, dT at the hot pixel was always greater than for the

cold pixel. In SEBAL$_B$ dT is used to predict the sensible heat, therefore hot pixels will

have greater H. For the image corresponding to 09/25/89, dT at the cold pixel was

negative, because the predicted H at that pixel ($H_{cp} = Rn_{cp} - G_{cp} - 1.05*ET_r$) was

negative, indicating the presence of advective conditions at the cold pixel, produced by

TABLE 6.4. Values of T_S and dT for Hot and Cold Pixels Corresponding to the Processed Landsat 5 Scenes (path 40, row 30) During 1989

Date of Image	Time of Image (GMT)	T_S cold pixel (K)	dT cold pixel (K)	T_S hot pixel (K)	dT hot pixel (K)
04/18/89	17 48'44"	294.8	0.13	310.5	4.83
05/04/89	17 48' 30"	292.3	0.38	311.7	3.77
05/20/89	17 48' 10"	293.4	1.77	314.0	3.67
06/05/89	17 47' 58"	295.5	1.71	315.2	4.68
06/21/89	17 47' 32"	293.8	2.07	317.0	5.50
07/07/89	17 47' 17"	302.2	1.23	329.1	4.75
07/23/89	17 46' 58"	299.8	1.58	321.4	4.99
09/25/89	17 45' 29"	296.0	-3.85	307.5	3.33

transport of sensible heat into the cold pixel, which made predicted ET greater than the available energy. The exact location of the cold and hot pixels for each image is included in Appendix K.

The positive values for dT at the cold pixels for other dates indicates that the predicted ET for the cold pixel (1.05 ET_r) was less than available energy at the satellite overpass time.

A plot of the linear relationship between T_S and dT for each image time is shown in Fig. 6.6. As seen in Fig. 6.6, the slopes of the curves are very similar from 5/4/89 to 7/23/89, being steeper for the early image of the year (04/18/89) and for the latest scene (09/25/89), where the variation between the cold and hot pixel surface temperatures was smaller. These T_S versus dT relationships are only valid for each image and the specific time of the satellite overpass.
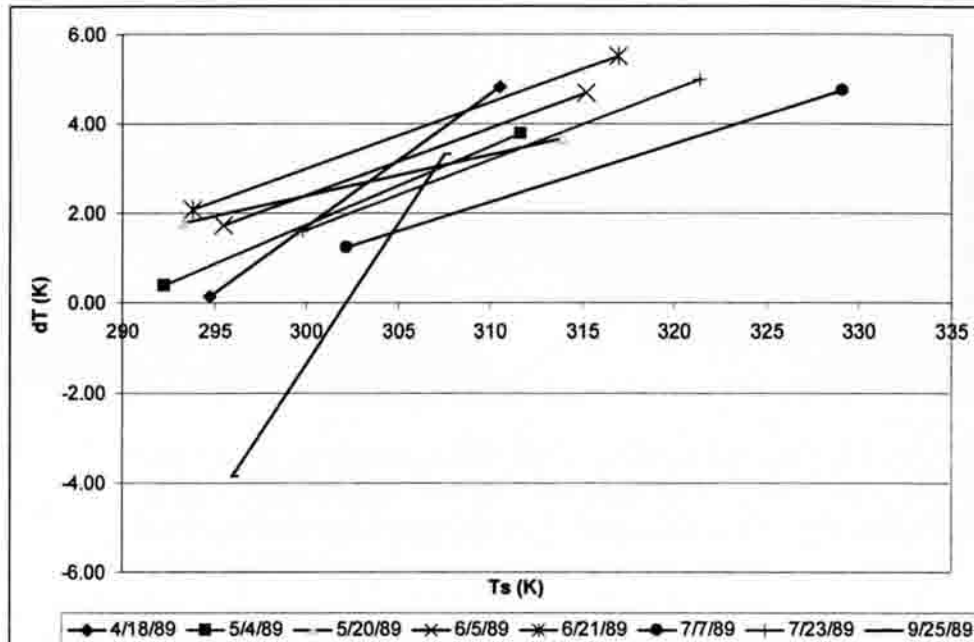
FIGURE 6.6. T_s vs dT Functions Corresponding to Each Processed Image During 1989.

Results of SEBAL$_{ID}$ Model Validation for
Prediction of Instantaneous ET Values

After applying SEBAL$_{ID}$ for each image, results from four 30x30 pixels around

the lysimeter site were taken and averaged. A geo-rectified airphoto (taken in 1995) was

utilized to provide the lysimeter approximate location. In Fig. 6.7 the airphoto of the

lysimeter location, and details of Landsat shortwave and thermal bands are shown..

Thermal pixels are not square because of resampling done during geo-rectification

and reprojection to true North-South. As mentioned before, the low spatial resolution of

Landsat 5 thermal band introduces uncertainties in the calculation of some energy

balance components of SEBAL.
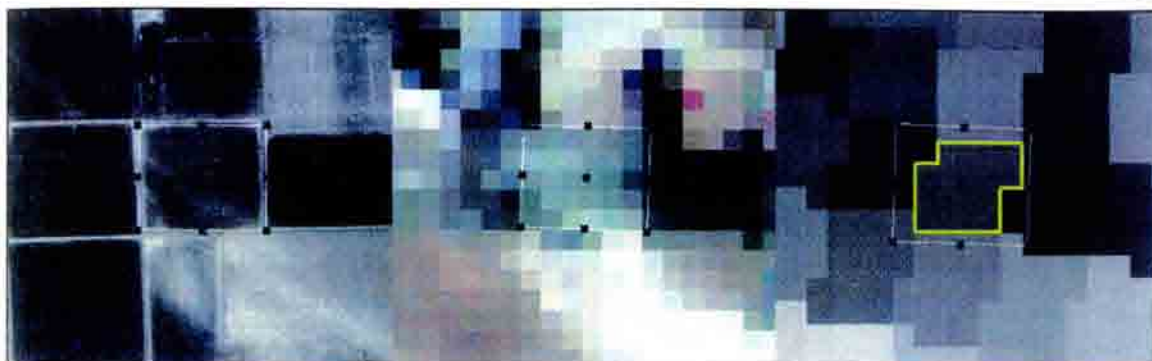
FIGURE 6.7.   Airphoto of Lysimeter 2 field (left), Landsat TM True Color at 6/21/89 (center), and Landsat TM Thermal Band at 6/21/89 (right). Outline Pixels in the right Image are from one original Thermal Band Pixel (120m·120m).

The band 6 (120m x 120 m) was resampling in 30 m x 30 m pixel size to be congruent with the shortwave bands. The left part of the photo shows the location of Lysimeter 2 field. The center part shows the shortwave pixels that are inside of the lysimeter field. The right portion of the Fig. shows how thermal pixels were distributed relative to the lysimeter field. In this case (scene corresponding to 6/21/89), a "pure" thermal pixel was located in the center of the lysimeter field, therefore a good estimation of ET from $SEBAL_{ID}$ was expected. However in most of the cases, the thermal pixel was strongly "contaminated" by surrounding areas.

Another case when the lysimeter 2 field included an almost "pure" thermal pixel was in the scene corresponding to 07/29/91. In this date the crop in the lysimeter was alfalfa. Figure 6.8 shows the Lysimeter 2 field, and the corresponding thermal and shortwave pixels for the 07/29/91 scene.

145
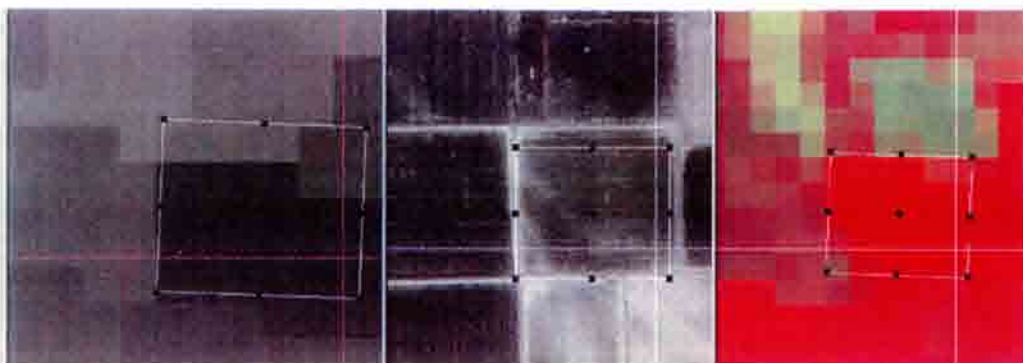
FIGURE 6.8.   Picture of Lysimeter 2 Field. Landsat TM Thermal Band at 07/29/91
(left). Airphoto of Lysimeter 2 Field (center), and Landsat TM True
Color at 07/29/91 (right).

On the other hand, Fig. 6.9 shows a case where the thermal pixels inside the

lysimeter were "contaminated" by surrounding areas. The lysimeter field on 07/07/89

contained information from 5 different thermal pixels, none of them completely inside of

it. Therefore, estimation of radiometric surface temperature, and all components of

$SEBAL_{ID}$ that are derived from it, is expected to be hampered by the mixing of thermal

information.
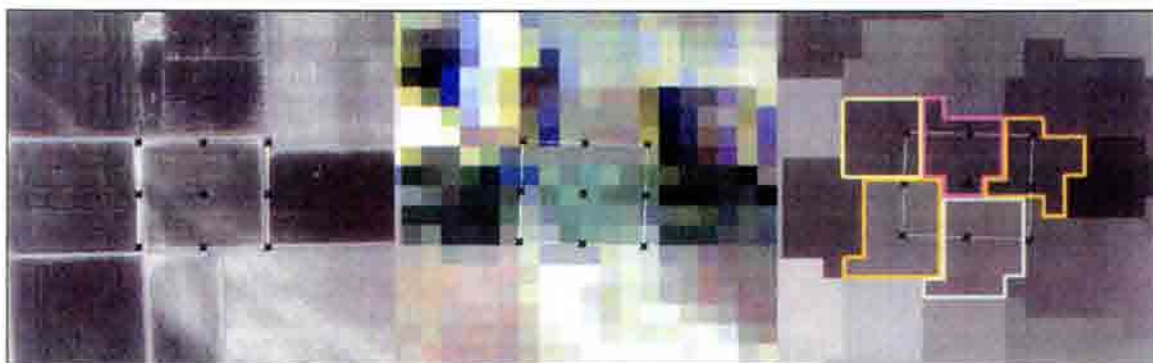
FIGURE 6.9.   Lysimeter 2 Field Airphoto (left), Landsat TM True Color at 7/7/89
(center), and Landsat TM Thermal Band on 7/7/89 (right). Each
Colored Pixel in the Right Image Represents a Different Thermal Pixel
(120m x120m).

Based on Figs 6.7, 6.8, and 6.9, a better estimation of ET from $SEBAL_{ID}$ is expected in the scenes corresponding to 06/21/89 and 07/29/91 and worse estimation for 07/07/89. The accuracy of $SEBAL_{ID}$ strongly depends on the quality of the thermal information which is used to retrieve the radiometric surface temperature of the pixel.

Table 6.5 shows a summary of the results obtained in the model validation. ET values from $SEBAL_{ID}$ were obtained averaging results from four 30 m x 30 m pixels approximately centered at the lysimeter site (see Appendix D). Table 6.5 includes the values of instantaneous ET (corresponding to the satellite overpass time) estimated from $SEBAL_{ID}$, and corresponding instantaneous ET measured at the lysimeter site. In addition, the corresponding values of reference ET are included for comparative purposes.

TABLE 6.5. Summary of Instantaneous ET Comparison for 1988 (Potatoes), 1989 (Sugar Beets), 1990 (Peas), and 1991 (Alfalfa)

Satellite Date 1989	Crop	Reference ET $ET_{r(inst)}$ mm/hr	Measured ET [1] $ET_{(inst)}$ mm/hr	$ET_rF_{(inst)}$	$SEBAL_{ID}$ ET [2] $ET_{(inst)}$ mm/hr	ET_rF	Difference $ET_{(inst)}$ [3] mm/hr	Normalized Error [4] %
8/21/88	Potatoes	0.75	0.63	0.84	0.57	0.76	-0.055	-7.4
04/18/89	Sugar B.	0.72	0.05	0.07	0.24	0.34	0.190	26.6
05/04/89	Sugar B.	0.68	0.60	0.88	0.45	0.66	-0.150	-22.0
05/20/89	Sugar B.	0.71	0.10	0.14	0.10	0.14	0.000	0.0
06/05/89	Sugar B.	0.71	0.18	0.25	0.15	0.21	-0.030	-4.2
06/21/89	Sugar B.	0.60	0.21	0.35	0.22	0.37	0.010	1.7
07/07/89	Sugar B.	0.74	0.70	0.95	0.45	0.61	-0.250	-33.8
07/23/89	Sugar B.	0.67	0.67	1.00	0.64	0.95	-0.030	-4.5
09/25/89	Sugar B.	0.87	0.53	0.61	0.77	0.89	0.240	27.6
06/24/90	Peas	0.81	0.78	0.96	0.78	0.97	0.004	0.5
07/29/91	Alfalfa	0.84	0.84	1.00	0.79	0.94	-0.049	-5.9

(1) Measured ET values were provided by Dr. James Wright, USDA/ARS
(2) The $SEBAL_{ID}$ ET is the averge of four 30m x 30m pixels that were centered at the lysimeter
(3) In "Difference" column, negative values indicated that $SEBAL_{ID}$ ET was lower than Lysimeter 2 ET.
(4) Normalized error was calculated as $100 \cdot$ Difference $ET_{(inst)} / ET_{r(inst)}$

Table 6.5 includes the difference between SEBAL$_{ID}$ estimated instantaneous ET values and instantaneous ET values measured at the lysimeter 2. The average difference was 12.2 % and the standard deviation of the differences was 12.6 %. A normalized error, calculated as the ratio between the instantaneous ET difference and the instantaneous ET$_r$ (taken as an index of the climate evaporative demand) is also included in Table 6.5.

As it can be seen in Table 6.5, the estimation of daily ET from SEBAL$_{ID}$ resulted in more than 10 % of normalized difference on four dates : 04/18/89, 05/04/89, 07/07/89, and 09/25/89. The significant underestimation of ET on 07/07/89 was expected, because of the contamination of thermal pixels shown in Figure 6.9. Thermal information was partially impacted by surrounding fields that according to the shortwave bands depicted in   Fig. 6.9 had less vegetation, and therefore a greater surface temperature. In SEBAL$_{ID}$ a greater temperature produces a higher dT value and a increment of sensible heat, which reduced the ET at the pixel.

For the other two scenes (04/18/89 and 05/04/89) the same problem with the thermal information occurred as can be seen in Fig. 6.10. The thermal pixel of the 4/18/89 date only had 4 of 16 pixels outside the lysimeter field. However, the outside pixels were clipped grass while the lysimeter field 2 was bare, dry soil. Therefore, the 4 outside pixels still contributed substantially to thermal contamination. Clipped grass pixels had lower temperature than the lysimeter field, therefore they reduced the surface temperature of the lysimeter field thermal pixel, which in SEBAL translates into smaller sensible heat flux and greater ET. In addition, the lysimeter field condition was before planting and during a period of drydown following precipitation. Bare soil surface conditions may have spatial variability.

148
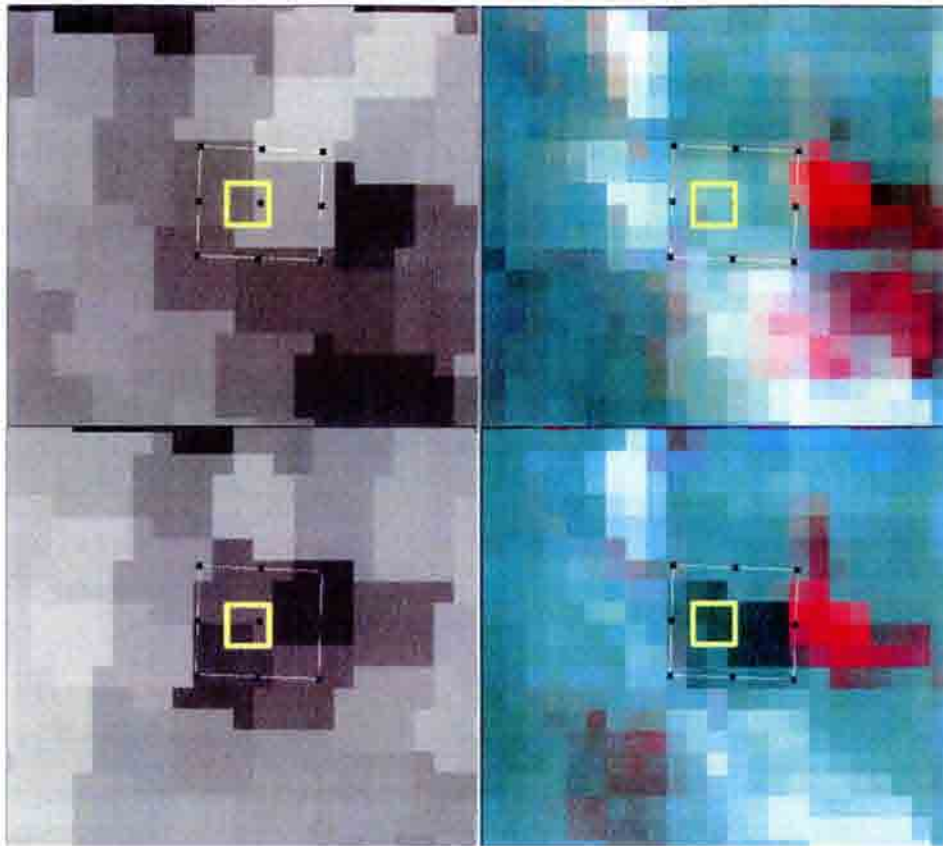
FIGURE 6.10. Thermal Band Information (left) and TM True Color Images (right) at
Kimberly Lysimeter Field, on 4/18/89 (top), 5/4/89 (bottom). The Four
30m x 30 m Pixels Taken in each Lysimeter Field Are Shown.

With regard to the 05/04/89 date, the lysimeter field was irrigated two days
before the image, whereas the lysimeter was irrigated only one day before. The –22%
normalized error (Table 6.5) reflects this difference in surface wetness, because SEBAL
retrieves thermal and shortwave information from the lysimeter field.   Therefore, in this
case, information measured by the lysimeter did not represent the conditions at the
lysimeter field.

With respect to to 09/25/1989, an electrical outage ocurred that precluded the
sampling and collection of weather data during the first half of the day, including the

satellite overpass time. Therefore, wind data for the first half of the day was estimated using wind patterns from previous days and a daily total wind run recorded by another weather station. Information concerning solar radiation, air temperature, and dewpoint temperature was estimated using trends borrowed from other days to allow calculation of the instantaneous and daily values of ET_r.

Figure 6.11 shows a plot of measured instantaneous ET and $SEBAL_{ID}$-ET. In general, $SEBAL_{ID}$ produced satisfactory estimates of instantaneous ET in seven of the eleven images. The standard deviation of the differences was 0.14 mm/hour, and eliminating the days were thermal information was mixed, this standard error reduces to 0.026 mm/hour, which is 5.4% of the average measured ET for the eleven dates.

Extrapolation of Instantaneous ET Values
to Daily ET Values

For the extrapolation of instantaneous values of ET two approaches were considered. The first one is based on the assumption that the value of instantaneous ETrF (ratio between actual ET and alfalfa reference ET_r) is similar to the daily average value of ETrF. This approach was used for the validation of $SEBAL_{ID}$.

The second one is based in the self-preservation of the evaporative fraction (EF), which is discussed later when considering the EF method. Results from application of both methodologies are compared as well.

150
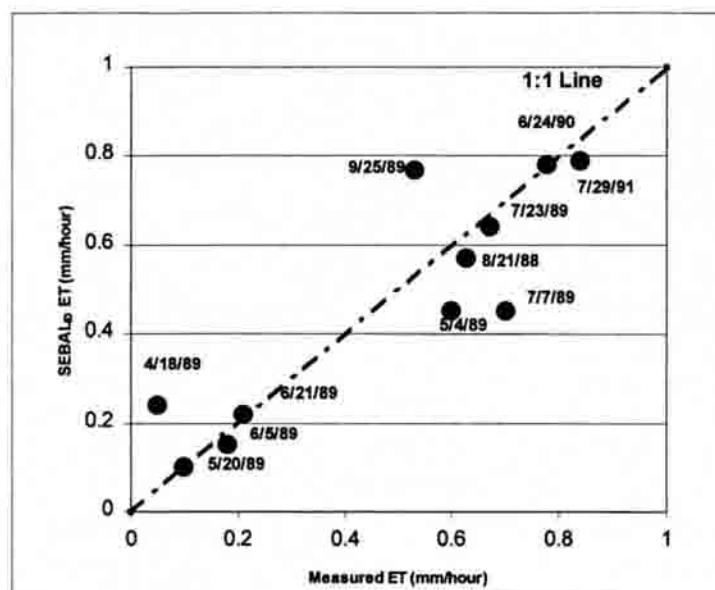
FIGURE 6.11   Comparison Between Measured and Estimated Instantaneous ET for the
Days Considered in the Validation of SEBAL$_{ID}$.

Validation of SEBAL$_{ID}$ Model Using ETrF Approach for Extrapolation of Instantaneous to Daily ET Estimates

An analysis of the diurnal behavior of ETrF was performed using lysimeter data

from 1988 and 1989 collected by Dr. J.L. Wright. The hypothesis was that the value of

ETrF remains relatively constant during daytime so that it can be used to extrapolate

instantaneous ET values produced by SEBAL$_{ID}$ to daily ET values.

The crop in lysimeter 1 was fescue grass in both years. The crop in lysimeter 2

was potatoes in 1988 and sugar beets in 1989. Figure 6.12.1 shows an example plot of

hourly evapotranspiration for grass corresponding to June 21, 1989. ETrF from 10:00 to

18:00 was relatively constant. Figure 6.12.2 shows example hourly values of ET for

sugar beets measured at lysimeter 2.
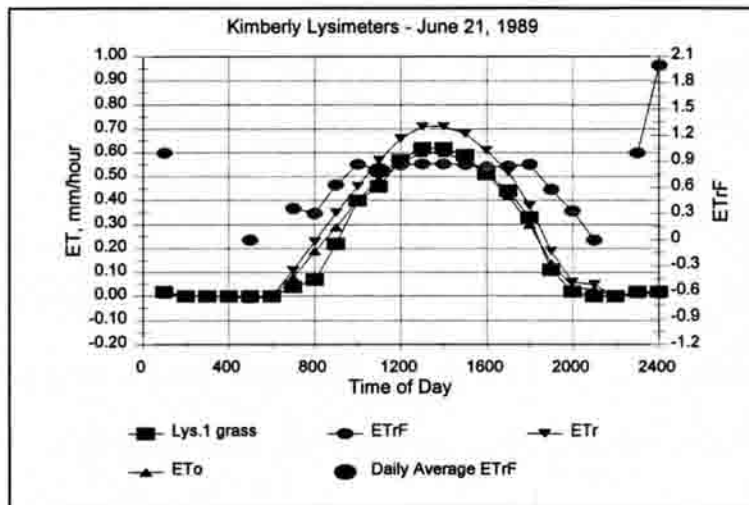
FIGURE 6.12.1. Plot of Hourly ET for Grass Measured at Lysimeter 1, at Kimberly. The Graph includes Alfalfa Reference ET (ET_r) Calculated from ASCE-EWRI(2002), Grass Reference ET (ET_o), ETrF for Each Hour and the Average Value of ETrF for the 24-hour Period. Data Provided by Dr. J.L. Wright.
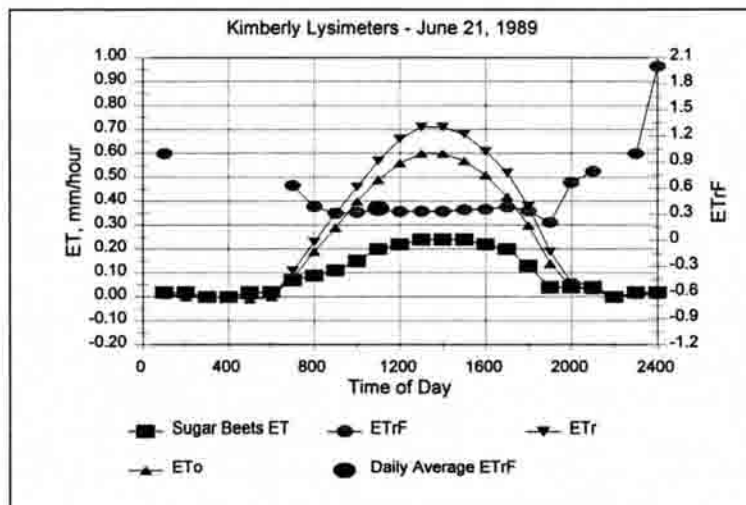
FIGURE 6.12.2. Plot of Hourly ET for Sugar Beets Measured at Lysimeter 2, at Kimberly. The Graph includes Alfalfa Reference ET (ET_r) Calculated from ASCE-EWRI(2002), Grass Reference ET (ET_o), ETrF for Each Hour and the Average Value of ETrF for the 24-hour Period. Data Provided by Dr. J.L. Wright.

As can be seen in both figures, ETrF was fairly constant from 09:00 to 18:00

hours, which is an indication that instantaneous values could be representative of daytime

values.

To determine whether ETrF can be used to estimate daily values of ET based on

instantaneous ETrF values ($ETrF_{inst}$), values of $ETrF_{inst}$ obtained as the ratio of

lysimeter 2 ET observations from sugar beets and potatoes and values of instantaneous

ET_r calculated from data obtained at the micrometeorological weather station were

compared with the respective daily values of ETrF ($ETrF_{24}$). The instantaneous values

of ETrF were calculated for the approximate time of satellite overpass. In Table 6.6 the

respective $ETrF_{inst}$ and $ETrF_{24}$ values area included.

TABLE 6.6.   Instantaneous and 24-Hour Values of ETrF Calculated from Lysimeter
ET and Weather Information at Kimberly. Data provided by Dr. J.L
Wright.

Satellite Date	Crop	Instantaneous ETrF (11:00 am)	24-hours ETrF
08/21/88	Potatoes	0.78	0.87
04/18/89	Sugar Beets	0.06	0.10
05/04/89	Sugar Beets	0.88	0.85
05/20/89	Sugar Beets	0.13	0.19
06/05/89	Sugar Beets	0.26	0.26
06/21/89	Sugar Beets	0.35	0.37
07/07/89	Sugar Beets	0.93	0.94
07/23/89	Sugar Beets	1.02	1.03
09/25/89	Sugar Beets	0.61	0.69

Figure 6.13 displays a plot of the information given in Table 6.6.
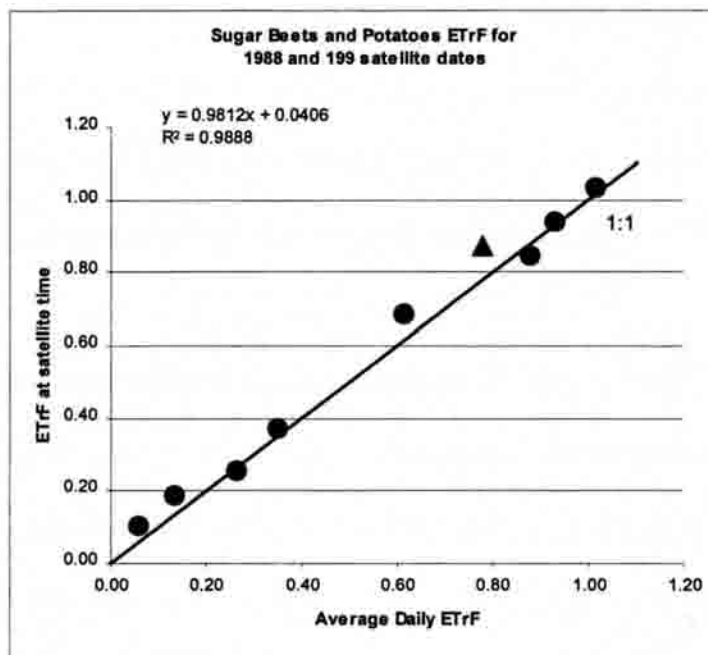
FIGURE 6.13.   Plot of Instantaneous and Daily (24 hours) Values of ETrF. Circular
Points Correspond to Sugar Beet Values from 1989. The Triangle
Corresponds to the Potato Value from 1988.

As indicated by the analysis of Fig. 6.13 and Table 6.6, the values of

instantaneous ETrF and 24-hour ETrF are highly correlated (R^2=0.99). In addition, the

slope of the correlation curve is nearly 1 (0.98) and the intercept is nearly 0 (0.04),

indicating that ETr_{inst} and ETr_{24} can be taken as similar enough to use for extrapolation

purposes . In addition, the standard error was small (SE=0.04), which is an indication

that $ETrF_{24}$ can be predicted from $ETrF_{inst}$ without introducing a significant error for the

satellite dates.

The relative constancy of the ETrF during the day is due to the fact that both ET

variables in ETrF, actual ET and reference ETr, are exposed to the same weather

parameters during the day. A higher variation in ETrF is expected if the actual crop and

the reference crop have substantially different surface resistance characteristics (stomata

control properties) or substantially different aerodynamic characteristics. The analysis

included in Fig. 6.13 is significant in that the sugar beet conditions ranged from almost

bare soil to full cover, while the reference alfalfa was always calculated using fixed

height, and fixed surface resistance values as indicated by the ASCE-EWRI procedure

(2002).

Figure 6.14 shows a plot of instantaneous and 24-hour average ETrF calculated

from measurements of ET from lysimeter 2 (sugar beets) for the period May to

September, 1989. Figure 6.14 shows that most of the time values of instantaneous and

24-hour ETrF are very close to the 1:1 line. Appendix J includes additional plots of

hourly values of ETrF at lysimeter 2.
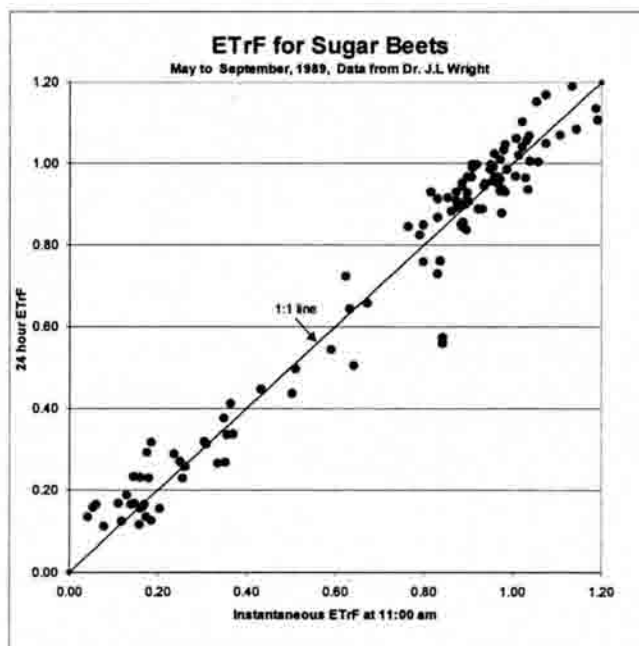
FIGURE 6.14.   Plot of Instantaneous (at satellite overpass time) and 24-hour ETrF for
                Sugar beets during 1989 (May to September).

In conclusion, the information obtained by the correlation analysis between

$ETrF_{inst}$ and $ETrF_{24}$, indicates that the assumption of $ETrF_{inst} \approx ETrF_{24}$ can be applied

for extrapolation of instantaneous to daily values of ET for the available satellite dates.

**Results of Estimation of Daily ET Values
Using SEBAL$_{ID}$ and ETrF Method**

The ETrF method was applied to extrapolate the instantaneous ET values

included in Table 6.5 to the corresponding values of 24-hour ET (ET_{24}). The results

obtained are included in Table 6.7.

TABLE 6.7.   Summary of Daily ET Comparison for 1988, 1989, 1990, and 1991

Satellite Date 1989	Crop	Reference ET ET_r mm/day	Measured ET [1] ET mm/day	SEBAL$_{ID}$ ET $ET_{(24)}$ mm/day	Difference $ET_{(24)}$ [2] mm/day	Normalized Error [3] %
8/21/88	Potatoes	7.8	6.7	6.0	-0.7	-8
04/18/89	Sugar B.	6.8	0.7	2.3	1.6	24
05/04/89	Sugar B.	7.8	6.6	5.1	-1.5	-20
05/20/89	Sugar B.	7.3	1.4	1.1	-0.3	-5
06/05/89	Sugar B.	6.7	1.7	1.4	-0.3	-5
06/21/89	Sugar B.	6.3	2.4	2.3	-0.1	-1
07/07/89	Sugar B.	8.4	8.0	5.2	-2.8	-33
07/23/89	Sugar B.	7.4	7.6	7.0	-0.6	-8
09/25/89	Sugar B.	8.0	5.5	7.1	1.6	20
06/24/90	Peas	8.8	8.8	8.5	-0.3	-3
07/29/91	Alfalfa	7.8	7.5	7.4	-0.2	-2

(1) Measured ET values were provided by Dr. James Wright, USDA/ARS

(2) In "Difference" column, negative values indicated that SEBAL$_{ID}$ ET was lower than Lysimeter 2 ET.

(3) Normalized error was calculated as 100*Difference $ET_{(24)}$ / $ETr_{(24)}$

From the analysis of the results included in Table 6.7, it can be concluded that the

extrapolation of instantaneous to 24-hour ET using the ETrF method did not increase the

normalized error obtained from the estimation of instantaneous ET from SEBAL$_{ID}$ (see

Table 6.5). Therefore, differences in the results are a product of the problems indicated

in the discussion of instantaneous ET estimates rather than the extrapolation procedure.

A plot of the results presented in Table 6.7 is given in Fig. 6.15. As can be seen, $SEBAL_{ID}$ estimations of daily ET are good when satellite thermal information was adequate.
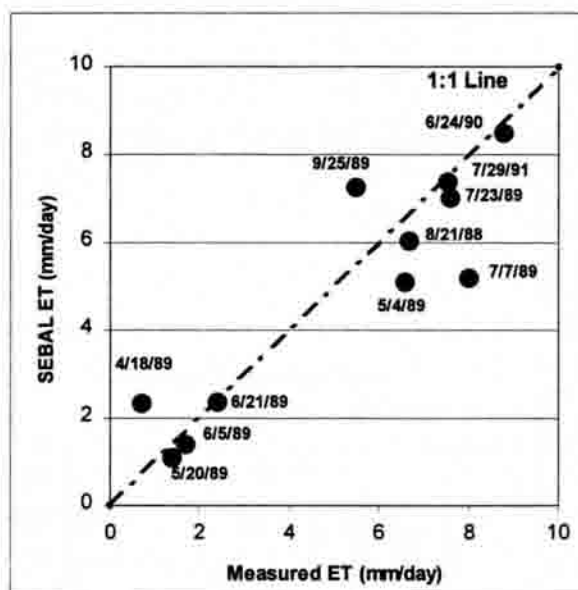
FIGURE 6.15.   Comparison Between Measure and Estimated Daily ET for the days
                Considered in the Validation of the Remote Sensing Algorithm.

Testing the EF Approach to Estimate
Daily ET Using $SEBAL_B$

The evaporation fraction (EF) is the ratio between ET and the available energy (R_n-G). In many remote sensing studies, daily values of ET have been inferred from instantaneous ET by assuming that the evaporative fraction remains relatively constant during the daytime (Brutsaert and Sugita, 1992). This means that as ET changes during the day, the available energy changes proportionally, so that the value of EF remains constant.

In the study area, where agricultural fields are surrounded by desert, transport of

warm and dry air into the agricultural areas can enhance the rate of ET, and increase the

value of EF. The warm and dry air transports heat from the desert so that saturation

deficit of the air in agricultural areas is increased resulting in a increase in the ET rate.

This mostly large-scale horizontal advection can make ET even greater than $R_n - G$.

This fact can be noticed by viewing a plot of the diurnal variation of EF as shown in

Fig. 6.16.
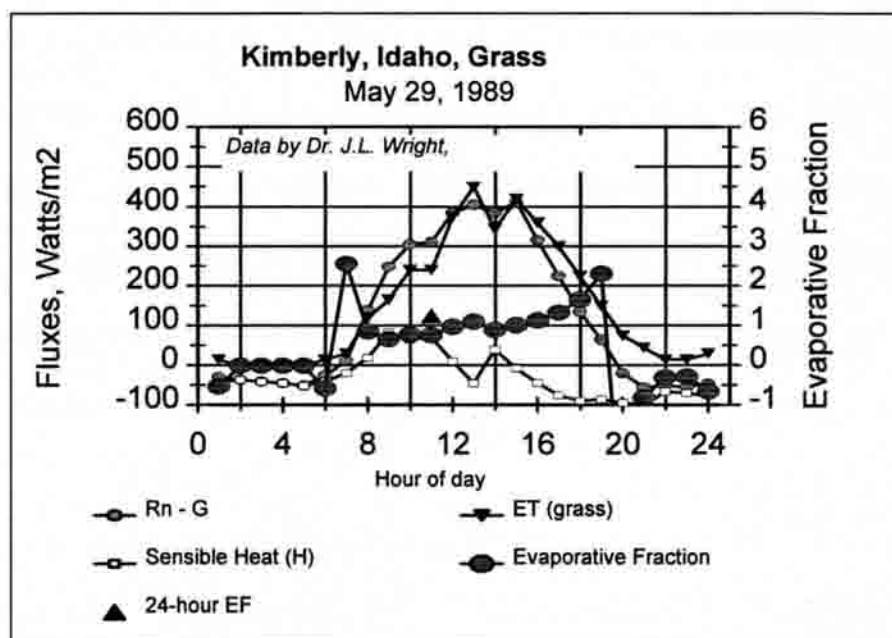
FIGURE 6.16.   Diurnal Variation of EF at the Lysimeter 1 (Grass) at Kimberly, Idaho for 05/29/1989.

Figure 6.16 illustrates how the value of EF increases during the day as extra

energy is brought in by the advection of warm and dry air from the desert. Therefore, in

the advective environment surrounding the study area, the value of EF may not be

preserved during the daytime, so that instantaneous values of EF will not be

representative of the daily average value of the same parameter. In the case of using Landsat imagery, the assumption of considering the value of EF at around 11:00 (satellite time) as equal to the average daily value will result in an underestimation of the daily fluxes.

Table 6.8 and Figure 6.17 contain instantaneous and daily values of EF for the satellite days in 1989, corresponding to the grass lysimeter. Unfortunately, this analysis could not be performed at the lysimeter 2, because net radiation data were not available there, and estimates of R_n for bare soil conditions were uncertain. On the basis of the values show in Table 6.7 and Fig. 6.17, it is concluded that instantaneous EF values are always smaller than average 24-hours EF (approximately 10% on average from Table 6.8), so that underestimation of daily latent heat flux is expected if one assumes that the value of EF is preserved during the day in the study area, at least during the satellite dates. A portion of the increase in EF, for a sample in April and early May, may be due to increasing afternoon winds.

TABLE 6.8.   Instantaneous and Daily Values of EF for Grass in 1989

Imagine Date	Instantaneous EF	EF_{24}	Difference	% Difference
04/18/89	0.83	0.93	-0.1	10.8
05/04/89	0.66	0.85	-0.19	22.4
05/20/89	0.68	0.82	-0.13	17.1
06/05/89	0.85	0.87	-0.02	2.3
06/21/89	0.61	0.73	-0.12	16.4
07/07/89	1.01	1.01	0.00	0.0
07/23/89	0.89	0.92	- 0.02	3.3
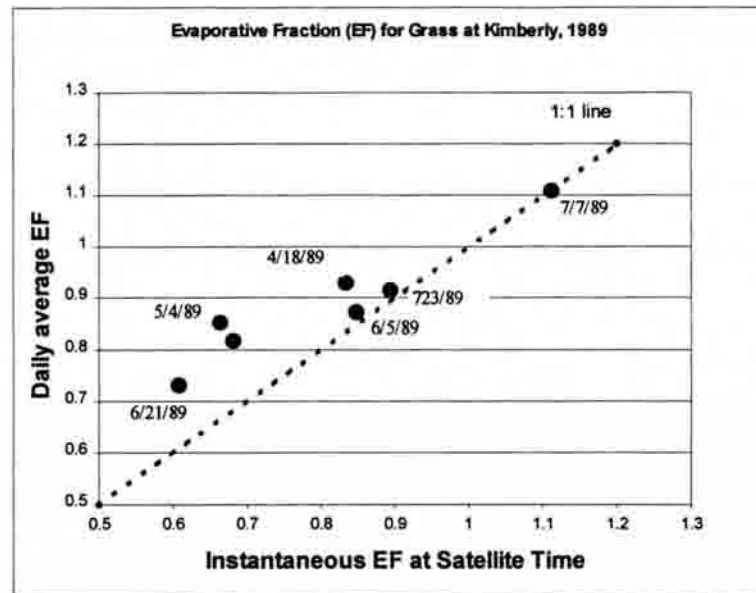
FIGURE 6.17   Plot of Instantaneous and Daily EF Values for the Lysimeter 1 (grass) for Satellite Image Dates in 1989. Data provided by Dr. J.L Wright.

Application of the EF Method with
SEBAL_B

The EF method was applied for all the scenes included in Table 6.5 to provide 24-hour ET from satellite images. The procedure for applying the the EF method followed the steps included in the original SEBAL_B model, described in Chapter III. Therefore, cold pixels were selected from water surfaces. Following Bastiaanssen et al. (1998) dT was assumed to be zero at the cold pixel. Hot pixels were selected from the nearly hottest population of pixels (Bastiaanseen 2002, personal communication), which happened to be located in desert areas, and the dT at the hot pixel was taken as $dT = Rn - G$, when a water balance model indicated the presence of dry conditions. This application of SEBAL_B is made to provide comparison to the proposed used of ETrF and $H \neq 0$ at cold pixels as described earlier in the definition of the SEBAL_ID model.

Figure 6.18 shows an example of areas selected for hot and cold pixels for the application of the EF method.

Table 6.9 lists values of surface temperatures for cold and hot pixels for the EF application and the corresponding dT values for the 1989 Landsat 5 processed images.

FIGURE 6.18   Approximate Location of the Cold (1) and Hot (2) pixels for the Scene of 06/21/89. Cold pixel is in Water, and Hot Pixel is in a Desert Area (EF method).

TABLE 6.9.   Values of T_S and dT for Hot and Cold pixels Corresponding to the Processed Landsat 5 Scenes (path 40, row 30) during 1989, Using the EF Method

Date of Image	Time of Image (GMT)	T_S cold pixel (K)	Assumed dT cold pixel (K)	T_S hot pixel (K)	dT hot pixel (K)
04/18/89	17 48'44"	286.8	0.00	308.2	5.33
05/04/89	17 48' 30"	287.0	0.00	308.3	4.25
05/20/89	17 48' 10"	287.0	0.00	316.9	6.06
06/05/89	17 47' 58"	290.3	0.00	318.3	5.27
06/21/89	17 47' 32"	291.9	0.00	319.7	6.05
07/07/89	17 47' 17"	296.9	0.00	332.0	5.03
07/23/89	17 46' 58"	296.1	0.00	322.9	5.22
09/25/89	17 45' 29"	291.1	0.00	311.5	3.77

A plot of the linear relationship between T_s and dT for each image time is shown in Fig. 6.19. Most of the slopes of the curves are very similar, being less steep for the image corresponding to (07/07/89) where there was the greatest difference between hot and cold pixel temperatures and one of the lowest wind speed situations (see Table 6.2).

Results. The EF method was applied to the same 1989 images (sugar beets), and the 1988 (potatoes), 1990 (peas), and 1991 (alfalfa) scenes as for the ETrF application described earlier. The results obtained are shown in Table 6.10. The results indicate that the version of SEBAL$_B$ as applied by Bastiaanssen (1998), predicted both the instantaneous and 24 hour ET values well for the dates where the measured ET was lower : 04/18/89, 05/20/89, and 06/05/89. In most of the other cases, the SEBAL$_B$ -EF method significantly underestimated daily values of ET. For comparison see Table 6.7.
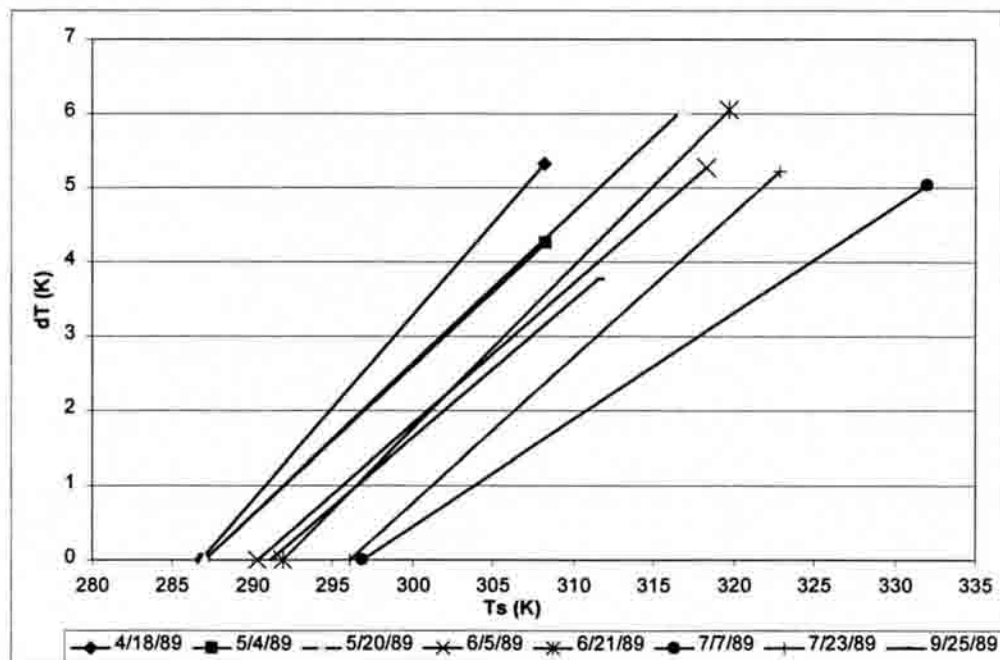
FIGURE 6.19. T_s vs dT Functions Corresponding to each Processed Image During 1989 Using the EF Method

TABLE 6.10 Summary of ET Comparison for 1988 (Potatoes), 1989 (Sugar Beets), 1990 (Peas) and 1991 (Alfalfa), Using the EF Method

Satellite Date	Crop	Reference ET Info		Measured ET Info		Sebal - ET			ET24 difference
		ETr inst mm/hr	ETr 24 mm/day	ET inst mm/hr	ET 24 mm/day	ET inst (mm/hr)	ET 24 mm/day	EF	mm
8/21/88	Potatoes	0.75	7.8	0.63	6.7	0.53	4.6	0.82	-2.1
04/18/89	Sugar B	0.72	6.8	0.05	0.7	0.08	0.8	0.17	0.1
05/04/89	Sugar B	0.68	7.8	0.60	6.6	0.32	3.2	0.45	-3.4
05/20/89	Sugar B	0.71	7.3	0.10	1.4	0.13	1.5	0.26	0.1
06/05/89	Sugar B	0.71	6.7	0.18	1.7	0.16	2.1	0.34	0.4
06/21/89	Sugar B	0.60	6.3	0.21	2.4	0.28	3.5	0.52	1.1
07/07/89	Sugar B	0.74	8.4	0.70	8.0	0.48	5.8	0.79	-2.2
07/23/89	Sugar B	0.67	7.4	0.67	7.6	0.69	6.7	0.92	-0.9
09/25/89	Sugar B	0.87	8.0	0.53	5.5	0.39	2.5	0.72	-3.0
06/24/90	Peas	0.81	8.8	0.78	8.8	0.62	6.4	0.82	-2.4
7/29/91	Alfalfa	0.84	7.8	0.84	7.5	0.68	6.1	0.89	-1.4

The fact that the EF method consistently produced underestimated 24-hour ET confirms the hypothesis that in an advective environment, such as is present in the study region, where agricultural fields are surrounded by desert areas, the use of the EF method is poorly grounded. The greater the ET value, the greater the contrast between agricultural areas and desert regions, so that advective effects tend to be greater, with more warm and dry air transported to the agricultural areas. On the other hand, where conditions of low ET are present (bare soil conditions, low vegetation cover, or low soil moisture), the advective effects tend to be smaller. Some of this latter effect is due to seasonality of desert moisture availability.

A side by side plot of the comparison of instantaneous ET from $SEBAL_B$ (EF method) and instantaneous ET from SEBAL (ETrF method) to measured lysimeter ET is shown in Fig. 6.20, and the comparison between the respective daily values is shown in Fig. 6.21.

Figure 6.20 shows a plot of $SEBAL_B$ -ET estimates based on the EF method, and daily ET values measured from lysimeter 2 . $SEBAL_B$ -EF method underestimated all

values of daily ET when the measured ET was more than 4 mm per day. This finding

agrees with the conclusion made from Table 6.8 and Fig. 6.18 where the instantaneous

EF values were lower than daily EF values, so that underestimation of daily ET was

likely to occur.

Figure 6.20 shows that application of the EF method increased the difference

between measure and $SEBAL_B$ ET estimates when going from instantaneous (Fig. 6.20)

to daily values (Fig. 6.21). Therefore, it can be concluded that in the study area,

application of the EF method for extrapolation purposes tends to produce underestimation

of daily ET values.

On the other hand, the use of the ETrF method seems to consider the

enhancement of ET during the day due to the import of heat from the desert areas and
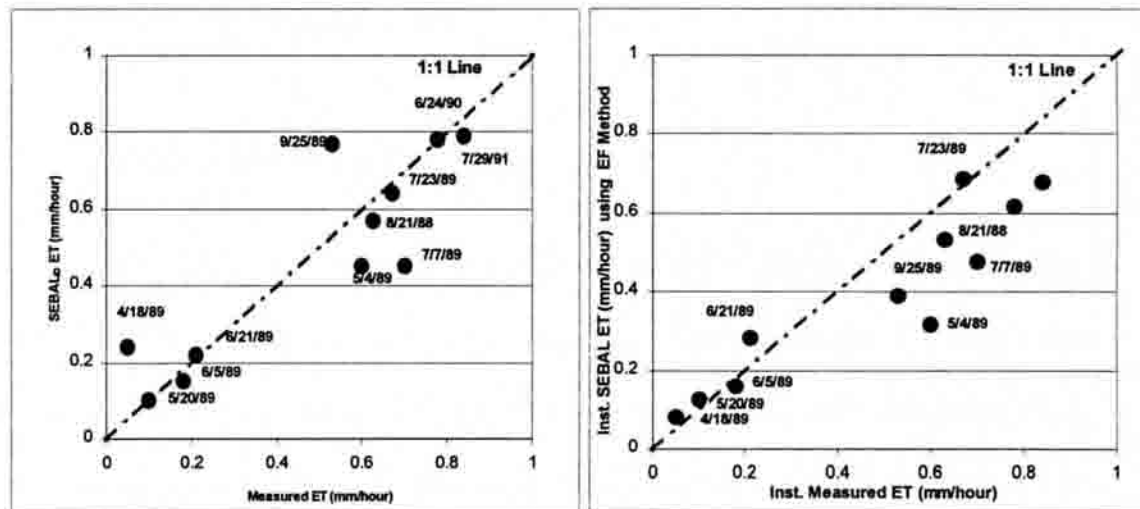
FIGURE 6.20.   Comparison Between Instantaneous Values of ET, Measured at the
Lysimeter, and Estimates of ET_{inst} using $SEBAL_{ID}$ Approach (left)
and $SEBAL_B$ Approach (right).

increased saturation deficit as reflected in the extrapolation from instantaneous (Fig.

6.21) to daily ET estimates (Fig. 6.22) using the ETrF method.
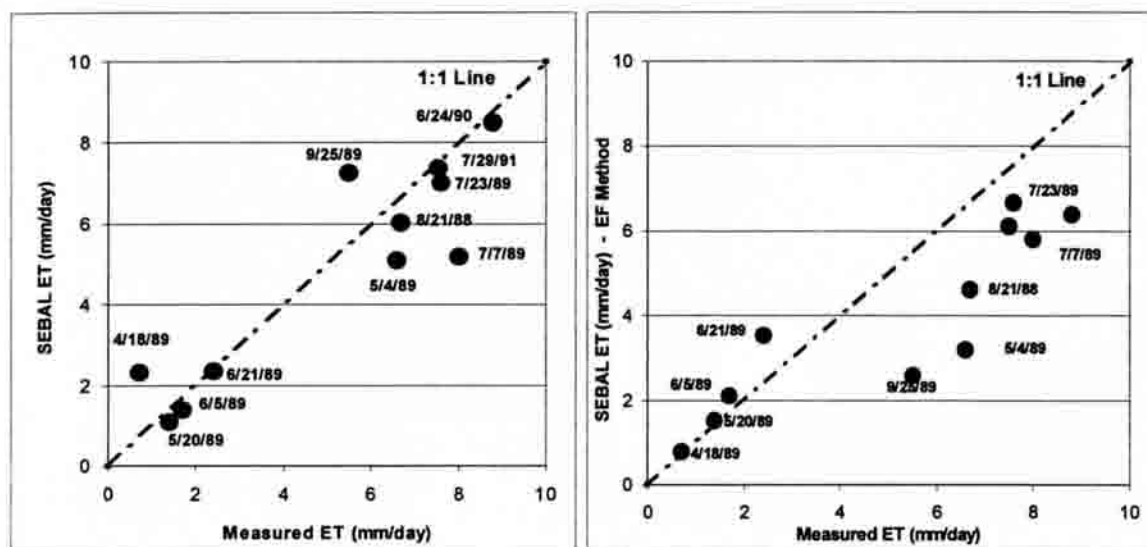
FIGURE 6.21.   Side by Side Comparison between Estimates of Daily ET from SEBAL
and Daily Measured Lysimeter ET, Using the ETrF Method (left) and
EF Method (right).

Analysis of the Behavior of SEBAL$_{ID}$ in
Agricultural Areas

In Fig. 6.22 a true color closeup of some agricultural fields in the Kimberly area

for 06/21/2000 is displayed where some individual fields are labeled. Table 6.11 shows

surface parameters and fluxes corresponding to subsamples from the five fields in Fig.

6.22. Samples 2 and 4 represent full-covered vegetated surfaces with the highest values

of LAI (see LAI map in the same figure).

According to Fig. 6.22 and Table 6.11, sample 2 is likely to be a small grain crop

(wheat or barley) and sample 4 is likely to be alfalfa. Sample 5 is a partially vegetated
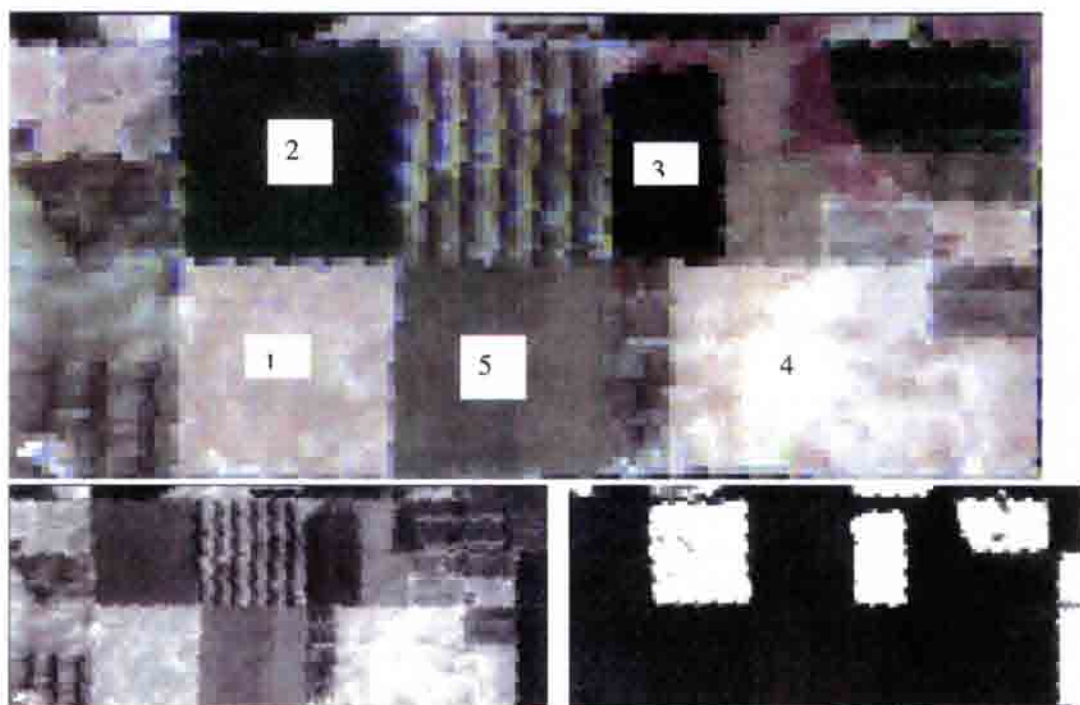
FIGURE 6.22   Closeup of an Agricultural Area for the Scene of 06/21/1989. True Color
of the Area (up), Albedo (bottom left), and Leaf Area Index (bottom
right).

surface (LAI = 1.08) that can be a immature row crop or cut alfalfa, and samples 1 and 4

are low covered surfaces (bare soil or bare soil recently planted to beans). Point 3 has

characteristics similar to those of a cold pixel (LAI = 6,   ETrF = 1.05), and its G/Rn

value matches that recommended by Allen et al. (1998) for alfalfa during daytime

conditions (G/Rn ≈0.04). Albedos in samples 2, 3, and 5 are between 0.18 and 0.22 with

are in the expected range of mid-day albedo for agricultural fields listed in Table 3.1.

Albedo in sample 4 is very high indicating that is possibly a dry bare surface, with high-

reflectance properties. Sample 1 is similar to sample 4, but albedo is smaller due to the

presence of a small amount of living vegetation.

TABLE 6.11.　Predicted Surface Parameters and Fluxes for the Samples Shown in Figure 6.22

Sample	1	2	3	4	5
Probable crop	Beans (bare)	small grain	alfalfa	bare soil	Immature crop
Albedo	0.27	0.21	0.18	0.38	0.22
LAI (m^2/m^2)	0.11	6	6	0.03	1.08
NDVI	0.17	0.79	0.86	0.12	0.51
z_{om} (m)	0.005	0.108	0.108	0.005	0.02
T_s (K)	316.1	294.5	292.9	311.9	306.9
Rn (Wm^{-2})	405.3	600.8	629.5	338.8	516.3
G/Rn	0.25	0.06	0.046	0.26	0.17
G (Wm^{-2})	101.3	41.6	29.0	87.6	88.4
H (Wm^{-2})	299.5	114.6	101.7	257.1	214.0
ETrF	0.01	1.02	1.05	0.0	0.5
ET$_{24}$ (mm/day)	0.07	6.8	7.6	0.0	3.4

Table 6.11 shows that the surface having the lower temperature (sample 3 T_s=292.9 K) is the one having the lowest predicted H, and the highest predicted ET (7.6 mm/day). On the other hand, samples 1 and 4 having higher temperatures, show the highest values of H, resulting in zero or near zero predicted ET.

In conclusion, all the values of surface parameters and surface fluxes are in the normal ranges expected for agricultural fields.

Seasonal ET

The daily values of ETrF calculated from each image date during 1989 (shown in Table 6.6) were used to estimate total ET, for given periods defined in Table 6.12, to allow an estimation of seasonal ET for the sugar beet field.

TABLE 6.12.   Computation of Seasonal ET (from April to September) During 1989

Image Date	Period ETrF applied From	To	Period length (days)	ETrF	Cumulative Etr for each period (mm)	SEBAL-ID Estimated ET (mm)	Lysimeter Measured ET (mm)	Average Estimated Error (mm/day)
04/18/89	4/1/89	4/25/89	25	0.34	140.4	48.0	14.5	1.3
05/04/89	4/26/89	5/11/89	16	0.66	98.5	64.5	83.8	1.2
05/20/89	5/12/89	5/27/89	16	0.15	88.3	13.0	17.0	0.3
06/05/89	5/28/89	6/12/89	16	0.21	115.4	24.0	29.4	0.3
06/21/89	6/13/89	6/28/89	16	0.37	120.6	44.5	45.7	0.1
07/07/89	6/29/89	7/14/89	16	0.61	125.1	76.8	118.5	2.6
07/23/89	7/15/89	8/23/89	40	0.95	257.3	244.6	265.0	0.5
09/25/89	8/24/89	9/30/89	38	0.91	203.5	184.3	139.9	1.2
-	4/1	9/30	183	-	1149.1	699.8	713.8	0.1

As is shown in Table 6.12, the value of ETrF obtained from $SEBAL_{ID}$ for

04/18/89 image was 0.34. This value of ETrF was assumed to be constant during the

period from 04/1/89 to 04/25/89. Therefore, by multiplying the accumulative ET_r

(calculated from weather station data) by the representative ETrF for the period, the

total ET was estimated as :   total ET = 0.34 * 140.4 = 48.0 mm. Comparing the real

total ET for that period (measured at the lysimeter site), which was ET = 14.5 mm, it

can be concluded that a significant overestimation was made. The absolute estimate error

for that period was 1.3 mm/day.

The assumption of constant ETrF during a period of time is undoubtedly

incorrect, considering that the value of ETrF changes in response to wetting events

(precipitation and irrigation), and the natural drying processes that occur in the soil

moisture from evaporation and transpiration.   However, the primary assumption here is

that, by using a sufficient number of images during the growing season, the error caused

by use of constant ETrF for a period tends to be randomized, and a compensation process

will occur, where situations of overestimation will offset situations of underestimation.

The cumulative error would tend to be smaller when more scenes are processed.   This

168

compensation process can be observed in Table 6.12 Even though individual errors were

as large as 2.6 mm/day (for the period from 6/29 to 7/14/89), the overall seasonal error

was just 0.1 mm/day. The total seasonal ET measured at the lysimeters was 714

millimeters and the SEBAL$_{ID}$-ET estimation was 700 mm so that modeled ET was just

2.5 % below the measured ET. Figure 6.23 shows a comparison between cumulative

measured and SEBAL$_{ID}$-estimated ET values. The good result obtained in the seasonal

estimation of ET using SEBAL$_{ID}$ is not a definitive proof of the adequacy of the

methodology. More research is obviously required in this topic.
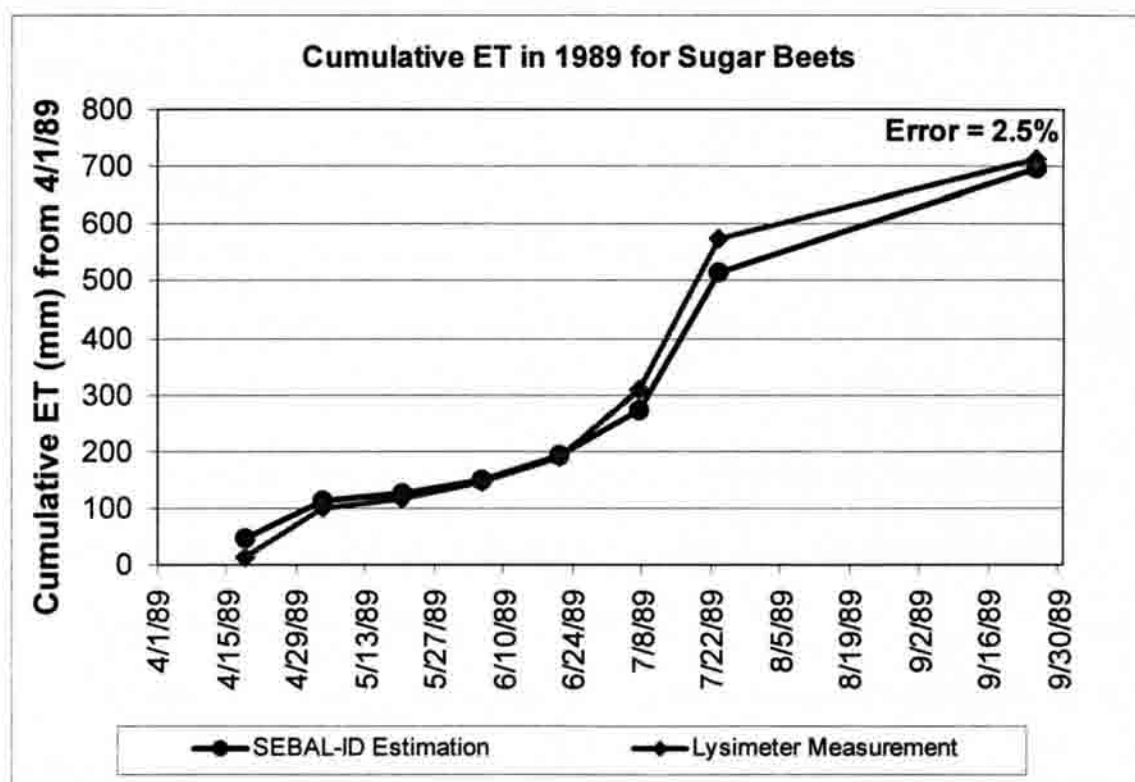
FIGURE 6.23   Cumulative Measured and Predicted ET for Lysimeter 2 (Sugar Beets) During 1989.

Application of SEBAL$_{ID}$ for 2000

The second phase of this study was to use the validated SEBAL$_{ID}$ to predict daily and seasonal ET for 2000, using 12 Landsat images from March to October (10 Landsat 7 ETM+ and 2 Landsat 5 TM scenes) corresponding to path 39, rows 29, 30, 31. The imagery covered the Eastern Snake River Plain in Idaho, and also some parts of Utah and Wyoming. The entire images were processed. However, results were concentrated on the Snake Plain portion of the images. The western portion of the Snake River Plain, residing in path 40, was also processed. This path is discussed by Tasumi (2003).

The image area contains several mountainous regions that allowed the qualitative evaluation of the enhancements of the SEBAL$_{ID}$ model included in Chapter V to improve predictions of surface fluxes in sloping terrains.

Weather Information

Several weather stations were utilized to represent the weather over the study area. Four Agrimet weather stations were selected: Aberdeen (ABEI), Rexburg (RXGI), MNTI Monteview (MNTI), and Ashton (AHTI), as seen in Fig. 4.4 . Analysis of the integrity of the weather data was made as described in Appendix A. These stations are automatic weather stations that report hourly measurements of solar radiation, wind speed, air temperature, dew point, and precipitation.

The relative similarity of the weather parameters (wind speed, solar radiation, air temperature, and dew point) among the weather stations, led to the conclusion that a weighted average of the weather data would be sufficient to characterize the weather conditions of the study area. More weight was assigned to the Aberdeen weather station because of its location relative to agricultural areas present in the path. Therefore, all of

the weather data that were input in SEBAL$_{ID}$, including the reference alfalfa

evapotranspiration (ET$_r$), were computed using a weight of 40 % for the ABEI weather

station, and a 20 % for each of the other stations: AHTI, MNTI, and RXGI.

Figure 6. 24 shows the variation of instantaneous wind speed registered in each of

the AGRIMET weather stations for the time of the satellite overpasses. In most of the

cases, wind speeds were similar among stations, which justified the use of a weighted

value for the image.
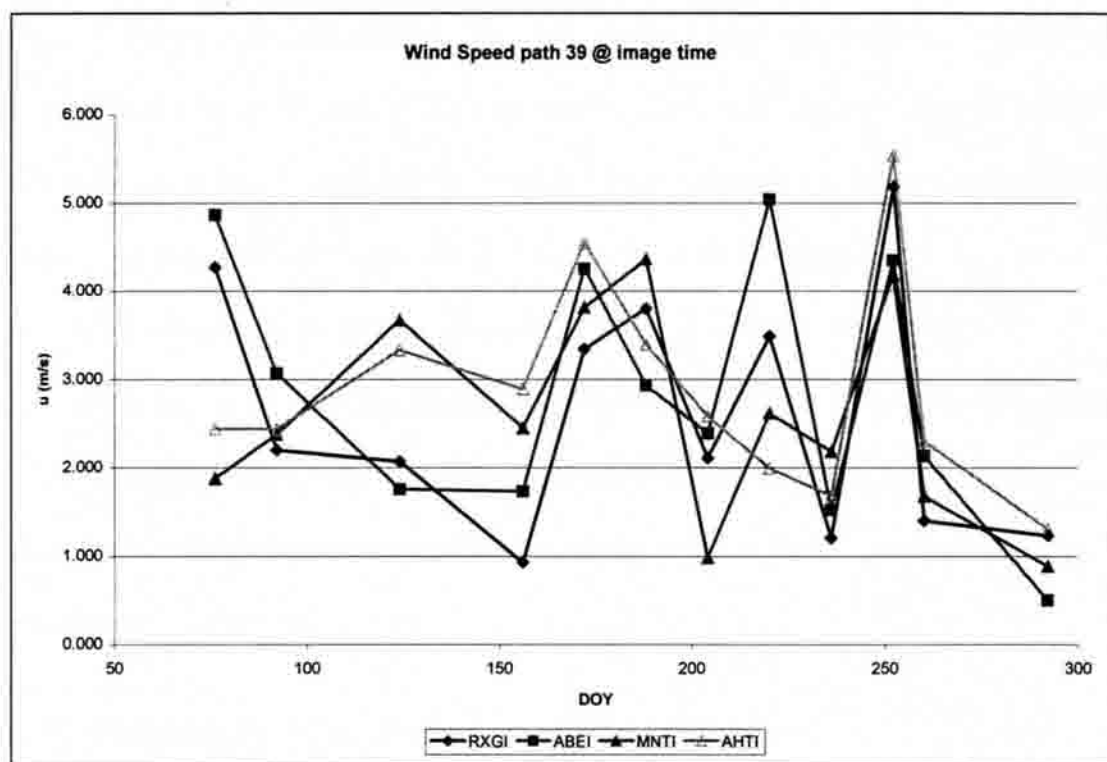
FIGURE 6.24.   Instantaneous Wind Speed (m/s) for Each Scene Overpass Time
Registered at the AGRIMET Weather Stations Considered for the 2000
Application.

<u>Selection of Cold and Hot Pixels</u>

Cold pixels were selected from agricultural fields that had full cover vegetation, and lower surface temperatures compared with other fully vegetated pixels. A uniform, low threshold in many fully-vegetated pixels was taken as an indication of good-irrigation conditions.

With regard to hot pixels, these were selected from bare agricultural soils that had higher temperature when compared with pixels having similar surface conditions. Higher temperature for similar surface conditions was taken as indication of lack of moisture in the top soil surface layer. The water balance model presented in Chapter V, was applied separately for each of the four weather stations to estimate the presence of moisture in hot pixels. Evaporation from the hot pixel selected was estimated from the water balance performed with data from the closest weather station.

After selecting cold and hot pixels from a specific portion of the image, a careful check was made in all the agricultural areas presented in the image to make sure that temperature conditions appeared on similar cold and hot pixels conditions. The selected cold and hot pixels were then used to define a T_s versus dT relationship for each date, which are plotted in Fig. 6.25.

<u>Cloud Masking and Snow Separation</u>

A real problem that was encountered in the 2000 application was the frequent presence of clouds in many of the images. The presence of clouds prevents $SEBAL_{ID}$ from successfully retrieving any surface temperature information. When image pixels are
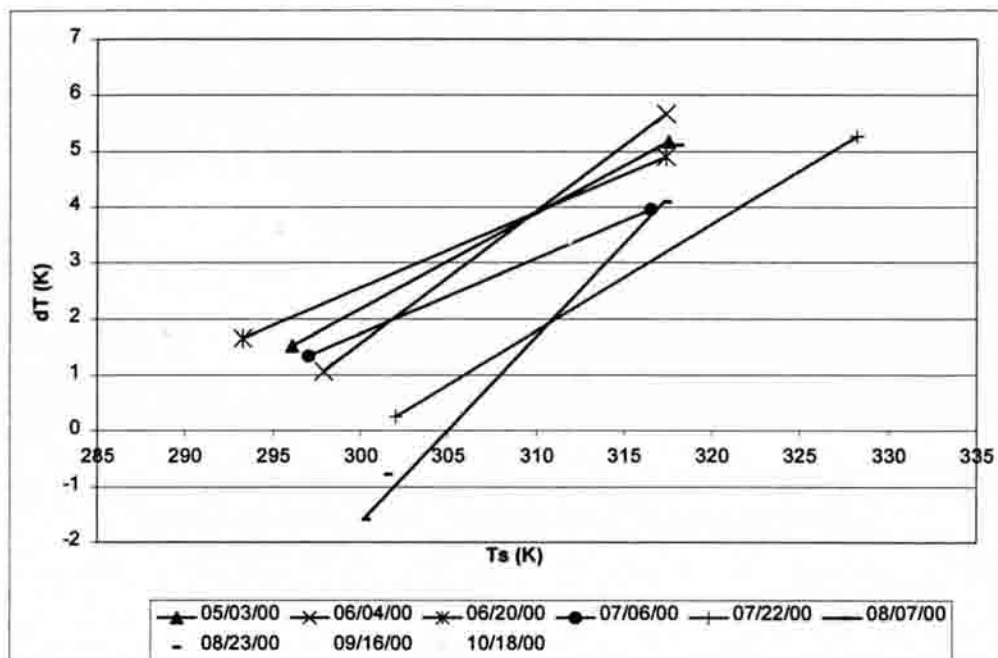
FIGURE 6.25.   dT vs T_s Functions for Each One of the Satellite Images Considered in the 2000 Application.

covered by clouds, much of the spectral information sensed by the satellite are in fact coming from the cloud and not from the surface bellow. Thin clouds were more difficult to identify than thick clouds (as shown in Fig. 6.26). Fortunately, both thick and thin clouds produced a identifiable drop of surface temperature that could be recognized in the Landsat thermal band.

Another problem was the shaded areas below clouds. Even though the information obtained from a shaded pixel represents the actual information for it (for example thermal information), shortwave reflectances do not represent clear sky conditions. SEBAL$_{ID}$ predicts incoming shortwave radiation ($R_s\downarrow$) assuming clear sky conditions, therefore the model is unable to reproduce the drop in $R_s\downarrow$ that takes place

FIGURE 6.26. Landsat 7 Image showing Thick (left) and Thin (right) Clouds for the Scene Date 08/23/2000. Shaded Areas Are Also Present.

FIGURE 6.27. Process of Masking Out a Cloud and Corresponding Shaded Area.

when the surface is shaded. For that reason, in $SEBAL_{ID}$, both clouds and derived shaded areas must be manually masked out, as shown in Fig. 6.27.

The separation of snow and clouds was performed by taking advantage of their contrasting reflectivity properties in some bands. Snow and clouds reflect similar amount of radiation in wavelengths smaller than 1.2 μm. From 1.2 to 3.0 μm clouds reflects significantly more shortwave radiation, therefore bands located in this range can be used

to separate clouds from snow areas. Figure 6.28 illustrates a cloud and snow separation

performed using Landsat band 7. The left of the image is snow covered mountains.

FIGURE 6.28.　　Cloud and Snow Separation Using Landsat Band 7 (04/01/2000).
　　　　　　　　　False Color (left) and Band 7 (right) Showing Contrasting Reflection.

Estimation of Daily and Seasonal ET
for 2000

All 12 images for 2000 were processed using the $SEBAL_{ID}$ model (see Appendix

C). Daily values of ET were estimated from instantaneous ET values using the ETrF

method. Instantaneous and daily values of ET_r were calculated using the standardized

ASCE Penman-Monteith method for reference alfalfa ASCE-EWRI (2002) presented in

Appendix B. A summary of the instantaneous and daily ET_r values are shown In Table

6.13.

After processing all the 12 images, a map of seasonal ET was produced holding

ETrF constant during a given period of time surrounding the processed image. Table

6.14 lists the periods considered. The total cumulative ET_r was calculated considering

TABLE 6.13.   Instantaneous and 24-Hour Values of ET_r for the 2000 Application for Path 39 (weighted average of four stations)

Image date	$ET_{r(inst)}$ (mm/hr)	ET_r (24) (mm/d)
03/16/00	0.39	3.2
04/01/00	0.42	3.4
05/03/00	0.71	8.3
06/04/00	0.77	7.4
06/20/00	0.69	7.5
07/06/00	0.73	7.5
07/22/00	0.83	8.0
08/07/00	0.92	9.3
08/23/00	0.72	6.5
09/08/00	0.81	8.1
09/16/00	0.67	6.3
10/18/00	0.35	2.8

TABLE 6.14.   Computation of ET_r for Each Period for the 2000 Application

	Period		Total
Dates	From	To	ET_r(mm)
3/16/00	March 1	March 24	55
4/1/00	March 25	April 17	111
5/3/00	April 18	may 19	163
6/4/00	May 20	June 12	180
6/20/00	June 13	June 28	129
7/6/00	June 29	July 14	124
7/22/00	July 15	July 30	114
8/7/00	July 31	August 15	123
8/23/00	August 16	August 31	111
9/8/00	Sep 1	Sept 12	60
9/16/00	Sep 13	Oct 2	92
10/18/00	Oct 3	Oct 31	65
		Total	1326

40 % of the weight for ABEI and 20 % for the rest of the stations MNTI, RXGI, and AHTI. ETrF values for cloudy areas were estimated by interpolating values of ETrF from neighbor images.

The map of seasonal ET (from March 1 to October 31, 2000) for the Eastern

Snake Plain River portion of path 39 is displayed in Fig. 6.29. Total values of seasonal

ET ranged from 180 mm for desert areas to 1100 mm for the highest agricultural fields.

The distribution of ET follows closely the distribution of vegetation and irrigation water

use on the plain.
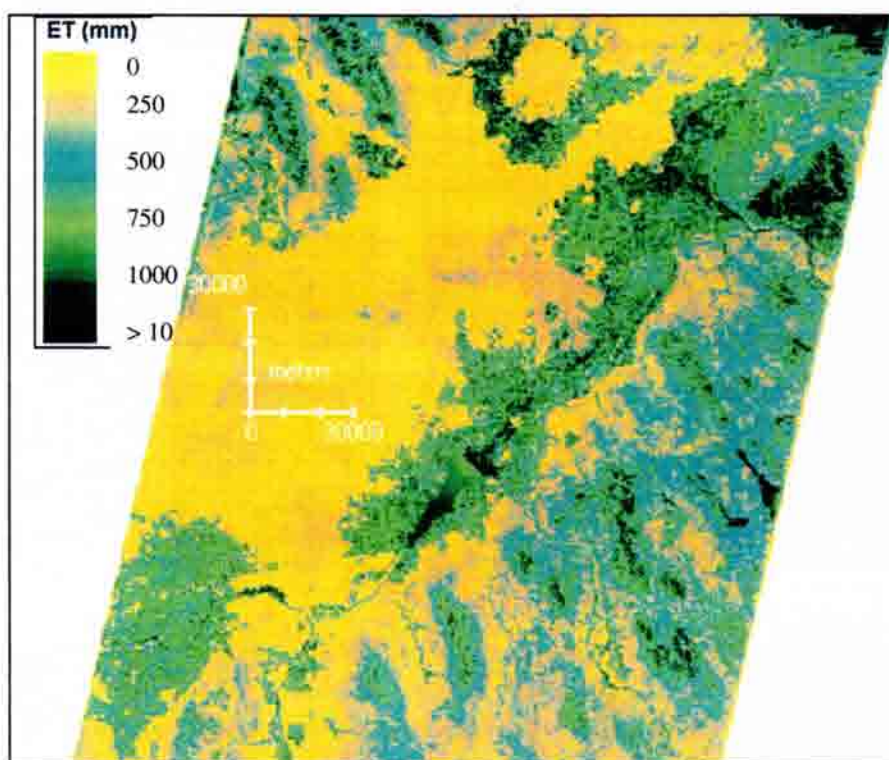
FIGURE 6.29.   Seasonal ET for 2000 (from March to October) for the Eastern Snake
River Plain Portion of Path 39 in Idaho.

ET from Agricultural Fields

Figure 6.30 is a closeup of estimated daily ET for the 12 images processed for

2000, with focus on an agricultural area located near Aberdeen, close to American Falls

Reservoir. The seasonal ET ranged from low values in March and April, to peak values

False color 06/04/2000   True color 06/04/2000

03/16/00 ET_r = 2.1 mm/day   04/01/00 ET_r = 2.4 mm/day

06/04/00 ET_r = 7.4 mm/day   06/20/00 ET_r = 7.5 mm/day
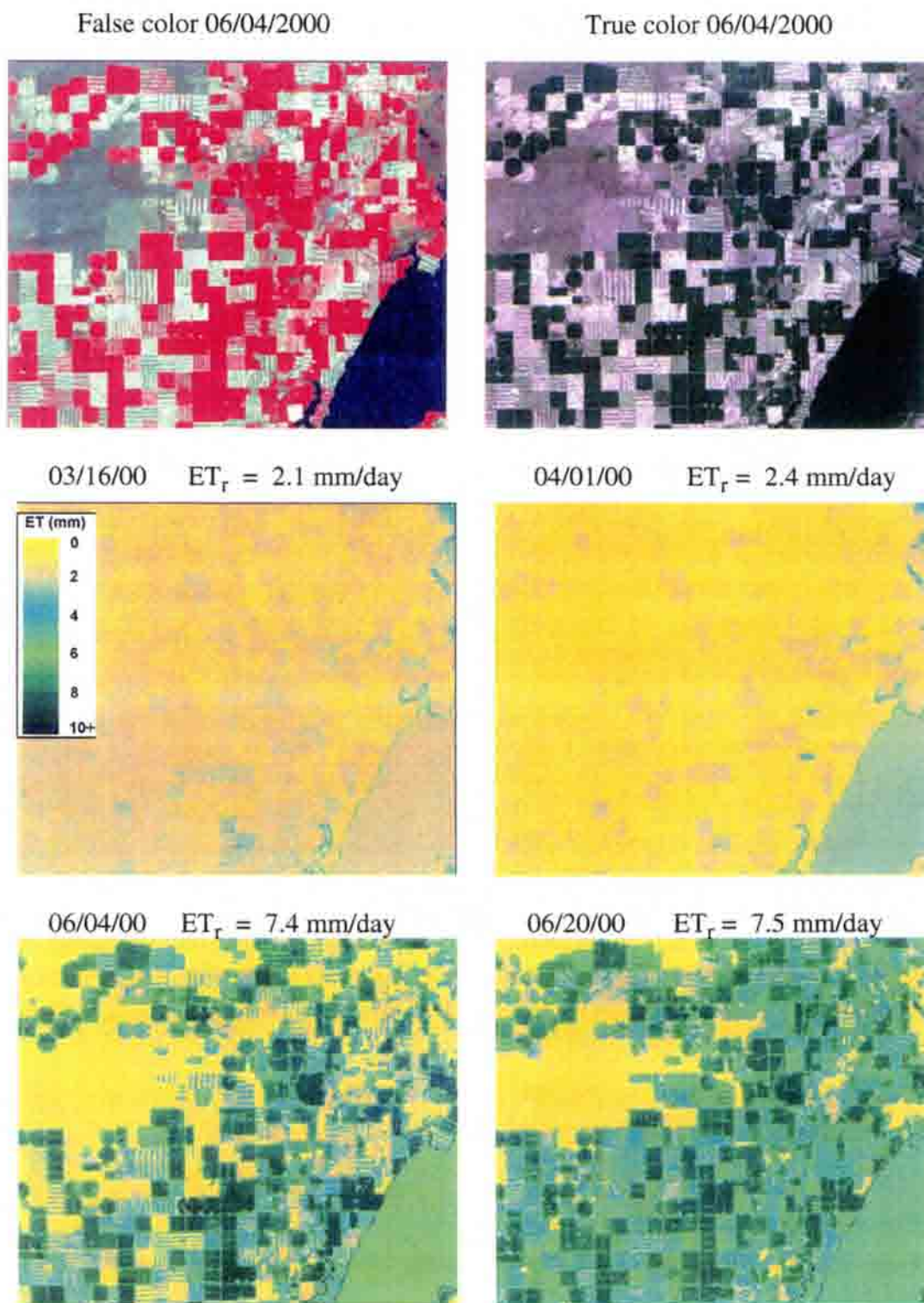
FIGURE 6.30.   ET Images for Aberdeen Area Near American Falls Reservoir. Landsat 7 False Color (up left) and True Color (up right), and Maps of Estimated Daily ET Maps for Different Dates.

07/22/00 ET_r = 8.0 mm/day

08/07/00 ET_r = 9.4 mm/day

08/23/00 ET_r = 6.5 mm/day

09/08/00 ET_r = 8.1 mm/day

09/16/00 ET_r = 6.1 mm/day

10/18/00 ET_r = 2.7 mm/day
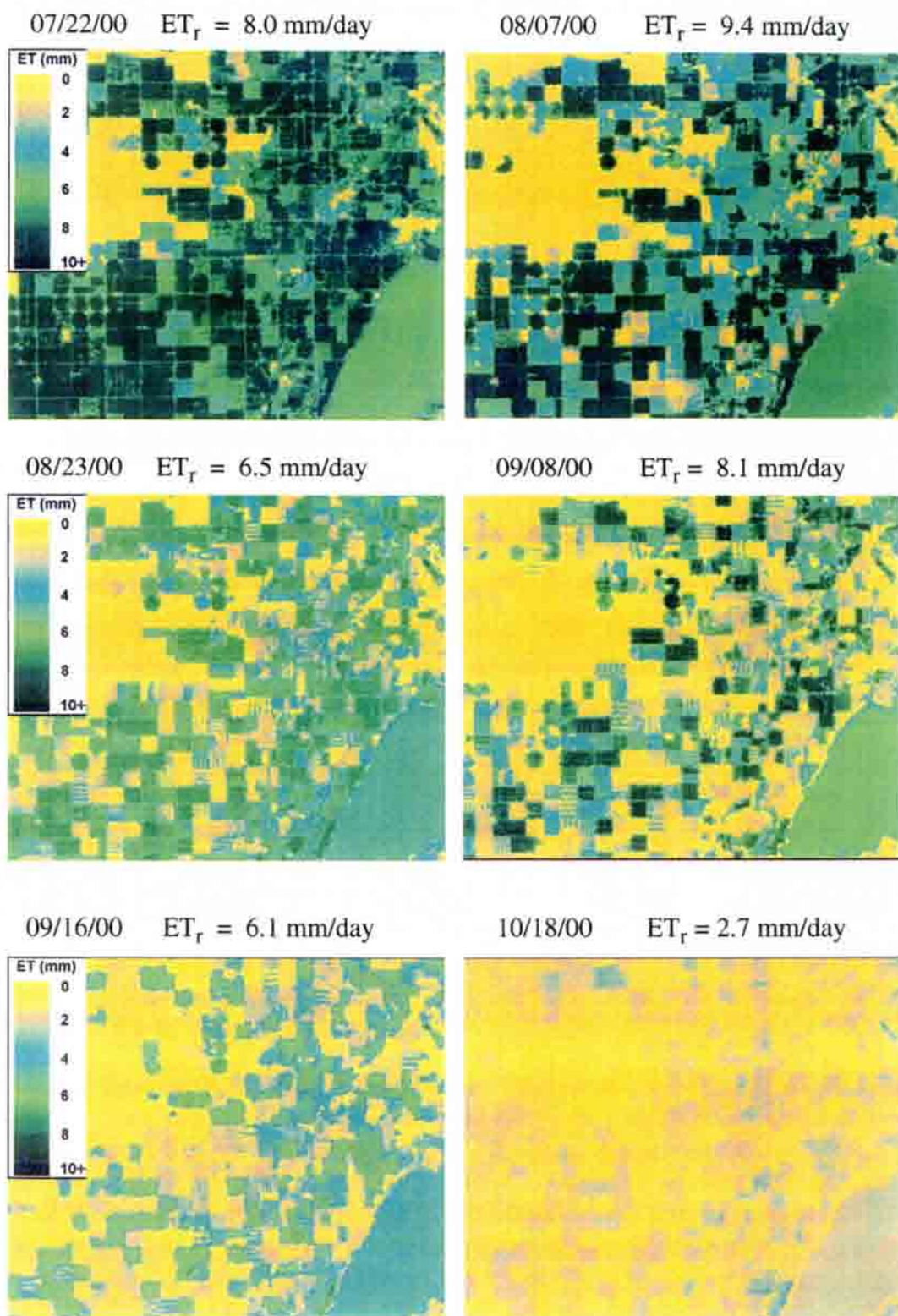
Figure 6.30.   (Cont.) ET images for Aberdeen Area Near American Falls Reservoir.

in midsummer (July-August), decreasing again in October. In addition to the seasonal variation of ET, the daily value of alfalfa reference evapotranspiration ET_r controlled the values of ET for each specific day. The consistency in ET from image to image for some fields (having alfalfa or long season row crop) and fading of others (small grains) is quite noticeable.

The subset image shown in Fig. 6.30 included a total of 387,600 pixels, which translates into a total area of 34,884.00 ha. Table 6.15 presents average ETrF, standard deviation, and total evapotranspiration for each subset image included in Fig. 6.30.

TABLE 6.15. Summary of Statistics for Subset Images Contained in Figure 6.30

Image Date	Mean ETrF	ETrF Standard Deviation	ETr (mm/day)	ET $(m^3 \times 10^3)$
03/16/2000	0.535	0.138	3.2	597.21
06/04/2000	0.507	0.399	7.4	1308.78
06/20/2000	0.61	0.344	7.5	1595.94
07/22/2000	0.705	0.369	8.0	1967.46
08/07/2000	0.526	0.357	9.3	1706.46
08/23/2000	0.533	0.396	6.5	1208.56
09/08/2000	0.368	0.346	8.1	1039.82
09/16/2000	0.359	0.330	6.3	788.97
10/18/2000	0.367	0.310	2.8	358.47

Estimation of ET in Mountainous Areas

The original $SEBAL_B$ model developed by Bastiaanssen (1995) was designed to describe the energy balance for flat areas. In this study, modification of the $SEBAL_B$ algorithms were made to account for variations in elevation and sloping terrain.

Incoming Solar Radiation

Chapter V describes the procedure to account for the variation in incoming solar radiation as function of pixel elevation, slope, and aspect. The incoming net radiation is one of the main components of the net radiation balance at the surface. A map of incoming shortwave radiation radiation ($R_s\downarrow$) for a mountainous area is shown in Fig. 6.31. The values of $R_s\downarrow$ corresponds to satellite overpass time, which in local standard time is around 11:00 am. At this time, south-east oriented slopes receive more incoming solar radiation that south-west slopes and north facing slopes. This feature can be seen in the left portion of Fig. 6.31 where slopes that are facing are brighter (more $R_s\downarrow$) that other surfaces. The Landsat 7 false color for 06/04/2000 is depicted to the right.
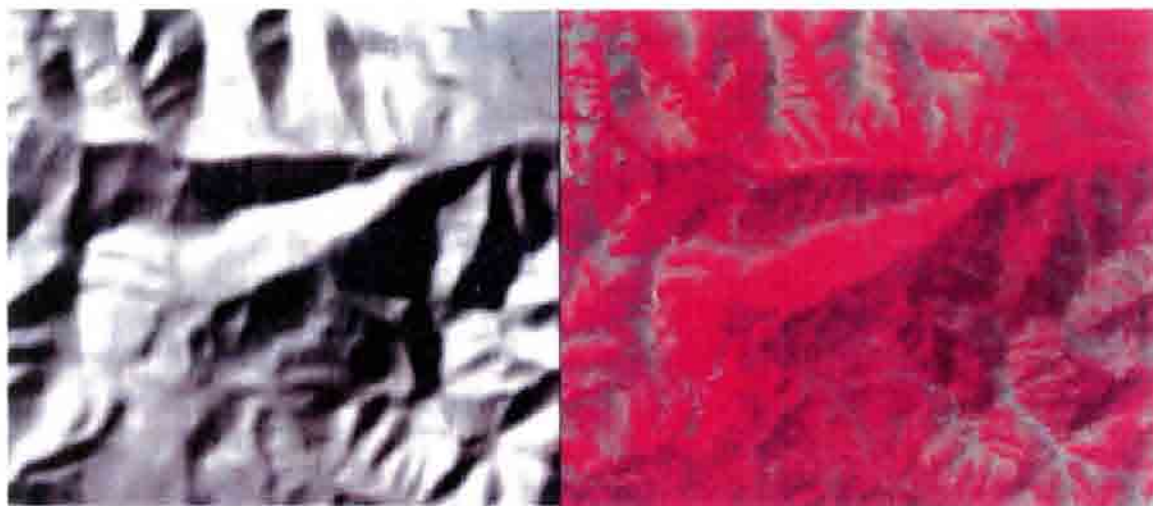
FIGURE 6.31.   A Map of Incoming Solar Radiation (Wm^{-2}) for a Range of Mountains in path 39 (left). The Landsat 7 ETM+ False Color for 06/04/2000 is Depicted to the Right.

Figure 6.32 contains a plot of net radiation values for various pixel aspects corresponding to the 06/04/2000 Landsat 7 scene. In this figure north-aspect corresponds

to 0 degrees, and south-aspect to 180 degrees. The higher values for net radiation occur

on south-east slopes (90 to 180 degrees) where there is a larger value of $R_s\downarrow$ during the

satellite overpass time (around 10:30 to 11:00 am in local time).
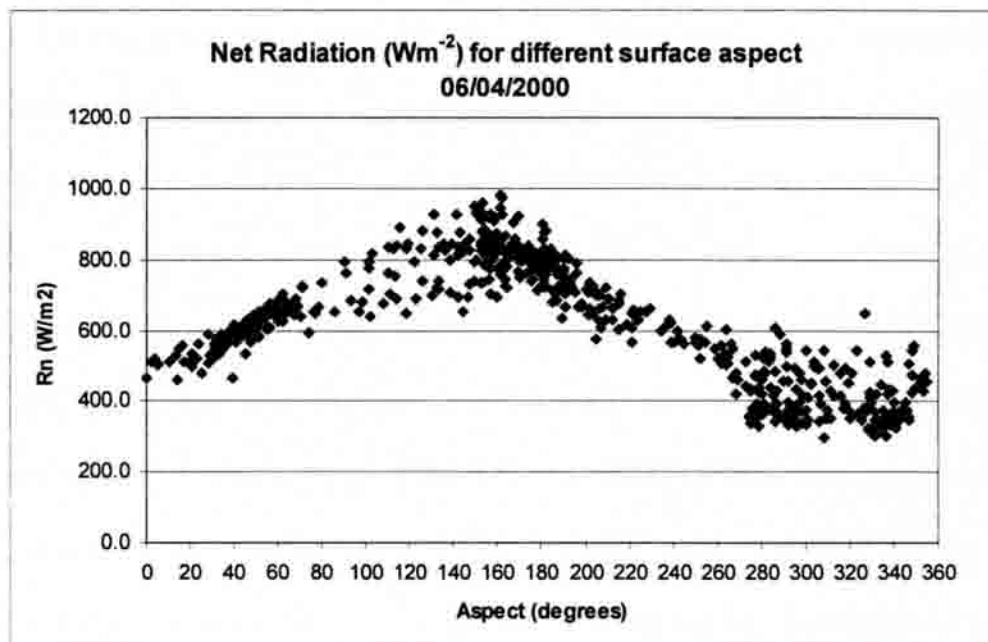
FIGURE 6.32   Instantaneous Values of Net Radiation for Satellite Overpass Time
(around 10:30 to 11:00 am) for the Scene Taken on 06/04/2000.

Adjustment of ETr due to Variation of
Incoming Solar Radiation in Sloping
Terrains

In sloping terrain, the amount of incoming radiation depends strongly on the

orientation of the surface at the moment of the satellite overpass. Fig. 6.32 shows that

south-east aspect surfaces receive more radiation than other surfaces at the time the

Landsat satellite image is taken.

However, the tendency for higher radiation on south-east slopes will not be constant during the day. In the afternoon, for example at 16:00, southeast slopes will receive less radiation than southwest slopes. Therefore, in sloping surfaces, it is obvious that a correction of the value of ETrF, used to compute 24-hour ET, has to be made to account for the variation in incoming solar radiation during the day due to slope and aspect conditions in each pixel. A correction was proposed in Chapter V (Eq. 5.17) to modify the value of the alfalfa reference ET_r in sloping surfaces, that reflects the variation of received $R_s\downarrow$ between a given surface and the weather station location (flat area) from where ETr was calculated, both for the image time and for the 24-hour period.

Figure 6.33 shows a plot of the values of the adjustment coefficient that accounts for incoming solar radiation ($C_{radiation}$) for different surface aspects calculated from the 06/04/2000 image. The shape of the curve is inverse of the one shown in Fig. 6.32, suggesting that the surfaces that receive more instantaneous incoming radiation at the satellite overpass time need a coefficient less than 1 to account for relatively lower fluxes of $R_s\downarrow$ throughout the rest of day. The scatter observed within each aspect interval stems from the different slopes that surfaces have for the same aspect.

Wind Speed and Surface Roughness

In mountainous areas, the surface roughness of pixels was increased to account for any increase of z_{om} caused by the presence of topographic irregularities that modify the transfer of momentum towards the surface. It was presumed that this effect increases in proportion to local slope. A map of z_{om} for different surfaces is shown in Fig. 6.34. The highest values of z_{om} (brighter areas) correspond to mountains.
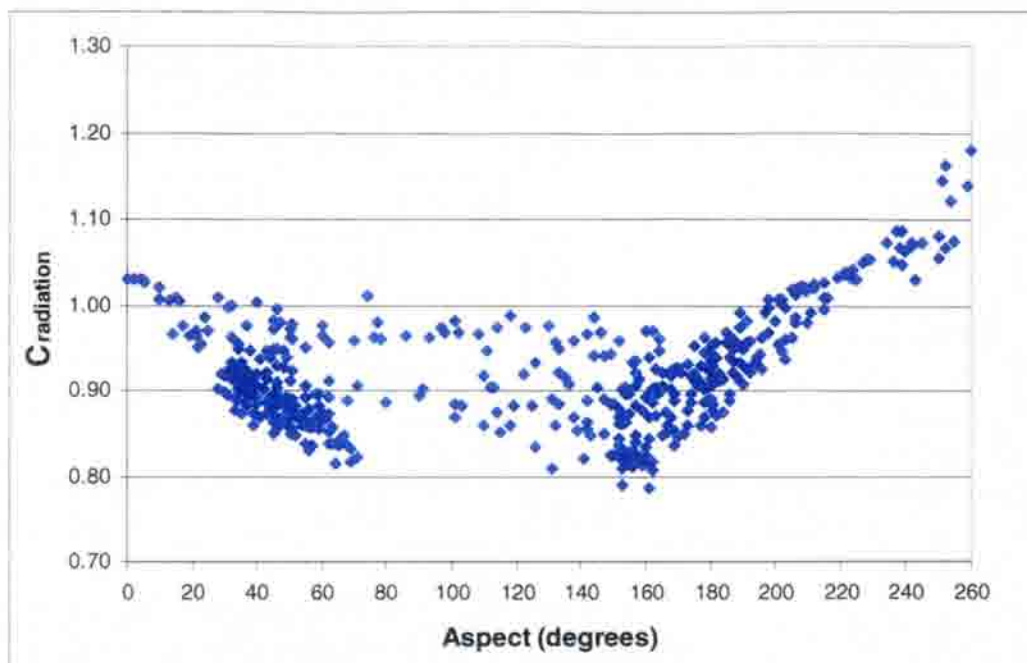
FIGURE 6.33. Variation of the Adjustment Coefficient $C_{radiation}$ for Different Surface Aspects (06/04/2000)
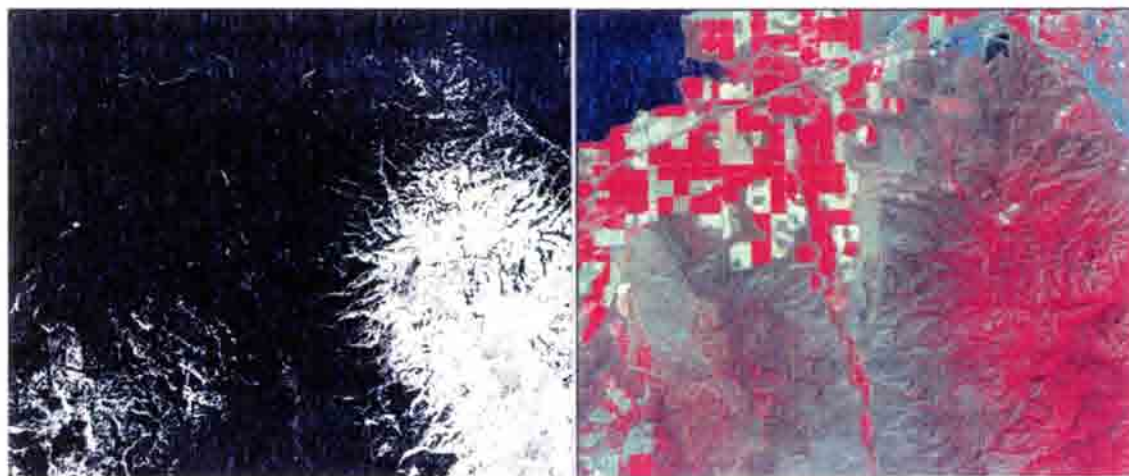
FIGURE 6.34. A Map of Surface Roughness z_{om} (left) for the Scene corresponding to 06/04/2000. The Landsat 7 False Color for the Area SE of American Falls Is Also Shown (right)

Figure 6.35 shows some results of daily ET predicted for mountain areas taken from the scene corresponding to 06/04/2000. The dependence of ET on surface temperature is very strong. The variation of ET at the same surface temperature is due to slope effects on R_n and T_s.
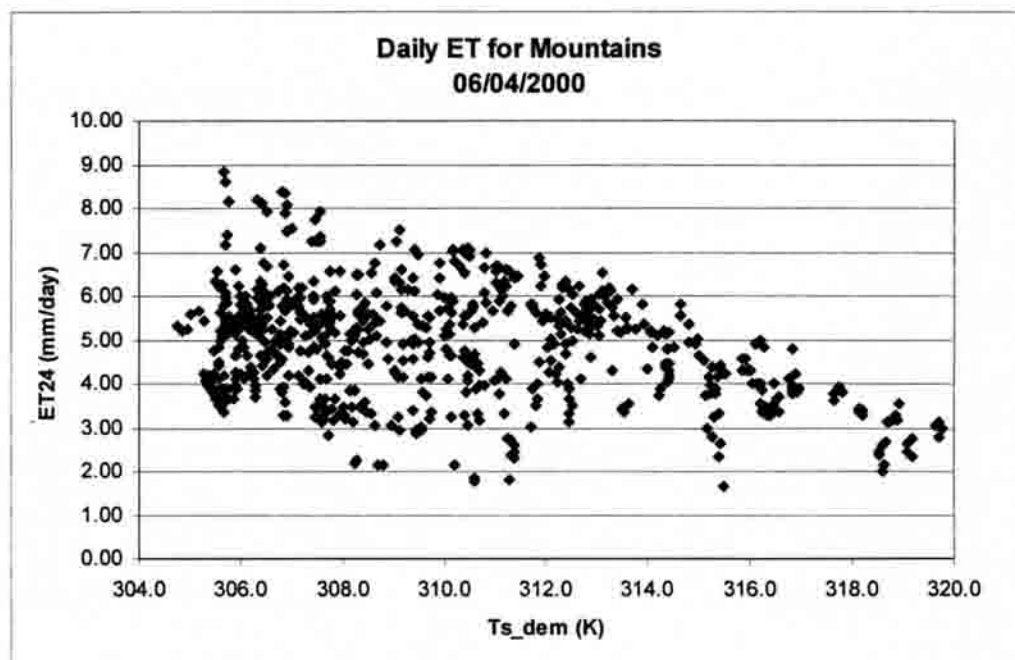
FIGURE 6.35. Values of 24-Hour ET (mm/day) for Forested Mountain Pixels Estimated from the 06/04/2000 Landsat 7 Scene (approximately a 4 Km^2 area centered at UTM 626692, 183478).

Application of SEBAL$_{ID}$ for Water

The estimation of evaporation from open water depends to a great degree on the correct estimation of G for the water body. Because this study focused on the estimation of ET for agricultural fields, G for water, was roughly estimated as $G_{water} = 0.5*R_n$, following findings by Kondo (1994), Amayreh (1995), Yamamoto and Kondo (1968), and Burba et al. (1999) as explained in Chapter IV.

The ratio of G/R_n in water is complicated, and depends on several parameters including turbidity, depth, currents, and season. Values of surface parameters and fluxes are included in Table 6.16 for several samples of water areas (reservoirs) in the region. Samples 1 and 2 located at American Falls reservoir and samples 3 and 4 located at Lake Wake.

TABLE 6.16 Surface Parameters and Fluxes for Samples of Water Pixels Taken from the 06/04/2000 Image

Sample	1	2	3	4
Albedo	0.024	0.022	0.020	0.021
NDVI	-0.15	-0.33	-0.30	-0.30
z_{om} (m)	0.001	0.001	0.001	0.001
T_S (K)	292.2	291.6	292.8	291.4
Rn (Wm^{-2})	823.9	829.2	824.4	826.4
G/Rn	0.5	0.5	0.5	0.5
G (Wm^{-2})	412.0	414.6	412.2	413.2
H (Wm^{-2})	-3.2	-5.3	-0.8	-3.2
ETrF	0.79	0.80	0.79	0.79
ET_{24} (mm/day)	5.9	5.9	5.8	5.9

The low albedo predicted for water (around 0.022) makes water a good absorber of both incoming short wave $(R_s\downarrow)$ and incoming longwave radiation $(R_L\downarrow)$. This tends to make net radiation a large component in the energy balance for water. In the cases shown in Table 6.16, the amount of sensible heat, predicted for water using the dT function is nearly zero, so that almost all net radiation is partitioned into G and LE. Thus, the fixed value of G/Rn = 0.5 used in the study substantially controlled the amount of LE predicted from open water.

Due to the uncertain prediction of G/R_n in this study, the results of ET for water are questionable, even though they appear to be reasonable values. More research needs to be done on this issue to help $SEBAL_{ID}$ predict accurate values of evaporation of water in the study area.

Estimation of ET in Desert Areas

In Southern Idaho, desert areas are characterized predominantly by two types of vegetation: sage brush and desert grass. In many areas only one of these vegetation types is predominant, but a combination of both is also commonly encountered.

Photos of desert vegetation are shown in Fig. 6.36.

FIGURE 6.36   Typical Desert Vegetation in the Study Area: Sage Brush and Grass
Mixture (left) and Closeup of Grassland (right).

In most of the images processed in 1989 and 2000, the radiometric surface temperature of desert areas was consistently higher than for dry bare soil surfaces in agricultural environments. Because in this study, hot pixels were taken from agricultural bare soil pixels in order to insure good estimates of dT for the range of agricultural conditions, the surface temperature (T_s) of desert pixels was often greater than the T_s of the hot pixel. Because in $SEBAL_{ID}$, the hot pixel is considered to have zero ET, this

often forced the estimated ET in desert areas to be negative, depending on R_n, G, and surface roughness.

Table 6.17 shows results obtained from the 06/20/2000 Landsat 7 scene. This table includes surface parameters and fluxes corresponding to the cold and hot pixels selected for the image, and a representative sage brush sample and a desert grass sample.

TABLE 6.17.   Surface Parameters and Fluxes for Several Desert Samples on 06/20/2000

Sample	Cold Pixel	Hot Pixel	Sage Brush	Grass
Albedo	0.18	0.25	0.18	0.22
LAI (m^2/m^2)	6.0	0	0.1	0.1
NDVI	0.86	0.1	0.2	0.18
z_{om} (m)	0.108	0.005	0.1	0.02
T_s (K)	293.5	317.6	318.9	321.0
Rn (Wm^{-2})	666.6	449.1	510.5	455.2
G/Rn	0.045	0.248	0.223	0.254
G (Wm^{-2})	30	111	114	116
H (Wm^{-2})	142.6	337.9	457.8	414.9
ETrF	1.05	0	-0.133	- 0.165
ET_{24} (mm/day)	7.9	0	- 1.0	-1.2

Table 6.17 shows that the surface temperature of the sage brush sample (T_s = 318.9 K), and the grass sample (321.0 K) are greater than the temperature for the hot pixel (317.6 K). The final daily evapotranspiration for the hot pixel was 0 mm/day (which is the main assumption of SEBAL$_{ID}$ for a dry hot pixel), and the corresponding ET_{24} was -1.0 and - 1.2 mm/day for the sage brush and grass sample respectively. These negative ET_{24} values are obviously erroneous. If one considers the satellite overpass time (around 11:00 am) and the season of the year (mid-summer), one should

expect ET values from desert areas to be zero or slightly positive, since essentially no rain occurs during May-September in Southern Idaho.

One possible explanation for this problem is that hot pixel was wrongly selected. In fact, one can argue that the hot pixel should have been taken in sage brush or desert grass to predict zero ET in those areas. However, this possibility was explored when processing the 2000 images, but the consistent higher temperature at the desert produced overestimation of ET for dry bare soil pixels.

An explanation for the higher T_s in desert includes uncertainty in prediction of G for desert and impacts of aerodynamic transfer of heat from sparse dry canopies. If the dT vs T_s relationship is in fact valid, then other possible explanations can be made. First, the estimation of G using Eq. 3.25) was developed for bare soil and relatively well watered vegetated surfaces, so that it can fail to predict the correct value of soil heat flux in the sparse-vegetated conditions of the desert areas of Southern Idaho. Under desert conditions, the soil structure tends to be more porous and dry, so that G may be smaller than predicted.

Also there is uncertainty involved in the value to use for surface roughness assumed for desert vegetation The sparse canopies represent a type of "two source" heat system (canopy + soil) that have differences in the source/sink elevations for momentum and heat. In sage brush, most momentum transfer is from the canopy, with the underlying soil relatively "protected." This causes the vegetation temperature to be lower than that of the soil. Therefore the true dT to use for sage brush or desert grass may be lower than the predicted. Because the satellite at nearly NADIR sees mostly soil, the T_s for the vegetation is overpredicted.

This problem is commonly solved by considering a two source model, which distinguishes the contributions from vegetation and soil. However, this requires distinguishing between T_s for vegetation and soil and determination of internal transfer coefficients, which is difficult to do from only Landsat information. SEBAL$_{ID}$ is basically a single-layer model so that it fails to predict accurately fluxes in conditions of sparse, arid vegetation.

To calculate the true value of sensible heat for a given pixel, the contributions of H from soil and vegetation would need to be averaged according to the specific area of soil and vegetation present in the pixel. Therefore, $H_{pixel} = area_{veg}*H_{veg} + area_{soil} * H_{soil}$. This assumes that surface fluxes scaled linearly. However, this does not account for convective and radiative transfers between soil and vegetation, plus the variables and parameters that govern the sensible heat flux (temperature and aerodynamic resistance) do not scale linearly. This means that, even if one used a weighted average of surface radiometric temperature (obtained from thermal band) and aerodynamic resistance (that includes z_{om}) for vegetation and soil , the actual value of H would be incorrect.

In conclusion, it seems that the relationship between surface temperature and dT developed for agricultural areas seems can not be extrapolated to desert areas. Desert areas need more concentrated study and flux measurements.

Application of SEBAL$_{ID}$ in Basalt Areas

In this study area, there are a significant areas covered by basalt rock that originated from volcanic activity. Two of this areas are portrayed in Fig. 6.37. One of them is part of the famous "Craters of the Moon" National Park in Idaho.

FIGURE 6.37   Photo of Basalt Rock Areas. False Color Landsat 7 ETM+ Image (left)
                showing Two Basalt Rock Areas, where "1" is the Crater of the Moon
                National Park. Photo of Area 1 (right).

In open basalt areas, surface temperature was consistently lower than surface

temperatures of the hot pixel. This feature confused $SEBAL_{ID}$ and overestimation of

ET occurred.   This is due to higher, but more variable G for basalt.

In Table 6.18, surface parameters and fluxes estimated from three samples of

basalt are compared to the hot pixel characteristics for 08/23/2000. This date was

selected for the analysis because it was the day when T_s at the hot pixel and basalt area

was nearly similar. In addition, on this date (that corresponds to mid-summer), ET from

basalt areas can be considered to be zero. Table 6.18 shows that the temperature of the

basalt sample number 1 (T_s = 317.4 K) and 2 (T_s=316.9 K) are lower than for the hot

pixel (T_{hot} = 318.2 K).

In basalt sample 3 the surface temperature was higher than for the hot pixel

(T_s=319.0). However in all cases, the latent heat flux, expressed as ET (mm/day) was

significant : 2.5 (sample 2 with lower temperature and lower albedo), 2.1 (sample 1), and

1.1mm/day (sample 3, with the highest temperature).

TABLE 6.18.   Surface Parameters and Fluxes for Hot Pixel and Basalt Pixels for
08/23/2000

Sample	Hot Pixel	Basalt 1	Basalt 2	Basalt 3
Albedo	0.3	0.11	0.10	0.14
T_S (K)	318.2	317.4	316.9	319.0
R_n (Wm^{-2})	373.3	538.3	552.6	501.0
G/R_n	0.26	0.193	0.186	0.211
G (Wm^{-2})	99	104	103	105
H (Wm^{-2})	274.31	276.2	263.1	314.2
ETrF	0	0	0.386	0.169
ET_{24} (mm/day)	0	2.1	2.5	1.10

Because during the middle of summer, evaporation occurring from basalt areas is
expected to be zero or negligible, it can be concluded that some assumptions of the
remote sensing algorithm produce overestimation of the latent heat flux for basalt.

As can be seen in Table 6.18 (and shown in Fig. 6.37) the dark color of basalt
rock results in a low value of predicted albedo, which might be taken as realistic. This
low albedo produces a high value for net radiation (net radiation in the hot pixel is 373.3,
whereas in basalt sample 1 is 538 Wm^{-2}). Predicted soil heat flux is similar among the
hot pixel and the basalt samples. Thus, a significant amount of "extra" available energy
is predicted to be present at the basalt samples, and because H is a strong function of the
surface temperature (which defines dT), some unexplained energy is left to latent heat,
when in reality it should be zero.

A obvious explanation of this behavior is that Eq. (3.25) does not apply in the
basalt rock so that G is significantly underestimated. In Fig. 6.38 a graph of residual G
for the basalt (calculated as R_n – H, assuming LE = 0) is plotted versus surface
temperature. There is a strong linear relationship between the ratio of $(R_n - H)/R_n$
versus T_s. However this linear relationship was found to vary with image date, so that a

unique function between G/R_n function of temperature could not be developed in this study. In addition, because the development of the residual-based G/R_n versus T_s function required the assumption that LE = 0, it was decided to be superfluous to develop the function only to predict the starting LE=0.
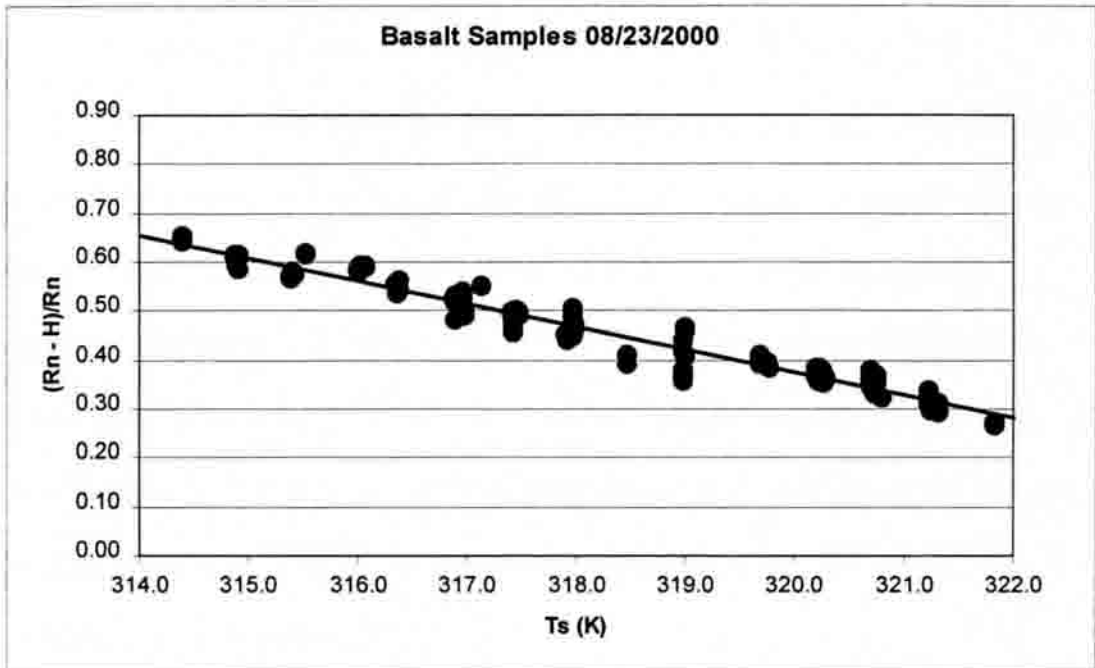
FIGURE 6.38   Linear Relationship between (Rn-H)/Rn versus Surface Temperature, calculated from Basalt Rock Samples on 08/23/2000.

Another possible explanation of the overestimation of ET from basalt, is based on uncertainties of the assigned value for surface roughness for basalt. The roughness of basalt rock is highly variable, depending on the flow rate, initial temperature, and cooling rate during formation.

Finally, the validity of the linear relationship between T_s vs dT (that was developed in an agricultural areas) for basalt surfaces needs to be further explored.

Sensitivity of SEBAL$_{ID}$ to Surface Temperature

Energy balance calculations in SEBAL$_{ID}$ make use of radiometric surface temperature in nearly every component of the surface energy balance. Net radiation calculations use T_s to compute outgoing and incoming longwave radiation, and later the ratio G/R_n uses surface temperature if Eq. 3.25 is applied. Finally the computation of sensible heat requires the definition of a T_s vs dT linear relationship (Eq.3.33).

This dependence of SEBAL$_{ID}$ on radiometric surface temperature indicates that the model needs a really accurate estimation of T_s. This argues for the need to correct radiometric surface temperature measurements taken by satellite for atmospheric interactions. Fortunately, the use in SEBAL$_{ID}$ of two indicator pixels (cold and hot pixels), that define the sensible heat for two extreme conditions of the dT functions, makes SEBAL$_{ID}$, in fact, not very sensitive to the use of corrected radiometric surface temperatures. This is because the specification of H on these two pixels incorporates biases present in the T_s layer.

In Fig. 6.39, estimated values for 24 hour ET using corrected radiometric surface temperature are compared with estimated 24 hour ET using uncorrected (apparent) surface temperature, for agricultural pixels. Corrected surface temperatures where determined with Eq 4.16 using MODTRAN (version 3), with radiosondes from Boise, Idaho, to retrieve narrowband longwave transmittance and path thermal radiance.

On the basis of Fig. 6.39, it is concluded that the way SEBAL$_{ID}$ defines the sensible heat flux at the cold and hot pixels, substantially offsets the biases introduced by
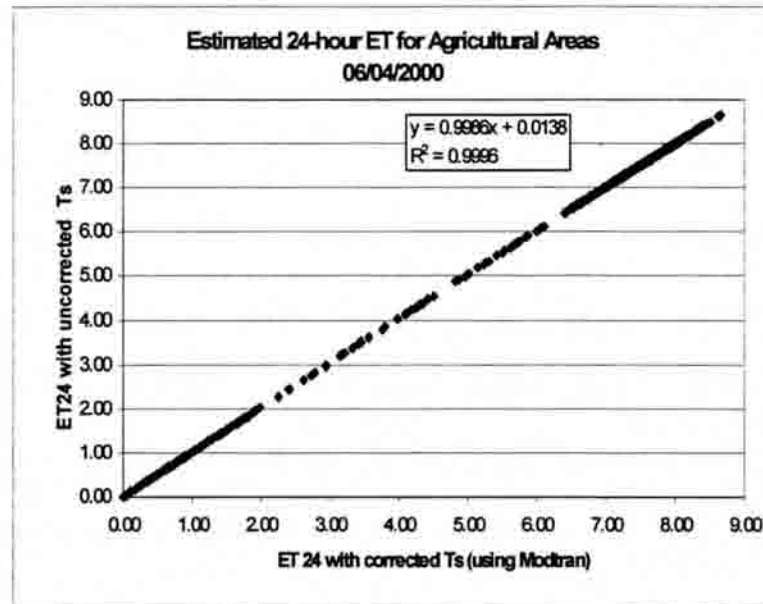
FIGURE 6.39.   Plot of Estimated 24 Hours ET Using Corrected and Uncorrected
Surface Temperature for the 06/04/2000 Image.

using uncorrected surface temperatures. The slope and intercept of the plot of estimated

ET, with and without corrections of T_s, shows that the use of thermally corrected

surface temperatures is not a strong requirement in SEBAL$_{ID}$. This is an extremely

valuable attribute of SEBAL$_{ID}$ and illustrates the importance and value of specifying

energy components at known pixels (cold and hot pixels).

A comparison is made between the components of the energy balance for the hot

and cold pixel, with and without correction of T_s, in Table 6.19. By correcting thermal

radiance for atmospheric effects, radiometric surface temperatures become larger,

especially for the hottest pixels. For example, for the cold pixel, the corrected surface

temperature is 1.6 K greater than the uncorrected surface temperature. In the hot pixel,

the corrected T_s is 3.4 K greater. The greater surface temperatures caused a decrease in

net radiation (outgoing longwave radiation became larger), and a slight increase occurred

in soil heat flux (G increased with T_s according to Eq. 3.25), which made the available energy smaller in both cold and hot pixels with T_s correction. Because the value of LE is predefined at the cold and hot pixel, this made predicted H smaller at the cold and hot pixels. Therefore, the whole energy balance was forced to reach a new equilibrium for the greater values of surface temperature, but the fact that LE was kept constant in both cold and hot pixels, controlled the values for sensible heat H and dT so that a compensation process occurs. Because the behavior of all other pixels in an image are similar, the compensation in the dT vs T_s function applies to them also.

TABLE 6.19.   Comparison Between the Hot and Cold Pixels for the 06/04/2000 Scene

	Cold Pixel		Hot Pixel	
	Using Ts (uncorrected)	Using Ts (corrected)	Using Ts (uncorrected)	Using Ts (corrected)
Surface Temperature (K)	296.3	297.9	314.0	317.4
dT (K)	1.2	1.1	5.9	5.7
R_n (Wm^{-2})	647.9	645.6	446.9	431.5
G (Wm^{-2})	38.5	41.2	105.4	110.3
$R_n - G$ (Wm^{-2})	609.4	604.4	341.5	321.2
H (Wm^{-2})	58.7	54.5	341.5	321.2
LE (Wm^{-2})	550.7	549.9	0	0
R_{ah} (s/m)	20.9	21.2	16.6	19.9
ET24 (mm/day)	7.45	7.45	0	0

Figure 6.39 shows a plot of the absolute differences between estimated daily ET using uncorrected and corrected radiometric surface temperatures for a wide range of pixels from the 06/04/2000 image. Differences tend to be smaller around cold and hot pixels, because of similarity of these pixels when LE is fixed in both cases. Thus, fixed values of latent heat in the hot and cold pixels control the presence of outliers in the two

extremes of the energy balance. Differences are larger around values of ETrF = 0.5, which are halfway between the cold (ETrF=1.05) and hot pixels (ETrF = 0). This is expected because it is near ETrF = 0.5 that pixels characteristics will be more different from either anchor pixel. However, maximum differences are very small, and certainly smaller than errors introduced by uncertainties in estimation of some other components of the energy balance.
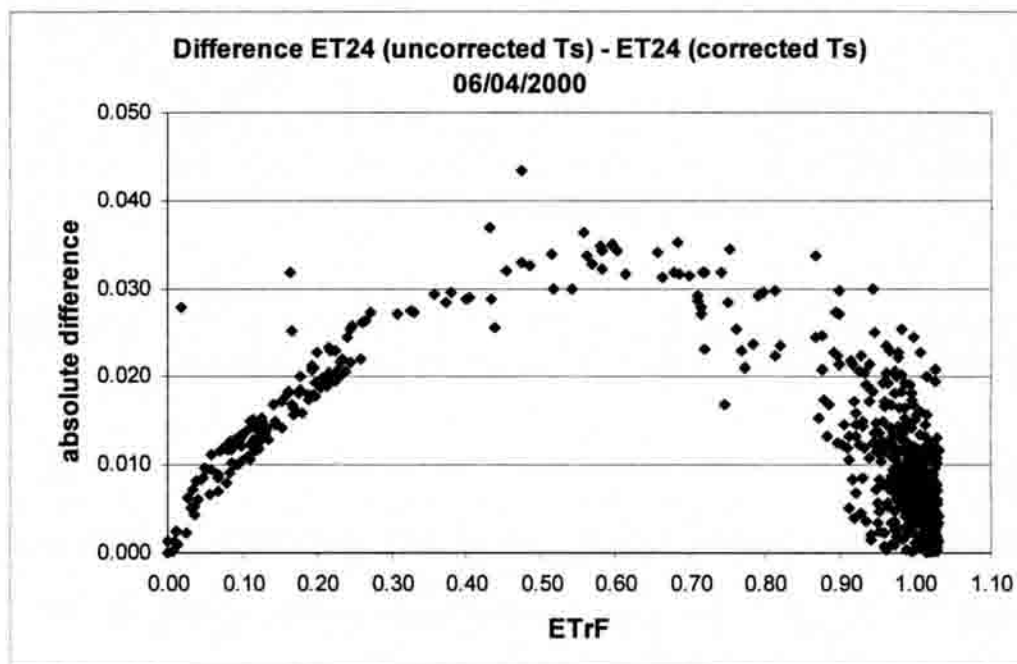
FIGURE 6.40.   Absolute Difference (in mm) Between Estimated ET Using Corrected and Uncorrected Surface Temperatures.

Figure 6.41 shows a plot of estimated ET using corrected and apparent surface temperature considering several surfaces: agricultural fields, water, basalt, desert, and cities , showing that results are still very similar and errors are not significant.
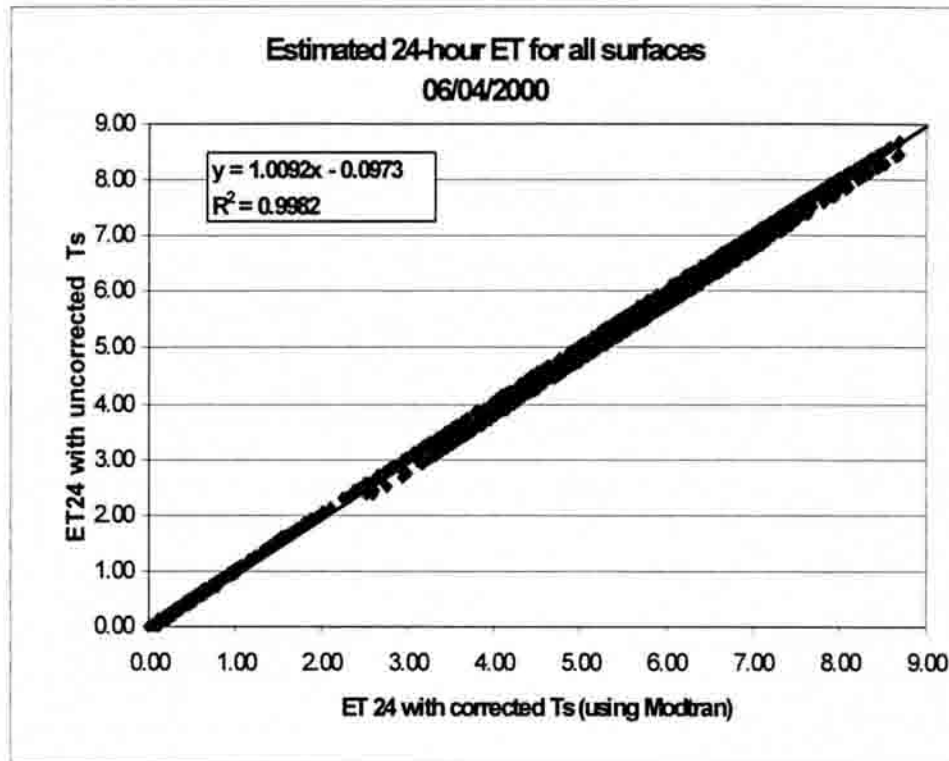
FIGURE 6.41.   Plot of Estimated 24 Hour ET using Corrected and Uncorrected
Surface Temperatures for Several Surfaces for the 06/04/2000 Image.

The fact that latent heat fluxes are fixed at the "anchor" pixels makes SEBAL$_{ID}$ a

very unique and robust remote sensing approach for determining ET as a residual of the

energy balance. Most other current methods that estimates $ET = R_n - G - H$ translate

any, if not, all the residual errors of the estimation of R_n, G, and H into ET. In

SEBAL$_{ID}$ much of the error and biases in the estimation of R_n and G is really translated

into the estimate for H, so that latent heat flux estimates are more substantially controlled

by the relative value of LE fixed at the cold and hot pixels which represent the two

extreme points in the surface energy balance.

Sensitivity of SEBAL$_{ID}$ to Atmospheric
Correction for Shortwave Radiances

Sensitivity of SEBAL for the use of atmospheric corrected radiances for the

shortwave bands was investigated by Tasumi (in preparation). The author found that,

even though the surface albedo values were different, these differences did not impact

substantially the final estimation of ET. In Fig. 6.42 a comparison between SEBAL

estimates of ET using albedo calculated from Eq (3.16) and SEBAL estimates of ET

using atmospheric corrected reflectances (using MODTRAN) is displayed.
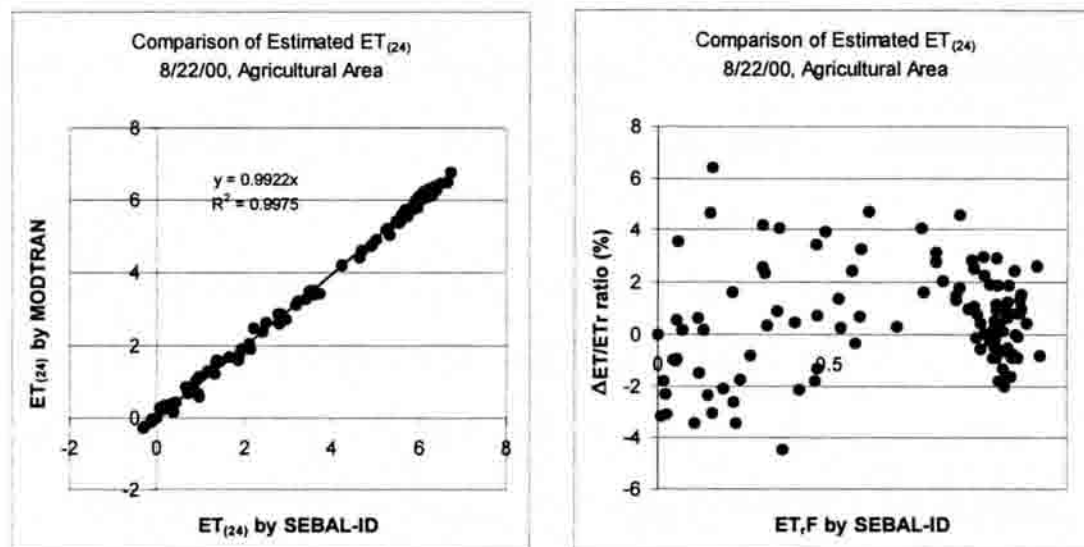
FIGURE 6.42.   Comparison of SEBAL ET Estimates using Albedo from Eq. (3.16)
and using Corrected Reflectances (Tasumi, in preparation).

As can be seen in Fig. 6.42, the normalized differences between estimates of ET

in agricultural areas are not significant, with a maximum of 4 % of the total ET$_r$. The

conclusion here is that the definition of ET at the hot and cold pixel is controlling part of

the biases and errors introduced for the application of Eq. (3.16) which considers a

broadband transmittance for shortwave radiation.

Application of the FAO-56 Soil Water Balance Model to Predict ET Between Images

The FAO-56 water balance model (Allen et al., 1998) to predict evaporation from bare soil conditions was explored as a way to describe the temporal variation of ETrF between satellite imagines. This water balance model is fully described in Appendix I.

To illustrate any advantage of using a daily soil water balance in extrapolation of ETrF, the FAO-56 soil water balance model was applied in SEBAL$_{ID}$ to describe the temporal variation of ETrF during the period between the 05/04/1989 and 05/20/1989 images. This period was selected because there was no irrigation occurring in the lysimeter 2 field, and an important amount of precipitation occurred between these two image dates. Information about precipitation, and alfalfa reference evapotranspiration is included in Table 6.20.

With regard to the soil characteristics needed to apply the FAO-56 soil water balance model, values of TEW = 35mm and REW = 9 mm were used for the top 0.15 m of soil, considering that the soil at the lysimeter 2 field is a Portneuf silt loam soil (Wright, 2002, personal communication). The lysimeter 2 field was selected because it represented an essentially bare soil surface condition.

Estimation of initial depletion for 05/04/89 The initial moisture content (or depletion) of the surface soil layer (0.15 m) was unknown for lysimeter 2 field on 05/04/89, therefore it had to be predicted as a starting condition for the model.

A plot of LAI versus ETrF was made using the results obtained from SEBAL$_{ID}$ for the 05/04/89 processed image. This plot is shown in Fig. 6.43.

TABLE 6.20.   Precipitation and ET_r Values for the Period 05/04 to 05/20/89

Date	Precip(mm)	ETr (mm/day)
05/04/89		7.8
05/05/89		5.5
05/06/89		7.7
05/07/89		4.7
05/08/89		6.0
05/09/89		7.9
05/10/89	2.0	5.7
05/11/89		5.9
05/12/89	3.3	2.0
05/13/89		3.6
05/14/89	0.8	5.2
05/15/89	12.2	1.2
05/16/89		7.1
05/17/89		7.1
05/18/89		4.6
05/19/89		6.2
05/20/89		7.3

From Fig. 6.43, a curve joining the points of minimum ETrF for each LAI range

was drawn. This curve is interpreted to represent the value of $ETrF_{basal}$ expected for each

value of LAI. Theoretically, points that are below the curve are presumed to be

moisture-stressed crops and points above the curve are presumed to have some degree of

soil surface wetness that increases the ETrF above the basal value. The placement of the

"basal" curve was somewhat arbitrary and was based on the judgment of the writer.

It is expected that ETrF approaches 1 (i.e., at least 0.97 as shown in Fig. 6.43)

when LAI exceeds 3 (Wright, 1982). Therefore the basal curve was forced to 0.97 when

LAI ≥ 3.
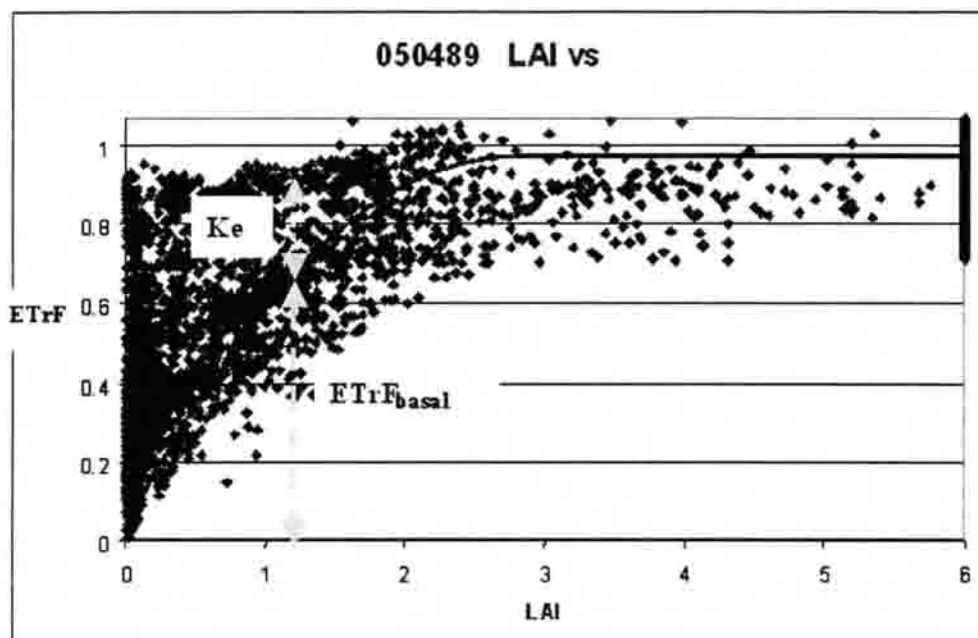
FIGURE 6.43.   Definition of the ETrF Basal Curve for the 05/04/89 Scene. The Points Came from Pixels from SEBAL$_{ID}$ Processed Image.

It is expected that ETrF approaches 1 (i.e., at least 0.97 as shown in Fig. 6.43) when LAI exceeds 3 (Wright, 1982). Therefore the basal curve was forced to 0.97 when LAI $\geq$ 3.

A polynomial equation was adapted to describe the variation of the ETrF$_{basal}$ curve with respect to LAI for the 05/04/89 image. The function is as follows:

$$\text{ETrF}_{basal} = 0.6632*\text{LAI} - 0.1188*\text{LAI}^2 + 0.045 \quad \text{for LAI} < 3 \quad (6.3)$$

$$\text{ETrF}_{basal} = 0.97 \quad \text{for LAI} > 3 \quad (6.4)$$

Eqs (6.3) and (6.4) are only valid for the date (05/04/89) and satellite overpass time. On this date, winter wheat would likely be the only crop with a LAI $\geq$3.

On 05/04/89, the value for LAI predicted by SEBAL for the lysimeter 2 field (averaged from 4 pixels) was 0.035. From this value, Eq. 6.3 predicts a value of $ETrF_{basal} = 0.068$. Considering that the value of ETrF calculated from SEBAL for the lysimeter on 05/04/89 was 0.66, it means that the value of the evaporation coefficient $K_e = 0.66 - 0.068 = 0.59$. The corresponding value of K_r calculated from Eq. I.10 (Appendix I) is 0.602. Finally, Eq. I.11 (Appendix I) predicts an initial depletion of the soil available moisture in the field of $D_e = 19.4$ mm.

Table 6.21 shows the predicted variation of ETrF during the period between the two Landsat images. Precipitation was considered to happen late in the day, so that the increment of ETrF due to precipitation is observed on the following date.

TABLE 6.21. Average Results from Lysimeter 2 Field (4 pixels) after Applying the FAO-56 Soil Water Balance

Date	ET_r (mm/day)	P (mm)	ETrF Basal[1]	D_e (mm)	K_e	ETrF	ET (mm)
05/04/89	7.8		0.070	19.35	0.59	0.66	5.1
05/05/89	5.5		0.071	25.10	0.37	0.44	2.4
05/06/89	7.7		0.073	27.65	0.28	0.35	2.7
05/07/89	4.7		0.074	30.31	0.18	0.25	1.2
05/08/89	6.0		0.075	31.34	0.14	0.21	1.3
05/09/89	7.9		0.077	32.37	0.10	0.18	1.4
05/10/89	5.7	2.0	0.078	33.35	0.06	0.14	0.8
05/11/89	5.9		0.079	31.67	0.12	0.20	1.2
05/12/89	2.0	3.3	0.081	32.41	0.10	0.18	0.4
05/13/89	3.6		0.082	29.30	0.21	0.29	1.1
05/14/89	5.2	0.8	0.083	30.08	0.18	0.27	1.4
05/15/89	1.2	12.2	0.085	30.28	0.18	0.26	0.3
05/16/89	7.1		0.086	18.29	0.62	0.71	5.0
05/17/89	7.1		0.087	22.76	0.45	0.54	3.8
05/18/89	4.6		0.089	25.99	0.33	0.42	1.9
05/19/89	6.2		0.090	27.54	0.28	0.37	2.3
05/20/89	7.3		0.090	29.27	0.21	0.30	2.2

(1) interpolated between 5/4/89 and 5/20/89

Table 6.22 shows a comparison between the measured ET (lysimeter 2), estimated SEBAL ET (using constant ETrF method), and estimated $SEBAL_{ID}$-ET using the water balance model. On the basis of the results shown in Table 6.21, both methods (constant ETrF, and variable ETrF with soil water balance model) produced similar results. Therefore, in this period, a cancellation process occurred that was in the favor of the constant ETrF method that provided good results.

The daily values of ET measured at the lysimeter and ET estimated by $SEBAL_{ID}$ using the soil water balance model are quite different because of the difference in initial ETrF. The Lysimeter 2 measured ETrF for 05/04/89 was 0.88 and the SEBAL estimated ETrF for that date was 0.66. The problem on this date was that lysimeter 2 field was irrigated 2 days before the image date (05/04/89) whereas lysimeter 2 was irrigated just on day before. This means that at the lysimeter there was more evaporation that the amount predicted by $SEBAL_{ID}$ from information retrieved from the lysimeter field. However at the end, both lysimeter ET and estimates of SEBAL had similar total ET during the period.

However, similar results cannot always be expected. For example, in the case of a bare soil that was dry during the time of the two satellite images, the value of ETrF for both images would be zero, even though a precipitation event between the two images could happen. In this case, the soil water balance model presented in Appendix I would be able to estimate a more realistic value of evapotranspiration.

In conclusion, the adaptation of the FAO-56 soil water balance model presented in Appendix I may be useful to track the variation of ETrF due to the occurrence of precipitation between images.

TABLE 6.22 . Comparison between Measured ET and Estimated SEBAL ET for Sugar Beets in 1989

Date	ETr (mm/day)	Measured ET[2]		SEBAL ETrF[3]	SEBAL ET[4] (mm)	SEBAL ETrF[5]	SEBAL-ET[6] (mm)
05/04/89[1]	7.8	6.6		0.66	5.1	0.66	5.1
05/05/89	5.5	3.5		0.66	3.6	0.44	2.4
05/06/89	7.7	2.1		0.66	5.1	0.35	2.7
05/07/89	4.7	1.4		0.66	3.1	0.25	1.2
05/08/89	6.0	1.6		0.66	4.0	0.21	1.3
05/09/89	7.9	1.3		0.66	5.2	0.18	1.4
05/10/89	5.7	1.9		0.66	3.8	0.14	0.8
05/11/89	5.9	1.7		0.66	3.9	0.20	1.2
05/12/89	2.0	0.8		0.15	0.3	0.18	0.4
05/13/89	3.6	1.6		0.15	0.5	0.29	1.1
05/14/89	5.2	1.2		0.15	0.8	0.27	1.4
05/15/89	1.2	1.0		0.15	0.2	0.26	0.3
05/16/89	7.1	4.6		0.15	1.1	0.71	5.0
05/17/89	7.1	2.4		0.15	1.1	0.54	3.8
05/18/89	4.6	1.5		0.15	0.7	0.42	1.9
05/19/89	6.2	1.4		0.15	0.9	0.37	2.3
05/20/89[1]	7.3	1.4		0.15	1.1	(0.15)[7]	2.2
Totals		35.9			40.4		33.4

(1) satellite images
(2) measured ET for sugar beets by Dr. J.L. Wright
(3) Sebal ETrF assuming constant ETrF around images: 0.66 (from 05/04/89 image), and 0.15 (from 05/20/89 image)
(4) Sebal ET using ETrF constant ETrF values
(5) Sebal ETrF values calculated from water balance model. The first and the last one corresponds to satellite processed image.
(6) Sebal ET using ETrF values calculated from soil water balance
(7) Value of ETrF estimate from processed image.

This methodology can be very valuable to assist SEBAL in the prediction of ET from nonirrigated areas as rangeland or bare soils. Because of the extremely large number of fields in a Landsat image, it is impossible to account for and track irrigation events.

CHAPTER VII

SUMMARY, CONCLUSIONS, AND RECOMMENDATIONS

Summary

The overall intent of this research was to improve means for generating ET maps

for the Eastern Plain Aquifer region in Southern Idaho, an area that has more than

7,000 square km of irrigated farmland. An operational remote sensing model is desired

for routine application by the Idaho Department of Water Resources (IDWR) as a means

for predicting ET over large areas, modeling ground water, solving water rights disputes,

and performing a better management of the water resources of the region.

The Surface Energy Balance Algorithm for Land (SEBAL) was selected as the

basis to develop a model that can be adapted to the prevailing conditions of the study

area. Several modifications of the original SEBAL where made to improve prediction

of some components of the surface energy balance and to adapt the model to the climate

and terrain of an arid region. The main modification was the standardization of the two

"anchor" points (cold and hot pixels), to improve prediction of ET in agricultural areas,

and to tie ET values to the local weather conditions of the region, which represents an

internal calibration of the model. In the original SEBAL cold and hot pixels are taken

from water and extremely hot surfaces, whereas in this study cold pixels were taken from

a well-watered full cover crop and hot pixels were taken from dry agricultural bare soils.

In addition, some refinements to surface energy balance components were made to

adapt SEBAL (originally developed for flat areas) to mountains and sloping terrains.

This adaptation included the development of procedures to account for the differences in

incoming solar radiation received in sloping surfaces, the inclusion of adjustment factors to account for the variation of wind speed over mountains, and the inclusion of functions to account for the impact of topography in surface roughness. The modified SEBAL model developed in this study was termed SEBAL$_{ID}$ where the subscript "ID" refers to the state of Idaho, the source of data used in the validation of the model.

To validate and refine SEBAL$_{ID}$, concurrent Landsat 5 TM imagery and measured ET values were used for 1988, 1989, 1990, and 1991. ET data were provided by measurements of ET performed at the USDA-ARS facility located at Kimberly, Idaho, under the supervision of Dr. James Wright (Wright, 1982). ET data were available for a wide range of weather conditions, surface covers, and crop types. In addition, measurements of net radiation, soil heat flux and plant canopy parameters were made at or near the lysimeter. This dataset provided valuable information to evaluate and refine the accuracy of SEBAL$_{ID}$ for instantaneous ET values as well as to verify procedures for extrapolating remote sensing algorithms over various time scales and for various types and categories of land cover. Thus, validation of SEBAL$_{ID}$ was focused on agricultural areas. Validation of SEBAL$_{ID}$ was jeopardized due to the spatial resolution of the Landsat 5 thermal band (120m x 120m) and the relatively small size of the lysimeter field (143 m x 179 m) which made the probability of getting a "pure" thermal pixel inside the lysimeter low. In addition, during one processed image there were differences in moisture regime between the lysimeter (with dimension of 1.83 m x 1.83 m), and the lysimeter field which introduced additional sources of uncertainties in the results. However, when thermal information was adequate, SEBAL$_{ID}$ produced good approximations of the value of predicted ET compared with the measured values.

SEBAL$_{ID}$ was applied to the Eastern Snake Plain Aquifer (ESPA) region in southern Idaho. Ten Landsat 7 ETM+ and two Landsat 5 TM images, corresponding to path 39, row 29,30, and 31 were utilized to predict daily and seasonal values (from March – October, 2000) of ET. Results from agricultural areas showed the consistency of SEBAL$_{ID}$ to predict the daily and seasonal variation of ET from these regions. Uncertainties in the prediction of soil heat flux, surface roughness, and in the extrapolation of the dT vs T_s function, produced some unreasonable results in desert and basalt-covered areas.

Conclusions

Even though SEBAL$_{ID}$ was just partially validated in this study, the author concludes that the application of SEBAL$_{ID}$ is promising for the operational estimation of ET , especially in agricultural areas. SEBAL$_{ID}$ has been developed in such a way that the need for extensive ground measurements is partly eliminated, and an accurate atmospheric corrected surface temperature is not a strong requirement. The fact that latent heat fluxes are fixed at the "anchor" pixels (cold and hot pixel), makes SEBAL$_{ID}$ a unique and robust remote sensing approach for determining ET as a residual of the energy balance. Most other current methods that estimate $LE = R_n - G - H$ translate many, if not, all of the residual errors of the estimation of R_n, G, and H into LE. In SEBAL$_{ID}$ any bias in the estimation of R_n and G is mainly translated into the estimate for H, but not LE, because in SEBAL$_{ID}$ latent heat flux estimates are substantially controlled by the value of LE fixed at the cold and hot pixels, which represent the two extreme

points in the surface energy balance. Therefore, biases in R_n, G, and H are isolated from LE.

Analysis of the behavior of ETrF in this study indicated that hourly average of ETrF remain fairly constant during daytime for the local Southern Idaho conditions . The relative constancy of the ETrF during the day is due to the fact that both ET variables in ETrF, actual ET and reference ET_r, are exposed to the same weather parameters during the day (which are affected by the regional advection present in the study area). A higher variation in ETrF is expected if the actual crop and the reference crop have substantially different surface resistance characteristics (stomatal control properties) or substantially different aerodynamic characteristics.

The fact that the value of ETrF remains relatively constant during the day was utilized to extrapolate instantaneous values of LE obtained from remote sensing to daily values. Comparison of predicted and measured daily values of ET showed that results were very close when adequate remote sensing data were available. Thus, the use of ETrF represents a real alternative for estimation of daily ET, from instantaneous ET values, in remote sensing applications.

Application of the evaporation fraction method (EF) to extrapolate instantaneous to daily values of LE was shown to be less adequate than the ETrF method in the study area. Instead of the relative constancy that EF values have displayed in different remote sensing applications, in the advective conditions of Southern Idaho, EF tends to increase during the day as extra energy and saturation vapor pressure deficit is brought into irrigated areas by the advection of warm and dry air from the upwind deserts . Therefore, it is concluded that ETrF is a more dependable and consistent means for extrapolating

instantaneous to 24-hour ET in the conditions present in the study area because the weather parameters included in the calculation of ET_r are affected by the advective conditions present in the region.

The value of ETrF changes in response to wetting events (precipitation and irrigation), the natural drying processes that occur in the soil moisture from evaporation and transpiration, and with vegetation development. However, seasonal ET calculated by assuming constant ETrF values around satellite images showed that, even though this assumption is undoubtedly incorrect, the use of a sufficient number of images during the growing season randomized the residual errors, and significant compensation occurred, with situations of overestimation tending to offset situations of underestimation. Predicted seasonal $SEBAL_{ID}$ (ET) from March to October was within 3 % of the total ET measured at the lysimeter for the same period. Although repetitions of a result as good as the obtained in this study are unlikely to occur, the results show that the procedure can provide estimation of seasonal ET with an acceptable margin of error.

The use of the FAO-56 water balance model to estimate the daily variation of ETrF between satellite images was very limited due to the lack of irrigation information for individual fields for the region, therefore the results of an application test are inconclusive. However, the application of this procedure can be very valuable in the prediction of ET between satellite images in nonirrigated regions, which is often required for groundwater and hydrologic models.

Results obtained from $SEBAL_{ID}$ in basalt areas in Southern Idaho are questionable. One of the reasons for the unreasonable results obtained from these areas are uncertainties in the prediction of the soil heat flux component of the energy balance.

In this study a general G/R_n equation developed by Bastiaanssen (Eq. 3.25) was applied and residual LE results indicated that this equation underestimates the value of G in basalt areas. In addition there are uncertainties in the prediction of surface roughness, and in the applicability of the dT versus T_s function to those areas.

In desert areas, results were unrealistic for much of the year. $SEBAL_{ID}$ consistently predicted negative values of latent heat flux in these areas. Here the problem of applying a single-source model to sparse vegetation, where sources and sinks of momentum and heat are significantly different from soil and vegetation, was one of the possible explanations for the negative values of ET predicted at desert areas. In addition, uncertainties in soil heat flux and extrapolation of the agricultural-calibrated T_s versus dT function are also possible explanations for the unrealistic results.

Results obtained by the application of $SEBAL_{ID}$ in mountains showed that the modifications made to the original SEBAL algorithm accounted for the variation of some components of the surface energy balance (i.e. incoming solar radiation, net radiation, surface roughness, and LE) in a correct direction, so that the refinements of the model produced progress in the adaptation of SEBAL for mountains and sloping surfaces.

Recommendations

In view of all the previous considerations, the author recognizes the value of SEBAL and $SEBAL_{ID}$ to estimate evapotranspiration for large areas in an operational manner. The author also recognizes that more work is needed to refine several components of SEBAL that introduce uncertainties into the results, especially in non-agricultural areas. In agricultural areas the training of the two extreme points of the

surface energy balance provides strong control over the final LE results, especially when the cold pixel is trained using a reference-type crop equation and high quality weather data.

It is recommended that the self-preservation of the value of ETrF during daytime and its consistency as a predictor of the 24-hour corresponding ratio, partially demonstrated in this study, be further explored for additional crops, years, and seasons. In this study, only the crops on the lysimeter fields that were concurrent with available remote-sensing data were analyzed (mainly sugar beets). However, the quality of the dataset used (both measured ET and weather data by Dr. J.L. Wright), made the analysis contained in this study very valuable.

In mountainous areas several points require more research. First the estimation of incoming solar radiation needs refinement to account for the topographic interactions among pixels. In $SEBAL_{ID}$ the value of R_s (for clear sky days) is calculated assuming the slope of the pixel is infinite; therefore the presence of shaded areas produced by the other surface features is not taken into account. The wind correction applied in $SEBAL_{ID}$ has to be further investigated. In $SEBAL_{ID}$ wind speed was modified considering only elevation and slope. Better functions need to be developed to incorporate factors such as wind direction (to recognize variations between upward and leeward slopes), mountain shape and variation in surface roughness. The lapse correction applied in $SEBAL_{ID}$ to convert radiometric surface temperatures to "equivalent" surface temperatures at a given reference level, for the application of the dT versus T_s relationship, also needs more verification through field measurements.

The linear relationship between T_s and dT that is assumed in SEBAL$_{ID}$ requires further investigation and validation to verify if it can be extrapolated for different conditions than that of the region where it was defined. In this study, extreme points of the dT versus T_s (cold and hot pixels) were taken from agricultural areas. Therefore, field measurements of near-surface air temperature and surface temperature need to be made to verify the validity of the linear relationship between dT versus T_s for the prediction of sensible heat in different surfaces. In addition, extrapolation of the dT versus T_s function to very rough surfaces such as forest is uncertain and needs more study.

Measurements of surface fluxes in desert and basalt areas are highly recommended to refine predictions of SEBAL in these areas. In basalt areas measurements of fluxes need to be more concentrated on soil heat flux. However, this task is very ambitious considering the high variability of soil structures present in the study area. In desert areas, measurements of soil and sensible heat fluxes are required to check the applicability of the linear relationship between dT versus T_s in these surfaces.

The relationship between G/R_n for water needs further investigation to assist SEBAL$_{ID}$ in the prediction of evaporation from these surfaces. Prediction and incorporation of turbidity for estimating penetration depths of solar radiation will be important.

Better methods to extrapolate predicted daily values of ET from SEBAL need to be developed. In SEBAL$_{ID}$ seasonal ET is estimated considering that the value of ETrF remains constant for a given period of time between images. For estimation of total amount of evapotranspiration for large scales, the use of more-frequent imagery can be

considered as an alternative to fill the information gaps between images. NOAA, and MODIS imagery can be considered for this task, even though the fine spatial resolution of surface fluxes obtained from application of SEBAL with Landsat data, will be jeopardized due to the lower spatial resolution of these sensors. Other alternatives would be the use of numerical models to predict the spatial variation of ET in the area. However the significant number of inputs that those models require would hamper the operational characteristics of SEBAL.

REFERENCES

Allen, R. 1996. Assessing integrity of weather data for reference evapotranspiration estimation. *Journal of Irrigation and Drainage Engineering* 122:97-106(No. 2).

Allen, R.G., W.O. Pruitt, J.A. Businger and M.E. Jensen. 1996. "Evaporation and transpiration," Hydrology handbook, ASCE, New York.

Allen, R., L. Pereira, D. Raes and M. Smith. 1998. Crop evapotranspiration, FAO, Rome.

Allen, R. 2000. Using the FAO-56 dual crop coefficient method over an irrigated region as part of an evapotranspiration intercomparison study. *Journal of Hydrology* 229:27-41.

Allen, R., H. De Bruin, O. Hartogensis, B. Tanner and C. Neale. 2000. "Regional advection perturbations in an irrigated desert (RAPID)-impacts on evapotranspiration," Biological and Agricultural Engineering Department, University of Idaho, Kimberly, Idaho.

Allen, R.G., M. Tasumi, R. Trezza and J.L. Wright. 2001. "Application of the SEBAL methodology for estimating evapotranspiration and comsumptive use of water trough remote sensing, Part II: Details on validation with Lysimeters and application to the Eastern Snake River Plain of Idaho," IDWR-University of Idaho, Submitted to the Raytheon Systems Company Earth Observation System Data and Information System Project.

Allen, R.G., W. Bastiaanssen, J. Wright, A. Morse, M. Tasumi and R. Trezza. 2002. "Evapotranspiration from satellite images for water management and hydrologic balances," *Proceedings of 18th International Congress on Irrigation and Drainage: July 2002*, Montreal, Canada.

Allen, R., A. Morse, M. Tasumi, R. Trezza, W. Bastiaanssen, J. Wright and W. Kramber. 2002. "Evapotranspiration from a satellite-based surface energy balance for the Snake Plain Aquifer in Idaho," *Proceedings of the Conference on Energy Climate, Environment and Water*, San Luis Obispo, California.

Allen, R.G., R. Trezza and M. Tasumi. 2002. "Algorithms for calculating 24-hour extraterrestrial solar radiation for sloping or mountainous areas," Internal Report 1, University of Idaho, Kimberly, Idaho.

Amayreh, J.A. 1995. "Lake evaporation: a model study," dissertation submitted in partial fulfillment of the requirements for the degree of Doctor of Philosophy in Biological and Agricultural Engineering, Utah State University, Logan, Utah.

ASCE- EWRI, 2002. "The ASCE Standardized reference evapotranspiration equation," ASCE-EWRI Standardization of Reference Evapotranspiration Task Comm. Report, available at http://www.kimberly.uidaho.edu/water/asceewri/.

Ayra. P. 1988. Introduction to micrometeorology, Academic Press Inc., San Diego.

Bastiaanssen, W.G.M. 1995. "Regionalization of surface flux densities and moisture indicators in composite terrain," dissertation submitted in partial fulfillment of the requirements for the degree of Doctor of Philosophy in Agricultural Engineering, Wageningen Agricultural University, Wageningen, Netherlands.

Bastiaanssen, W.G.M. 1998. Remote Sensing in Water Resources Management: The State of the Art, IWMI, Sri Lanka.

Bastiaanssen, W.G.M. 2000. SEBAL-based sensible and latent heat fluxes in the irrigated Gediz Basin, Turkey. *Journal of Hydrology* 229:87-100.

Bastiaanssen, W., M. Menenti and Feddes RA. 1998. A remote sensing surface energy balance algorithm for land (SEBAL) 1. Formulation. *Journal of Hydrology* 229: 198-212.

Bastiaanssen, W., D. Molden and I. Makin. 2000. Remote sensing for irrigated agriculture:examples from research and possible applications. *Agricultural Water Management* 46:137-155.

Bastiaanssen, W., H. Pelgrum, P. Droogers, M. Menenti and H. De Bruin. 1997. Area-average estimates of evaporation, wetness indicators and top soil moisture during two golden days in EFEDA. *Agricultural and Forest Meteorology* 87:119-137.

Bastiaanseen, W.G.M., R.A.L. Brito, M.G. Bos, R.A. Souza, E.B. Cavalcanti and M.M. Bakker. 2001. Low cost satellite data for monthly irrigation performance monitoring: benchmarks from Nilo Coelho, Brazil. *Irrigation and Drainage Systems* 15:53-79.

Bausch, W. 1995. Remote sensing of crop coefficients for improving the irrigation scheduling of corn. *Agricultural Water Management* 27:55-68.

Brutsaert, W.H. 1982. Evaporation into the atmosphere, D. Reidel Publ., Boston.

Brutsaert, W. and M. Sugita. 1992. Application of self-preservation in the diurnal evolution of the surface energy budget to determine daily evaporation. *Journal of Geophysical Research* 97:18,377-18,382.

Burba, G.G., S.B. Verma and J. Kim. 1999. Surface energy fluxes of Phragmites australis in a prairie wetland. *Agricultural and Forest Meteorology* 94:31-51.

Carlson, T, and R. Buffum 1989. On estimating total daily evapotranspiration from remote surface temperature measurements. *Remote Sensing of Environment* 29:197-207.

Caselles, V., M. Artigao, E. Hurtado, C. Coll and A. Brasa. 1998. Mapping actual evapotranspiration by combining Landsat TM and NOAA-AVHRR Images: Application to the Barrax Area, Albacete, Spain. *Remote Sensing of the Environment* 63:1-10.

Chehbouni, A., C. Watts, Y.H. Kerr and F. Santiago. 2000. Methods to aggregate turbulent fluxes over heterogeneous surfaces: Applications to SALSA data set in Mexico. *Agricultural and Forest Meteorology* 105:133-144.

Chen, F., Z. Janjic and K. Mitchell. 1997. The NCEP Mesoscale ETA Model. *Boundary Layer Meteorology* 85:391-421.

Choudhury, B. 2000. Seasonal and interannual variations of total evaporation for the Gediz Basin area. *Journal of Hydrology* 229: 77-86.

Choudhury, B. and J.L. Monteith. 1988. A four-layer model for the heat budget of homogeneous land surfaces. *Journal of the Royal Meteorological Society* 114:373-398.

Choudhury, B. and N. DiGirolamo. 1998. A biophysical process-based estimate of global land surface evaporation using satellite and ancillary data. I. Model description and comparison with observations. *Journal of Hydrology* 205:164-185.

Choudhury, B.J., R.J. Reginato and S.B. Idso. 1986. An analysis of infrared temperature observations over wheat and calculation of latent heat flux. *Agricultural and Forest Meteorology* 37:75-88.

Choudhury, B.J., S.B. Idso and R.J. Reginato. 1987. Analysis of an empirical model for soil heat flux under a growing wheat crop for estimating evaporation by and infrared-temperature based energy balance equation. *Agricultural and Forest Meteorology* 39:283-297.

Choudhury, B., N. Ahmed, S. Idso, R. Reginato and S. Daughtry. 1994. Relations between evaporation coefficients and vegetation indices studied by model simulations. *Remote Sensing of Environment* 50:1-17.

Choudhury, B., N. DiGirolamo, J. Susskind and W. Darnell. 1998. A biophysical process-based estimate of global land surface evaporation using satellite and ancillary data. II Regional and global patterns of seasonal and annual variations. *Journal of Hydrology* 205:186-204.

Clothier, B.E., K.L. Clawson, P.J. Pinter Jr., M.S. Moran, R.J. Reginato and R.D. Jackson, 1986. Estimation of soil heat flux from net radiation during the growth of alfalfa. *Agriculture and Forest Meteorology* 37:319-329.

Crago, R. 1996. Comparison of the evaporative fraction and the Priestley-Taylor alpha for parameterizing daytime evaporation. *Water Resources Research* 32:1403-1409.

D'Urso, G., M. Menenti and A. Santini. 1999. Regional application of one-dimensional water flow models for irrigation management. *Agricultural Water Management* 40:291-302.

Daughtry, C.S., W.P. Kustas, M.S. Moran, R.D. Jackson and J. Pinter. 1990. Spectral estimates of net radiation and soil heat flux. *Remote Sensing of Environment* 32:111-124.

Dolman. 1993. A multiple-source land surface energy balance model for use in general circulation models. *Agriculture and Forest Meteorology* 65:21-45.

Doorenbos, J. and W.O. Pruitt. 1977. Crop water requirements, Rome, Italy.

Droogers, P. and W. Bastiaanssen. 2002. Irrigation performance using hydrological and remote sensing modeling. *Journal of Irrigation and Drainage Engineering* 128:11-18.

Duffie, J.A. and W.A. Beckman. 1980. Solar engineering of thermal processes, John Wiley and Sons, New York.

Farah, H. 2000. "Estimation of regional evaporation under different weather conditions from satellite and standard weather data: A case study of the Naivasha Basin, Kenya," dissertation submitted in partial fulfillment of the requirements for the degree of Doctor of Philosophy in Agricultural Engineering, Wageningen Agricultural University, Wageningen, Netherlands.

Franks, S. and K. Beven. 1997. Estimation of evapotranspiration at the landscape scale: A fuzzy disaggregation approach. *Water Resources Research* 33:2929-2938.

Friedl, M. 1995. Modeling land surface fluxes using a sparse canopy model and radiometric surface temperature measurements. *Journal of Geophysical Research* 100(D12):25,435-24,446.

Gilles R, Carlson, T, Kustas, W, Humes, K. (1995) A verification of the triangle method for obtaining surface soil water content. *International Journal of Remote Sensing* 18:3145-3166.

Granger, R.J. 2000. Satellite-derived estimates of evapotranspiration in the Gediz Basin. *Journal of Hydrology* 229:70-76.

Hamimed, A. 2000. "Mapping actual evapotranspiration and water stress degree with TM data," *Proceedings of the 20th EARSEL Symposium - Remote Sensing in the 21st Century*. Dresden, Germany.

Hipps, L. 1999. Class notes of biometeorology, Utah State University, Logan, Utah.

Huete,A.R., 1988. A Soil-Adjusted Vegetation Index (SAVI). *Remote Sensing of Environment* 25:295-309

Itenfisu, D. 1998. "Adaptation of resistance based evapotranspiration function to row crops," dissertation submitted in partial fulfillment of the requirements for the degree of Doctor of Philosophy in Biological and Agricultural, Utah State University, Logan, Utah.

Jackson, R.D., R.J. Reginato and S.B.Idso. 1977. Wheat canopy temperatures: A practical tool for evaluating water requirements. *Water Resources Research* 13:651-656.

Jackson, R.D., P.J. Pinter and R.J. Reginato. 1987. Net radiation calculated from remote multispectral and ground station meteorological data. *Agricultural and Forest Meteorology* 35:153-164.

Jackson, T.J., J. Schmugge and E.T. Engman. 1996. Remote sensing applications to hydrology: soil moisture. *Hydrological Sciences* 41(4):517-530.

Jensen, M.E. and R.G. Allen. 2000. "Evolution of practical ET methods," *Proceedings of the 4th National Irrigation Symposium, ASAE*, Phoenix, Arizona.

Jensen, John. 2000. Remote sensing of the environment. An earth resource perspective, Prentice and Hall, New York.

Kizer, M. and R. Elliott. 1991. Eddy correlation systems for measuring evapo-transpiration. *Transactions of the ASAE* 34:141-149.

Kniezys, F. 1996. "The MODTRAN 2/3 report and Lowtran 7 model," Phillips Lab, Geophysics Directorate, PL/GPOS, Hanscom AFB, MA 01731.

Kondo, J. 1994. Meteorology for hydrological environment. Asakura Shoten Publishing, Japan (in Japanese).

Kustas, W.P., B.J. Choudhury, M.S. Moran, R.J. Reginato and R.D. Jackson. 1989. Determination of sensible heat flux over sparse canopy using thermal infrared data. *Agricultural and Forest Meteorology* 44:197-216.

Kustas, W.P., M.S. Moran, R.D. Jackson and L.F. Duell. 1990. Instantaneous and daily values of the surface enegy balance over agricultural fields using remote sensing and a reference field in an arid environment. *Remote Sensing of Environment* 32:125-141.

Kustas, W.P., M.S. Moran, K.S. Humes, D.I. Stannard, J. Pinter, L. Hipps and D.C. Goodrich. 1994. Surface energy balance estimates at local and regional scales using optical remote sensing from an aircraft platform and atmospheric data collected over semiarid rangelands. *Water Resources Research* 30(5):1241-1259.

Kustas, W.P. and J.M. Norman. 1996. Use of remote sensing for evapotranspiration monitoring over land surfaces. *Hydrological Sciences* 41(4):495-515.

Kustas, W. and J. Norman. 1997. A two-source approach for estimating turbulent fluxes using multiple angle thermal infrared observations. *Water Resources Research* 33(6):1495-1508.

Kustas, W. and J. Norman. 1999. Evaluation of soil and vegetation heat flux predictions using a simple two-source model with radiometric temperatures for partial canopy cover. *Agricultural and Forest Meteorology* 94:13-29.

Lhomme, J. P., Monteny, and Amadou , M. 1994. Estimating sensible heat flux from radiometric temperature over sparse millet. *Agricultural and Forest Meteorology* 68:77-91.

Li, F. and T.J. Lyons. 1999. Estimation of regional evapotranspiration through remote sensing. *Jounal of Applied Meteorology* 38:1644-1654.

Markham,B.L. and J.L. Barker. 1986. "Landsat MSS and TM Post-Calibration Dynamic Ranges, Exoatmospheric Reflectances and At-Satellite Temperatures. EOSAT Landsat Technical Notes 1:3-8," Earth Observation Satellite Company, Lanham, Maryland

Markham, B.L. and J.L. Barker. 1987. Thematic mapper bandpass solar exoatmospheric irradiances. *International Journal of Remote Sensing* 8(3):517-523.

Massman, W.J. 1992. Correcting errors associated with soil heat flux measurements and estimating soil thermal properties from soil temperature and heat flux plate data. *Agricultural and Forest Meteorology* 59:249-266.

Mauser, W. and R. Schadlich. 1998. Modelling the spatial distribution of evapotranspiration on different scales using remote sensing data. *Journal of Hydrology* 212-213.

Mekonnen, M. and W.G.M. Bastiaanssen. 2000. A new simple method to determine crop coefficients for water allocation planning from satellites: Results from Kenya. *Irrigation and Drainage Systems* 14:237-256.

Moran, S. and R. Jackson. 1991. Assesing the spatial distribution of evapotranspiration using remotely sensed inputs. *Journal of Environmental Quality* 20:725-735.

Moran, M.S., T.R. Clarke, Y. Inoue and A. Vidal. 1994. Estimating crop water deficit using the relation between surface-air temperature and spectral vegetation index. *Remote Sensing of Environment* 49:246-263.

Moran, M.S., A.F. Rahman, J.C. Washburne and W.P. Kustas. 1996. Combining the Penman-Monteith equation with measurements of surface temperature and reflectance to estimate evaporation rates of semiarid grassland. *Agricultural and Forest Meteorology* 80:87-109.

Morse, A., M. Tasumi, R. Allen and W. Kramber. 2000. "Application of SEBAL methodology for estimating comsumptive use of water and streamflow depletion in the Bear River Basin of Idaho trough remote sensing: Final report," IDWR No.1, http://www.kimberly.uidaho.edu/water/sebal/index.htlm.

NASA. 2002. "Landsat 7 Handbook," http://ltpwww.gsfc.nasa.gov/IAS/handbook.

Neale, C., W. Bausch and D. Heermann. 1989. Development of reflectance-based crop coefficients for corn. *Transactions of ASAE* 32:1891-1899.

Nemani, R. and S. Running. 1989. Testing a theoretical climate-soil-leaf area hydrology equilibrium of forest using satellite data and ecosystem simulation. *Agricultural and Forest Meteorology* 44:245-260.

Nichols, W. and R. Cuenca. 1993. Evaluation of the evaporative fraction for parameterization of the surface energy balance. *Water Resources Research* 29:3681-3690.

Norman, J. and F. Becker. 1995. Terminology in thermal infrared remote sensing of natural surfaces. *Agricultural and Forest Meteorology* 77:153-166.

Norman, J.M., W.P. Kustas, and K.S. Humes. 1995. Source approach for estimating soil and vegetation energy fluxes in observations of directional radiometric surface temperature. *Agricultural and Forest Meteorology* 77:263-293.

Norman, J.M., W.P. Kustas, J.H. Prueger and G.R. Diak. 2000. Surface flux estimation using radiometric temperature: A dual-temperature-difference method to minimize measurement errors. *Water Resources Research* 36(8):2263-2274.

Ohmura, A. 1982. Objective criteria for rejecting data for bowen ratio flux calculations. *Journal of Applied Meteorology* 21:595-598.

Oke, T.R. 1996. Boundary Layer Climates, University Press, Cambridge.

Olioso, A., H. Chauki and D. Courault. 1999. Estimation of evapotranspiration and photosynthesis by assimilation of remote sensing data into SVAT models. *Remote Sensing of Environment* 68:341-356.

Ottle, C. and D. Vidal-Madjar. 1994. Assimilation of soil moisture inferred from infrared remote sensing in a hydrologycal model over the HAPEX-MOBILHY region. *Journal of Hydrology* 158:241-264.

Payero, J. 1997. "Estimating evapotranspiration of reference crops using the remote sensing approach," dissertation submitted in partial fulfillment of the requirements for the degree of Doctor of Philosophy in Biological and Agricultural Engineering, Utah State University, Logan, Utah.

Payero, J., C. Neale and J. Wright. 2001. "Estimating diurnal variation of soil heat flux for alfalfa and grass," *Proceedings of the 2001 ASAE Annual International Meeting*, Sacramento, California.

Pelgrum, H. and W. Bastiaanssen. 1996. An intercomparison of techniques to determine the area-average latent heat flux from individual in situ observations: A remote sensing approach using the European Field Experiment in a desertification-threatened area data. *Water Resources Research* 32(9):2775-2786.

Qi, J., M.S. Moran, D.C. Goodrich, R. Marsett, R. Scott, L. Hipps and A. Chehbouni. 1998. "Estimation of evapotranspiration over the San Pedro riparian area with remote and in situ measurements," *Proceedings of the Special Symposium on Hydrology*, Phoenix, Arizona.

Qualls, R., W. Brutsaert and W. Kustas. 1993. Near-surface air temperature as substitute for skin temperature in regional surface flux estimation. *Journal of Hydrology* 143:381-393.

Qualls, R., M. Wagstaff and R. Crago. 1999. Equilibrium evaporation and positive evaporation surface temperature relationships across a grassland. *Journal of the American Water Resources Association* 35(5):1125-1133.

Reginato, R.J., R.D. Jackson and J. Pinter. 1985. Evapotranspiration calculated from remote sensing and ground station meteorological data. *Remote Sensing of Environment* 18:75-89.

Schultz, G. 1988. Remote sensing in hydrology. *Journal of Hydrology* 100:239-265.

Seguin, B.,D. and B. Itier. 1983. Using midday surface temperature to estimate daily evapotranspiration from satellite thermal IR data. *International Journal of Remote Sensing* 4:371-383.

Seguin, B.,D. and B. Itier. 1983. Using midday surface temperature to estimate daily evapotranspiration from satellite thermal IR data. *International Journal of Remote Sensing* 4:371-383.

Seguin, B., D. Courault and M. Guerif. 1994. Surface temperature and evapotranspiration: applications of local scale methods to regional scales using satellite data. *Remote Sensing of Environment* 49:287-295.

Shott, J. and W. Volchock. 1985. Thematic Mapper Infrared Calibration. *Photogrametric Engineering and Remote Sensing*, 43(12), 1541-1552.

Shih, S. and J. Jordan. 1992. Landsat mid-infrared data and GIS in regional surface soil-moisture assessment. *Water Resources Bulletin* 28(4):713-719.

Shuttleworth, J. and J.S. Wallace. 1985. Evaporation from sparse crops - an energy combination theory. *Quartely Journal of the Royal Meteorological Society* 111:839-855.

Shuttleworth, W.J., R.J. Gurney, A.Y. Hsu and J.P. Ormsby. 1989. "The variation in energy partition at surface flux sites," *Proceedings of the IAHS Thrid International Assembly*, Baltimore, Maryland.

Shuttleworth, J. and R. Gurney. 1990. The theoretical relationship between foliage temperature and canopy resistance in sparse crops. *Quarterly Journal of the Royal Meteorological Society* 116:497-519.

Silberstein, R.P., M. Sivapalan and A. Wyllie. 1999. On the validation of a coupled water and energy balance model at small catchment scales. *Journal of Hydrology* 220:149-160.

Soegaard, H. 1999. Fluxes of carbon dioxide, water vapour and sensible heat in a boreal area of Sweden - scaled from canopy to landscape level. *Agricultural and Forest Meteorology* 98-99:463-478.

Souch, C., C. Wolfe and C. Grimmond. 1996. Wetland evaporation and energy partitioning: Indiana Dunes National Lakeshore. *Journal of Hydrology* 184:189-208.

Stewart, J.B., W.P. Kustas, K.S. Humes, W.D. Nichols and H.A.R. De Bruin. 1994. Sensible heat flux-radiometric surface relationship for eight semiarid areas. *Journal of Applied Meteorology* 33:1110-1117.

Sucksdorff, Y. and C. Ottle. 1990. Application of satellite remote sensing to estimate areal evapotranspiration over a watershed. *Journal of Hydrology* 121:321-333.

Tanner, B. 1988. Use requirements for Bowen ratio and eddy correlation determination of evapotranspiration. *Management of Irrigation and Drainage Systems* 1: 605-616.

Tasumi (in preparation). "Progress in operational estimation of ET through remote sensing," dissertation submitted in partial fulfillment of the requirements for the degree of Doctor of Philosophy in Biological and Agricultural Engineering, University of Idaho, Idaho.

Thunnissen, H.A. and J.A. Nieuwenhuis. 1990. A simplified method to estimate regional 24-h evapotranspiration from thermal infrared data. *Remote Sensing of Environment* 31:211-220.

Troufleau, D., J.P. Lhomme, B. Monteny and A. Vidal. 1997. Sensible heat flux and radiometric surface temperature over sparse Sahelian vegetation. I. An experimental analysis of the kB-1 parameter. *Journal of Hydrology* 188-189:815-838.

Van Der Keur, P., S. Hansen and K. Svhelde. 2001. Modification of the DAISY SVAT model for potential use of remotely sensed data. *Agricultural and Forest Meteorology* 106:215-231.

Vanderkimpem, P. 1991. "Estimation of crop evapotranspiration by means of the Penman-Monteith equation," dissertation submitted in partial fulfillment of the requirements for the degree of Doctor of Philosophy in Biological and Agricultural Engineering, Utah State University, Logan, Utah.

Verhoef, A., H.A.R. De Bruin and J.M. Van Den Hurk. 1997. Some practical notes on the parameter kB-1 for sparse vegetation. *Journal of Applied Meteorology* 36:560-577.

Vidal, A. and A. Perrier (1989). "Analysis of a simplified relation for estimating daily evapotranspiration from satellite thermal IR data." *International Journal of Remote Sensing*, 10(8):1327-1337.

Walter, I.A., R.G. Allen, R. Elliott, M.E. Jensen, D. Itensifu and B. Mecham. 2000. "ASCE's standarized reference evapotranspiration equation," *Proceedings of the 4th National Irrigation Symposium, ASAE*, Phoenix, Arizona.

Webb, E.K., G.I. Pearman and R. Leuning. 1980. Correction of flux measurements for density effects due to heat and water vapour transfer. *Quarterly Journal of the Royal Meteorological Society* 106:85-100.

Wright, J.L. 1982. New evapotranspiration crop coefficients. *Journal of Irrigation and Drainage* 108:57-74.

Wright, J.L. 1991. "Using weighing lysimeters to developed evapotranspiration crop coefficients," *Proceedings of the International Symposium on Lysimetry*, ed. R.G. Allen. Honolulu, Hawaii:.

Wukelic, G.E., D.E. Gibbons, L.M. Martucci and H.P. Foote. 1989. Radiometric calibration of landsat thematic mapper thermal band. *Remote Sensing of Environment* 28:339-347.

Yamamoto, G. and J. Kondo. 1968. Evaporation from lake Nojiri. *J. Meteor. Soc. Japan* 46:166-176.

Zhan, X., W.P. Kustas and K.S. Humes. 1996. An intercomparison study of models of sensible heat flux over partial canopy surfaces with remotely sensed surface temperature. *Remote Sensing of the Environment* 58:242-256.

APPENDICES

Appendix A

Lysimeter and Weather Data Integrity
Check and Correction

Trezza, R., Allen, R.G, Tasumi, M, and J.L Wright

Assessment of Weather Data Integrity

The integrity of the weather data, measured at the micrometeorological weather station located at the Kimberly lysimeter site operated by Dr. J.L Wright, was determined using the approaches described in Allen (1996) and Allen et al (1998). These integrity procedures were applied for 1988, and 1989 for every day and poor quality data were flagged as such. The integrity analysis is important to insure that weather data used in SEBAL as well in computing ET_r are correct

Air Temperature

The existence of two air temperature sensors at the Kimberly weather station allowed us to compare both readings as a means of evaluating their accuracy. Both sensors were located over clipped grass. In Fig. A-1 a plot of air temperature measured by General Eastern (GE) and R.M. Young (RMY) air temperature sensor is shown, both were in aspirated and radiation shielded devices. Hourly temperature values were plotted to ensure that maximum and minimum values occur at the expected time of the day. Plotting of the hourly temperature also indicated the presence of unusual values that did not follow the general trend of the air temperature readings due to malfunctioning
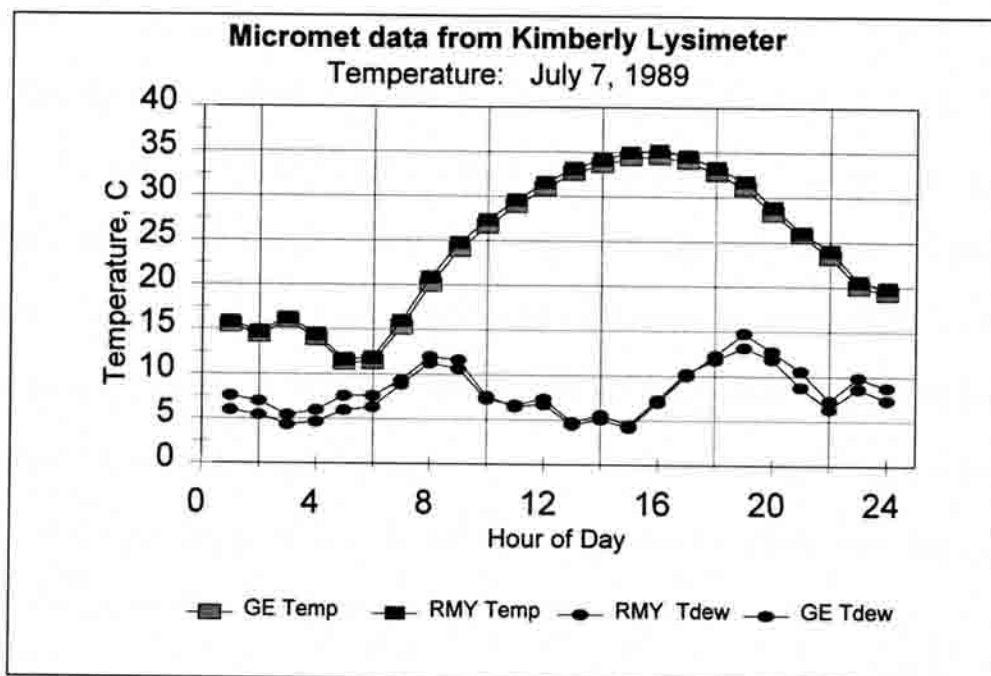
FIGURE A-1.   Air temperature and Dewpoint Temperature Plots for July 7, 1989,
Measured by Dr. J. Wright   at the Micromet Station Located at the
Kimberly Lysimeter Fields.

of the equipment or the data storage system. In the case shown in Fig. A.1, the good

agreement between the two air temperature readings is indication of the correct

functioning of the sensors.

Dew Point Temperature

In the Kimberly micromet weather station, two sensors provided measurements

of dew point temperature (T_{dew}). One was a General Eastern Chilled Mirror (GE Tdew),

and the other an R.M. Young Lithium-Chloride dew probe (RMY Tdew). Agreement

between the two sensors readings was taken as a strong indication that both devices were

working well. Allen et al (1998) indicated that dew point temperature should remain

relatively constant during a 24-hour period when there is not advection of dry air from

outside the weather station area. In addition , values of dew point temperature should be

compared to daily minimum temperatures (T_{min}). According to Allen et al (1998), T_{dew} under irrigated, semiarid conditions, will be similar to T_{min}, and may be 2 to 5 °C degrees lower than T_{min} if the measurement site is subjected to local aridity. If T_{dew} consistently deviates substantially from T_{min} then one should evaluate the calibration of the sensor. Figure A.1 shows a plot of dewpoint temperature from both sensors, where good agreement between the readings was presented. In addition, T_{dew} at 06:00 am is around 3.5 °C lower than T_{min}. Therefore in this case, there is strong indication that the two sensors are working properly. Both the plots and evaluation procedure show the extreme value of having two sensors for each weather parameter.

Wind Speed

Hourly wind speed values were plotted to inspect for unusual readings that may indicate a malfunction of the instruments. When more than one wind speed sensor was available (as shown in Fig. A-2), comparisons between readings was taken as a valid way for assessing their accuracy.

Solar Radiation

In the micrometeorological weather station located at the lysimeter fields, two Eppley pyranometers were operated by Dr. J. L Wright. One of them was an Eppley Precision Spectral Pyranometer (PSP) and the other was an Eppley Model 15 pyranometer.

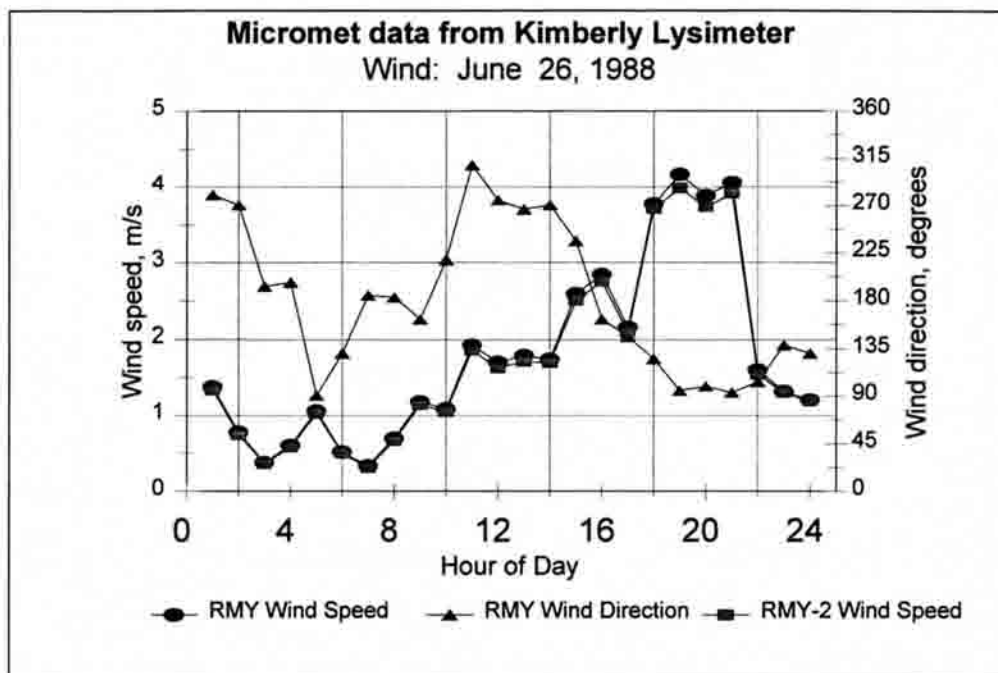A plot of solar radiation measurements is displayed in Fig. A.3.

FIGURE A.2. Wind Speed and Wind Direction plots for June 26, 1988, Measured by
Dr. J.L Wright at the Micromet Station Located at Kimberly Lysimeter
Field. The two Instruments were RM Young Propeller Anemometers.

The accuracy of solar radiation readings was assessed by comparing the readings
with each other (when $R_s < R_{so}$) and by comparing measured values against theoretical
clear sky envelopes for hourly and daily periods. It is expected that values for solar
radiation during clear sky conditions will be close to the values obtained from theoretical
expressions.

To calculate theoretical values of clear-sky solar radiation (R_{so}), the
methodology presented in Allen et al (1998) and modified by ASCE-EWRI (2002) was
used. This methodology includes the influence of sun angle, turbidity, atmospheric
thickness, and precipitable water on the incoming solar radiation, and is based in the
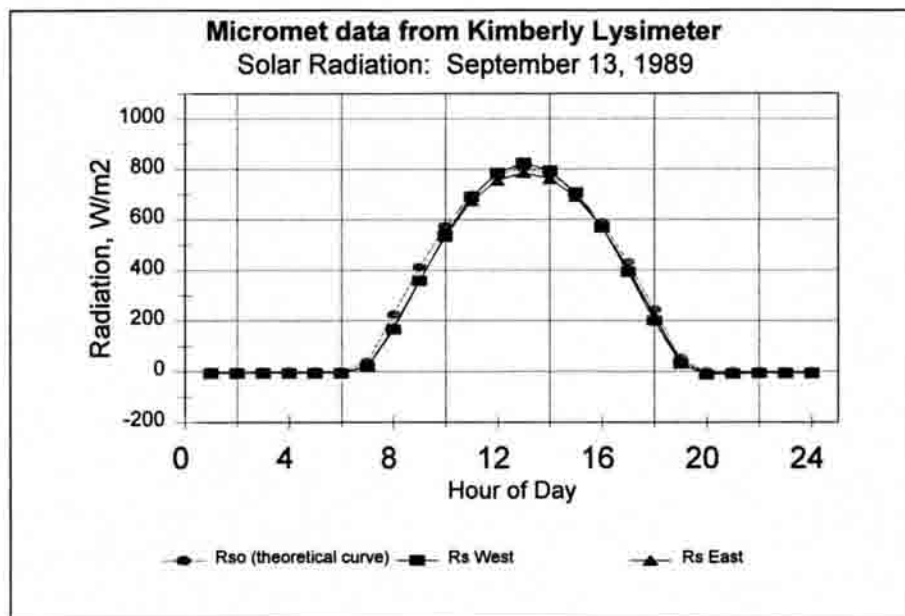following equation:

230

FIGURE A.3. Measured and Theoretical Solar Radiation Plots for September 13, 1988,
Measured by Dr. J Wright at the Micromet Station Located at the
Kimberly Lysimeter Field. The R_{so} (Theoretical) was calculated with
ASCE-EWRI (2002) procedure.

$$R_{so} = (K_B + K_D) R_a \tag{A.1}$$

where K_B is the clearness index for direct beam radiation [dimensionless], K_D is the

clearness index for direct beam radiation [dimensionless], and R_a is the extraterrestrial

radiation.

The description of the calculation of K_B, and K_D is included in Chapter 4. For

hourly steps, the value of R_a is computed using the following equation:

$$R_a = \frac{12\,(60)}{\pi} G_{sc}\, d_r \left[(\omega_2 - \omega_1)\sin(\varphi)\sin(\delta) + \cos(\varphi)\cos(\delta)(\sin(\omega_2) - \sin(\omega_1)) \right] \tag{A.2}$$

where R_a is extraterrestrial radiation [MJ m^{-2} hour^{-1}], G_{sc} is the solar constant = 0.0820 MJ m^{-2} min^{-1}, dr is the inverse relative distance Earth-Sun (Eq. 3.10), δ is the solar declination [rad], φ is the latitude [rad] , ω_1 is the solar time angle at beginning of period [rad] , and ω_2 is the solar time angle at end of period [rad].

The solar time angles are calculated by :

$$\omega_1 = \omega - \frac{\pi\, t_1}{24} \tag{A.3}$$

$$\omega_2 = \omega + \frac{\pi\, t_1}{24} \tag{A.4}$$

where ω is the solar time angle at midpoint of the hourly period [rad], and t_1 is the length of the calculation period [hour]. For hourly time steps $t_1 = 1.0$.

The solar time angle at the hour midpoint (from Duffie and Beckman, 1980) is:

$$\omega = \frac{\pi}{12} \left[(t + 0.06667(L_z - L_m) + S_c) - 12 \right] \tag{A.5}$$

where t is the standard clock time at the midpoint of the period [hour]. For instance, to calculate ω between 11.00 and 12.00 hours, t = 11.5, L_z is the longitude of the center of the local time zone [degrees west of Greenwich], where L_z = 75, 90, 105 and 120° for the Eastern, Central, Rocky Mountain and Pacific US time zones respectively, L_m is the longitude of the study area [degrees west of Greenwich], and S_c is the seasonal correction for solar time [hour].

The seasonal correction for solar time is computed as follows:

$$S_c = 0.1645 \sin(2\,b) - 0.1255 \cos(b) - 0.025 \sin(b) \tag{A.6}$$

where

$$b=\frac{2\pi(J-81)}{364} \qquad (A.7)$$

where J is the number of the day in the year.

According to Allen et al (1998), if the values of measured solar radiation are more than 3 to 5 % different from R_{so} under perceived clear sky days, one should evaluate the maintenance and calibration of the R_s sensor. In this study, when two sensor where available, the sensor agreeing closely with R_{so} was flagged for use. If neither sensor agreed with the R_{so} curve (within 3 %), then an adjustment of the measured values was done by dividing R_s by the average value of R_s / R_{so} on clear sky days. This procedure was adopted to select the best sensor at the Kimberly micromet station for the period 1988-1991, and to correct wrong values obtained from this station as well as for the Agrimet weather stations during 2000.

Figure A.3 shows a plot of measured values of solar radiation obtained from the Eppley PSP (Rs west) and Eppley Model 15 (Rs east) pyranometers located at the micrometeorological weather station at the lysimeter site. As it can be seen in Fig. A.3, readings from both pyranometers agreed well with the theoretical value of R_{so} obtained from Eq. A.1 during a clear sky day.

Net Radiation

To evaluate the integrity of net radiation measurements, Allen et al (1998) and ASCE-EWRI (2002) recommend comparing measured values against estimates of R_n

made from solar radiation information. The publications recommended the following

FAO-56 equation for estimating hourly R_n over clipped grass:

$$R_n = (1-\alpha)Rs - \left[\sigma T^4 (0.34 - 0.14\sqrt{e_a})(1.35\frac{R_s}{R_{so}} - 0.35) \right] \qquad (A.8)$$

where R_n is the net radiation , σ is the Stefan-Boltzmann constant [4.901 x 10^{-9} MJ K^{-4} m^{-2} d^{-1}], T is the mean air temperature [K] , e_a actual vapor pressure [kPa], R_s/R_{so} relative solar radiation (limited to ≤ 1.0), R_s is the measured solar radiation , and R_{so} is the calculated clear-sky radiation.

According to Allen et al (1998) if measured values consistently deviate by more than 3 to 5 %, then the calibration of the net radiometer should be evaluated. Of course one cannot expect that estimated and measured values be exactly the same because of uncertainties in the value of parameters such as albedo.

The presence of two Swissteco net radiometers sited over grass at the lysimeter 1 site made possible the comparison between readings as a means of assessing the integrity of the data. In Fig. A.4 a plot of net radiation readings from the two net radiometers is presented. Fig. A.4 also shows the theoretical curve (Rn-56) for net radiation over grass obtained from Eq. A.8.

Soil Heat Flux

A theoretical expression developed by Choudhury et al (1987) was used to evaluate the accuracy of soil heat flux measurements:
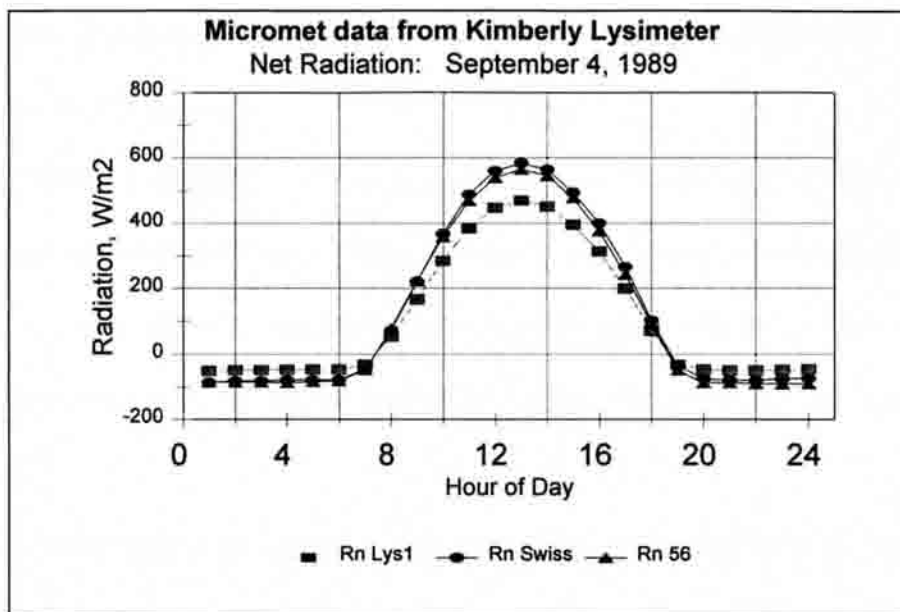
FIGURE A.4. Measured and Theoretical Net radiation Radiation Plots for September
4, 1989, Measured by Dr. J.L Wright at the Micromet Station located at
the Kimberly Lysimeter Fields. The Rn 56 (Theoretical Net Radiation
Over Grass) was calculated with FAO-56 (Allen et al, 1998) procedure

$$G = 0.4 * R_n * e^{-0.5 * LAI} \qquad (A.9)$$

where G is the soil heat flux, and LAI the leaf area index

According to Allen et al (1998) Eq. A.9 gives just an approximation of the soil

heat flux during daytime conditions because it does not consider effects of plant spacing,

sun angle, and soil characteristics. Bastiaanssen (1995) has suggested that the G/R_n ratio

changes during the day with surface temperature and sun angle.

Assessment of Lysimeter Data Integrity

To assess the integrity of the data obtained from the lysimeters, the procedure

developed by Itensifu (1998) was adapted to the Kimberly lysimeter data. Itenfisu used

a methodology based on comparing the hourly evolution of ET from a precision

lysimeter in Fresno, California, with the hourly behavior of the grass reference evapotranspiration (ET_o).

In Kimberly, two lysimeters were operated by Dr. J. Wright at the USDA-ARS, each one containing a different crop. At the lysimeter site, a micrometeorological station recorded net and solar radiation, air temperature, wind speed, and dew point temperature, which made it feasible to use Itensifu's approach to assess and potentially correct the hourly data.

The procedure to assess the integrity of the hourly lysimeter data for a specific day was the following:

a) Determine the hourly value of ET_o (grass reference ET) and ET_r (alfalfa reference ET) using the ASCE-EWRI (2002) procedure and weather data collected near the lysimeters. In Appendix B the calculations needed to compute ET_r and ET_o are explained. ET_o values are more comparable (aerodynamically) with the crop present on Lysimeter # 1 that was usually grass. On the other hand, ET_r values are more comparable with crops planted in Lysimeter 2: sugar beets, potatoes, and alfalfa. Since all ET_o, ET_r and Lysimeter ET are exposed to similar weather conditions, a similar hourly variation of the ET values is expected.

b) Plot the hourly ET_o, ET_r and lysimeter ET versus the hour of the day on the same graph to determine if abrupt variations (spikes) of the Lysimeter ET are explained by a change in any of the weather parameters (as reflected in ET_o and ET_r).

c) Side plot of hourly K_{cr} (K_{cr} = ET/ ET_r). The hourly K_{cr} trend gives additional information about the consistency of the lysimeter measured ET relative to ET_o and ET_r. Since ET_o , ET_r and Lysimeter ET are exposed to similar weather conditions, a smooth variation in K_{cr} values with time of day is expected. The K_{cr} term is synonymous with ETrF.

d) Side plot hourly wind speed and direction. Abrupt changes in wind speed can explain electronic or mechanical noises in the lysimeter ET.

e) Plot both hourly ET values obtained from Lysimeter 1 and 2 in the same graph. If both Lysimeters show the same trend in ET values, including "spikeness", one can consider that the variations are valid.

Often spikes were present in Lysimeter reading. Some of these were caused by mechanical problems due to wind or human interactions. Some were caused by misreading of the ink charts or by electronic-induced noise.

An example of the spreadsheet designed to conduct the integrity analysis is shown in Fig. A.5

To correct the hourly lysimeter data, the following procedure was applied:

1) Sum the total measured ET for the day for each lysimeter. Daily ET valu`es (midnight to midnight) obtained from Kimberly Lysimeters are considered to be relatively precise (Wright, J.L 2002, personal communication) because they are independent of daytime variations. Therefore, corrections made to hourly data must preserve the total ET recorded for a specific day. In other words, any increase in ET for a period must be offset by adjustment of ET for some other period.

237

FIGURE A.5. Graphical Overlay used to conduct the Integrity Analysis of ET Data for Lysimeter 1 (grass) and Lysimeter 2 (Sugar Beets) for DOY = 246 of 1989

2) Check the occurrence of precipitation (P) and/or irrigation during the day. Because of the way Kimberly's Lysimeter ET was recorded, the precipitation values reported with the data are in fact P - ET , because ET values were generally assumed to be zero whenever precipitation occurred and was measured. In such cases estimations of the real ET and P value were made.

3) Data were first corrected by correcting any "compensating spikes". Compensating spikes are abrupt variations occurring for adjacent ET values (one being clearly too low and the other too high). Compensating spikes are common in weighing lysimeters and are caused by an error in measurement of lysimeter mass at the end of a single period. This occurred because ET is computed as a difference in mass for period to period end. Removal of compensating spikes was done by subtracting and adding their deviation from the general hourly trend of ET computed by

comparing with ET_o or ET_r values. In this adjustment the original 24 hour ET was preserved.

4) Correcting other poor values. The correction of obvious erroneous values during a given hour i , was made using several approaches. The primary approach was the one used by Itensifu (1998) which is based on smoothing the K_{cr} curve using adjacent K_{cr} values, as well as the general trend of the K_{cr} curve during the day, and then multiplying the smoothed K_{cr} by the hourly ET_r for that hour so that:

$$ET(Lysimeter)_i = (Kcr_{i-1} + Kcr_{i+1})/2 \times ET_{r,i} \tag{A.10}$$

In some cases, several hours (i) had to be skipped before a representative value for K_{cr} was usable.

The approach described by Eq. A.10 is based in the assumption that the hourly ET relatively to reference ET_r is expected to be fairly stable during the day, because of the "parallel" response of ET_o , ET_r, and Lysimeter ET, to the variation in weather parameters. This helps to distinguish weather effects from the electronic or mechanical noise. Again, the corrections made for a given day have to agree with the original 24 hour ET value.

A excel spreadsheet was created to evaluate the integrity of lysimeter data based on a similar one designed by Itensifu (1998). The spreadsheet layout is displayed in Fig. A.6, showing an example of spike correction.

The example of Fig. A.6 shows how the correction to lysimeter measurements was performed. In the upper graph ET for grass, ET for sugar beets was plotted with

ET_o and ET_r. In the second and third graph the value of K_{cr} for grass and sugar beets are displayed. Finally , in the lower graph wind speed and direction are shown. In general, small, random, spikes occurring at night were not corrected, since they occured during low ET and represent mean lysimeter error. In the illustrated example, the trend of ET values and K_{cr} for grass looked reasonable so they were not modified.

On the other hand, in the case of the sugar beet ET, two unusual values occurred at 11:00 and 12:00 in the form of to two consecutive spikes in the K_{cr} graph. No abrupt changes in wind speed could explain those variations in ET. In addition, the grass' lysimeter did not show the same rapid variation in ET values. These two values were flagged initially as questionable (flag=2) and corrected taking the average K_{cr} of the previous and succeeding periods using Eq. A.9.

As illustrated in the example of Figs. A.5, and A.6, only obvious erroneous values were corrected, so that the integrity of most of the hourly ET values was kept. All original lysimeter data were retained for posterity and corrected data were added as new columns as shown in Fig. A.6. As an interesting point, from the K_{cr} plots one can observe the stability of the K_{cr} values during daytime (i.e. ETrF), a feature that was taken into consideration when extrapolation of instantaneous to 24 hour ET values was needed from satellite estimates of ET using SEBAL.
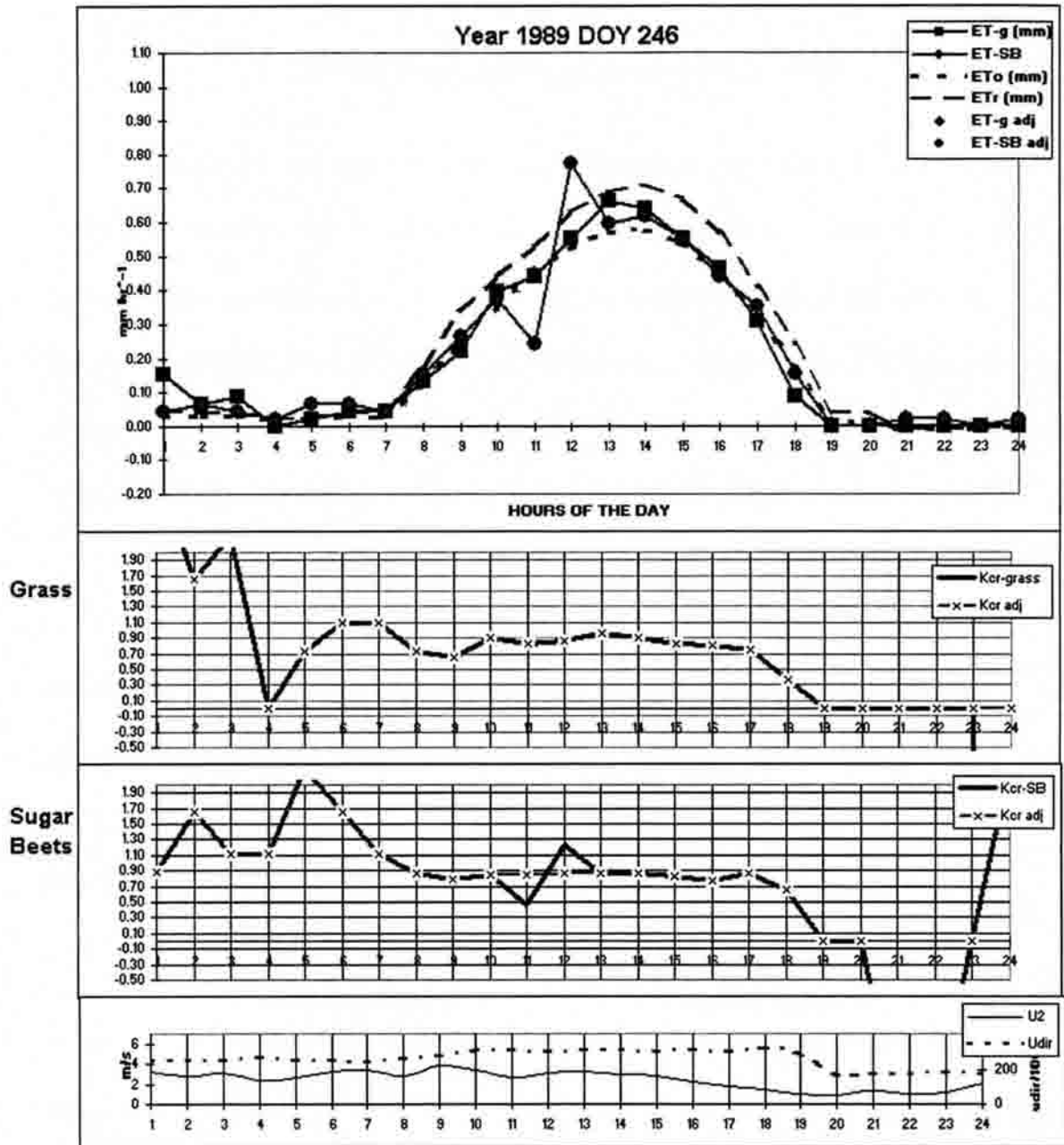
FIGURE A.6. Graphical Overlay used in Spike Correction for Lysimeter 1 (grass) and Lysimeter 2 (Sugar Beets) for DOY = 246 of 1989

Appendix B

Calculation of Reference Evapotranspiration

In this study, the energy balance at the cold pixel was defined considering that the evaporation at the cold pixel can be represented by an alfalfa covered surface which is transpiring at its potential rate. To estimate the evapotranspiration at the cold pixel, the Standardized ASCE Penman-Monteith alfalfa-reference equation developed by ASCE-EWRI (2002) was used. According to ASCE-EWRI (2002), this equation is equipped with hourly surface resistance values to perform well for hourly time steps.

The ASCE-EWRI standardized reference evapotranspiration equation allows the calculation of reference evapotranspiration for two different reference surfaces: a short crop having an approximate height of 0.12 m (similar to grass) and a tall crop with an approximate height of 0.50 m. (similar to alfalfa), using the following equation :

$$ET_{ref} = \frac{0.408 \Delta (R_n - G) + \gamma \dfrac{C_n}{T+273} u_2 (e_s - e_a)}{\Delta + \gamma (1 + C_d u_2)} \qquad (B.1)$$

where ET_{ref} is standardized reference crop evapotranspiration for short (ET_o) or tall (ET_r) surfaces [mm d^{-1} for daily time steps or mm h^{-1} for hourly time steps], R_n and G are the net radiation and soil heat flux respetively [MJ m^{-2} d^{-1} or MJ m^{-2} h^{-1}], e_s and e_a are the saturation and actual vapor pressure of the air [kPa] , C_n and and C_d are constants that change with reference crop type and calculation time step.

The coefficients C_n and C_d were developed assuming different surface resistance values for grass and alfalfa, and different time steps. In Table B.1 the different terms used in the calculation of ET_o or ET_r are shown.

The values of C_n and C_d for each time step and for the two different reference surfaces are depicted in Table B.2.

Calculation Procedures

The following equations are recommended by Allen et al (1998) and ASCE-EWRI (2002) to be used in the application of the standardized ASCE Penman-Monteith calculations. Because in this study hourly values of reference evapotranspiration are considered, only the corresponding equations for hourly calculations are presented. Daily values of reference evapotranspiration (ET_{r24}) were calculated by summing the corresponding hourly values of ET_r calculated from Eq. B.1.

TABLE B.1.   Penman Monteith Terms for Standardized Reference Evapotranspiration Equations (ASCE-EWRI, 2002)

Term	ET_o	ET_r
Reference vegetation height, h	0.12 m	0.50 m
Height of air temperature and humidity measurements, z_h	1.5 – 2.5 m	1.5 – 2.5 m
Height of wind measurements, z_w	2.0 m	2.0 m
Zero plane displacement height	0.08 m	0.08 m [a]
Latent heat of vaporization	2.45 MJ kg^{-1}	2.45 MJ kg^{-1}
Surface resistance, r_s, daily	70 s m^{-1}	45 s m^{-1}
Surface resistance, r_s, daytime	50 s m^{-1}	30 s m^{-1}
Surface resistance, r_s, nighttime	200 s m^{-1}	200 s m^{-1}
Value of R_n for predicting daytime	> 0	> 0
Value of R_n for predicting nighttime	≤ 0	≤ 0

a The zero plane displacement height for ET_r assumes the measurement is over grass.

TABLE B.2. Values for C_n and C_d to be used in Eq. B.1. ASCE –EWRI (2002)

Calculation Time Step	Short Reference, ET_o		Tall Reference, ET_r		Units for ET_o, ET_r	Units for R_n, G
	C_n	C_d	C_n	C_d		
Daily	900	0.34	1600	0.38	mm d^{-1}	MJ m^{-2} d^{-1}
Hourly during daytime	37	0.24	66	0.25	mm h^{-1}	MJ m^{-2} h^{-1}
Hourly during nighttime	37	0.96	66	1.7	mm h^{-1}	MJ m^{-2} h^{-1}

Latent Heat of Vaporization (λ)

Latent heat of vaporization is defined as the amount of energy that is required to evaporate a unit mass of water. The value of latent heat of vaporization is 2.45 MJ kg^{-1} when the air temperature is 20 °C, and it changes slightly as a function of the variation of the temperature of the air:

$$\lambda = 2.501 - (2.361 \times 10^{-3})\, T \qquad\qquad (B.2)$$

where λ is the latent heat of vaporization [MJ kg^{-1}], and T is the mean air temperature [°C]

Atmospheric Pressure (P)

The atmospheric pressure is calculated with the following equation:

$$P = P_o \left(\frac{T_K - \alpha_1 (z - z_o)}{T_{Ko}} \right)^{\frac{g}{\alpha_1 R}} \qquad\qquad (B.3)$$

where P is the atmospheric pressure at elevation z [kPa], P_o is the atmospheric pressure at sea level = 101.3 [kPa], z is the elevation [m], z_o is the elevation at reference level

[m], g= 9.807 [m s^{-2}], R is the specific gas constant = 287 [J kg^{-1} K^{-1}], α_1 is the lapse rate for moist air = 0.0065 [K/m], and T_{ko} is the reference temperature [K] at elevation z_o which is given by

$$T_{Ko} = 273.16 + T \tag{B.4}$$

where T is the mean air temperature for the time period of calculation [^oC]

Atmospheric Density (ρ)

The density of the air is calculated with the following equation:

$$\rho = \frac{1000\,P}{T_{Kv}\,R} = 3.486\frac{P}{T_{Kv}} \tag{B.5}$$

where: ρ is the atmospheric density [kg m^{-3}], R is the specific gas constant given by $R = 287$ J kg^{-1} K^{-1}, and T_{Kv} is the mean virtual temperature for period [K] which is computed as:

$$T_{Kv} = T_K\left(1 - 0.378\frac{e_a}{P}\right)^{-1} \tag{B.6}$$

where: T_K is the mean absolute temperature [K] : $T_K = 273.16 + T$ [^oC], and e_a is the actual vapor pressure [kPa].

An approximation of virtual temperature is given in ASCE (2002):

$$T_{Kv} \approx 1.01(T + 273) \tag{B.7}$$

Psychrometric Constant (γ)

The psycrometric constant is defined as follows:

$$\gamma = \frac{C_p P}{\varepsilon \lambda} = 0.00163 \frac{P}{\lambda}$$

(B.8)

where γ is the psychrometric constant [kPa°C^{-1}], C_p is the specific heat of moist air = 1.013 x 10^{-3} MJ kg^{-1} °C^{-1}, P is the atmospheric pressure [kPa], ε is the ratio of molecular weight of water vapor/dry air = 0.622, and λ is the latent heat of vaporization [MJ kg^{-1}].

Slope of the Saturation Vapor Pressure
Curve

To calculate the slope of the saturation vapor pressure vs air temperature curve, at a given temperature, the following equation is presented in ASCE-EWRI (2002):

$$\Delta = \frac{2504 \exp\left(\frac{17.27 \, T}{T + 237.3}\right)}{(T + 237.3)^2}$$

(B.9)

where: Δ is the slope of vapor pressure curve [kPa°C^{-1}], and T is the air temperature [°C] For hourly calculations T refers to the hourly mean air temperature.

Saturation Vapor Pressure (e$_S$)

The saturation vapor pressure equation is:

$$e^\circ(T) = 0.6108 \exp\left(\frac{17.27 \, T}{T + 237.3}\right)$$

(B.10)

where: $e^o(T)$ is the saturation vapor pressure function [kPa], and T is the air temperature [°C]. For hourly calculations T refers to the hourly mean air temperature .

Actual Vapor Pressure (e_a)

Allen et al (1998) presented procedures to calculate actual vapor pressure from either dewpoint temperature, relative humidity data, or wet and dry bulb temperature. In this study, dewpoint temperature was utilized. By definition, the actual vapor pressure (e_a) is the saturation vapor pressure at the dewpoint temperature (T_{dew}) [°C], and it can be calculated with the following equation:

$$e_a = e^o(T_{dew}) = 0.6108 \exp\left[\frac{17.27\ T_{dew}}{T_{dew} + 237.3}\right]$$ (B.11)

where T_{dew} is the dewpoint temperature

Net Radiation (R_n)

The calculation of net radiation is calculated as described by Eq. A.8 of the Appendix A.

$$R_n = (1-\alpha)Rs - \left[\sigma T^4(0.34 - 0.14\sqrt{e_a})(1.35\frac{R_s}{R_{so}} - 0.35)\right]$$

where R_n is the net radiation , σ is the Stefan-Boltzmann constant [2.043 10^{-10} MJ K^{-4} m^{-2} h^{-1}], T is the mean hourly air temperature [K] , e_a actual vapor pressure [kPa], R_s/R_{so} relative solar radiation (limited to ≤ 1.0), R_s is the measured solar radiation , and R_{so} is the calculated clear-sky radiation.

Soil Heat Flux Density (G)

For hourly calculations, the soil heat flux beneath a dense cover of alfalfa having a height of h = 0.5 m and LAI of about 4.5, is calculated as :

$$G_{hr\,daytime} = 0.04\,R_n \tag{B.13}$$

$$G_{hr\,nighttime} = 0.2\,R_n \tag{B.14}$$

and for full cover grass having a height of 0.12 m:

$$G_{hr\,daytime} = 0.1\,R_n \tag{B.15}$$

$$G_{hr\,nighttime} = 0.5\,R_n \tag{B.16}$$

Appendix C

Adaptation of Sebal in Erdas – Imagine Modelmaker

R. Trezza and M. Tasumi

In this appendix the general format of the SEBAL model used in this study is presented. The model was coded using the Model Maker in ERDAS Imagine 8.5 Remote Sensing Software. The codification followed the equations included in Chapters III , IV, and V. The SEBAL applied in this work is comprised by 12 sub-models.

The ERDAS Imagine Model Maker

ERDAS Imagine Model Maker is a user-friendly model development tool. In the Model Maker, model components (inputs, calculations, and outputs) are visualized so that the model composition and computational flow is easily tracked. Figure C.1 shows the primary dialogs used in ERDAS Imagine Model Maker. The "Raster Object" represents raster data, either for input/output images and for storage of intermediate calculation results. For input data, the data name and the stored location are specified. For output data, data type and names are specified. The "Scalar Object" is used for scalar data input (i.e. constants), and the "Table Object" is used for input of a series of scalars as a table. The "Function Definition" is for defining the calculation equations and programming functions. These dialogs are sequentially connected by arrows. Figure C.2 shows an example of an small model.
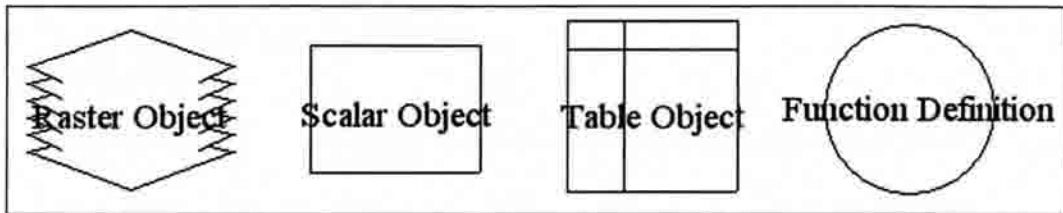
FIGURE C.1.   Shapes of Primary Dialogs in ERDAS Imagine Model Maker.

Pre-Calculations for using SEBAL in
Mountainous and Sloping areas

Before beginning the surface energy balance computations for each pixel, some

parameters that are needed for the estimation of incoming solar radiation are calculated,

as described in the following PM01, PM02, PM03, PM04, PM05, and PM06 sub-

models. The application of these models are only required if the image has mountains or

sloping surfaces. If the study area is approximately flat, then these sub-models can be

skipped.
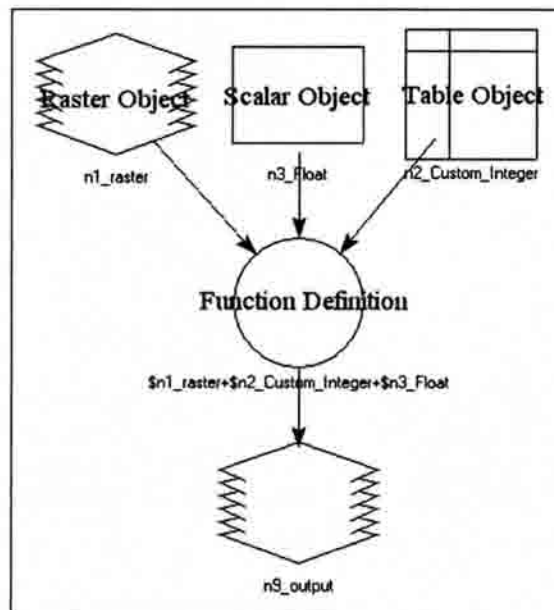
FIGURE C.2.   Model Example in ERDAS Imagine Model Maker.

PM01: Calculations of Sine and Cosine of
Slope and Aspect

Input Images: Surface slope and aspect images derived by DEM

Output Images: sin(slope), sin(aspect), cos(slope), and cos(aspect)

Description: This model is for calculating the sin and cosine of surface

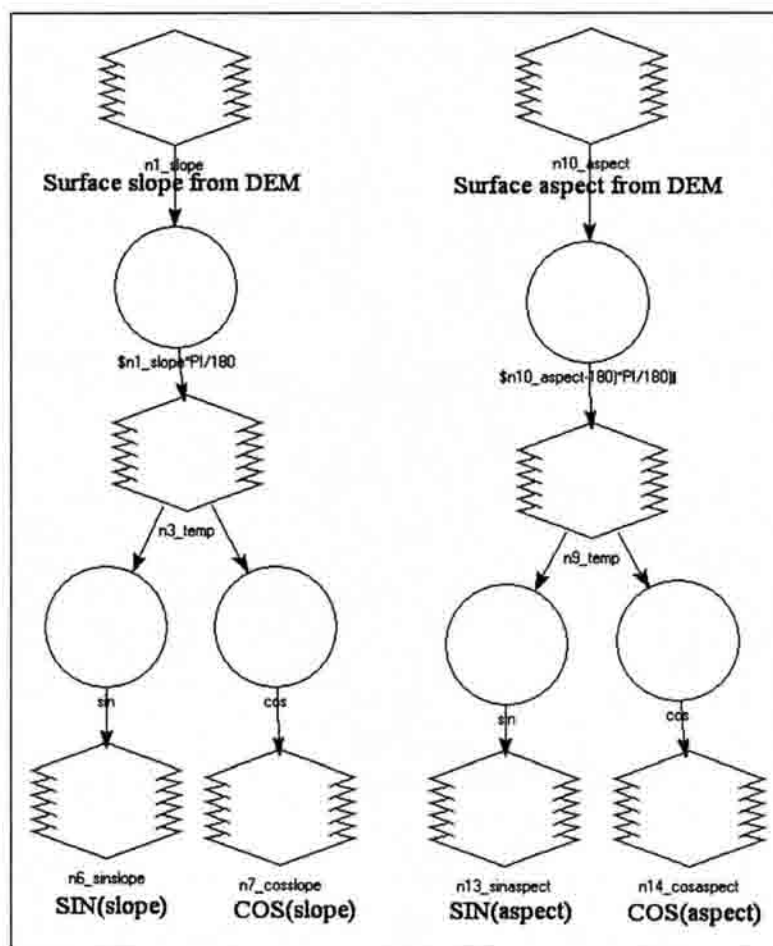slope and aspect. These four outputs are used for later

models.

FIGURE C.3.   Flow Chart of the PMO1 Model

PM02: Cos(θ) Calculation

Input Images: sin(slope), sin(aspect), cos(slope), and cos(aspect)

Input Values: calculated δ (declination), φ (latitude), and ω (solar angle) values

for the image

Output Images: cos(θ)

Description: This model is for calculating cosine of solar incident angle (θ)

for each pixel. Because SEBAL Mountain Model calculates all

components of the energy balance in Wm^{-2}, for a horizontal

equivalent surface, the cos(θ) is divided by cos(slope).
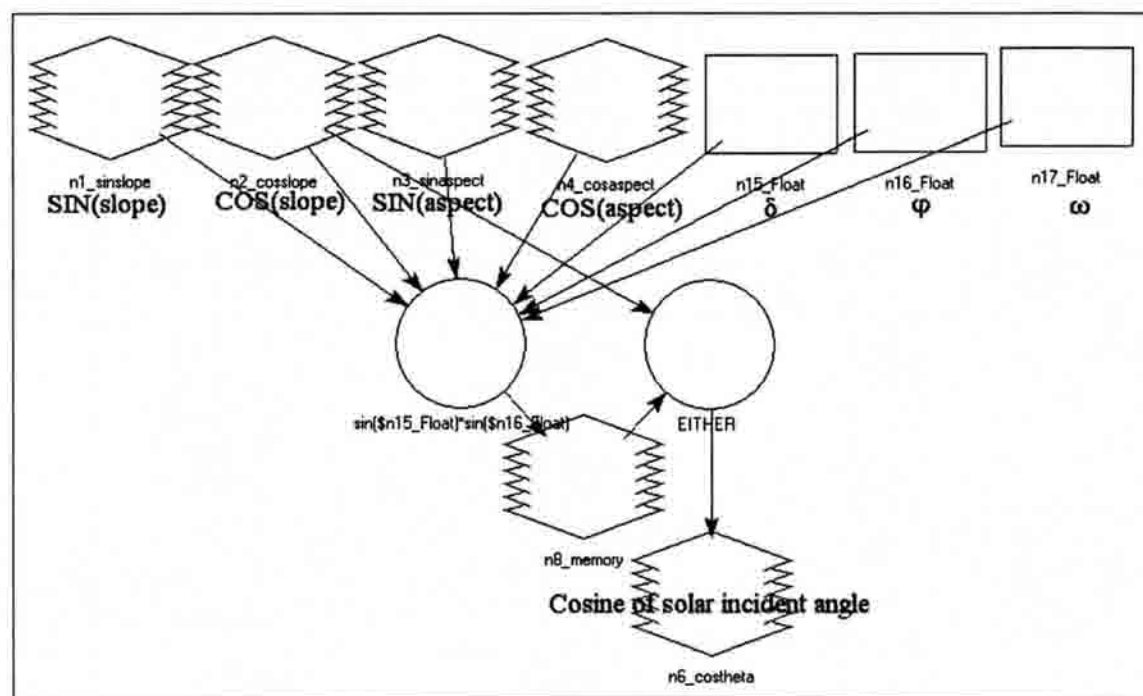
FIGURE C.4.   Flow Chart of the PMO2 Model

PM03: Instantaneous R_{SO} Calculation

Input Images: slope (derived by Digital Elevation Model -DEM), $\cos(\theta)$, and DEM (elevation)

Input Values: calculated $R_{a(inst)}Flat$, d_r, K_t, $\sin(\phi_{inst})$, and $e_{a(inst)}$

Output Images: $R_{so(inst)}Flat$, and $R_{so(inst)}Pixel$

Description: This model is for calculating instantaneous R_{SO}, both for the actual slope/aspect conditions of each pixel and for a equivalent horizontal pixel located at the same elevation. The value of R_{SO} for a flat area depends on the pixel elevation, so that this value is also stored as a raster image. The calculated $R_{so(inst)}$ images are used at the very end of the SEBAL procedure (Model M05).
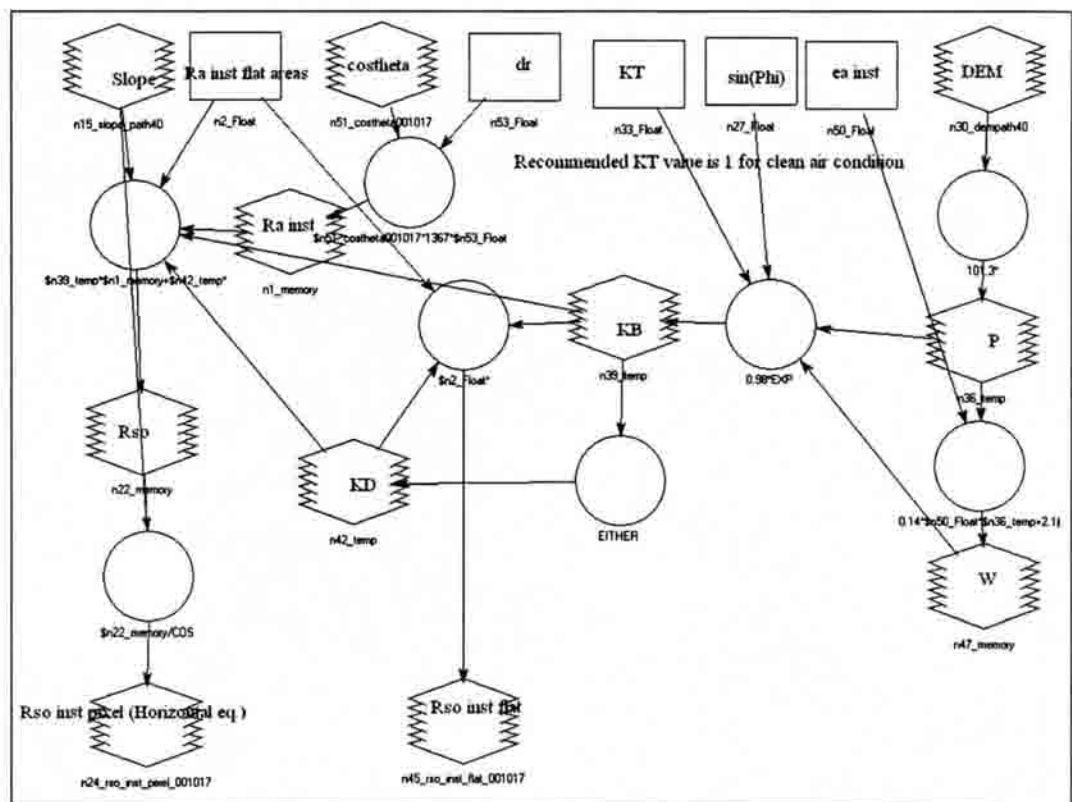

FIGURE C.5.   Flow Chart of the PMO3 Model

PM04: 24 Hours R_a Calculation

Input Images: sin(slope), sin(aspect), cos(slope), and cos(aspect)

Input Values: calculated $\sin\delta\sin\varphi$, $\sin\delta\cos\varphi$, $\cos\delta\sin\varphi$, $\cos\delta$, $\omega_{(sunrise)}$, $\omega_{(sunset)}$, and G_{sc}_related_constant..

Output Images: $R_{a(24)}$

Description: This model is for calculating 24 hour R_a for sloping surfaces, which is later used to 24 hour R_{so} estimation. This model is the most complicated model in SEBAL (Appendix D). The "G_{sc}_related_constant" is the product of d_r and the solar constant (1367 Wm^{-2}), and it is previously calculated in a spreadsheet to reduce coding in ERDAS

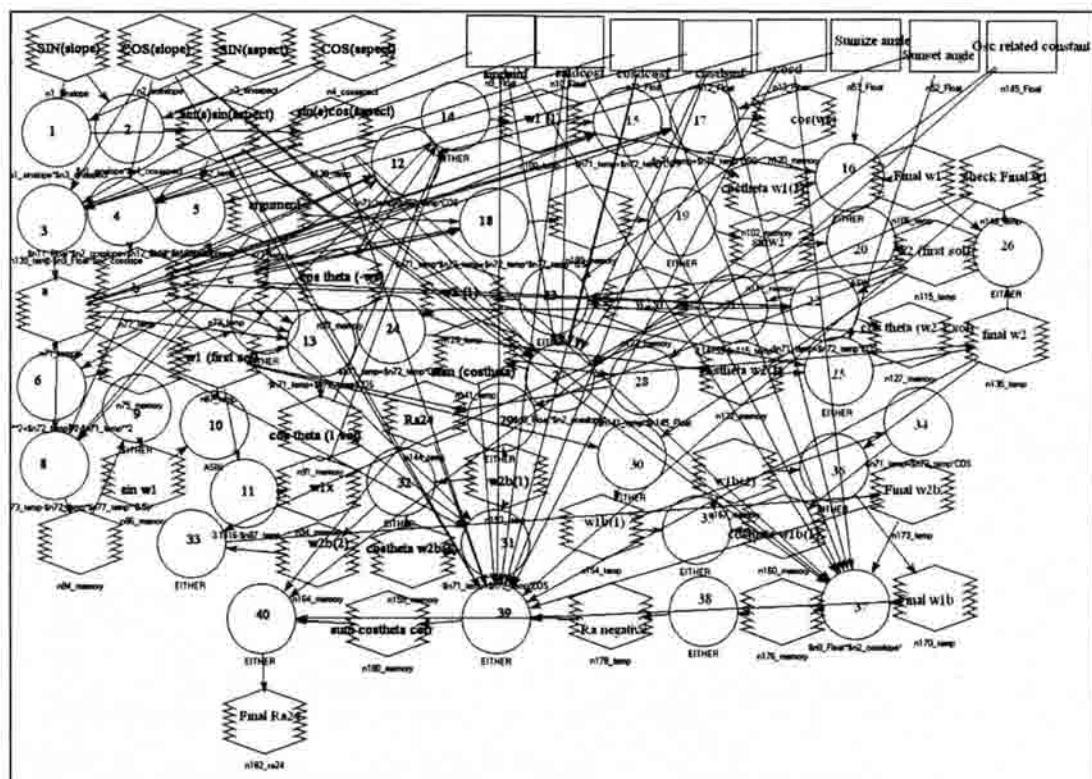FIGURE C.6.   Flow Chart of the PMO4 Model

PM05: 24 Hour R_{so} Calculation

|	
Input Images:	slope (derived by DEM), $R_{a(24)}$, and DEM
Input Values:	calculated $R_{a(24)}Flat$, K_t, $\sin(\phi_{(24)})$, and $e_{a(24)}$
Output Images:	$R_{so(24)}Flat$, and $R_{so(24)}Pixel$
Description:	This model is similar to the model for instantaneous R_{so} calculation. This calculates 24 hour R_{so}, both for a horizontal flat surface and for the actual value of each pixel. The value of R_{so} depends on the elevation, so that this value is also stored as a raster image.
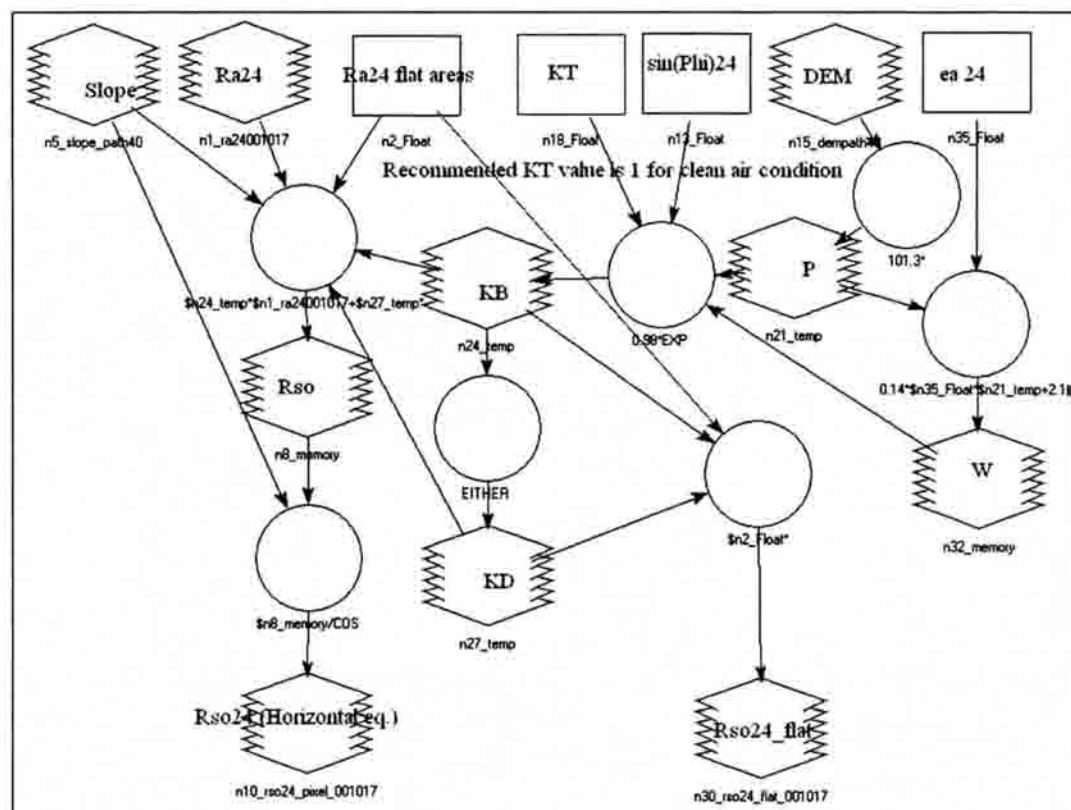
FIGURE C.7.   Flow Chart of the PMO5 Model

PM06: Shortwave Transmittance
Calculation

Input Images: DEM

Output Images: τ_{SW}

Description: This simple model calculates shortwave Atmospheric trans-
mittance by Eq. 4.12, therefore the estimated transmittance is
only function of DEM. The use of this simplified method
reduces operation time when multiple dates of the same image
need to be processed. In Southern Idaho where atmospheric
conditions are related to a clean, and dry environment,
application of Eq. 4.8 and Eq 4.12 produce similar results.

**Sebal Models for Computing The Surface
Energy Balance**

The following models are required in SEBAL to perform the surface energy
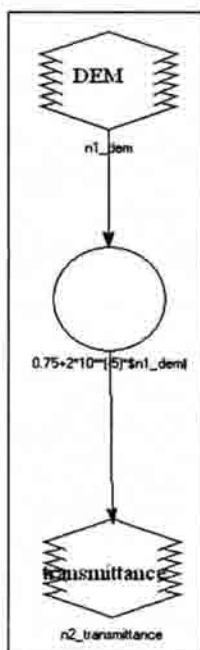
balance for each pixel

FIGURE C.8.   Flow Chart of the PMO6 Model

l.M01: Calculation of Surface Reflectances,
Vegetation indices and Surface Temperature

Input Images: Landsat TM/ETM+ 7 band data, $\cos\theta$, τ_{sw}, and DEM

Input Values: d_r, R_A, R_{sky}, τ_{NB}, Image specific constants (LMIN, LMAX, ESUN$_\lambda$, w_λ, K_1 and K_2 for Band 6 calibration), and representative elevation of the study area.

Output Images: α, NDVI, LAI, ε_0 (broadband emissivity), T_s, and T_{s_DEM}

Description: This model derives the basic information from the satellite image. The radiometric surface temperature correction terms (R_A, R_{sky} and τ_{NB}) can be calculated with an atmospheric model like MODTRAN or set as 0,0,1 respectively, if uncorrected temperature is being used. For flat areas , DEM is not used, $\cos\theta$, and τ_{sw} are fixed values (if Eq.4.12 is applied), Also,for flat areas $T_{s(DEM)} = T_s$.
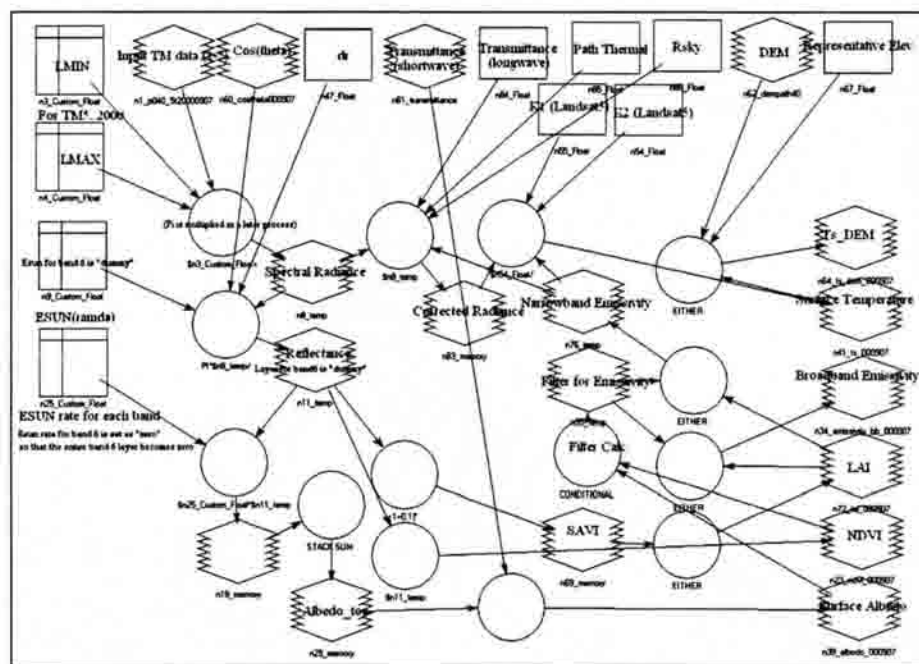

FIGURE C.9.   Flow Chart of the MO1 Model

M02: R_n and G calculations

Input Images: $\cos\theta$, τ_{sw}, α, ε_o, T_s, NDVI, Landuse Map, and DEM

Input Values: d_r, T_{s_dem} (cold_pixel), and representative elevation

Output Images: R_n, and G

Description: This model calculates R_n and G values.   Landuse Map previously created is used for discriminating   special surfaces such as water and snow, for application of different G equations and prediction of aerodynamic roughness. If Landuse map is not available, negative values of NDVI can be used as an indicator of the presence of water.   DEM is used to adjust the value of $R_L\downarrow$ for differences in pixel elevation.   In flat areas, $R_L\downarrow$ $\cos\theta$, and τ_{sw} are taken as constants. The T_{s_DEM} (cold_pixel) is used for the calculation of $R_L\downarrow$.

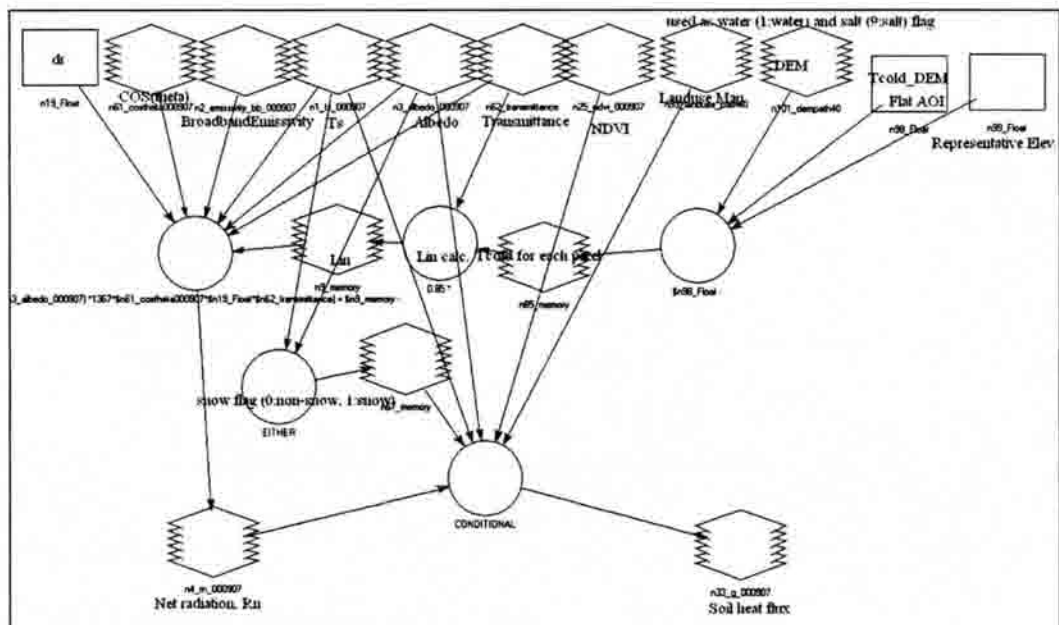FIGURE C.10.   Flow Chart of the MO2 Model

<u>M03:</u> z_{om}, u_{200}, $u*(1st)$ and $r_{ah}(1st)$
<u>Calculation (First Guesses of , $u*$ and r_{ah})</u>

       Input Images: LAI, Surface slope, Landuse Map, and DEM

       Input Values: u_{200} at weather station, Elevation at weather station

       Output Images: z_{om}, u_{200} (wind speed at 200 m), $u*(1st)$, and $r_{ah}(1st)$

       Description: This model calculates z_{om}, u_{200}, $u*(1^{st} guess)$ and $r_{ah}(1^{st} guess)$. z_{om} values are basically assigned by the landuse map, and LAI is used to estimate z_{om} for agricultural areas only. Slope map and DEM are used for mountain correction of z_{om} and u_{200}. In the flat areas, mountain correction is not applied so that slope map and DEM are not required as input. The u_{200} map is assumed constant in flat areas.

FIGURE C.11.   Flow Chart of the M03 Model

M04: H Calculation

Input Images: T_s, $T_{s(DEM)}$, z_{om}, u_{200}, $u*(1st)$, $r_{ah(1st)}$, and DEM

Input Values: The final values of "a" and "b" on Eq. 3.33 (after Monin-Obukov iteration, made in spreadsheet) for developed dT function.

Output Images: H

Description: The Monin-Obukov iterative process to compute sensible heat is applied in this model. If the area is flat DEM is not required. Coefficients and b for the Ts versus dT function need to be calculated in spreadsheet.

M05: ETrF$_{(24)}$ and ET$_{(24)}$ Calculation

Input Images: T_s, R_n, H, G, $R_{so(inst)Flat}$, $R_{so(inst)Pixel}$, $R_{so(24)Flat}$, and $R_{so(24)Pixel}$

Input Values: Instantaneous and 24 hour ET_r

Output Images: ETrF$_{(24)}$ and ET$_{(24)}$

Description: This model calculates instantaneous and 24 hour ET. R_{so} maps are for radiation correction for sloped land surfaces (as explained in Chapter V). For flat areas, $R_{so(inst)Flat}$, $R_{so(inst)Pixel}$, $R_{so(24)Flat}$, and $R_{so(24)Pixel}$ are not needed, therefore, ETrF$_{(inst)}$ = ETrF$_{(24)}$.

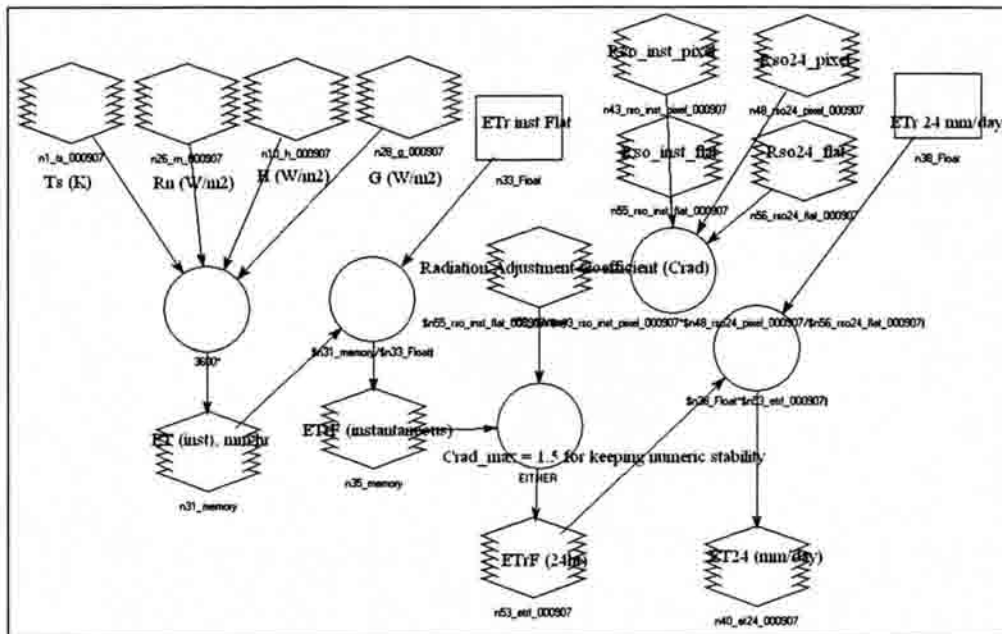Details of the calculation of R_{so} are included in Appendix E and Chapter V.

FIGURE C.12.   Flow Chart of the MO5 Model

M06: Seasonal ET Calculation

|	
Input Images:	$ETrF_{(24)}$ for each period
Input Values:	Cumulative ET_r for each period
Output Images:	$ET_{(season)}$
Description:	In this model, the cumulative ETr for each period is directly assigned in the equation in the function definition dialog. Therefore, these values are not shown in the model. If cloud masked areas are present at least at one date, the user must determine how the masked area is to be treated. In this study, $ETrF_{(24)}$ values at cloud masked areas were interpolated using neighbor images.
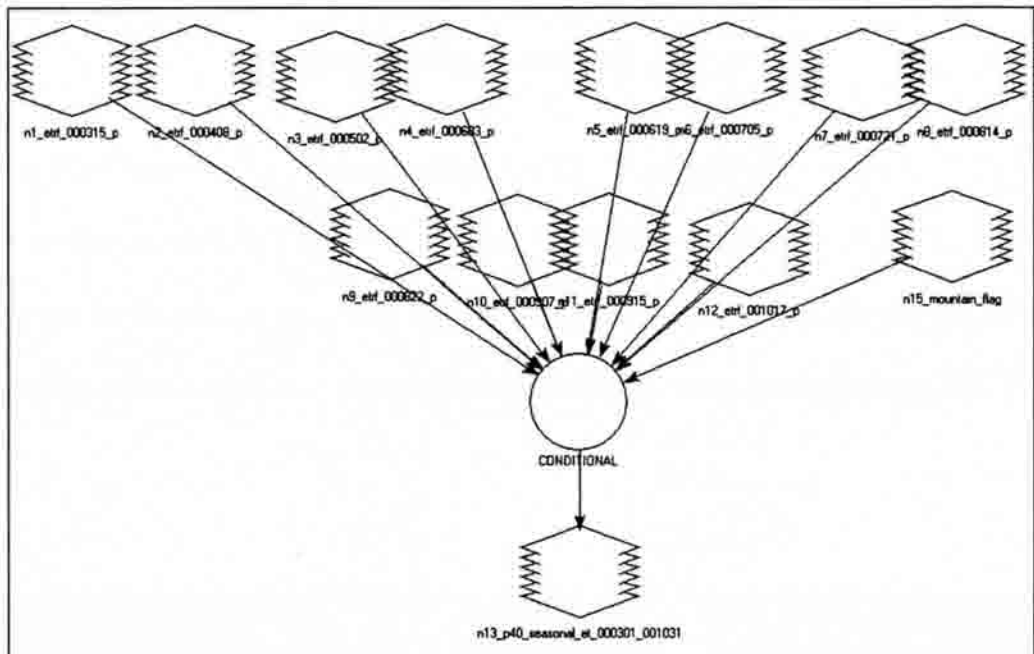
FIGURE C.13.   Flow Chart of the MO6 Model

Appendix D

## Lysimeter Field Spectral Information

In this Appendix, the location of the 4 pixels taken around Lysimeter 2 to calculate average values of predicted ET from SEBAL is included. In all the graphs, the picture at the left is the Landsat 5 TM band 6 thermal information, and the picture in the right is a false color composite. Bellow each graph is the corresponding image date.
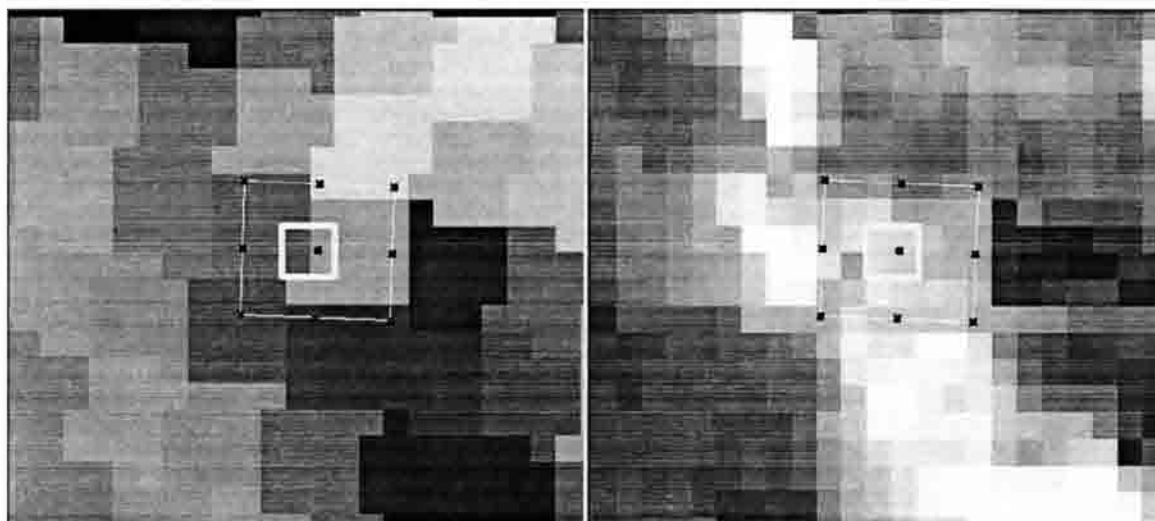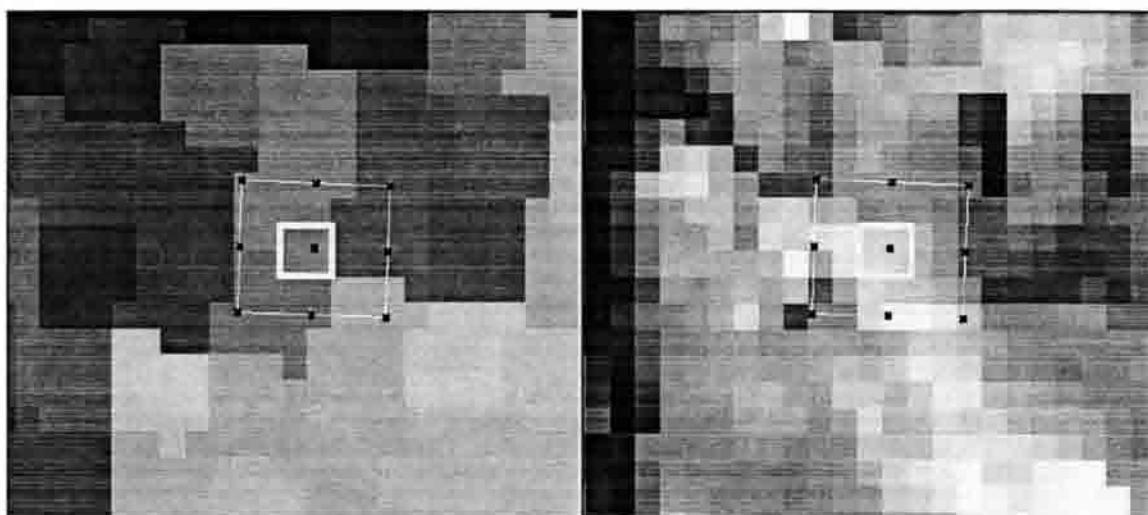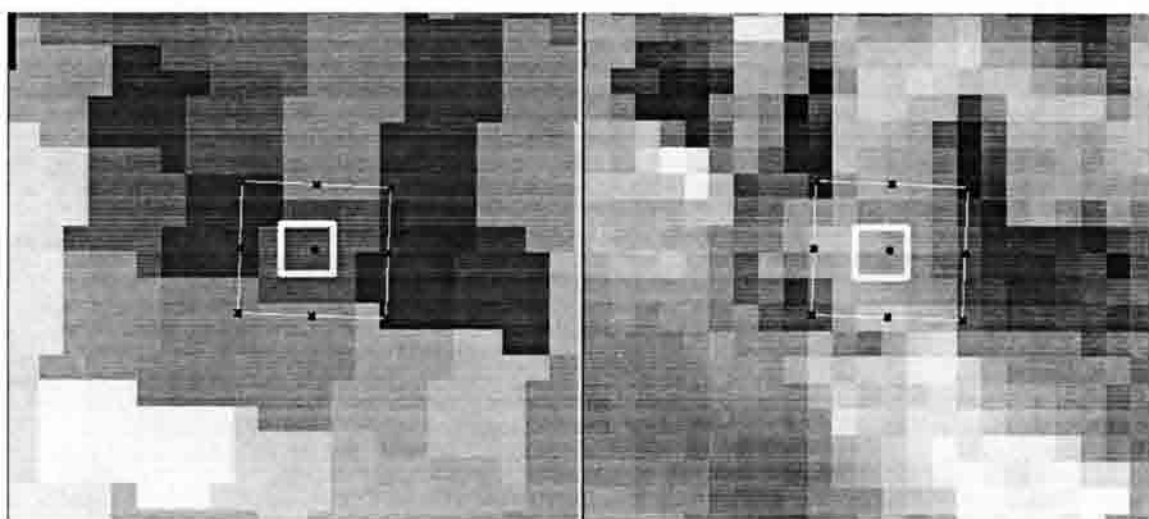

04/18/1989
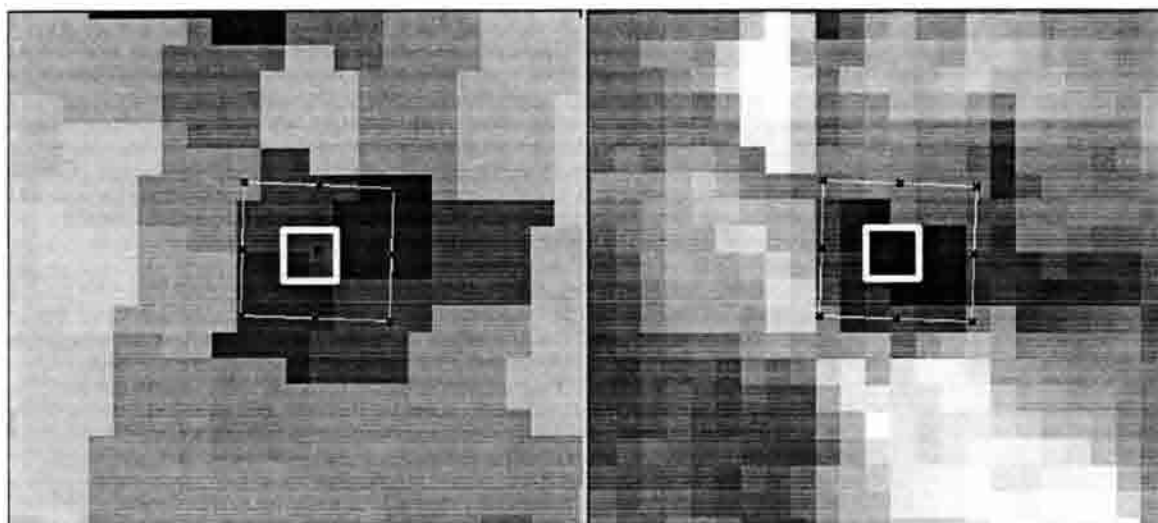
05/04/1989
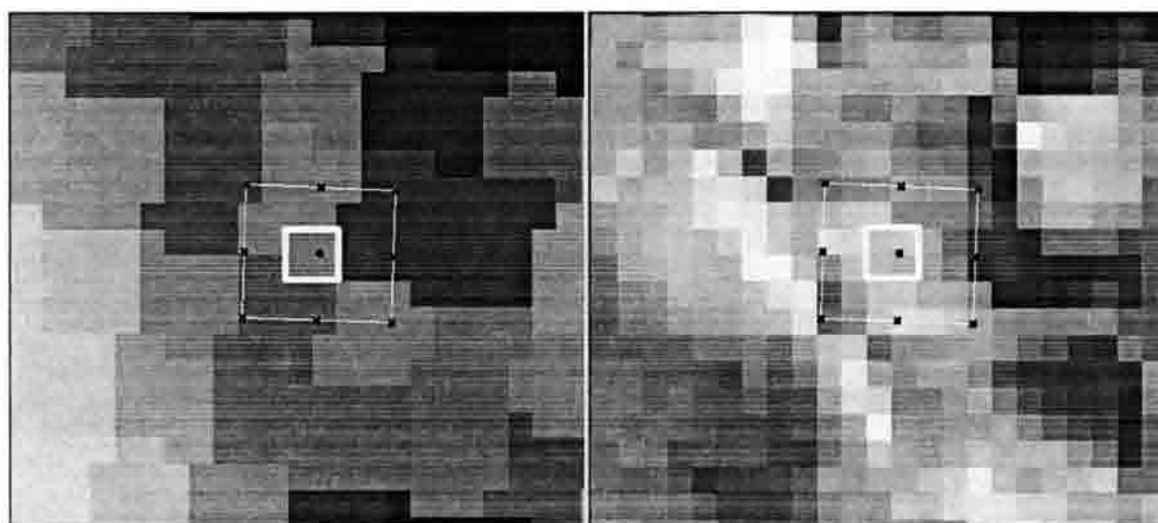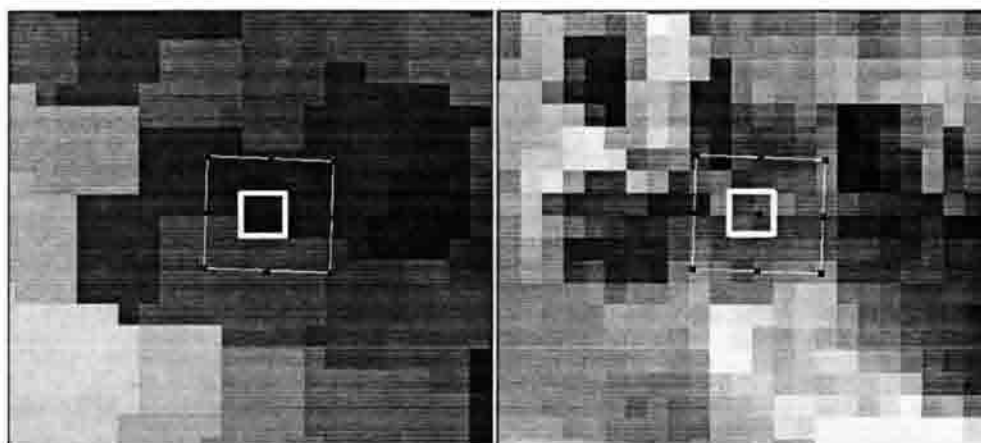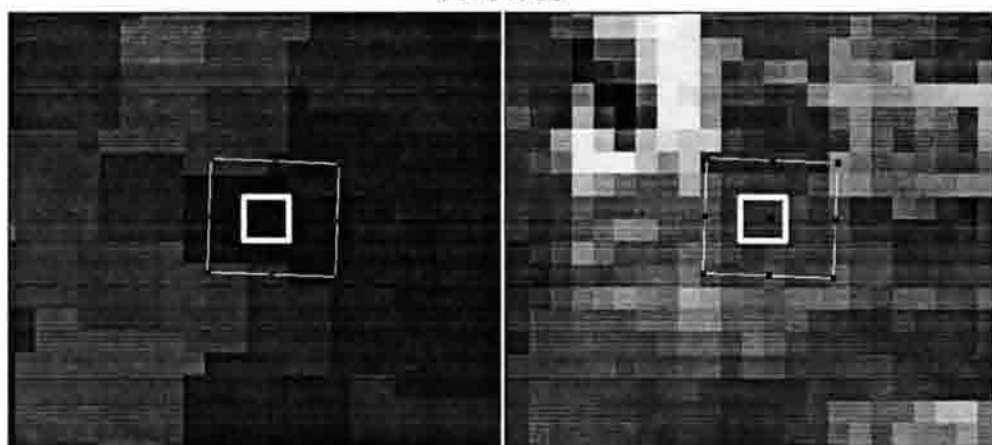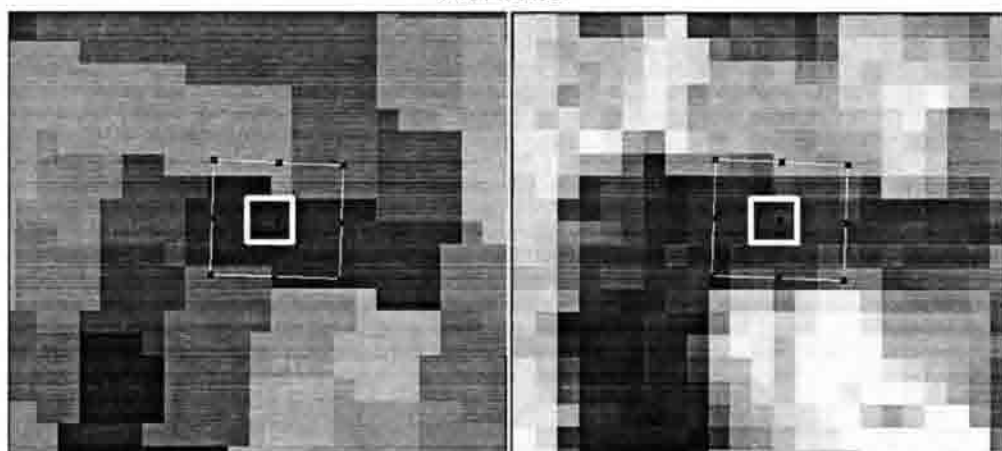
05/20/1989

06/05/1989

06/21/1989

07/07/89

07/23/89

09/25/89

Appendix E

Estimation of Clear Sky Incoming Radiation

In this Appendix, the procedure for obtaining clear sky solar radiation (R_{so}) is presented. All the equations were taken from Allen et al (1998) and ASCE-EWRI (2002)

Estimation of Instantaneous Clear Sky Radiation for Flat Areas

To obtain the amount of radiation received in a flat surface in a given moment, and considering clear sky conditions, the following equation was applied:

$$R_{so(inst)Flat} = (K_B + K_D)R_a \qquad (E.1)$$

where $R_{so(inst)Flat}$ is the value of instantaneous value of R_{so} for a flat surface, where K_B is the clearness index for direct beam radiation [-], and K_D is the corresponding index for diffuse beam radiation [-], which is calculated as follows:

$$K_B = 0.98 \exp\left[\frac{-0.00146\,P}{K_t \sin\phi} - 0.075\left(\frac{W}{\sin\phi} \right)^{0.4} \right] \qquad (E.2)$$

where K_t is a turbidity coefficient, $0 < K_t \le 1.0$ where $K_t = 1.0$ for clean air and $K_t = 0.5$ for extremely turbid, dusty or polluted air, P is the atmospheric pressure [kPa], ϕ is the angle of the sun above the horizon [radians], and W is the precipitable water in the atmosphere [mm] that is computed as:

$$W = 0.14\,e_a\,P + 2.1 \qquad (E.3)$$

where W is the precipitable water in the atmosphere [mm], ea is actual vapor pressure [kPa], and, P is the atmospheric pressure [kPa].

The diffuse radiation index is computed from K_B as :

$$
\begin{aligned}
K_D &= 0.35 - 0.36 K_B \quad \text{for } K_B \geq 0.15 \\
K_D &= 0.18 + 0.82 K_B \quad \text{for } K_B < 0.15
\end{aligned}
$$

(E.4)

For instantaneous R_{so} calculation, $\sin\phi$ is calculated by:

$$
\sin\phi = \sin\varphi\sin\delta + \cos\varphi\cos\delta\cos\omega
$$

(E.5)

where, φ is latitude in radians (positive for northern hemisphere), δ is solar declination (positive in summer in northern hemisphere), ω is hour angle. "$\omega = 0$" at solar noon, ω is negative in morning and ω is positive in afternoon.

Solar declination (δ) is calculated by:

$$
\delta = 0.409\sin\left(\frac{2\pi}{365}\cdot \text{DOY} - 1.39\right)
$$

(E.6)

where, DOY is the sequential day of year (= Julian day). Use 366 instead of 365 for leap years.

Hour angle (ω) is calculated by:

$$
\omega = \frac{\pi}{12}\left[\left(t + \frac{L_z - L_m}{15} + S_c\right) - 12\right]
$$

(E.7)

where, t is local standard time (daylight saving time should not be applied), L_z is longitude of the center of the local time zone (degrees west of the Greenwich), L_m is longitude of the measurement site (degrees west of the Greenwich), and S_c is seasonal correction for solar time calculated by the next equation:

$$S_c = 0.1645\sin\left(\frac{4\pi(DOY-81)}{364}\right) - 0.1255\cos\left(\frac{2\pi(DOY-81)}{364}\right) - 0.025\sin\left(\frac{2\pi(DOY-81)}{364}\right)$$ (E.8)

Estimation of 24 hours Clear Sky Radiation for Flat areas

To estimate the value of Rso corresponding to a 24 hour period, and for a flat surface, the following equation was applied

$$R_{so(24)Flat} = (K_B + K_D)R_a 24$$ (E.9)

To obtain the coefficients KB and KD, Eqs. (E.2) and (E.4) also used, considering daily average values of ea and air temperature. The value of sin(φ) is calculated for 24 hours applications as:

$$\sin\phi_{24} = \sin\left[0.85 + 0.3\varphi\sin\left(\frac{2\pi}{365}\cdot DOY - 1.39\right) - 0.42\varphi^2\right]$$ (E.10)

Appendix F

Parameterization of Surface Variables

Tasumi, M., R.G Allen, R. Trezza, and J.L Wright

In this appendix the development of functions to describe surface parameters are included. These functions were defined from data collected by Dr. J.L. Wright at the USDA/ARS facility located at Kimberly, Idaho.

LAI versus Crop Height Relationship

Wright (2002, personal communication) periodically measured vegetation height (h) and leaf area index (LAI) at the lysimeter 2 site. This information was used to develope a general relationship between h and LAI that can be used to predict height from LAI. Table F.1 shows the different years and crops that were used to developed the mentioned relationships.

TABLE F.1   Different Crops Grown on Lysimeter 2 where LAI and Vegetation Height Information was Measured by Dr. J.LWright (Wright, Personal Communication 2002)

Year	Crop
1971	Alfalfa
1972	Potatoes
1973	Beans
1974	Beans
1975	Beets
1976	Corn
1977	Peas
1978	Wheat
1979	Wheat

Figure F.1 shows a plot of LAI and h for the different crops included in Table

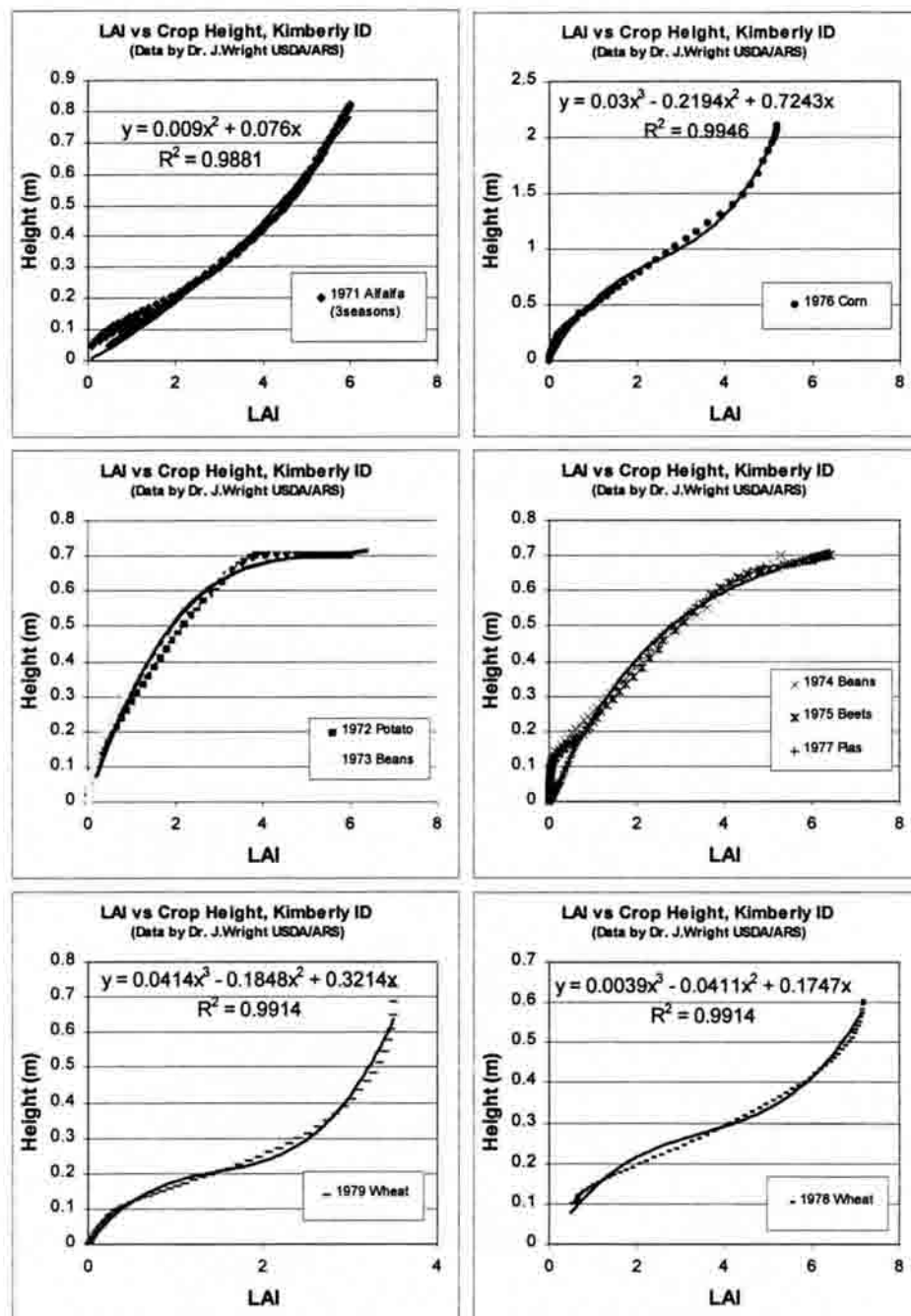F.1 as well as polynomial equations that produced the best fit of the observed data

FIGURE F.1. Relationships Between LAI versus Height for Different Crops

Figure F.2 shows a plot of LAI versus vegetation height values for all crops included in Table F.1. The mentioned figure displays a straight line that best described a linear relationship between the two variables for most of the crops. This line fails to describe the h versus LAI behavior for corn, which has a large height/LAI ratio, but it is able to give a reasonable estimation for the majority of crops (alfalfa, potatoes, beans, beets, peas, and wheat). The equation that produced the most reasonable estimation of vegetation height (h) from LAI for all the crops (except corn) is the following:

$$h = 0.15 * LAI \tag{F.1}$$

where h is the vegetation height and LAI is the leaf area index
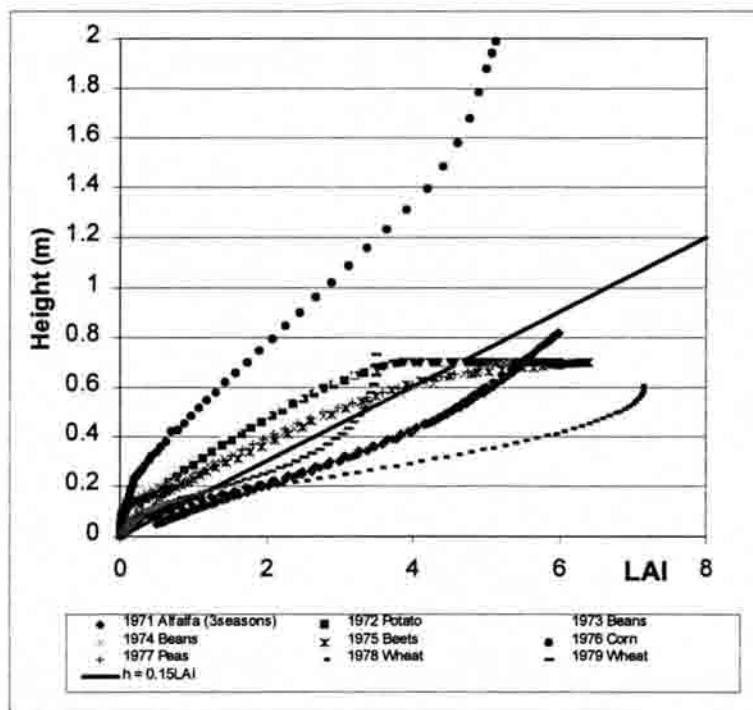

FIGURE F.2.   Development of a Relationship Between Height and Leaf Area Index for Crops Presented at the Kimberly Lysimeters.

Because of differences in shapes of curves for individual crops, there was not justification to fit a general curvilinear equation. The development of Eq. F.1 was necessary to predict H from LAI in SEBAL where specific crop type was unknown.

Surface Roughness

Surface Roughness for Agricultural Areas

For agricultural areas surface roughness (z_{om}) was estimated combining Eq. F.1 and the following equation, commonly used to estimate z_{om} from vegetation height (Brutsaert, 1982):

$$z_{om} = 0.123 * h \tag{F.2}$$

Therefore, the equation used to estimate z_{om} from vegetation height for agricultural areas used in this study is the following:

$$z_{om} = 0.018 * LAI \tag{F.3}$$

The value of LAI was estimated from SAVI using the relationship developed by Bastiaanssen (1998):

$$LAI = -\frac{\ln\left(\dfrac{0.69 - SAVI_{L=0.1}}{0.59}\right)}{0.91} \tag{F.4}$$

where $SAVI_{L=0.1}$ is the value of SAVI calculated with Eq. 4.26 and considering L=0.1. The value of L=0.1 minimized the standard deviation between measured values of LAI and predicted vales of LAI in Eq. F.4 (Tasumi, 2003). It is important to note that Eq. F.4

using the coefficients by Bastiaanssen (1998) overestimated LAI of Idaho crops when the commonly used value of L=0.5 is used.

Surface Roughness for other Surfaces

Values of z_{om} for other surfaces were assigned using common values extracted from literature (Brutsaert, 1982; Oke, 1996, Jensen, 2000). In Table F.2 the different values of z_{om} for each surface identified in the study area are included. To assign the value of z_{om} for each corresponding surface, a land classification was performed using Landsat 5 TM and 7 ETM+ imagery corresponding to path 39, and 40, and rows 29, 30, and 31.

TABLE F.2.   Surface Roughness for Each Landuse Type, Applied for the Study Area

Landuse	z_{om} (m)
Agriculture	0.018 * LAI (min = 0.005)
Water	0.0005
City	0.2
Forest	0.5
Desert Grassland	0.02
Desert Sage Brush	0.1
Salty Soil	0.002
Basalt Rock	0.07
Mountain Bare Soil	0.05
Mountain Forest	0.5
Snow	0.005

Landuse Map

In this study, a map was produced to describe the general use of the lands in the area. Unsupervised classification was used to generate 13 different classes of landuse types : water, city, agricultural, forest, grassland, sagebrush, bare soil, burned areas, salty areas, basalt, wetlands, forest in mountains (slope > 5°) , and bare soil in mountains

(slope > 5°), included in Table F.2. These classes were associated with different values

of surface roughness, needed for the computation of sensible heat. In the Kimberly area,

as it can be seen in Fig. F.3. most of the lands are dedicated to agricultural purposes

(agricultural fields and bare soil). There are also desert areas with grass and sage brush

as the main types of vegetation as well as water bodies. This image included also the

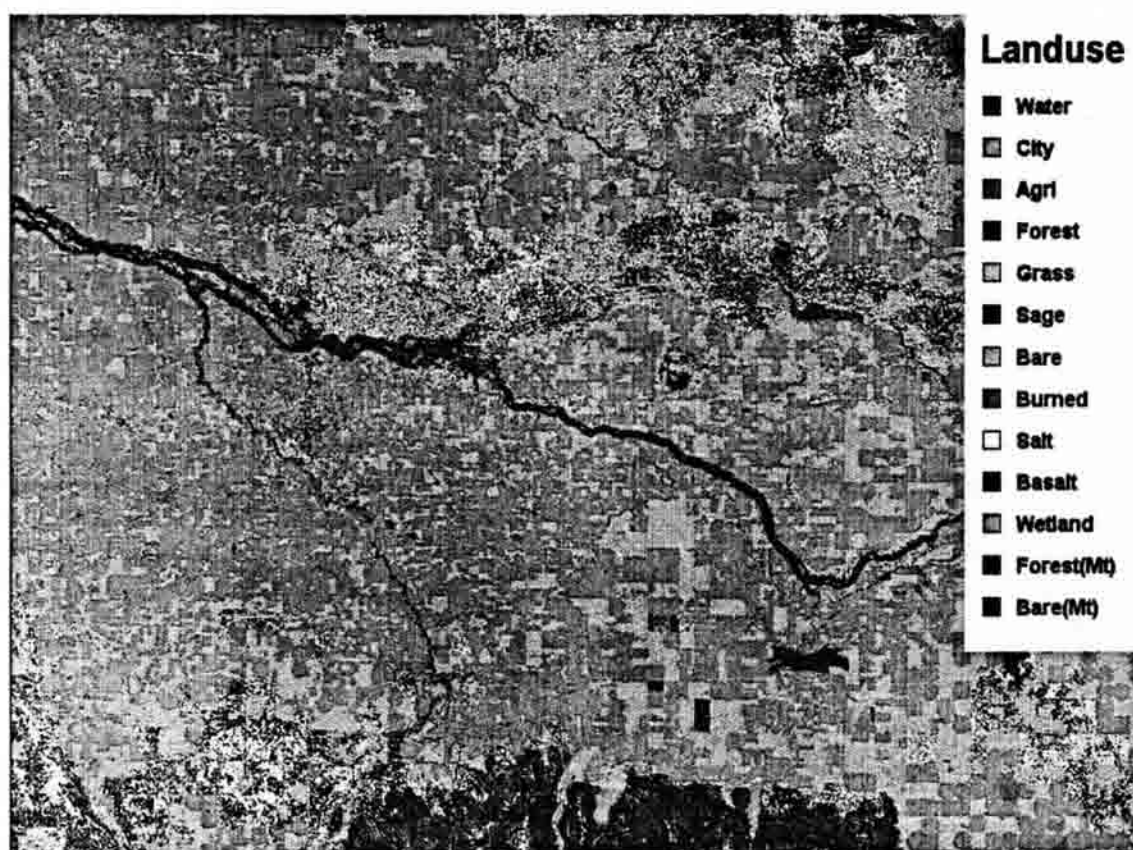cities of Kimberly and Twin Falls, Idaho.

Figure F.3   Landuse Classification for the Kimberly area

The classification included in Fig. F.3 was used in the application of the SEBAL

model performed for the years 1988, 1989, 1990, and 1991. Figure F.3 corresponds to

Landsat path 40, row 30.

In addition, for the 2000 application of SEBAL a landuse classification was made

using Landsat 7 ETM+ imagery corresponding to path 39, rows 29, 30, 31. In Fig. F.4 a

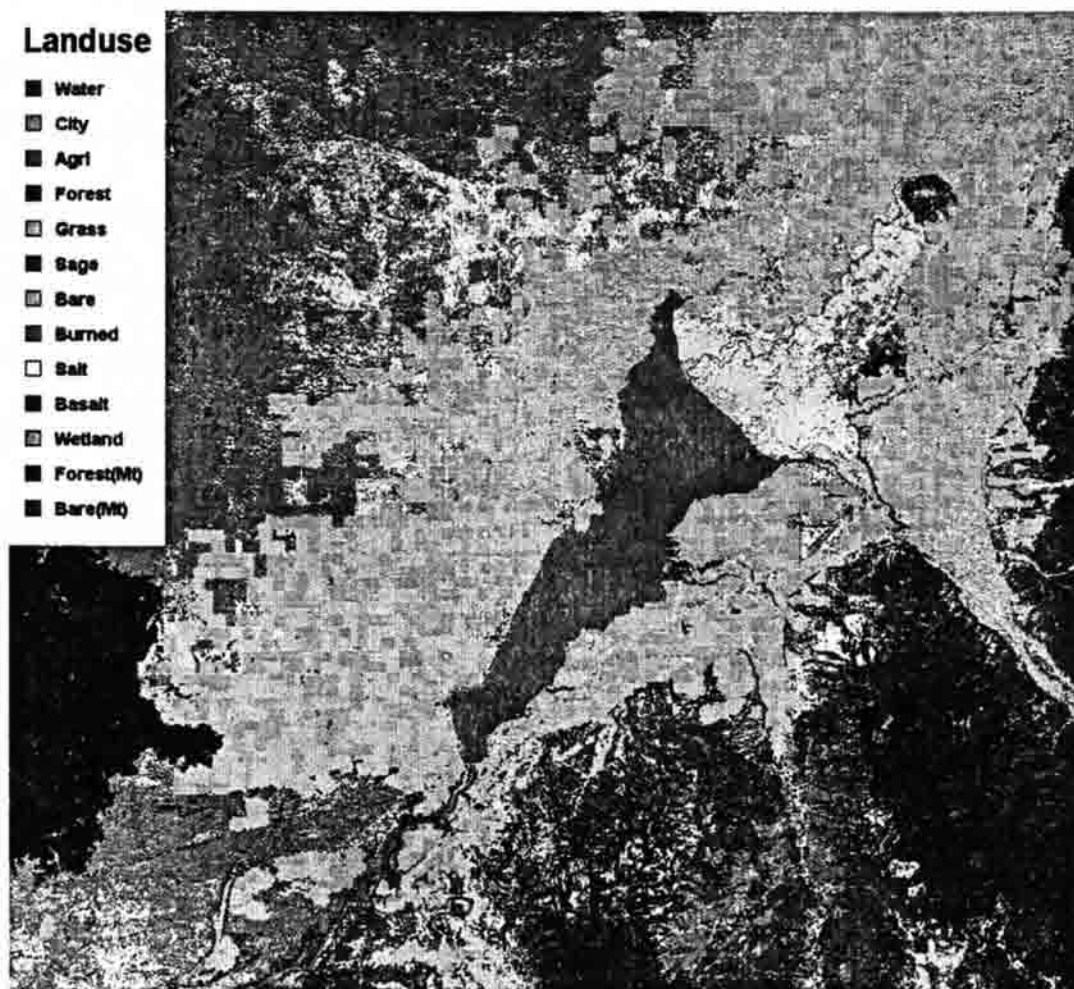close-up of the classification shows the area around American Falls reservoir.

FIGURE F.4. Landuse Map of the Aberdeen Area, Around American Falls Reservoir, Idaho

In Fig. F.4 a variety of surfaces can be seen : water (American Falls reservoir, and

Snake river), cities (Pocatello), agricultural areas (bare soil and agricultural fields),

desert areas (sage brush and grass), basalt, and mountains.

M. Tasumi, R.G. Allen, R. Trezza, and J.L Wright

Appendix G

Parameterization of Soil Heat Flux

An estimation method of soil heat flux was developed from field data measured under alfalfa, potato and bean fields, provided by Dr. J.Wright, USDA/ARS. For estimation of soil heat flux, many researchers such as Choubdhury et al. (1987), Kustas and Daughtry (1990), and Clothier et al (1986) have developed functions from relationships between G/R_n ratio and vegetation indices. In this study, a locally-calibrated function was developed to predict the ratio between G and R_n for the conditions presented at the Kimberly lysimeter fields.

Data Description

During 1971-1974, Dr.J.L Wright measured weather and energy balance components of Alfalfa (1971), Potatoes (1972) and Beans (1973-74) . This study used measured Net Radiation, Soil Heat Flux and Leaf area index (LAI) data.

Net radiation was observed using a net radiometer installed at the field near the Lysimeter. Soil heat flux was observed from heat flux plates at two locations in the field, at the same time. Total heat flux at the surface was calculated by Vanderkimpen (1991). LAI and plant height was periodically monitored by Dr. Wright.

Figure G.1 shows observed crop height and LAI for the 4 years included in this analysis . Alfalfa (1971) had 3 cuttings.
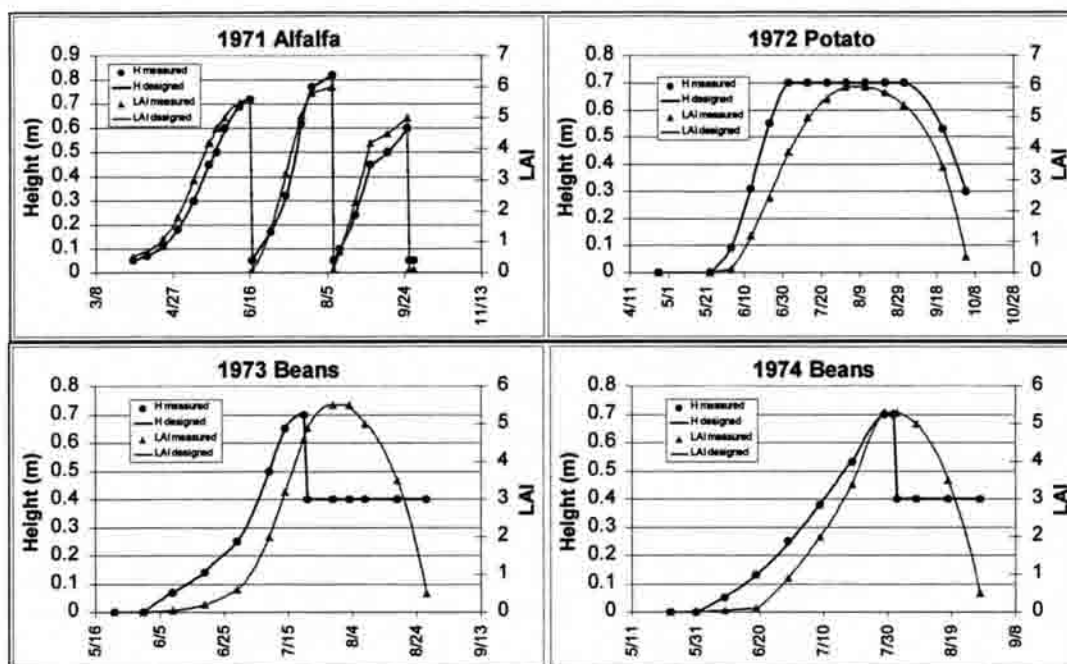
FIGURE G.1.   Crop Height and LAI for 1971 - 1974

The sudden drop of crop height in the bean field (1973-74) was due to damage of the crop by high winds (therefore, these periods were not used for analysis).

Data Evaluation and analysis

First, measured soil heat flux (G) data at 2 locations in the field (one location was inside the lysimeter) were compared and evaluated (Fig. G.2).   Some extreme values were rejected as outliers.   There were occasionally significant differences between the two G measurements that were interpreted as measurement errors or biases due to differences in the locations (soil type, soil moisture, vegetation cover, or other soil-related characteristics).   These large differences between G measurements were difficult to reconcile, because there were only two measurements. A third measure would have been valuable in these cases.
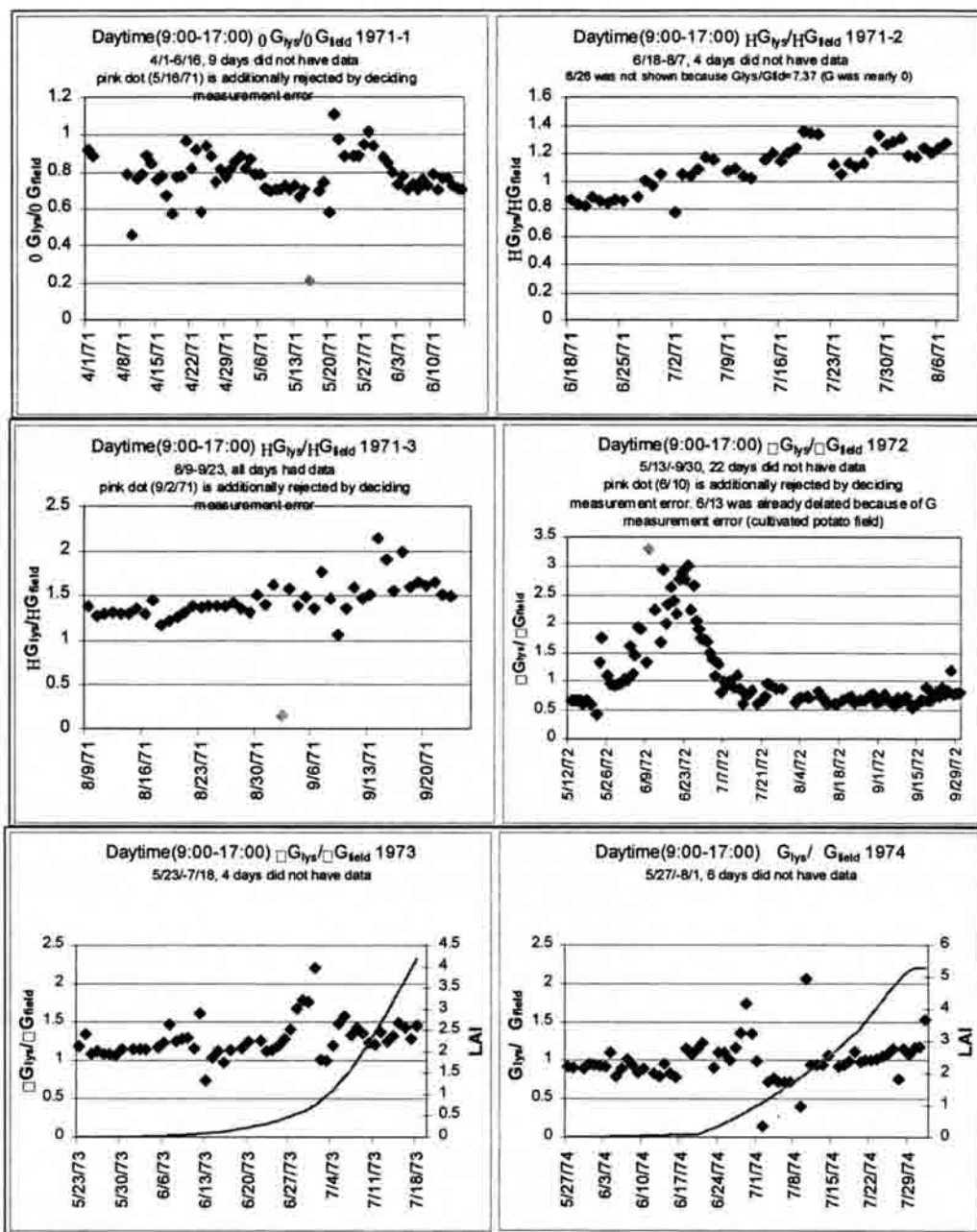
FIGURE G.2. Comparison of the Two G measurements from the Various Crops. The Original G Values used for Calculating the Ratios are Accumulation of Daytime in MJ/m² (9:00-17:00). Alfalfa (1971) was Separated into Three Cutting Periods (first 3 figures).

Averaged G values were taken, where there was no reason to reject either measurement, considering that these values should somewhat be closer to the actual field average. In general, similarity and congruency between the two measurements was evaluated by plotting the ratio of the two G measurements (Glys / G field) where Glys is the soil heat flux measured in the lysimeter and Gfield is the soil heat flux measured in the field (Fig. G.2). Consistency of average ratios near 1.0 were used to confirm reasonable integrity and representativeness of the data

Figure G.3 shows the temporal variation of G/R_n for different crops and weather conditions. By analysis of the G data, it was found that rain and irrigation disturbed the measurement of soil heat flux. Therefore, these rainfall/irrigation dates were eliminated.

When a significant amount of vegetation was present, no significant change of G/R_n was observed with change in soil moisture content (this agrees with Clothier et al ,1986). In addition, it was observed that the drop of solar radiation (due to the presence of clouds) did not impact G/R_n ratios significantly. Therefore G/R_n was considered to be a consistent means for expression of G and was mostly influenced by the amount of vegetation.

On the other hand, in bare soil conditions (where LAI was zero or very small), a wide range of G/R_n was observed. During bare soil conditions, high soil moisture reduced the G/R_n ratio. For example, the G/R_n ratio in bare soil conditions was relatively low on 1 day after rainfall/irrigation as can be seen in Fig. G.3
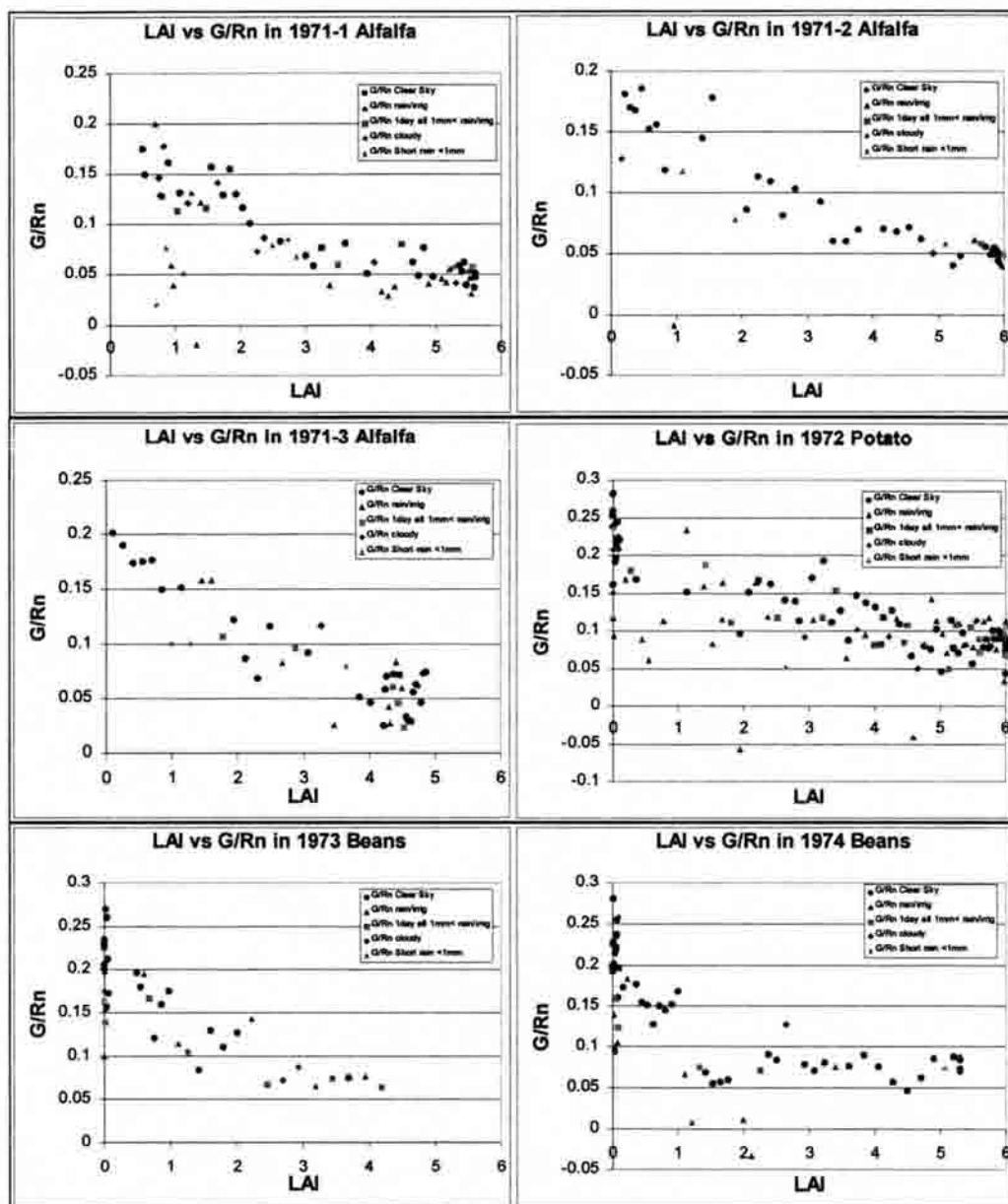
FIGURE G.3. G/R_n Ratio in Different Weather Conditions (1971-1974)

Parameterization of G Functions

Figure G.4 shows the plots of the G/R_n ratio versus LAI observed at the Alfalfa

field in 1971, as well as the corresponding correlation equation. As indicated in Fig. G.1,

the first cutting was in spring, the second cutting was in summer, and the final cutting

was in fall period. The G/R_n ratio of three cuttings agreed well with one another, although each cutting period had different solar radiation input.

In the 1972 Potato Field, a situation of "hysteresis" was observed between the growing period and the senescencing period (Fig. G.5). The G/R_n ratio during approximately the senescencing period was slightly higher, which might be related to the difference of the condition of leaves between these periods.

Only the growing period was used for developing the G function for potatoes for the local conditions. Also, it was determined that G/R_n for bare soil condition averaged 0.25. The result of the regression analysis is shown in Fig. G.6.
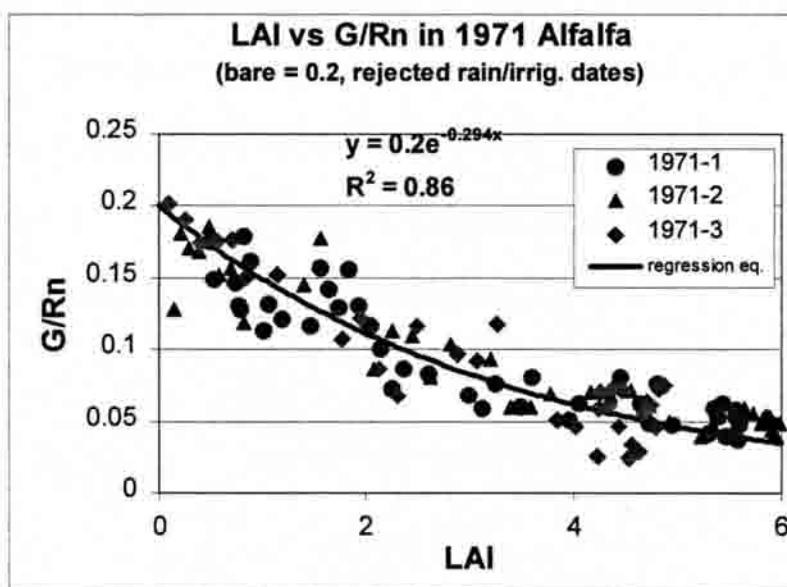
FIGURE G.4. G/R_n vs LAI in 1971 Alfalfa (3 cuttings)
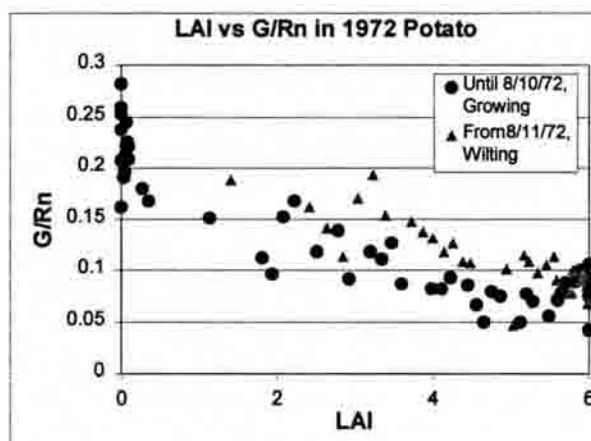
FIGURE G.5. G/R_n vs LAI in 1972 Potato Field. Growing Period and Senescencing Period.

Similarly, G/R_n versus LAI values of 1973-74 Bean fields were plotted (Fig. G.7). From observation of the G measured under beans , a possible bias was confirmed between the years 1973 and 1974. The bias was probably related to the location of the instruments for soil heat flux measurement. Therefore, by assuming that G/R_n values should act similarly for the same LAI values, G measurements that were considered to be the better measurements of G were selected and used each year.

FIGURE G.6. G/R_n vs LAI in 1972 Potato Field. Growing Period Only
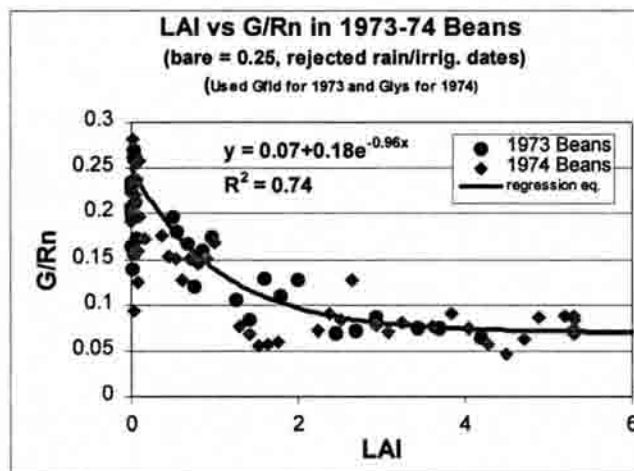
FIGURE.G.7. G/R_n vs LAI in 1973-74 Beans Field

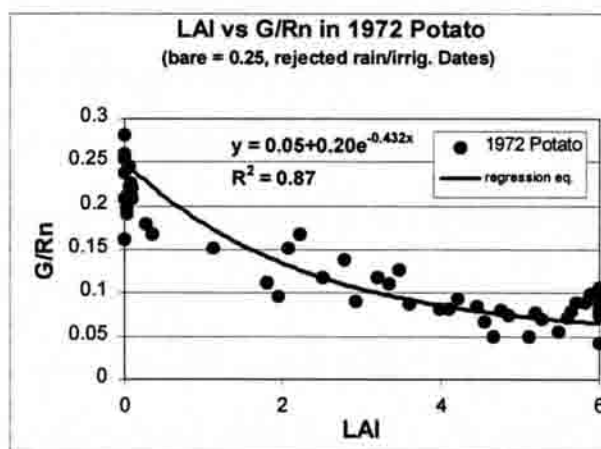To obtain a representative G equation for these three crops, a general equation which has the following format was developed:

$$G/R_n = C_1 + C_2 e^{C_3 LAI}$$ (G.1)

where C_1, C_2 and C_3 are constants.

Eq. G.1 follows the general format of Choudhury et al (1987). The equation for vegetated conditions was determined by equally averaging curves for the three crop equations (Fig. G.8), after determining the G/R_n level for bare soil conditions. In the alfalfa field (1971) G data were available for nearly bare soil conditions (LAI = 0), and estimated G/R_n for LAI = 0 extrapolated to 0.2. For potatoes and beans fields (1972-74), a wide range of G/R_n ratios were observed for bare soil conditions, and the G/R_n ratio for bare soil condition was determined as 0.25. Finally, for the general equation, G/R_n for bare soil condition was assumed to average 0.23. These values of G/R_n for LAI=0 were selected to produce best estimates for when LAI > 0.5. G/Rn for LAI < 0.5 was predicted by separated functions developed in the next section.
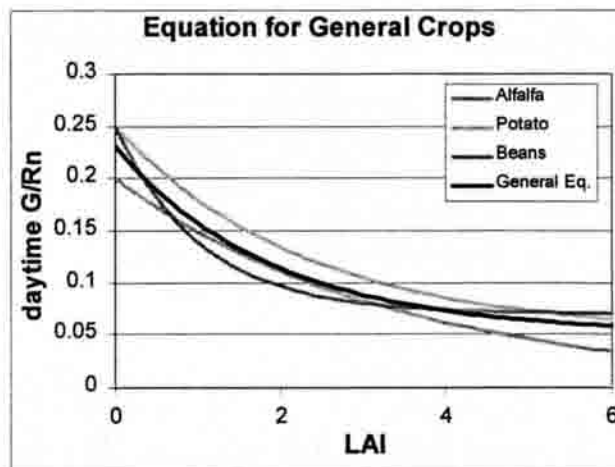
FIGURE G.8.   G/R$_n$ vs LAI for All Vegetated Surfaces.

Table G.2 shows the constants for Eq. G.1 that are adapted to the local conditions. Therefore, the general equation for vegetated surfaces, and for the conditions present at Kimberly Lysimeter fields, becomes:

$$G/R_n = 0.05 + 0.18e^{-0.521LAI}$$
(G.2)

G Estimation for Bare Soil Conditions

The value of   G/R$_n$ for bare soil condition was highly variable. This is because G/R$_n$ for bare soil conditions are not function of LAI but are function of other factors. Therefore, Eq. G.2 was concluded to be applicable only for surfaces that have a fair amount of vegetation cover (LAI around 0.5 or more).   A preliminary multiple regression analysis was performed using SAS, considering surface temperature, air temperature, and windspeed as main inputs. Soil moisture content was not included to the preliminary analysis because of lack of the data for all periods and due to the difficulty in obtaining soil moisture data in remote sensing applications

TABLE G.2.   Constant for Eq. G.1 to be used in this study

	C1	C2	C3
Alfalfa	0	0.20	-0.294
Potato	0.05	0.20	-0.432
Beans	0.07	0.18	-0.960
General	0.05	0.18	-0.521

The multiple regression showed that windspeed was one of the strongest factors impacting G/R_n under bare soil condition. A strong relationship between G/R_n and windspeed is understandable considering the aerodynamic factors involved in the surface energy balance. In a high wind condition, mechanical turbulence is enhanced, and therefore the transfer of heat from the surface is increased. This causes the surface temperature to drop. The drop of surface temperature reduces the temperature gradient in the soil profile, so that the transfer of heat (G) into the soil decreases. Figure G.9 shows the plot of G/R_n ratio and windspeed in 1973-74 bare soil conditions. However, a problem is that windspeed is difficult to use as an input to application of SEBAL with satellite imagery. Therefore, surface temperature was considered as a predictor of G estimation, as it is parameter closely connected to wind speed and additionally, to soil moisture.

Because, surface temperature was not observed at the lysimeter fields, values of T_s were back-calculated using observed soil, latent heat flux, net radiation, air temperature and windspeed, with estimated aerodynamic resistance to heat transport (r_{ah}) stability corrected by the Monin-Obukov length. On using the surface temperature (T_s) for estimating G/R_n ratio, T_s/R_n was applied rather than T_s itself. This was to "normalize" the seasonal difference in surface temperature.
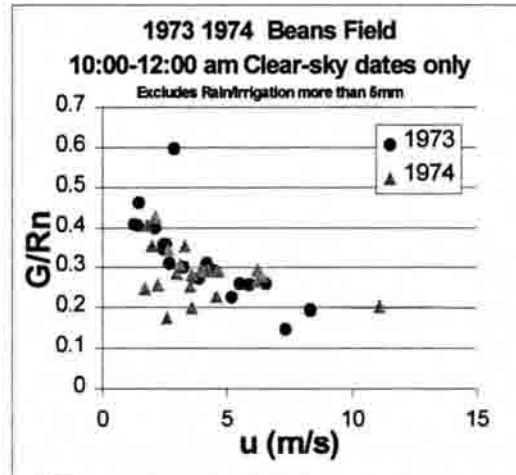
FIGURE G.9. G/R_n versus Windspeed at 2m for Bare Soil Conditions.

Figure G.10 shows the plots of G/R_n vs T_s/R_n for LAI than 0.5. Through this

analysis, the following equation was developed:

$$G/R_n = 1.80(T_s - 273.16)/R_n + 0.084 \qquad (G.3)$$

where T_s is in K, and Rn is in W/m². Eq. G.3 is applicable for LAI < 0.5.
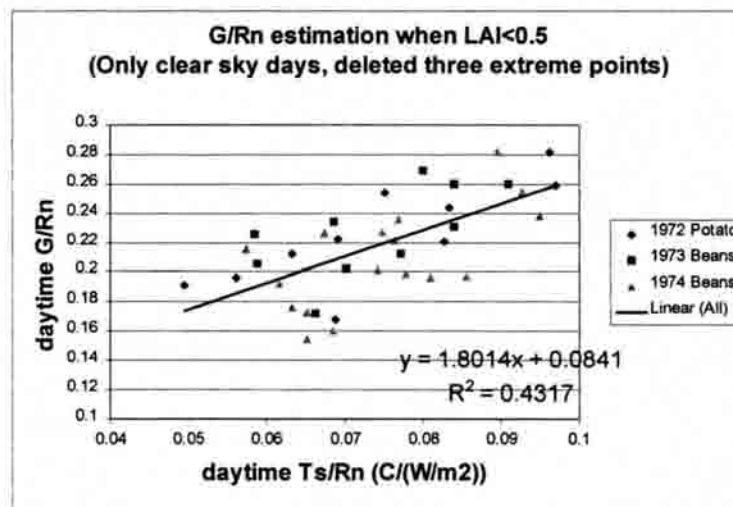
FIGURE G.10. G/R_n vs T_s/R_n

Appendix H

Surface Emissivity Analysis

R. Trezza, M. Tasumi, and R.G. Allen

General

Surface emissivity is the ratio between the radiation emitted by a given body and the radiation emitted from a blackbody at the same temperature as described by Plank's Law. In this study, expressions for surface emissivity were needed for two applications:

1. Broadband Emissivity: To be used in the Stephan Boltzman equation to predict longwave radiation emitted by the surface, according to Eq. 3.14.

$$R_L\uparrow = \varepsilon_o \, \sigma \, T_s^4$$

where ε_o is the broadband surface emissivity, and T_s is the radiometric surface temperature.

2. Narrowband Emissivity: To be used in Eq. 4.17 to retrieve surface temperature from Landsat band 6 thermal radiance:

$$T_s = \frac{K_2}{\ln\left(\dfrac{K_1}{R_c / \varepsilon_{NB}} + 1\right)}$$

where R_c is the atmospheric-corrected blackbody radiance, and ε_{NB} is the narrow band emissivity for the $10.4 - 12.5 \ \mu m$ band.

Procedure

There is a significant lack of information in the literature about emissivity of natural surfaces. Some information was obtained from the MODIS emissivity library at http://www.icess.ucsb.edu/modis/EMIS/html/em.html.

In this study surface emissivity for soils and rock surfaces in the area was evaluated as follows:

1. <u>Field Measurements</u>: An estimation of emissivity was performed using the methodology proposed by Jensen (2000). The methodology uses a thermometer and handheld thermal infrared radiometer. In this work, an Everest Infrared Thermometer was used to measure the radiometric surface temperature (T_{rad}), and a Cu-Constant thermocouple was used to measure the true or kinetic temperature of the surface (TC). The infrared thermometer was calibrated to a constant emissivity of 0.98 and it measures radiation in the $8 - 14$ μm range. Then, the emissivity of the surface was estimated as follows:

$$\varepsilon = \left(\frac{T_{rad} * 0.98^{0.25}}{TC} \right)^4 \tag{H.1}$$

Corrections for reflected atmospheric incoming longwave radiation were not considered. The results obtained are shown in Tables H.1, H.2, and H.3. From analysis of Table H.2 an average emissivity of 0.97 was calculated for basalt rock (the area of study includes a significant exposed basalt extension). However, because of the presence of several varieties of lichens on the rock surface, which have lower emissivity,(see Table H.1), this value was reduced to 0.96

TABLE H.1.   Estimated Values of Emissivity for Different Surfaces taken near
             Shoshone, ID, on 09/24/2001 by M. Tasumi, R. Trezza, and R. Allen.

Sample #	Trad, C	Trad, K	TC, C	TC, K	Emiss	Surface Description
1	25.55	298.71	27.68	300.84	0.952	bare brown basalt
2	26.60	299.76	28.35	301.51	0.957	white lichens
3	28.15	301.31	30.55	303.71	0.949	gray lichens
4	26.60	299.76	29.40	302.56	0.944	green lichens
5	26.75	299.91	29.00	302.16	0.951	white lichens
6	28.25	301.41	30.45	303.61	0.952	bare basalt dark brown semi glossy
7	28.90	302.06	31.65	304.81	0.945	black lichens
8	34.25	307.41	33.00	306.16	0.996	fresh rock dark brown
9	22.10	295.26	25.22	298.38	0.940	reddish brown basalt slightly glossy
10	18.80	291.96	22.25	295.41	0.935	green brown rock
11	33.40	306.56	33.35	306.51	0.981	sage brush
12	39.75	312.91	40.10	313.26	0.976	dead grass
13	31.10	304.26	31.05	304.21	0.981	rabbit bush
14	22.70	295.86	23.75	296.91	0.966	green grass
15	22.00	295.16	25.05	298.21	0.941	dry bare soil
16	19.10	292.26	20.45	293.61	0.962	wet bare soil
17	23.90	297.06	27.05	300.21	0.940	asphalt (normal)
18	17.40	290.56	18.88	292.04	0.960	bare soil (wet, in grass)

TABLE H.2.   Estimated Values of Emissivity for Different Surfaces taken in Basalt
             Surfaces of Craters of the Moon, National Park in Idaho, on 09/25/2001
             by M. Tasumi, and R. Trezza.

Sample #	Trad, C	Trad, K	TC, C	TC, K	Emiss	Surface Description
1	12.45	285.61	13.35	286.51	0.968	gray lichens
2	12.00	285.16	13.22	286.38	0.963	reddish basalt
3	11.65	284.81	12.30	285.46	0.971	black basalt
4	12.75	285.91	13.05	286.21	0.976	reddish basalt
5	12.15	285.31	12.70	285.86	0.972	black basalt
6	13.60	286.76	14.95	288.11	0.962	gray lichens
7	14.15	287.31	15.65	288.81	0.960	reddish basalt
8	13.90	287.06	14.75	287.91	0.968	reddish basalt
9	13.55	286.71	13.40	286.56	0.982	brown basalt
10	14.55	287.71	15.10	288.26	0.973	black basalt
11	14.95	288.11	15.25	288.41	0.976	black basalt
12	14.70	287.86	15.30	288.46	0.972	eroded rock
13	14.75	287.91	15.75	288.91	0.967	no porous black basalt glossy
14	14.60	287.76	16.05	289.21	0.960	reddish basalt
15	14.55	287.71	15.80	288.96	0.963	black basalt
16	21.15	294.31	20.70	293.86	0.986	Fresh Water

Table H.3.   Estimated Values of Emissivity for Different Surfaces taken near the USDA Facility at Kimberly, Idaho, on September 26, 2001, by M. Tasumi, and R.G Allen.

Sample #	Trad, C	Trad, K	TC, C	TC, K	Emiss	Surface Description
1	40.40	313.56	42.88	316.04	0.950	dry, sandy loam, greenhouse
2	40.60	313.76	43.42	316.58	0.946	dry, crust soil, full sun
3	36.13	309.29	36.22	309.38	0.979	dry, crust soil, full sun
4	30.53	303.69	30.52	303.68	0.980	dry, crumbled soil, full sun
5	27.37	300.53	28.02	301.18	0.972	dry, crumbled soil, full sun
6	25.33	298.49	26.58	299.74	0.964	dry, crumbled soil, full sun
7	22.73	295.89	23.42	296.58	0.971	dry, dirty sand, shaded
8	24.08	297.24	24.65	297.81	0.973	dry, dirty sand, shaded
9	24.62	297.78	25.45	298.61	0.969	dry, rain compacted silt loam, shaded
10	23.68	296.84	26.02	299.18	0.950	dry, rain compacted silt loam, shaded
11	31.30	304.46	32.35	305.51	0.967	dry, rain compacted silt loam, shaded
12	33.57	306.73	34.38	307.54	0.970	dry, rain compacted silt loam, shaded
13	39.05	312.21	39.25	312.41	0.977	dry, bare soil in wheat stable w/ crust, full sun
14	30.30	303.46	32.25	305.41	0.955	dry, bare soil in wheat stable w/ crust, partial sun

2) Using information from other datasets: A review of emissivity values in MODIS Emissivity Library was made. This emissivity library is presented in the following web page:

http://www.icess.ucsb.edu/modis/EMIS/html/em.html

The MODIS emissivity library is a collection of spectral emissivity measurements of natural and manmade materials that may be used as a source of spectral emissivities for different studies.

The analysis was made looking at the emissivity values included in the following wavelength ranges:

2.1) $8 - 14$ μm   (infrared thermometer range)

2.2) $10.4 - 12.5$ μm   (Landsat Band 6 , thermal)

2.3) broadband emissivity (using the entire spectrum given in the library , approximately from 3.3 to 15.1 μm)

Soils: A total of 48 samples of soils were considered. Emissivity values were

weighted according Plank's Law considering a blackbody temperature of 300 K and 293

K (20 °C).

Figure H.1 shows the emissivity values obtained for all the samples for the ranges

of 8-14 and 10.4 to 12.5 µm considering T=293 K for blackbody radiation calculations.

The average emissivity was 0.971 for 10.4 to 12.5 µm and 0.948 for 8-14 µm.

Figure H.2 shows the emissivity values obtained for all samples for the ranges of

8-14 and 10.4 to 12.5 µm considering T=300 K for blackbody radiation calculations.

The average emissivity was 0.971 for 10.4 to 12.5 µm and 0.947 for 8-14 µm.

FIGURE H.1. Weighted Emissivity Values (using Plank's Law with T=293 K), for 48
Bare Soil Samples and corresponding to Wavelength Ranges of 8 – 14
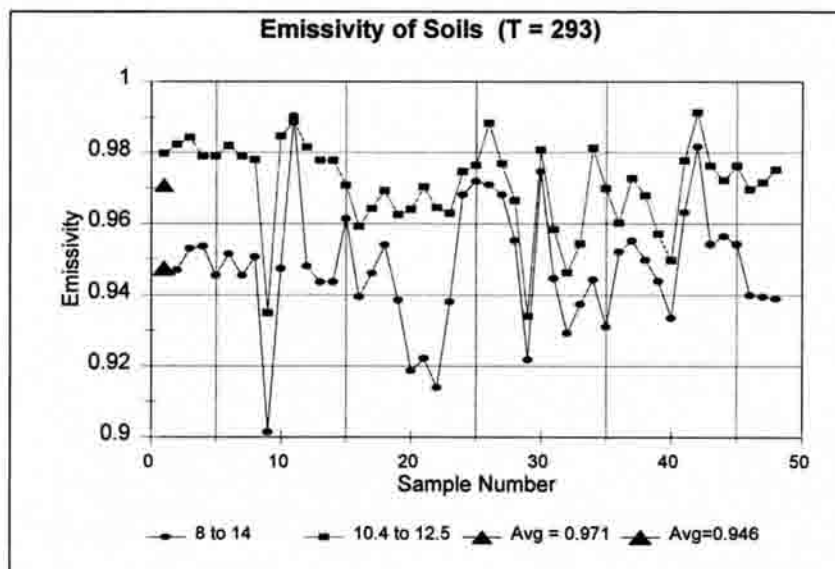µm and 10.4 – 12.5 µm. Data from the MODIS Library.

FIGURE H.2.   Weighted Emissivity Values (using Plank's Law with T=300 K), for 48
Bare Soil Samples and corresponding to Wavelength Ranges of 8 – 14
µm and 10.4 – 12.5 µm. Data from the MODIS Library.

Figure H.3 shows the values of emissivity corresponding to the range between

3.3 and 15.1 µm, taken as representative of broadband emissivity.   The average value for

the 49 samples was 0.951 (when T=293 K) and 0.950 (T=300 K). In Table H.4 the

results obtained from each sample are included
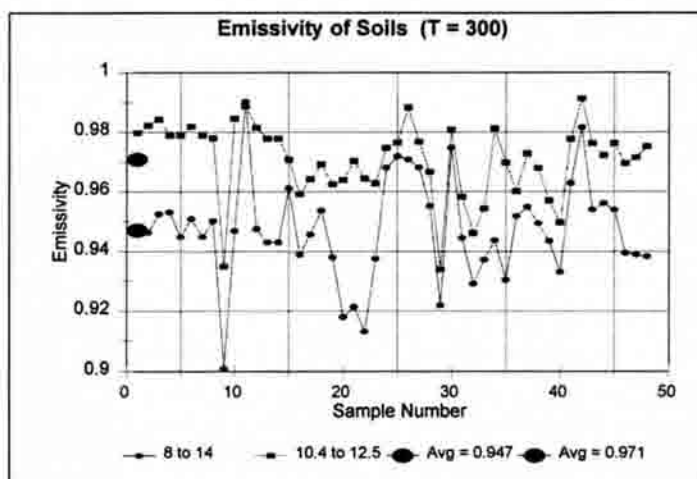

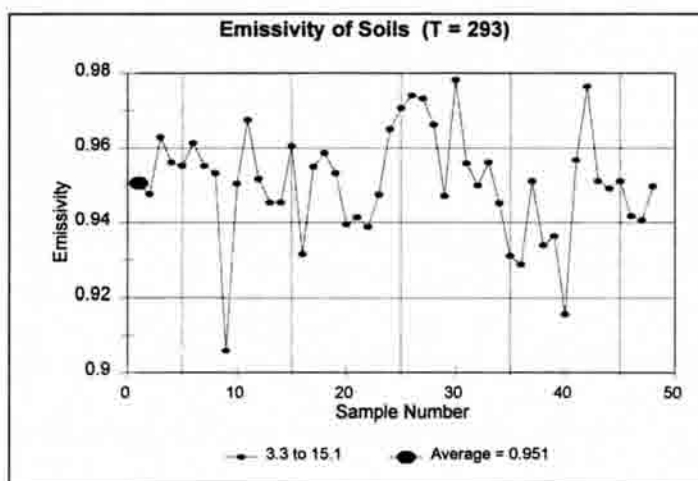FIGURE H.3.   Weighted Emissivity Values (using Plank's Law with T=293 K), for 48
Bare Soil Samples and corresponding to Wavelength Ranges of 3.3 –
15.1 µm. Data from the MODIS Library.

Table H.4.   Values of Emissivities for Different Bare Soil Surfaces corresponding to Broadband (3.3 to 15.1   μm), 8 – 14 μm, and   10.4 – 12.5 μm ranges

Sample				Broadband	8-14	10.4-12.5
1	OKLAHOMA	Sample	3101	0.949	0.946	0.980
2	OKLAHOMA	Sample	2	0.946	0.946	0.982
3	OKLAHOMA	Sample	3	0.963	0.953	0.984
4	OKLAHOMA	Sample	4	0.955	0.953	0.979
5	OKLAHOMA	Sample	5	0.955	0.945	0.979
6	OKLAHOMA	Sample	6	0.961	0.951	0.982
7	OKLAHOMA	Sample	7	0.955	0.945	0.979
8	OKLAHOMA	Sample	8	0.952	0.950	0.978
9	OKLAHOMA	Sample	9	0.905	0.901	0.935
10	OKLAHOMA	Sample	10	0.949	0.947	0.985
11	OKLAHOMA	Sample	11	0.968	0.990	0.989
12	OKLAHOMA	Sample	12	0.951	0.948	0.982
13	OKLAHOMA	Sample	13	0.944	0.943	0.978
14	OKLAHOMA	Sample	14	0.944	0.943	0.978
15	DEATH VALLEY, California	Sample	1	0.960	0.961	0.971
16	DEATH VALLEY, California	Sample	2	0.930	0.939	0.959
17	DEATH VALLEY, California	Sample	3	0.955	0.946	0.964
18	DEATH VALLEY, California	Sample	4	0.958	0.954	0.969
19	DEATH VALLEY, California	Sample	5	0.953	0.938	0.963
20	DEATH VALLEY, California	Sample	6	0.939	0.918	0.964
21	DEATH VALLEY, California	Sample	7	0.941	0.922	0.970
22	DEATH VALLEY, California	Sample	8	0.938	0.913	0.965
23	DEATH VALLEY, California	Sample	9	0.947	0.938	0.963
24	DEATH VALLEY, California	Sample	10	0.965	0.968	0.975
25	RAIL ROAD VALLEY, Nevada	Sample	1	0.970	0.972	0.977
26	RAIL ROAD VALLEY, Nevada	Sample	2	0.974	0.971	0.988
27	RAIL ROAD VALLEY, Nevada	Sample	3	0.973	0.968	0.977
28	RAIL ROAD VALLEY, Nevada	Sample	4	0.967	0.955	0.967
29	RAIL ROAD VALLEY, Nevada	Sample	5	0.948	0.922	0.934
30	RAIL ROAD VALLEY, Nevada	Sample	6	0.978	0.975	0.981
31	RAIL ROAD VALLEY, Nevada	Sample	7	0.956	0.945	0.958
32	RAIL ROAD VALLEY, Nevada	Sample	8	0.951	0.929	0.946
33	RAIL ROAD VALLEY, Nevada	Sample	9	0.957	0.937	0.954
34	RAIL ROAD VALLEY, Nevada	Sample	10	0.944	0.944	0.981
35	Soil(Nebraska Soil Lab)	Sample	476	0.929	0.931	0.970
36	Soil(Nebraska Soil Lab)	Sample	3715	0.926	0.952	0.960
37	Soil(Nebraska Soil Lab)	Sample	4255	0.950	0.955	0.973
38	Soil(Nebraska Soil Lab)	Sample	4172	0.931	0.949	0.968
39	Soil(Nebraska Soil Lab)	Sample	3921	0.935	0.944	0.957
40	Soil(Nebraska Soil Lab)	Sample	3101	0.912	0.933	0.950
41	Soil(Nebraska Soil Lab)	Sample	4643	0.955	0.963	0.978
42	Soil(Nebraska Soil Lab)	Sample	HALIIA	0.976	0.982	0.991
43	Soil(Nebraska Soil Lab)	Sample	2535	0.950	0.954	0.976
44	Soil(Nebraska Soil Lab)	Sample	2535 s	0.948	0.956	0.972
45	Soil(Nebraska Soil Lab)	Sample	3101	0.950	0.954	0.976
46	PAGE, ARIZONA	Sample	7	0.941	0.940	0.970
47	PAGE, ARIZONA	Sample	8	0.939	0.939	0.972
48	PAGE, ARIZONA	Sample	9	0.949	0.938	0.975
			Average	0.950	0.947	0.971

Other surfaces: The MODIS emissivity Library includes a reduced dataset of emissivities for other surfaces. Table H.5 includes weighted values of emissivities for several surfaces: grass, snow, and water. Table H.6 shows representative values for salty soils

294

TABLE H.5   Values of Emissivities for Different Surfaces corresponding to 3.3 to
             15.1 μm (broadb), 8 – 14 μm, and 10.4 to 12.5 μm ranges

			Broadba	8-14	10.4-12.5
Grass	Sample	1	0.960	0.966	0.953
Grass	Sample	2	0.960	0.967	0.951
Grass	Sample	3	0.960	0.966	0.953
Eucalyptus Tree	Sample	1	0.926	0.956	0.942
Pavement	Sample	1	0.951	0.954	0.965
Snow	Sample	1	0.985	0.985	0.982
Snow	Sample	2	0.993	0.993	0.991
Water	Sample	1	0.983	0.986	0.990

Broadband Emissivity Equation

From the results included in Fig. H.3, and Table H.4, an average emissivity value of 0.95 was adopted for bare soil, representative of the 3.3 to 15.1 μm range (taken as broadband emissivity).

In addition, considering that a common value of emissivity for full cover vegetation is 0.98 (Jensen, 2000), the following expression for broadband emissivity is proposed:

$$\varepsilon_0 = 0.95 + 0.01*LAI \qquad (H.2)$$

where ε_0 is the broadband emissivity of the surface, and LAI is the leaf area index.

Eq. H.2 predicts $\varepsilon_0 = 0.95$ when LAI = 0, and $\varepsilon_0 = 0.98$ when LAI = 3. Eq. H.2 is valid for values of LAI ≤ 3. If LAI > 3 then $\varepsilon_0 = 0.98$.

TABLE H.6   Values of Emissivities for Salty Soil Samples corresponding to 3.3 to
             15.1 μm (broadb), 8 – 14 μm, and 10.4 to 12.5 μm ranges

			Broadba	8-14	10.4-12.5
SALTY SOIL	Sample	1	0.958	0.960	0.971
SALTY SOIL	Sample	1	0.959	0.961	0.971
SALTY SOIL	Sample	1	0.953	0.966	0.969

The value of emissivity = 0.95 agreed with the minimum values of measured emissivity for bare soil in the study area, reported in Table H.3.

Narrowband Emissivity Equation

From the results included in Figs. H.1, H.2, and H.3, and Table H.4 , an average value of emissivity for bare soil, representative of the 10.4 to 12.5 μm range (Landsat thermal band) of 0.97 can be adopted. Therefore, the following expression for broadband emissivity is proposed:

$$\varepsilon_{NB} = 0.97 + (0.01/3)*LAI \tag{H.3}$$

where ε_{NB} is the narrowband emissivity of the surface in the 10.4 to 12.5 μm range, and LAI is the leaf area index. Eq. H.3 predicts $\varepsilon_o = 0.97$ when LAI = 0, and $\varepsilon_o = 0.98$ when LAI = 3. Eq. H.3 is valid for values of LAI ≤ 3. If LAI > 3 then $\varepsilon_o = 0.98$.

Appendix I

Soil Water Balance Model

In Chapter IV the standard procedure to estimate the amount of evapotrans-
piration between satellite images was described. That procedure holds the value of
ETrF, computed from a specific image, as constant during a given period (Eq. 5.9).
However, the value of ETrF changes continuously through the season due to the
occurrence of wetting events (irrigation and precipitation), as well as due to the drying of
the surface from depletion of the soil available moisture by evapotranspiration and crop
development.

In this appendix, a soil water balance model (based on FAO-56, Allen et al 1998),
is proposed to be used in SEBAL$_{ID}$ as an interface to calculated the variation of ETrF
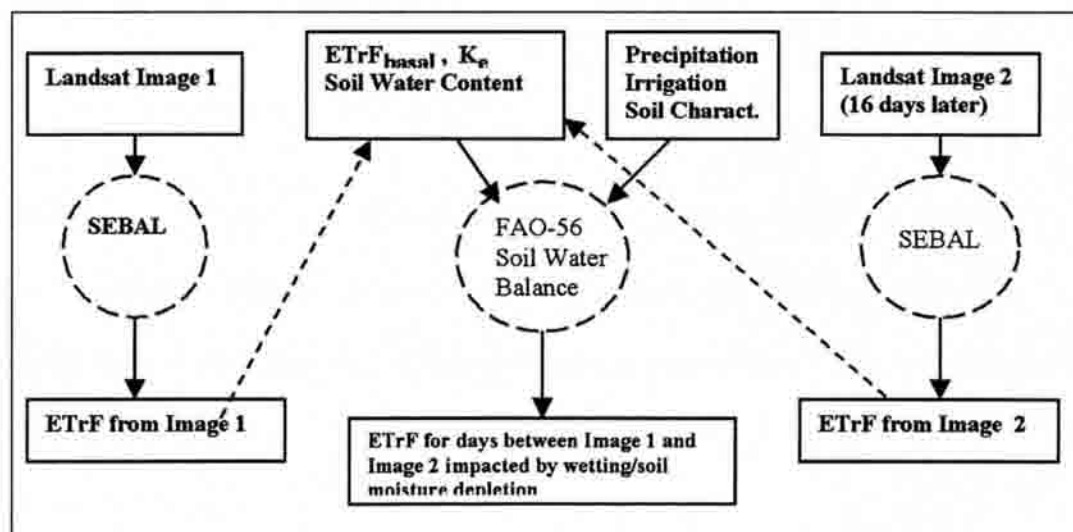between images. The general concept is illustrated in Fig. I.1

FIGURE I.1.   General Flow Chart of the Water Balance Model

Application of the FAO-56 Water Balance Model in this Study

In this study, due the lack of spatial-distributed irrigation information the application of the water balance model was significantly limited. In this appendix, the application of this methodology is illustrated to explore ways to retrieve important inputs for the water balance model and to account for impact of precipitation in the temporal variation of ETrF between images. This approach would be especially useful to monitor ET in non-irrigated areas of deserts, and bare soils. In addition, it is important to note that precipitation produces an abrupt increase in ETrF pixel wide, so that methodologies that can track the variation of ETrF due to the occurrence of precipitation are important.

Description of the methodology

To adjust the value of ETrF between images, the proposed methodology is based on monitoring the soil moisture in the top soil layer (first $10 - 15$ cm). The adjusted value of ETrF (ETrF$_{adjusted}$) is computed as follows:

$$ETrF_{adjusted} = ETrF_{basal} + K_e \tag{I.1}$$

where ETrF$_{basal}$ is defined as the ratio of crop evapotranspiration (ET) over alfalfa reference evapotranspiration (ET$_r$) when the soil surface is dry but transpiration is occurring at a potential rate. K_e is the coefficient of evaporation which is calculated with the following equation:

$$K_e = K_r (ETrF_{max} - ETrF_{basal}) \leq f_{ew} ETrF_{max} \tag{I.2}$$

where ETrF_{max} is the maximum value of ETrF following rain or irrigation, K_r is a dimensionless evaporation reduction coefficient which is dependent on the cumulative depth of water depleted (evaporated), and f_{ew} is the fraction of the soil that is both exposed to solar radiation and that is wetted. The value of K_r is calculated as explained in Chapter V (Eq. 5.4). Following a significant precipitation event, the value of f_{ew} is computed as follows:

$$f_{ew} = \min(1\text{-}f_c, f_w) \tag{I.3}$$

where $1\text{-}f_c$ is the fraction of soil that is covered by vegetation $[0.01 - 1]$, f_c is the fraction of cover, and f_w is the average fraction of soil surface wetted by precipitation or irrigation. After precipitation occurs, the value of f_{ew} becomes $f_{ew} = 1 - f_c$, bare soil $f_{ew} = 1$, and for full cover conditions $f_{ew} = 0.01$.

The value of ETrF_{max} is calculated as follows:

$$\text{ETrF}_{max} = \max(1.05, \{\text{ETrF}_{basal}\}) \tag{I.4}$$

The cumulative depletion of soil moisture ($D_{e,i}$) is computed by performing a daily water balance for the exposed and wetted fraction of the surface soil layer as follows:

$$D_{e,i} = D_{e,i-1} - (P - RO_i) - \frac{I_i}{f_w} + \frac{E_i}{f_{ew}} + T_{ew,i} + DP_{e,i} \tag{I.5}$$

where $D_{e,i-1}$ is the cumulative depth of evaporation following complete wetting from the exposed and wetted fraction of the topsoil at the end of day i-1 [mm], $D_{e,I}$ is the

cumulative depth of evaporation (depletion) following complete wetting at the end of day i [mm], P_i is the precipitation on day i [mm], RO_i is the precipitation runoff from the soil surface on day i [mm], I_i irrigation depth on day i that infiltrates the soil [mm], E_i is the evaporation on day i ($E_i = K_e ET_r$, where K_e is the top soil evaporation coefficient) [mm], $T_{ew,i}$ is the depth of transpiration from the exposed and wetted fraction of the soil surface layer on day i [mm], $DP_{e,1}$ is the deep percolation loss from the topsoil layer on day i if soil water content exceeds field capacity [mm], f_w is the fraction of soil surface wetted by irrigation [0.01 - 1], and f_{ew} is the exposed and wetted soil fraction [0.01 - 1].

When just accounting for precipitation events, Eq. I.6 is reduced to :

$$D_{e,i} = D_{e,i-1} - (P - RO_i) + \frac{E_i}{f_{ew}} \qquad (I.7)$$

In Eq. I.7 the value of $D_{e,i}$ is constrained to the following range:

$$0 \le D_{e,i} \le TEW$$

If $D_{e,i}$ is greater than TEW then the amount of precipitation is exceeding the soil storage in the evaporative layer, therefore the quantity $D_{e,i} - TEW$ represents drainage of water from the top soil ($DP_{e,i}$).

Estimation of Initial Inputs for the Water Balance Model

This section is necessary to account for potential wetness on some fields at the image time from antecedent irrigation or precipitation. The accounting for evaporation

from irrigation is done only once, at the image time, because both irrigation dates and amount of water from irrigation are unknown.

The ETrF calculated by SEBAL from a particular image includes basically the evaporation from the soil and transpiration from plants. This means that:

$$ETrF = ETrF_{basal} + K_e \tag{I.8}$$

where $ETrF_{basal}$ corresponds to the ETrF when the soil surface is dry and transpiration is occurring at potential rate and K_e represents the evaporation component from the top soil. To partition the ETrF obtained from SEBAL in its two components, the following procedure is proposed:

1. A plot of LAI vs ETrF is made using a considerable number of pixels from the processed image. In Fig. I.2 a plot of LAI versus ETrF is shown corresponding to the 05/20/1989 image. From this plot, one can draw a curve that joins the points of minimum ETrF over the LAI range. The curve represents the value of $ETrF_{basal}$ versus LAI. Theoretically, points that are below the curve are presumed to be moisture-stressed and points above the curve are presumed to have some degree of soil surface wetness that increases the ETrF above the basal value. Thus, the amount of ETrF that is over the $ETrF_{basal}$ corresponds to the part of ETrF that represents the evaporation component (i.e. K_e). With regard to the points below the curve, some of them might correspond to pixels where the thermal information was "mixed" with dryer surfaces.

2. From the plot of LAI vs ETrF one can make an initial estimation of the value of K_e as :
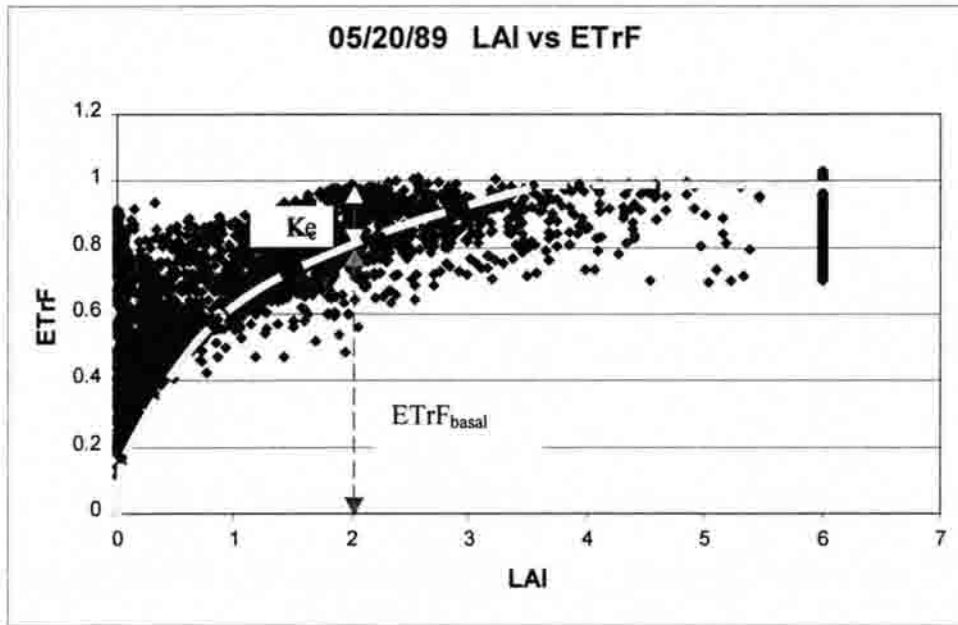
FIGURE I.2.   Definition of the $ETrF_{basal}$ Curve for the 05/20/89 Scene

$$K_e = ETrF - ETrF_{basal} \text{ (initial guess)} \qquad (I.9)$$

3. However according to FAO-56 the value of K_e can not exceed the product of $f_{ew}*EtrF_{max}$, therefore:

$$K_e = ETrF - ETrF_{basal} \quad \text{if} \quad ETrF - ETrF_{basal} \leq f_{ew}*EtrF_{max}$$

or

$$K_e = f_{ew}*ETrF_{max} \qquad \text{if} \quad ETrF - ETrF_{basal} > f_{ew}*EtrF_{max}$$

4. Then, $ETrF_{basal}$ is recalculated to adjust it for the cases when

$$K_e > f_{ew}*EtrF_{max}.$$

$$ETrF_{basal} = ETrF - K_e$$

5. A value of the coefficient K_r is obtained by inverting Eq (I.2):

$$K_r = \frac{K_e}{ETrF_{max} - ETrF_{basal}} \qquad (I.10)$$

6 Finally, initial depletion in the soil is calculated by inverting Eq (5.4):

$$D_{e,i-1} = TEW - K_r * (TEW - REW) \qquad (I.11)$$

Eq. I.11 is able to estimate the value of initial depletion of soil moisture in the soil, for the situations when $D_{e,i-1} > REW$ ($K_r < 1$). When $K_r = 1$ then Eq. I.11 always estimates $D_{e,i-1} = TEW$, so that it is not able to predict values of D_e that are in the range $REW < D_e < TEW$. In these instances (when $K_r = 1$), $D_{e,i-1}$ is set equal to $D_{e,i-1} = 0.5 * REW$ as an estimate.

To follow the procedure included in steps (3) and (4), a function that provides estimation of fraction of cover (f_c) from LAI is needed. If this function is not available, then the value of $ETrF_{basal}$ calculated in step (2) has to be assumed as the final $ETrF_{basal}$, and the fraction of cover can be estimated as (FAO-56, Allen et al 1998):

$$f_c = \left(\frac{ETrF_{basal} - ETrF_{min}}{ETrF_{max} - ETrF_{min}} \right)^{(1+0.5h)} \qquad (I.12)$$

where f_c is the fraction of cover, $ETrF_{min}$ is the minimum ETrF for dry bare soil with no ground cover [$\approx 0.15 - 0.20$], and h is the mean plant height [m].

Appendix J

ETrF Analysis

An analysis of the hourly behavior of ETrF during daytime is made in this

Appendix. In addition, a comparison between instantaneous ETrF (ETrF$_{inst}$)obtained at

Landsat overpass time ($\approx$ 11:00 am) to daily average of ETrF (ETrF$_{24}$) is included to

verify whether or not, ETrF can be used for extrapolation of instantaneous to daily

values of ET in SEBAL$_{ID}$ application.

Analysis of ETrF in Sugar Beets for 1989

The next series of graphs show consecutive four day periods of ET and ETrF for

sugar beets for July to September 1989.
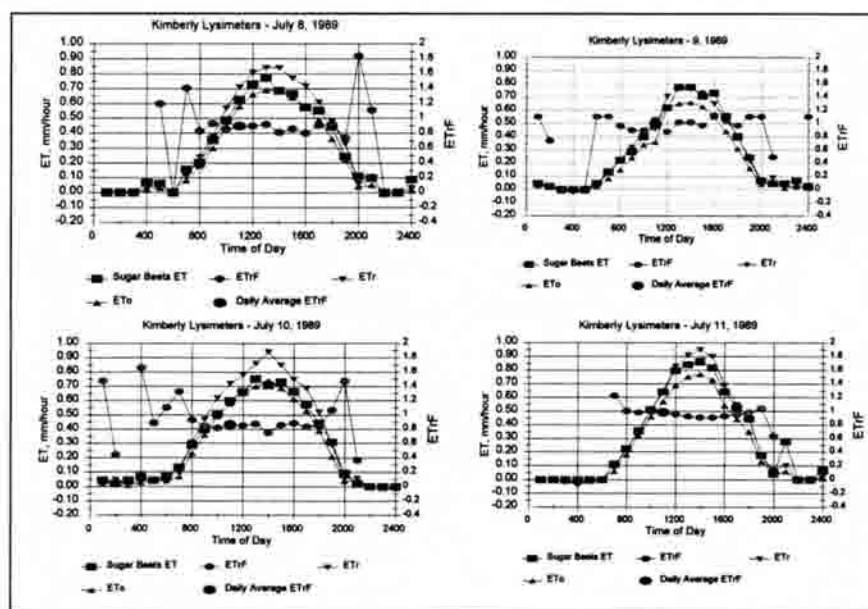
FIGURE J.1.   Hourly Variation of ET, and ETrF for Sugar Beets During a Four-Day
Period in July 1989. ETr and ETo were calculated using ASCE-EWRI
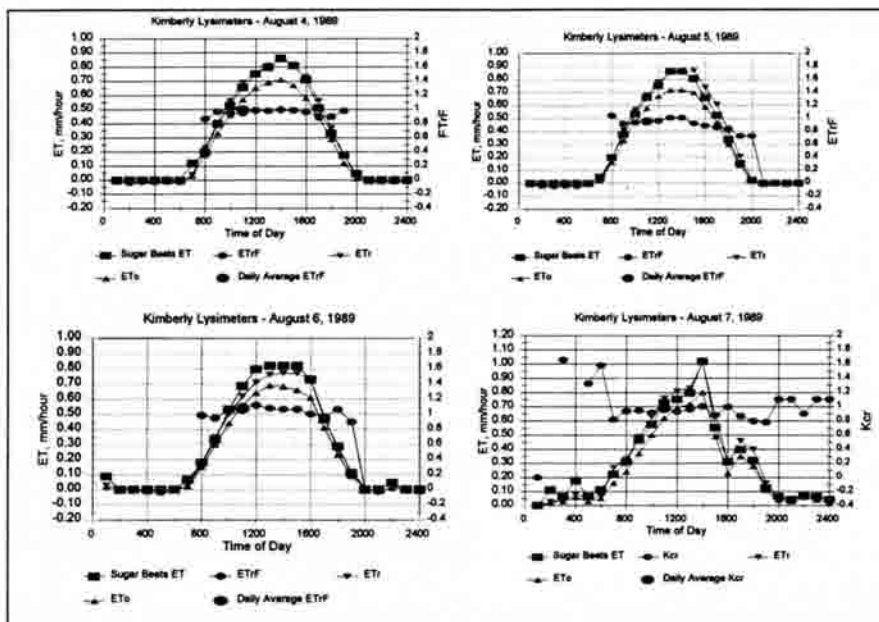(2002).

FIGURE J.2.   Hourly Variation of ET, and ETrF for Sugar Beets during a Four-Day Period in August, 1989. ETr and ETo were calculated using ASCE-EWRI (2002). Data provided by Dr. J.L Wright (USDA-Kimberly,ID)
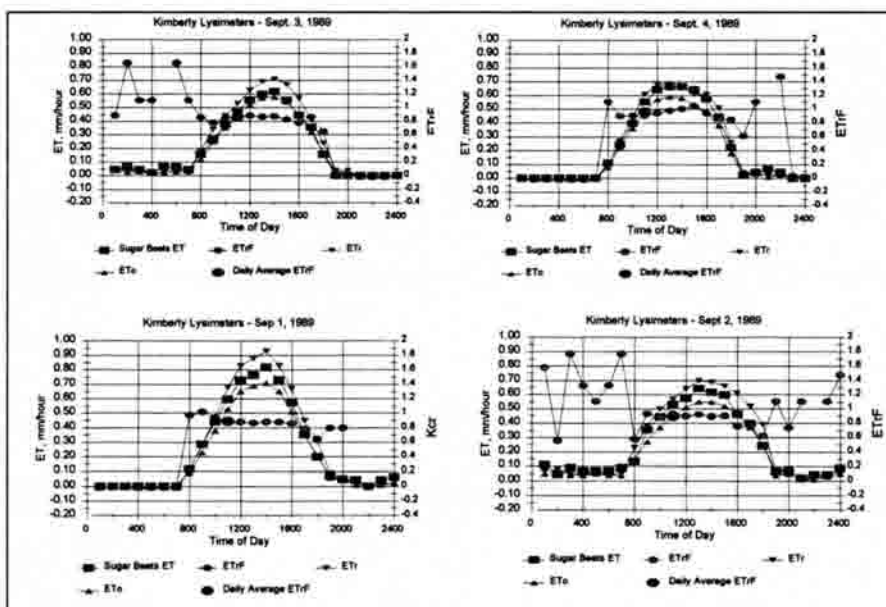

FIGURE J.3.   Hourly Variation of ET, and ETrF for Sugar Beets during a Four-Day Period in September, 1989. ETr and ETo were calculated using ASCE-EWRI (2002). Data provided by Dr. J.L Wright (USDA-Kimberly,ID)

As seen in Figs. J.1, J.2, and J.3, there is a relative constancy of the value of ETrF during daytime time. As explained in Chapter V, this behavior is expectable if one considers that both ET variables included in the calculation of ETrF: actual ET and alfalfa reference ET, are exposed to the variation of the same weather parameters: wind speed, air temperature, solar radiation, and humidity. Therefore, in the advective environment of Southern Idaho, variation in the weather parameters due to advection of warm and dry air from desert to the Kimberly area affects both actual ET and ET_r, so that the value of ETrF can remain relatively constant.

A plot of $ETrF_{inst}$ and $ETrF_{24}$ for all July, August and September days is shown in Fig. J.4. Even though a significant scatter is observed for values of ETrF greater than 1.05, most of the points lay around the 1:1 line. The standard deviation of the difference between instantaneous and 24-hour ETrF is 0.06, and the average of the differences is 0.05. It is important to note that the average ETrF for the day was calculated using the total measured ET for the day and the total value of ET_r. This was made to be able to extrapolate instantaneous to total 24-hour values of ET. If just daytime values were considered, the similarity between instantaneous and daytime averages of ETrF would be greater.

Figure J.5 shows a plot of ETrF for the satellite day of 1988, where the crop in lysimeter 2 was potatoes. As can be seen, the hourly behavior of ETrF is fairly constant during the day.
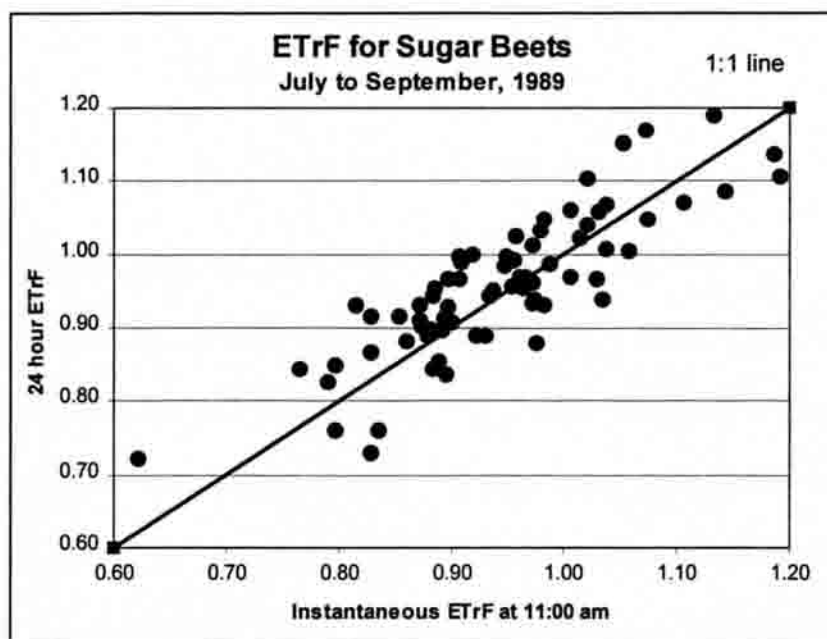
306

FIGURE J.4.   Plot of Instantaneous and Daily Averages of ETrF for Sugar Beets,
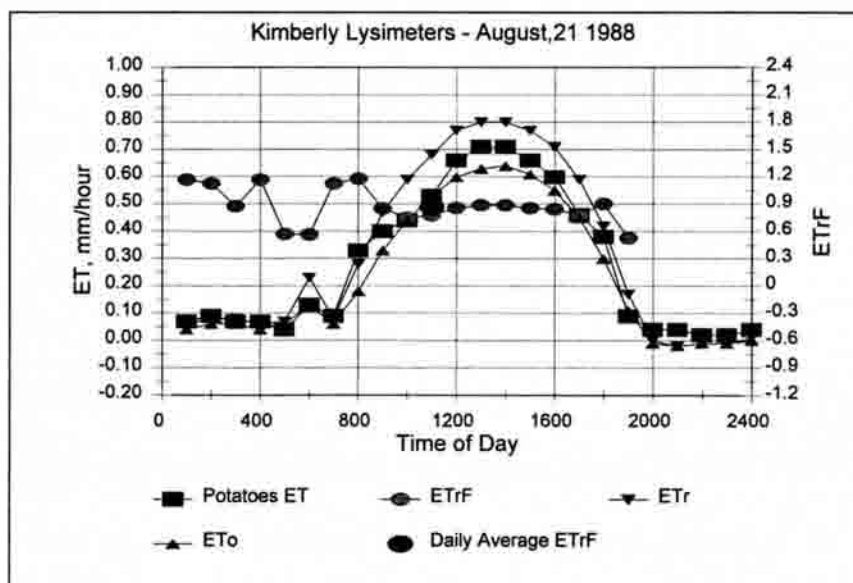during the Period July – September 1989.

FIGURE J.5.   Hourly Behavior of ETrF for Potatoes during the Satellite Date
corresponding to 08/21/88. Data Provided by Dr. J.L Wright (USDA-
ARS Kimberly, Idaho.

<center>**Appendix K**

SEBAL$_{ID}$ – Special Topics

M. Tasumi and R. Trezza</center>

DEM Adjusted Surface Temperature

As explained in Chapter V, the surface temperature that is used in SEBAL$_{ID}$

needs to be uniformly adjusted to a common reference elevation for accurate prediction

of dT when land elevation varies. Otherwise, high elevations that appear to be "cool"

(due to orographic cooling) may be misinterpreted as having low sensible heat flux (low

dT) and therefore high evaporation. SEBAL$_{ID}$ assumes that the lapse rate of surface

temperature with height is 6.5°C/km, which is a general lapse rate for moist air. Figure

K.1 shows examples of the trend of T_s and calculated $T_{s(DEM)}$ for three mountainous

areas. It seems that by applying the 6.5°C/km lapse rate, the distribution of $T_{s(DEM)}$

becomes random with elevation. This indicates that $T_{s(DEM)}$ efficiently eliminates the

elevation effects from the surface temperature. Therefore, most of the variation in

$T_{s(DEM)}$, after correction for lapse, is due to slope and aspect of the surfaces in the

mountains.

SEBAL$_{ID}$ Sensitivity Analysis

It was demonstrated in Chapter VI that the estimation of ET using SEBAL$_{ID}$ was

quite insensitive to the use of both corrected radiometric surface temperature and

corrected surface albedo. In this Appendix, sensitivity of SEBAL$_{ID}$ to other model key
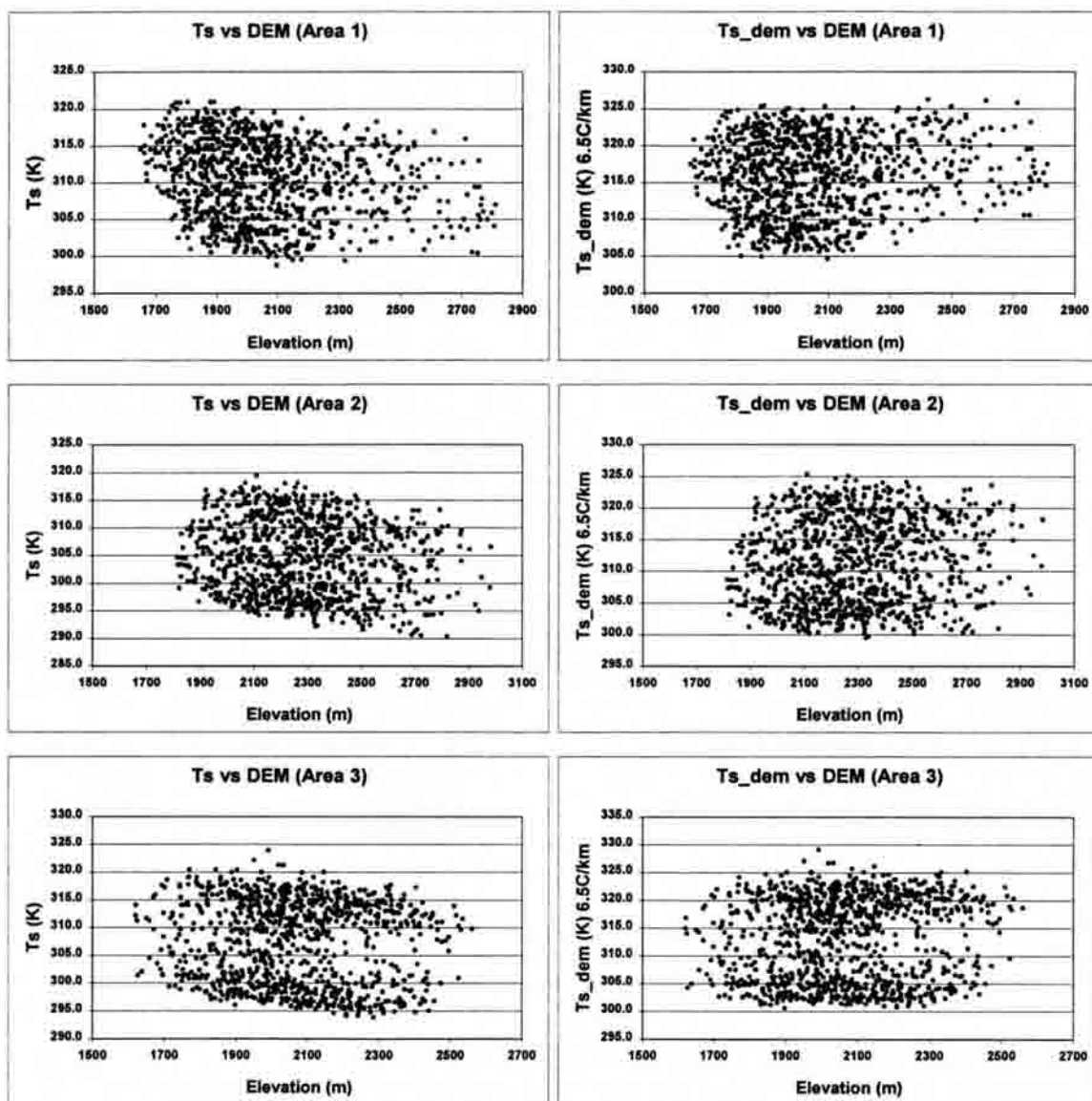
inputs is discussed.

FIGURE K.1. Calculated T_s (left) and $T_{s(DEM)}$ (right) in different Elevation Ranges, for Three Mountain Areas in Path 40, Row 29, 9/15/2000.

Surface Roughness of Momentum
Transport, z_{om}

The estimation of z_{om} is a weak point in $SEBAL_{ID}$. Especially, the accuracy of z_{om} estimation for land uses other than agriculture is limited. However, ET estimation is not very sensitive to z_{om}. Therefore, the low quality of z_{om} estimation in $SEBAL_{ID}$ does

not cause large error in ET. This is especially true for areas having high ET where H is

small. In agricultural areas, estimated ET is not impacted even if z_{om} is doubled or

halved (Fig. K.2). This is because the z_{om} value is applied as a log of $200/z_{om}$ in u_*

estimation (Eq. 3.43) and also because the range of z_{om} for agricultural pixels is

relatively narrow. In addition, because ET at the cold pixel is fixed as $1.05ET_r$, any

change in roughness for pixels similar to the cold pixel will automatically be
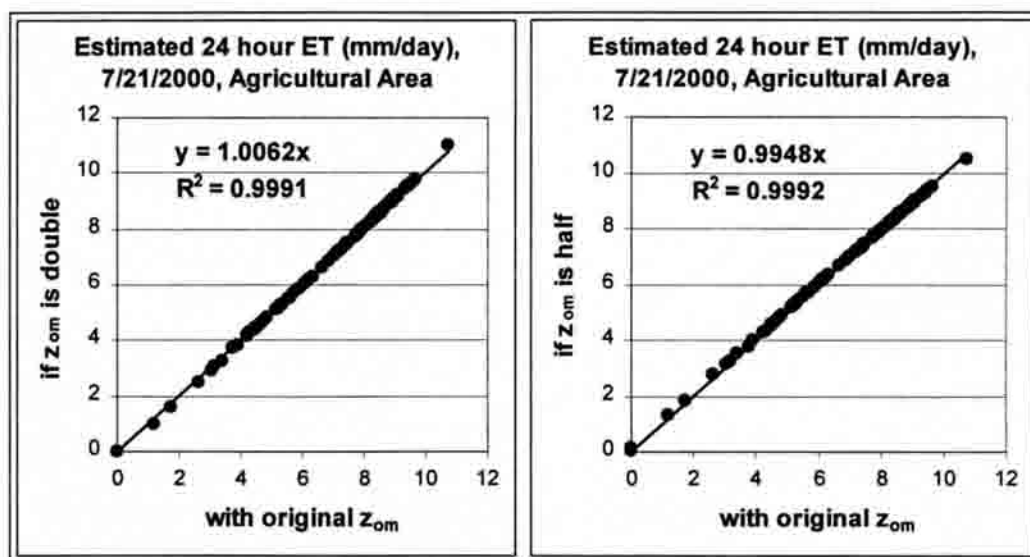
compensated for by a change in predicted dT.

FIGURE. K.2   Impact of Error in z_{om} Values on Estimated $ET_{(24)}$, from Agricultural
areas in Path40 Row30, 7/21/2000

However, in city areas, the quality of estimated z_{om} is much lower than for

agricultural areas, and therefore the high uncertainty in z_{om} values affects ET estimation

somewhat. For example, in the $SEBAL_{ID}$ application of Southern Idaho, a fixed z_{om}

value of 0.2m was applied to city areas. This value was assigned to a broad range of

surfaces, from smooth interstate highways to very rough building areas. ET can be impacted if the estimated z_{om} value is far from the actual value (See Fig. K.3). To improve the ET estimation for landuses other than agricultural areas, one should consider developing a better z_{om} map for SEBAL$_{ID}$. Using a finer land use classification and applying the representative z_{om} values for each sub land use type would improve ET estimation. Further study is needed for both z_{om} and H for cities and for other surfaces.
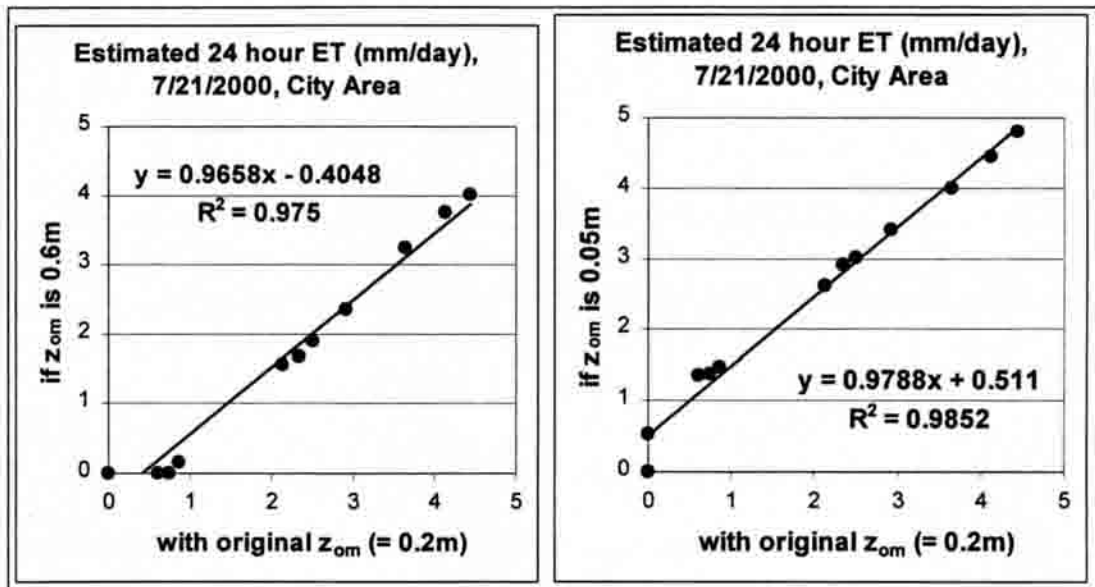

FIGURE. K.3   Impact of error in z_{om} values on estimated ET$_{(24)}$, from City Areas in Path40 Row30, 7/21/2000

dT Function and the Effect of Windspeed on
Surface Temperature

In SEBAL$_{ID}$, ET estimation is not significantly sensitive to the wind speed input. For example, the estimated windspeed at 200m above the weather station was estimated to be 6.5m/s in 7/21/2000, based on a measurement at 2 meters at Kimberly Idaho. However, estimated ET does not change even if the windspeed input is double the actual

measurement (see Fig. K.4). This is due to the effect of strong internal calibration of the

energy balance and dT vs T_s function at the cold and the hot pixels.
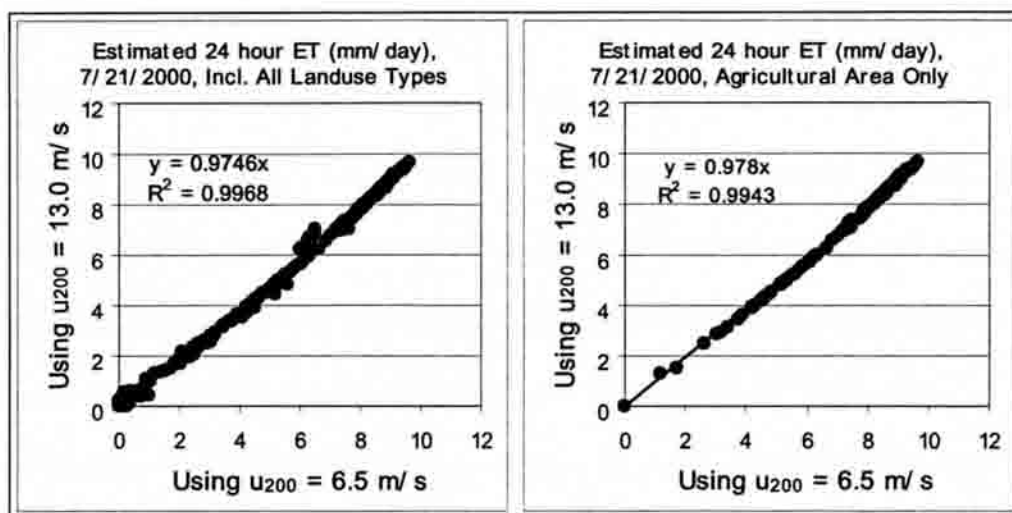

FIGURE K.4 .   Estimated ET Values using the Measured windspeed (x axis), and
                  using Doubled windspeed (y axis) as input, for all Landuse Types (left)
                  and for Agricultural Fields only (right).

The H estimation procedure in SEBAL$_{ID}$ is quite stable and little impacted by the

overestimation of windspeed. However, SEBAL$_{ID}$ can be somewhat sensitive,

numerically, to the underestimation of windspeed due to numerical problems in the

stability correction. In the case of the 7/21/2000 image, the H estimation process failed

to converge when windspeed input was half of the actual value. In 7/21/2000, the

estimated H at the selected cold pixel was -69 W/m^2 which means that the surface

temperature at the cold pixel was colder than the predicted air temperature because of the

effect of regional advection. In that case, the artificially calm windspeed created an

aerodynamic resistance that was too large to allow the transfer of negative 69 W/m^2 of H,

and therefore the H iteration process became numerically instable (or in other word, diverged). This numerical phenomenon needs to be protected against.

These evaluations of effects of overestimation and underestimation of windspeed are for the cases when windspeed of the entire area of interest is equally over/under estimated. However, the most challenging problem occurs when windspeed changes significantly with location within an image. For example, for the a dry bare soil, one can expect a higher surface temperature in locations where the wind is calm, and a lower temperature in locations where the wind speed is higher within the same image; however this trend can be inverted if regional or local advection is present. In any case, estimation of aerodynamic resistance, r_{ah} , and the dT function are affected by the magnitude of wind speed (See Eq. 3.28).

To illustrate the relationship between wind speed and surface temperature, Fig. 6.5 shows a hypothetical "Area 1" where $u_{200} = 6.5$m/s, and a hypothetical "Area 2" , which has a much higher wind speed $u_{200} = 13$ m/s. In Sebal, cold and hot pixels would selected from Area 1 so that the dT function is derived based on the lower wind speed ($u_{200} = 6.5$m/s). The problem is that the dT function developed for Area 1 might not be representative of the conditions present in Area 2, because the higher wind speed in this area can affect the surface temperature of cold and hot pixel candidates in Area 2.

An analysis performed by Tasumi (2003) indicated a clear correlation between windspeed and surface temperature. Figure K.6 shows surface temperatures from two desert locations on the Snake River Plain, and measured windspeed from the nearest weather stations. Desert site PB is located in the middle of a large desert near *Potter*
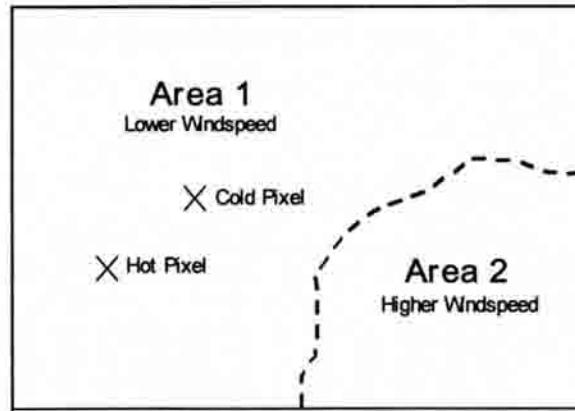
FIGURE K.5.   Sketch of two different weather conditions within one image.

Butte, and the other desert site TF is about 70 km to *Twin Falls*. Difference in local

advection were observed in the surface temperatures due to proximity of the TF location

to agricultural areas. However, by eliminating this difference by drawing a ΔT_s trend

curve between the two locations, windspeed is shown to clearly reduce the surface

temperature.

Returning to the problem illustrated in Fig. K.5, not only the windspeed condition

but also the surface temperature condition may be different between Area 1 and Area 2,

so that the appropriate dT function can be different for each area. The error generated by

the windspeed difference should be greater in "dry" areas than in "wet" areas, since the

windspeed primarily affects the H estimation. In such cases, the most appropriate

solution is to separate an image into two sub-areas based on the weather condition, and

operate SEBAL$_{ID}$ separately, using different cold and hot pixels and weather data.

Generally, one can regard the windspeed condition as similar if hot pixel candidates over

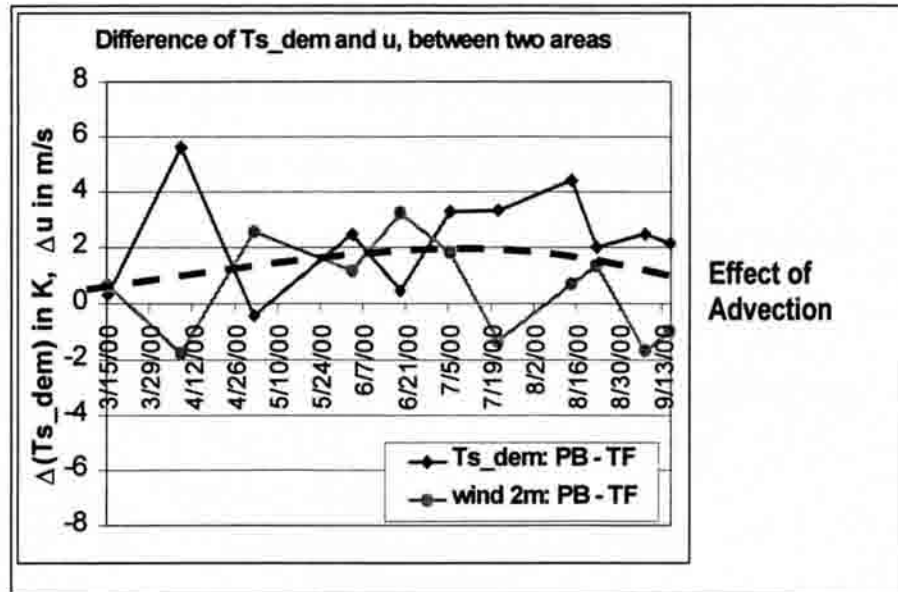the area of interest have a similar surface temperature range.

FIGURE K.6. Surface Temperature and Windspeed for Satellite Image date/time at two Locations (PB: Potter Butte, and TF: Twin Falls, Idaho). Tasumi, 2003.

In the SEBAL application in Idaho, Tasumi (2003) separated the area

corresponding to path 40 in the Snake River Plain into two sub-areas, one being the

Snake River Plain and the other being Northern Mountain Areas. These two sub-areas

had different dT functions. In this study, the area corresponding to path 39 was treated as

a whole, because wind speed was similar within locations during the satellite dates.

Sensitivity of SEBAL$_{ID}$ for Atmospheric Stability

SEBAL$_{ID}$ uses a procedure based on the Monin-Obukov length (Eq. 3.34) to

estimate sensible heat at each pixel. Fig. K.7 shows a comparison between 24 hour ET

obtained considering stability correction for sensible heat flux and without considering

stability correction (this means assuming $\psi_{z1} = \psi_{z2} = \psi_{200m} = 0$ in Eqs. 3.29 and 3.43) for

the scene corresponding to 08/14/2000. The maximum difference between the two ET

estimates was less than 0.4 mm/day, which represents just 6 % of the $ET_r = 6.8$ mm/day. The relatively low sensitivity of $SEBAL_{ID}$ to the use of stability parameters, shows the high control that the definition of LE in the cold and hot pixels produces in the final estimation of ET. This does not mean that $SEBAL_{ID}$ does not require the correction of H for atmospheric stability, but it is an indication that some uncertainties involved in the calculation of H are cancelled out, so that the final ET is not dramatically impacted.
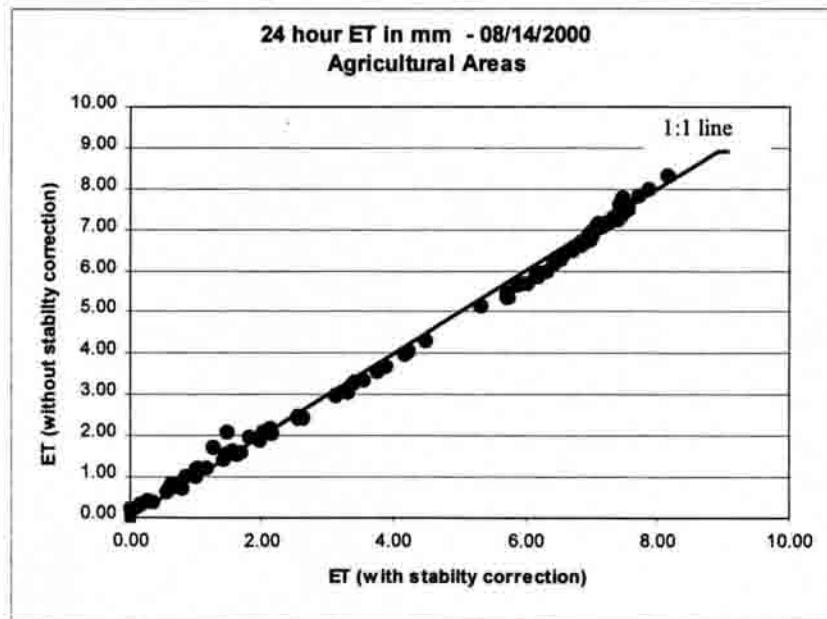

FIGURE K.7   Comparison Between 24 hour ET using and neglecting Stability
Corrections for Sensible Heat Calculation for the Scene of 08/14/2000.

Location of the Hot and Cold Pixels
selected for validation of $SEBAL_{ID}$

The exact locations of the cold and hot pixels considered for the validation of

$SEBAL_{ID}$ are included in Table K.1.

TABLE K.1.   Location of Hot and Cold Pixels corresponding to the Processed Landsat
5 Scenes (path 40, row 30) during 1989.

Date of Image	Cold Pixel (UTM) X	Cold Pixel (UTM) Y	Hot Pixel (UTM) X	Hot Pixel (UTM) Y
04/18/89	484362	156372	470894	152450
05/04/89	468319	159471	471930	153150
05/20/89	482534	150705	473640	155791
06/05/89	483130	150720	471247	158680
06/21/89	472936	161862	490124	161006
07/07/89	447782	165425	488226	159428
07/23/89	480907	167848	489942	160059
09/25/89	458402	157204	469786	163593

VITA

Ricardo Trezza

Candidate for the Degree of

Doctor of Philosophy

Dissertation: Evapotranspiration Using A Satellite-Based Surface Energy Balance With Standardized Ground Control

Major Field: Biological and Agricultural Engineering

Biographical Information:

Personal Data: Born in Valera, Venezuela, son of Antonio and Dalia Trezza; married to Neyle Trezza; daughter Rebecca Paola Trezza.

Education: Graduated as Agricultural Engineering from University of Los Andes, Venezuela in 1988; Received Master of Science Degree in Irrigation and Drainage Engineering from CIDIAT-University of Los Andes, Venezuela, in 1995; in 2002 completed the requirements for the Doctor of Philosophy degree, with a major in Biological and Agricultural Engineering from Utah State University in Logan, Utah.

Professional Experience: Assistant Engineer, Inter-American Center for Environmental Research (CIDIAT) 1987-1989; Graduate Research Assistant at the University of Idaho, Idaho, 2001-2002; Associate Professor at the University of Los Andes, Venezuela 1990-present.

Awards and Honors: Fulbright Scholar 1997-1999; member of Phi Kappa Phi, National Honor Society